

Tailored Optical Properties on the Macroscale  
by Template-Assisted Self-Assembly of  
Plasmonic Nanoparticles

# Dissertation

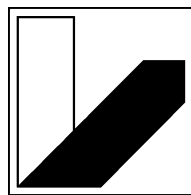
zur Erlangung des akademischen Grades eines

**Doktors der Naturwissenschaften**

**(Dr. rer. nat.)**

an der

Bayreuther Graduiertenschule für Mathematik  
und Naturwissenschaften der Universität Bayreuth



**UNIVERSITÄT  
BAYREUTH**

vorgelegt von

Moritz Jan Tebbe

geboren in Henstedt-Ulzburg

Juli 2015

Die vorliegende Arbeit wurde im Zeitraum vom April 2012 bis Juli 2015 an der Universität Bayreuth in Bayreuth am Lehrstuhl Physikalische Chemie II unter der Betreuung von Herrn Professor Dr. Andreas Fery angefertigt.

Vollständiger Abdruck der von der Bayreuther Graduiertenschule für Mathematik und Naturwissenschaften (BayNAT) der Universität Bayreuth genehmigten Dissertation zur Erlangung des akademischen Grades eines Doktors der Naturwissenschaften (Dr. rer. nat.).

Dissertation eingereicht am: 10.07.2015

Zulassung durch das Leitungsgremium am: 28.07.2015

Wissenschaftliches Kolloquium am: 27.11.2015

Amtierender Direktor: Professor Dr. Stephan Kümmel (seit 01.10.2015)

Prüfungsausschuss:

Professor Dr. Andreas Fery (Erstgutachter)

Professor Dr. Matthias Karg (Zweitgutachter)

Professor Dr. Josef Breu (Vorsitz)

Professor Dr. Andreas Greiner

Dr. Tobias Kraus (Drittgutachter)

Meiner Familie



# Contents

<b>Contents</b> .....	<b>I</b>
<b>Abbreviations</b> .....	<b>III</b>
<b>List of Publications</b> .....	<b>V</b>
<b>1. Introduction</b> .....	<b>1</b>
<b>2. Overview of the Thesis</b> .....	<b>11</b>
<b>3. Theory and Status of the Field</b> .....	<b>39</b>
3.1 Plasmonics .....	41
3.2 Surface-Enhanced Raman Scattering.....	48
3.3 Metamaterials .....	51
3.4 Gold Nanorod Synthesis.....	54
3.4.1 Synthesis of Penta-Twinned Gold Nanorods.....	56
3.4.2 Synthesis of Single-Crystalline Gold Nanorods .....	57
3.5 Surface Functionalization of Gold Nanorods .....	61
3.6 Colloidal Surface-Assemblies.....	63
3.6.1 The Forces at Work in Colloidal Self-Assembly .....	65
3.6.2 Self-Assembly Methods.....	67
3.6.3 Self-Assembly of Gold Nanorods.....	69
3.6.4 Lithography-free Templates.....	71
<b>I. Synthesis of Plasmonic Building Blocks</b> .....	<b>101</b>
<b>4. Silver-Overgrowth-Induced Changes in Intrinsic Optical Properties of Gold Nanorods: From Non-Invasive Monitoring of Growth Kinetics to Tailoring Internal Mirror Charges</b> .....	<b>103</b>

5.	Colloidally Stable and Surfactant-Free Protein-Coated Gold Nanorods in Biological Media .....	147
<b>II.</b>	<b>Controlled Alignment of Gold Nanorods .....</b>	<b>177</b>
6.	Optically Anisotropic Substrates <i>via</i> Wrinkle-Assisted Convective Assembly of Gold Nanorods on Macroscopic Areas .....	179
7.	Reversible Gold Nanorod Alignment in Mechano-Responsive Elastomers .....	211
<b>III.</b>	<b>Close-Packed Nanoparticle Assemblies as SERS Platforms.....</b>	<b>241</b>
8.	Organized Solid Thin Films of Gold Nanorods with Different Sizes for Surface-Enhanced Raman Scattering Applications .....	243
9.	Macroscale Plasmonic Substrates for Highly Sensitive Surface-Enhanced Raman Scattering.....	261
10.	SERS Platforms of Plasmonic Hydrophobic Surfaces for Analyte Concentration: Hierarchically Assembled Gold Nanorods on Anodized Aluminum.....	289
11.	<b>Perspectives.....</b>	<b>309</b>
	11.1 Investigation of Metal Nanocrystal Synthesis utilizing slow Reaction Kinetics.....	311
	11.2 Towards a Rational Design Approach for Self-Assembled Metamaterials .....	312
12	<b>Summary/Zusammenfassung.....</b>	<b>317</b>
	<b>Acknowledgements/Danksagungen.....</b>	<b>I</b>

## Abbreviations

AA	Ascorbic acid
AAO	Anodized aluminum oxide
AFM	Atomic force microscopy
AR	Aspect ratio
AuNR	Gold nanorod
AuNS	Gold nanosphere
BC	Boundary conditions
BDAC	Benzyltrimethylhexadecylammonium chloride
BEM	Boundary element method
BSA	Bovine serum albumin
CFA	Capillary force assembly
CMC	Critical micelle concentration
CTAB	Cetyltrimethylammonium bromide
CTAC	Cetyltrimethylammonium chloride
DDA	Discrete dipole approximation
DLVO	Derjaguin-Landau-Verwey and Overbeek
DMEM	Dulbecco's modified eagle's medium
DNA	Deoxyribonucleic acid
EDL	Electric double-layer
EF	Enhancement factor
EM	Electromagnetic
fcc	face centered cubic
FDTD	Finite-difference time-domain
FON	Film over nanosphere
FWHM	Full width at half maximum
HQ	Hydroquinone
ITO	Indium tin oxide
LBL	Layer-by-layer

## Abbreviations

---

LSPR	Localized surface plasmon resonance
MMP	Multiple multipole
NCS	New born calf serum
NIM	Negative index material/metamaterial
NIR	Near-infrared
NPs	Nanoparticles
NSL	Nanosphere lithography
PBS	Phosphate-buffered saline
PDMS	Poly(dimethylsiloxane)
PEG	Poly(ethylene glycol)
pNIPAM	Poly(N-isopropylacrylamide)
SAXS	Small-angle X-ray scattering
SEM	Scanning electron microscopy
SERS	Surface-enhanced Raman scattering/spectroscopy
SM	Single molecule
SRR	Split ring resonator
TASA	Template-assisted self-assembly
TEM	Transmission electron microscopy
TISIT	Thiol-isoprene-styrene-isoprene-thiol
UV	Ultraviolet
vdW	Van der Waals

## List of Publications

### Peer-Reviewed Publications included in this Thesis

#### Chapter 4

##### **Silver-Overgrowth-Induced Changes in Intrinsic Optical Properties of Gold Nanorods: From Noninvasive Monitoring of Growth Kinetics to Tailoring Internal Mirror Charges**

**Tebbe, M.**; Kuttner, C.; Mayer, M.; Maennel, M.; Pazos-Perez, N.; König, T. A. F.; Fery, A., *Journal of Physical Chemistry C* **2015**, *119*, 9513-9523.

#### Chapter 5

##### **Colloidally Stable and Surfactant-Free Protein-Coated Gold Nanorods in Biological Media**

**Tebbe, M.**; Kuttner, C.; Maennel, M.; Fery, A.; Chanana, M., *ACS Applied Materials & Interfaces* **2015**, *7*, 5984–5991.

#### Chapter 6

##### **Optically Anisotropic Substrates *via* Wrinkle-Assisted Convective Assembly of Gold Nanorods on Macroscopic Areas**

**Tebbe, M.**; Mayer, M.; Glatz, B. A.; Hanske, C.; Probst, P. T.; Müller, M. B.; Karg, M.; Chanana, M.; König, T. A. F.; Kuttner, C.; Fery, A., *Faraday Discussion* **2015**, *118*, 243-260.

#### Chapter 7

##### **Reversible Gold Nanorod Alignment in Mechano-Responsive Elastomers**

Pletsch, H.; **Tebbe, M.**; Dulle, M.; Förster, B.; Fery, A.; Förster, S.; Greiner A.; Agarwal, S., *Polymer* **2015**, *66*, 167-172.

Chapter 8

**Organized Solid Thin Films of Gold Nanorods with Different Sizes for Surface-Enhanced Raman Scattering Applications**

**Tebbe, M.**; Maennel, M.; Fery, A.; Pazos-Perez, N.; Alvarez-Puebla, R. A., *Journal of Physical Chemistry C* **2014**, *118*, 28095–28100.

Chapter 9

**Macroscale Plasmonic Substrates for Highly Sensitive Surface-Enhanced Raman Scattering**

Alba, M.; Pazos-Perez, N.; Vaz, B.; Formentin, P.; **Tebbe, M.**; Correa-Duarte, M. A.; Granero, P.; Ferré-Borrull, J.; Alvarez, R.; Pallares, J.; Fery, A.; de Lera, A. R.; Marsal, L. F.; Alvarez-Puebla R. A., *Angewandte Chemie International Edition* **2013**, *52*, 6459-6463.

Chapter 10

**SERS Platforms of Plasmonic Hydrophobic Surfaces for Analyte Concentration: Hierarchically Assembled Gold Nanorods on Anodized Aluminum**

**Tebbe, M.**; Cherepanov, P.; Skorb, E. V.; Poznyak, S. K.; Garcia de Abajo, J.; Fery, A.; Andreeva, D. V.; Alvarez Puebla, R. A.; Pazos-Perez, N., *Particle & Particle Systems Characterization* **2014**, *13*, 1134-1140.

**Further Publications not included in this Thesis**

[1] Mayer, M.; Scarabelli, L.; March, K.; Altantzis, T.; **Tebbe, M.**; Kociak, M.; Bals, S.; Garcia de Abajo, J.; Fery, A.; Liz-Marzan, L. "Controlled Living Nanowire Growth – Precise Control over the Morphology and Optical Properties of AgAuAg Bimetallic Nanowires", *Nano Letters*, **2015**, *15*, 5427–5437.

[2] Glatz, B. A.; **Tebbe, M.**; Kaoui, B.; Aichele, R.; Kuttner, C.; Schedl, A. E.; Schmidt, H.-W.; Zimmermann, W.; Fery, A., "Hierarchical Line-Defect Patterns in Wrinkled Surfaces", *Soft Matter* **2015**, *11*, 3332-3339.

- [3] Hanske, C.; **Tebbe, M.**; Kuttner, C.; Biber, V.; Tsukruk, V.; Chanana, M.; Koenig, T. A. F.; Fery, A. „Strongly Coupled Plasmonic Modes on Macroscopic Areas via Template-Assisted Colloidal Self-Assembly“, *Nano Letters* **2014**, *14*, 6863–6871.
- [4] Hanske, C.; Müller, M. B.; Bieber, V.; **Tebbe, M.**; Jessl, S.; Wittemann, A.; Fery, A., “The Role of Substrate Wettability in Nanoparticle Transfer from Wrinkled Elastomers: Fundamentals and Application towards Hierarchical Patterning”, *Langmuir* **2012**, *28*, 16745–16750.
- [5] Kuttner, C.; **Tebbe, M.**; Schlaad, H.; Burgert, I.; Fery, A., “Photochemical Synthesis of polymeric Fiber Coatings and their Embedding in Matrix Material: Morphology and nanomechanical Properties at the Fiber-Matrix Interface”, *ACS Applied Materials & Interfaces* **2012**, *4*, 3485-3492.
- [6] Mueller, M.; **Tebbe, M.**; Andreeva, D. V.; Karg, M.; Alvarez-Puebla, R.; Pazos-Perez, N.; Fery, A., “Large-Area Organization of pNIPAM-Coated Nanostars as SERS Platforms for Polycyclic Aromatic Hydrocarbons Sensing in Gas Phase”, *Langmuir* **2012**, *28*, 9168-9173.
- [7] Claussen, K. U.; **Tebbe, M.**; Giesa, R., Schweikart, A.; Fery, A.; Schmidt, H.-W., “Towards Tailored Topography: Facile Preparation of Surface-Wrinkled Gradient Poly(dimethyl siloxane) with Continuously Changing Wavelength”, *RSC Advances* **2012**, *2*, 10185-10188.

## Patents

- [1] Alvarez-Puebla, R.A.; Pazos-Perez, N.; Alba, M.; Vaz, B.; Tormentín, P.; **Tebbe, M.**; Correa-Duarte, M.A.; Granero, P.; Ferré-Borrull, J.; Alvarez, R.; Pallares, J.; Fery, A.; de Lera, A.R.; Marsal, L.F., "Procedimiento para la fabricación de supercristales coloidales con campos electromagnéticos altamente localizados y su utilización para la detección y monitorización de analitos", P26763ES00-27032013, **2013**, Spain.



# ***1***

## Introduction



The research field of plasmonics explores the interaction of electromagnetic radiation and conduction electrons bound to metallic interfaces or metallic nanostructures as part of the intriguing field of nanophotonics.<sup>1,2</sup> Resonant excitation of conduction electrons in metal nanostructures gives rise to collective oscillations, so called plasmon resonances and allows to confine the electromagnetic field on subwavelength dimensions.<sup>1,2</sup> This leads to optical near-field enhancement and results in strong absorption and scattering cross-sections of metal nanoparticles that provide the beautiful colors of metal nanocrystal dispersions and have been used since ancient times to stain glass.<sup>1,2</sup> The mathematical description of plasmonics is based on classical electrodynamics and has been established already at the turn of the 20<sup>th</sup> century, *e.g.* by Mie for localized surface plasmon resonances in metal nanoparticles.<sup>1-3</sup>

However, the modern renaissance of plasmonics, that took place within the last decades, is due to significant advances within the fields of metal nanostructure fabrication, optical characterization, and numerical modelling, which greatly enhanced our fundamental understanding of plasmonics and paved the road towards the rational design of metal nanostructures for a wide range of potential applications.<sup>1,2</sup> Especially the discovery of the surface-enhanced Raman scattering effect within the 70ies awakened the interest of researchers in manufacturing well-defined metal nanostructures to gain control over the electromagnetic near-field enhancement effect.<sup>4,5</sup> Today this technique allows to detect molecules even on the single-molecule level.<sup>6,7</sup>

Besides this example, a plethora of other potential applications of plasmonic nanostructures have been proposed based on the ability to push optics into the nanometer size-regime, below the diffraction limit and research activities within this field take place at an astonishing pace.<sup>1,2</sup>

The tunable absorption and scattering properties of individual and coupled plasmonic nanoparticles render them interesting candidates for various different applications, *e.g.* as bio-labels,<sup>8,9</sup> for drug-delivery,<sup>8,9</sup> for hyperthermia therapy,<sup>8,9</sup> as plasmonic color filters<sup>10,11</sup> and for multi-dimensional high-density optical data storage.<sup>12</sup> Strong localized field enhancement enables highly sensitive optical sensing, *e.g.* the already mentioned surface-enhanced Raman or IR spectroscopy,<sup>13-17</sup> and gives rise to non-linear optical effects.<sup>18,19</sup> Based on the strong distance and orientation dependency of plasmonic coupling the concept of plasmon rulers was developed<sup>20,21</sup> and the strong

dependency of the resonance frequencies of metal nanostructures on the dielectric environment is used for refractive index sensing.<sup>22,23</sup> The ability to efficiently transport energy *via* subdiffraction limit waveguiding and to confine and manipulate plasmons within optical nanocircuits on length-scales comparable to electronic components is very promising for the design of compact optoelectronic devices.<sup>24-27</sup> Furthermore, light-management based on plasmonic nanostructures within solar cells might lead to significantly enhanced energy conversion efficiencies.<sup>28-30</sup> Plasmonic building blocks can even give rise to negative magnetic permeability and electric permittivity and, thus, can be used as artificial atoms to design materials with unusual effective medium constants, *e.g.* negative index of refraction,<sup>31,32</sup> which might find application in subdiffraction limit imaging (perfect lenses)<sup>33</sup> and optical cloaking.<sup>31</sup>

All the above mentioned design approaches rely on precise spatial placement and distinct control over the dimensions and orientation of the individual plasmonic building blocks within one-, two- or three-dimensional plasmonic arrays.<sup>1,2,31,34,35</sup> For the nanofabrication of metal nanostructures at surfaces, most often lithographic approaches, *e.g.* e-beam lithography or ion-beam milling are applied, due to their versatility and precision.<sup>1,2,34,35</sup> However, these techniques come along with several drawbacks such as limited scalability, limited resolution, limited compatibility with silicon manufacturing techniques, damping effects due to the polycrystalline nature of prepared metal nanostructures and low sample throughput.<sup>2,34,36-38</sup> Thus, there is a great demand for alternative approaches for the fabrication of metal nanostructures to overcome abovementioned limitations.

Directed self-assembly of nanoscale plasmonic building blocks is a versatile bottom-up approach that represents a compelling alternative to commonly used top-down nanofabrication methods.<sup>39-41</sup>

Recent advances in wet-chemical seed-mediated metal nanocrystal synthesis provide a huge library of plasmonic building blocks with well-defined shapes, sizes, compositions, and tailored optical properties.<sup>8,42</sup> Especially gold nanorods have gained a lot of attention, due to their tunable anisotropic optical properties and the ability to prepare these metal nanocrystals with narrow size distribution and in large quantities.<sup>9,43</sup>

The evaporation induced template-assisted self-assembly of colloidal particles allows control over spatial position and orientation within one-, two-, and three-dimensional

colloidal surface-assemblies.<sup>41,44</sup> Consequently, this technique holds great potential as highly efficient means for the large-area bottom-up fabrication of nanostructured plasmonic surface-assemblies with tailored macroscopic optical properties while overcoming aforementioned restrictions.<sup>37,45-48</sup>

Within this context, the objective of this thesis is the preparation of nanostructured hierarchical plasmonic surface-assemblies with tailored optical properties on the macroscale.

To achieve this goal, tailoring the spatial dimensions, surface-chemistry, and optical properties on the level of individual plasmonic building blocks is a pivotal requirement. Therefore, surfactant-mediated wet-chemical synthesis and subsequent surface functionalization of anisotropic metal nanocrystals will be applied and optimized to provide compatibility with convective self-assembly techniques and gain control over interparticle spacing within close-packed organizations.

Depending on the targeted optical properties, *e.g.* high localized field enhancement or anisotropic optical response on the macroscale, different types of nanostructures, *e.g.* close-packed assemblies or precisely aligned chains of gold nanorods, need to be realized. Convective self-assembly of metal nanocrystals on topographic templates, which possess nanoscale features with tailorable dimensions, represents an ideal means to achieve this goal. This technique enables precise control over spatial placement and orientation of plasmonic entities within prepared hierarchical surface-assemblies. Furthermore, in combination with templates prepared in a scalable fashion, this approach allows fabrication of plasmonic arrays on macroscopic sample areas.

Consequently, the central aim of my work is to identify and optimize the key parameters that control the directed convective self-assembly of anisotropic metal nanocrystals to eventually prepare well-defined macroscopic plasmonic nanostructures with tailored optical properties.

## References

- (1) Maier, S. A., *Plasmonics: Fundamentals and Application*. Springer Science + Business Media: United States of America, New York, 2007; p 223.
- (2) Pelton, M.; Bryant, G., *Introduction to Metal-Nanoparticle Plasmonics*. John Wiley & Sons: United States of America, New Jersey, 2013; p 275.
- (3) Mie, G., Beiträge zur Optik trüber Medien, speziell kolloidaler Metallösungen. *Ann Phys* **1908**, *330*, 377-445.
- (4) Jeanmaire, D. L.; Van Duyne, R. P., Surface raman spectroelectrochemistry: Part I. Heterocyclic, aromatic, and aliphatic amines adsorbed on the anodized silver electrode. *J Electroanal Chem Interfacial Electrochem* **1977**, *84*, 1-20.
- (5) Albrecht, M. G.; Creighton, J. A., Anomalously intense Raman spectra of pyridine at a silver electrode. *J Am Chem Soc* **1977**, *99*, 5215-5217.
- (6) Nie, S.; Emory, S. R., Probing Single Molecules and Single Nanoparticles by Surface-Enhanced Raman Scattering. *Science* **1997**, *275*, 1102-1106.
- (7) Kneipp, K.; Wang, Y.; Kneipp, H.; Perelman, L. T.; Itzkan, I.; Dasari, R. R.; Feld, M. S., Single Molecule Detection Using Surface-Enhanced Raman Scattering (SERS). *Phys Rev Lett* **1997**, *78*, 1667-1670.
- (8) Dreaden, E. C.; Alkilany, A. M.; Huang, X.; Murphy, C. J.; El-Sayed, M. A., The golden age: gold nanoparticles for biomedicine. *Chem Soc Rev* **2012**, *41*, 2740-2779.
- (9) Chen, H.; Shao, L.; Li, Q.; Wang, J., Gold nanorods and their plasmonic properties. *Chem Soc Rev* **2013**, *42*, 2679-2724.
- (10) Pérez-Juste, J.; Rodríguez-González, B.; Mulvaney, P.; Liz-Marzán, L. M., Optical Control and Patterning of Gold-Nanorod–Poly(vinyl alcohol) Nanocomposite Films. *Adv Funct Mater* **2005**, *15*, 1065-1071.
- (11) Kuemin, C.; Nowack, L.; Bozano, L.; Spencer, N. D.; Wolf, H., Oriented Assembly of Gold Nanorods on the Single-Particle Level. *Adv Funct Mater* **2012**, *22*, 702-708.

- 
- (12) Zijlstra, P.; Chon, J. W. M.; Gu, M., Five-dimensional optical recording mediated by surface plasmons in gold nanorods. *Nature* **2009**, *459*, 410-413.
- (13) Le Ru, E. C.; Etchegoin, P. G., Quantifying SERS enhancements. *MRS Bull* **2013**, *38*, 631-640.
- (14) Sharma, B.; Frontiera, R. R.; Henry, A.-I.; Ringe, E.; Van Duyne, R. P., SERS: Materials, applications, and the future. *Mater Today* **2012**, *15*, 16-25.
- (15) Stiles, P. L.; Dieringer, J. A.; Shah, N. C.; Van Duyne, R. R., Surface-Enhanced Raman Spectroscopy. *Annu Rev Anal Chem* **2008**, *1*, 601-626.
- (16) Wang, H.; Kundu, J.; Halas, N. J., Plasmonic Nanoshell Arrays Combine Surface-Enhanced Vibrational Spectroscopies on a Single Substrate. *Angew Chem, Int Ed* **2007**, *46*, 9040-9044.
- (17) Adato, R.; Altug, H., In-situ ultra-sensitive infrared absorption spectroscopy of biomolecule interactions in real time with plasmonic nanoantennas. *Nat Commun* **2013**, *4:2154*, 1-10.
- (18) Kauranen, M.; Zayats, A. V., Nonlinear plasmonics. *Nat Photonics* **2012**, *6*, 737-748.
- (19) Metzger, B.; Schumacher, T.; Hentschel, M.; Lippitz, M.; Giessen, H., Third Harmonic Mechanism in Complex Plasmonic Fano Structures. *ACS Photonics* **2014**, *1*, 471-476.
- (20) Sönnichsen, C.; Reinhard, B. M.; Liphardt, J.; Alivisatos, A. P., A molecular ruler based on plasmon coupling of single gold and silver nanoparticles. *Nat Biotechnol* **2005**, *23*, 741-745.
- (21) Liu, N.; Hentschel, M.; Weiss, T.; Alivisatos, A. P.; Giessen, H., Three-Dimensional Plasmon Rulers. *Science* **2011**, *332*, 1407-1410.
- (22) Anker, J. N.; Hall, W. P.; Lyandres, O.; Shah, N. C.; Zhao, J.; Van Duyne, R. P., Biosensing with plasmonic nanosensors. *Nat Mater* **2008**, *7*, 442-453.

- (23) Liu, N.; Mesch, M.; Weiss, T.; Hentschel, M.; Giessen, H., Infrared Perfect Absorber and Its Application As Plasmonic Sensor. *Nano Lett* **2010**, *10*, 2342-2348.
- (24) Atwater, H. A., The promise of plasmonics. *Sci Am* **2007**, *296*, 56-62.
- (25) Maier, S. A.; Kik, P. G.; Atwater, H. A.; Meltzer, S.; Harel, E.; Koel, B. E.; Requicha, A. A. G., Local detection of electromagnetic energy transport below the diffraction limit in metal nanoparticle plasmon waveguides. *Nat Mater* **2003**, *2*, 229-232.
- (26) Maier, S. A.; Brongersma, M. L.; Kik, P. G.; Meltzer, S.; Requicha, A. A.; Atwater, H. A., Plasmonics-a route to nanoscale optical devices. *Adv Mater* **2001**, *13*, 1501-1505.
- (27) Huang, K. C. Y.; Seo, M.-K.; Sarmiento, T.; Huo, Y.; Harris, J. S.; Brongersma, M. L., Electrically driven subwavelength optical nanocircuits. *Nat Photonics* **2014**, *8*, 244-249.
- (28) Atwater, H., Bending light to our will. *MRS Bull* **2011**, *36*, 57-62.
- (29) Atwater, H. A.; Polman, A., Plasmonics for improved photovoltaic devices. *Nat Mater* **2010**, *9*, 205-213.
- (30) Karg, M.; König, T. A. F.; Retsch, M.; Stelling, C.; Reichstein, P. M.; Honold, T.; Thelakkat, M.; Fery, A., Colloidal self-assembly concepts for light management in photovoltaics. *Mater Today* **2015**, *18*, 185-205.
- (31) Cai, W.; Shalaev, V. M., *Optical Metamaterials: Fundamentals and Applications*. Springer Science + Business Media: United States of America, New York, 2010; p 200.
- (32) Shalaev, V. M., Optical negative-index metamaterials. *Nat Photonics* **2007**, *1*, 41-48.
- (33) Pendry, J. B., Negative refraction makes a perfect lens. *Phys Rev Lett* **2000**, *85*, 3966-3969.

- (34) Meinzer, N.; Barnes, W. L.; Hooper, I. R., Plasmonic meta-atoms and metasurfaces. *Nat Photonics* **2014**, *8*, 889-898.
- (35) Liu, N.; Giessen, H., Coupling Effects in Optical Metamaterials. *Angew Chem, Int Ed* **2010**, *49*, 9838-9852.
- (36) Solis, D.; Willingham, B.; Nauert, S. L.; Slaughter, L. S.; Olson, J.; Swanglap, P.; Paul, A.; Chang, W.-S.; Link, S., Electromagnetic Energy Transport in Nanoparticle Chains via Dark Plasmon Modes. *Nano Lett* **2012**, *12*, 1349-1353.
- (37) Hanske, C.; Tebbe, M.; Kuttner, C.; Bieber, V.; Tsukruk, V. V.; Chanana, M.; König, T. A. F.; Fery, A., Strongly Coupled Plasmonic Modes on Macroscopic Areas via Template-Assisted Colloidal Self-Assembly. *Nano Lett* **2014**, *14*, 6863-6871.
- (38) Akselrod, G. M.; Argyropoulos, C.; Hoang, T. B.; Ciraci, C.; Fang, C.; Huang, J.; Smith, D. R.; Mikkelsen, M. H., Probing the mechanisms of large Purcell enhancement in plasmonic nanoantennas. *Nat Photonics* **2014**, *8*, 835-840.
- (39) Grzelczak, M.; Vermant, J.; Furst, E. M.; Liz-Marzán, L. M., Directed Self-Assembly of Nanoparticles. *ACS Nano* **2010**, *4*, 3591-3605.
- (40) Klinkova, A.; Choueiri, R. M.; Kumacheva, E., Self-assembled plasmonic nanostructures. *Chem Soc Rev* **2014**, *43*, 3976-3991.
- (41) Zhang, S.-Y.; Regulacio, M. D.; Han, M.-Y., Self-assembly of colloidal one-dimensional nanocrystals. *Chem Soc Rev* **2014**, *43*, 2301-2323.
- (42) Xia, Y.; Xiong, Y.; Lim, B.; Skrabalak, S. E., Shape-Controlled Synthesis of Metal Nanocrystals: Simple Chemistry Meets Complex Physics? *Angew Chem, Int Ed* **2009**, *48*, 60-103.
- (43) Vigderman, L.; Khanal, B. P.; Zubarev, E. R., Functional Gold Nanorods: Synthesis, Self-Assembly, and Sensing Applications. *Adv Mater* **2012**, *24*, 4811-4841.

- (44) Xia, Y.; Yin, Y.; Lu, Y.; McLellan, J., Template-Assisted Self-Assembly of Spherical Colloids into Complex and Controllable Structures. *Adv Funct Mater* **2003**, *13*, 907-918.
- (45) Kraus, T.; Malaquin, L.; Schmid, H.; Riess, W.; Spencer, N. D.; Wolf, H., Nanoparticle printing with single-particle resolution. *Nat Nanotechnol* **2007**, *2*, 570-576.
- (46) Fan, J. A.; Bao, K.; Sun, L.; Bao, J.; Manoharan, V. N.; Nordlander, P.; Capasso, F., Plasmonic Mode Engineering with Templated Self-Assembled Nanoclusters. *Nano Lett* **2012**, *12*, 5318-5324.
- (47) Solis, D.; Paul, A.; Olson, J.; Slaughter, L. S.; Swanglap, P.; Chang, W.-S.; Link, S., Turning the Corner: Efficient Energy Transfer in Bent Plasmonic Nanoparticle Chain Waveguides. *Nano Lett* **2013**, *13*, 4779-4784.
- (48) Slaughter, L. S.; Willingham, B. A.; Chang, W.-S.; Chester, M. H.; Ogden, N.; Link, S., Toward Plasmonic Polymers. *Nano Lett* **2012**, *12*, 3967-3972.

# 2

## Overview of the Thesis



The objective of this thesis is the development of comprehensive strategies for tailoring effective optical properties on the macroscale *via* controlled hierarchical surface-assembly of plasmonic nanoparticles. The fundamental concept pursued in this thesis can be divided into three sub-goals that are addressed in individual publications: (I) controlled large-scale synthesis of nanoscale building blocks, (II) organization of these building blocks into large-scale nanostructured surface-assemblies with tailored optical properties, and (III) characterization of the resulting optical properties.

Along this line, this thesis is divided into three parts that are intimately linked by the underlying general concept. The first part addresses the controlled large-scale synthesis and subsequent surface modification of plasmonic building blocks. The second part deals with tailored effective anisotropic optical properties of macroscopic arrangements of aligned gold nanorods. The third part focuses on the efficient and homogeneous field-enhancement of close-packed assemblies of gold nanoparticles that serve as platforms for surface-enhanced Raman scattering (SERS) spectroscopy. This overview outlines the content of the thesis and reviews the main results of the individual chapters, followed by a declaration of the contributions of all co-authors to the presented joint publications.

## **I. Synthesis of Plasmonic Building Blocks**

High-quality plasmonic building blocks, prepared in large quantities and with low polydispersity, are of central importance for the controlled fabrication of large-area surface-assemblies *via* template-assisted self-assembly (TASA). Wet-chemical seed-mediated synthesis is highly suitable for the preparation of nanoscale noble metal particles with tailored optical properties. Various parameters can be utilized to tune their size, shape, and quality, *e.g.* seed crystallinity or growth directing agents. In this context, surfactants play an important role as they provide colloidal stability and act as growth directing agents. In particular noble metal nanorods are interesting building blocks, due to their inherent anisotropic optical response. In **Chapter 4**, I studied the influence of two different surfactants on the kinetics of controlled anisotropic overgrowth of single-crystalline gold nanorods with silver into Au@Ag cuboids. Controlling and understanding the growth mechanism of nanoparticles is a key challenge to gain control over their optical properties and enhance their quality. The prepared Au@Ag cuboids exhibited complex resonance mode structures that

could be precisely tuned within the optical frequency range. Finite-difference time-domain (FDTD) simulations revealed that Au@Ag cuboids display internal mirror charges at their metal-core metal-shell interface. Mirror charges can give rise to current loops providing negative magnetic permeability. Consequently, Au@Ag cuboids are interesting building blocks potentially providing intrinsic magneto-optical properties and, thus, might find application as meta-atoms.

For implementation of plasmonic nanoparticles into TASA processes surface properties of both, the building block and the template are key properties. Amphiphilic surfactants such as cetyltrimethylammonium bromide (CTAB), interfere with template-assisted capillary force driven assembly strategies, as they strongly impair wetting properties. In **Chapter 5**, I present a procedure for the efficient replacement of CTAB with bovine serum albumin (BSA) at gold nanorod surfaces. Such protein coatings provide colloidal stability, tunable surface charges, and high hydrophilicity and, thus, facilitate the TASA of protein functionalized particles. Furthermore, such nanoparticles can be lyophilized to powders, for storing and easy handling. The absence of CTAB was proven *via* SERS, making the particles also suitable for biological applications.

In summary, this part introduces concepts to precisely tune the optical properties and adjust the surface chemistry on the individual nanoparticle level, which is a central prerequisite for the preparation of well-defined large-scale surface-assemblies.

## II. Controlled Alignment of Gold Nanorods

Hierarchical organization of nanoscale anisotropic plasmonic building blocks, on macroscopic scales with high spatial precision down to the individual constituent level, is a fundamental requirement for the bottom-up fabrication of metamaterials. In **Chapter 6**, template-assisted self-assembly of functionalized gold nanorods on wrinkle-substrates is employed as a powerful, scalable tool providing high spatial control over the position and the orientation within large-scale arrangements. With this approach, single lines and parallel double lines of close-packed tip-to-tip aligned gold nanorod assemblies were realized by precisely tuning the wrinkle amplitude. The resulting single line surface-assemblies exhibited periodicities below the wavelength of light and were characterized by interparticle coupling and a strong optical anisotropy. On the other hand, side-by-side aligned noble metal nanorod

dimers separated by a dielectric spacer, represent a central motif of metamaterials that can provide hybridized bonding modes and, consequently, negative permeability. Besides well-defined two-dimensional organizations of gold nanorods with tailored optical properties, incorporation of nanoparticles into polymeric matrices is of high interest for preparing functional nanocomposites. In **Chapter 7**, I present a strategy to transfer CTAB stabilized gold nanorods from aqueous solution into a hydrophobic, thermoplastic elastomer matrix. If the resulting elastomeric nanocomposite is subject to mechanical strain, the incorporated, isolated gold nanorods are oriented along their major axis. As a consequence, the optical properties of the nanocomposite become anisotropic. This process is reversible and the degree of alignment and, thus, of the optical anisotropy directly scales with the applied strain.

In summary, this part presents the controlled alignment of gold nanorods into one-dimensional surface-assemblies, as well as, reversible alignment of gold nanorods incorporated into an elastomer matrix. As a consequence, these materials exhibited pronounced anisotropic optical properties on the macroscale.

### **III. Close-Packed Nanoparticle Assemblies as SERS Platforms**

Highly sensitive SERS spectroscopy relies on templates that provide strong localized field enhancement in combination with a well-defined spatial distribution of hot spots. Similar to bottom-up self-assembled metamaterials, this can be achieved for close-packed, well-organized surface-assemblies of coupled plasmonic nanoparticles. In **Chapter 8**, the enhancing effects of cleaning procedures on SERS efficiency of gold nanorods in solution and arranged in close-packed lying-down superlattices is investigated. Furthermore, I showed that the obtained SERS intensities scale with the aspect ratio of the organized nanorods, presumably due to a shift of the coupled resonance modes.

Close-packed pyramidal assemblies of gold nanospheres give rise to strong field enhancement at their nanoscale apex. In **Chapter 9**, such well-defined assemblies, prepared *via* self-assembly on structured silicon templates, are presented. Subsequent functionalization with a molecule that reversibly traps toxic carbon monoxide provides a highly sensitive optical sensor platform, which can be driven in cyclic fashion.

Linear assembled coupled gold nanorods in tip-to-tip configuration provide strong field enhancement within the nanoscale interparticle gaps. In **Chapter 10**, anodized

aluminum oxide (AAO) substrates with linear surface corrugations were used as templates for the controlled self-assembly of CTAB stabilized gold nanorods. The prepared organizations provided high and homogeneous SERS intensities, compared to a commercial SERS substrate.

In summary, this part presents new approaches towards highly efficient and homogeneous SERS sensor platforms based on close-packed organizations of spherical and anisotropic nanoparticles.

In the following, each chapter will be briefly summarized and main aspects and important results will be discussed.

## I. Synthesis of Plasmonic Building Blocks

### Chapter 4

#### **Silver-Overgrowth-Induced Changes in Intrinsic Optical Properties of Gold Nanorods: From Non-Invasive Monitoring of Growth Kinetics to Tailoring Internal Mirror Charges**

In **Chapter 4**, I studied the surfactant dependent kinetics of the anisotropic silver overgrowth of single-crystalline gold nanorods into gold-core silver-shell cuboids (Au@Ag cuboids). Detailed knowledge of the growth mechanism enabled us to synthesize these building blocks in a highly controlled and well-defined fashion and, consequently, allowed tailoring of their optical properties.

Precise tuning of the optical response of nanoscale building blocks within the optical frequency range is a fundamental requirement for bottom-up fabrication of metamaterials. The huge scientific effort that has been applied in recent years on controlled synthesis of nanoscale plasmonic building blocks teach us that new synthesis strategies and the discovery of new optical features will pave the road towards implementation of plasmonic building blocks into various important applications in close future. However, there is still a lack of detailed fundamental knowledge of the processes governing the controlled anisotropic wet-chemical nanocrystal growth, which is intimately linked to their optical properties.

For the investigation of the silver overgrowth process, we prepared single-crystalline gold nanorods with low polydispersity in large quantities *via* wet-chemical seed-

mediated synthesis. Here, CTAB is utilized as a stabilizer and in combination with silver nitrate as growth directing agent. Reduction was performed with hydroquinone. For subsequent controlled overgrowth with silver, CTAB was replaced by cationic surfactants that contain chloride as counterion. Chloride selectively stabilizes the  $\{100\}$  facets of silver and, thus, induces anisotropic lateral overgrowth. In other words, chloride ions facilitate the transition from octagonal (gold nanorod) to rectangular cross-sections (Au@Ag cuboid) (see **Figure 2.1A**).

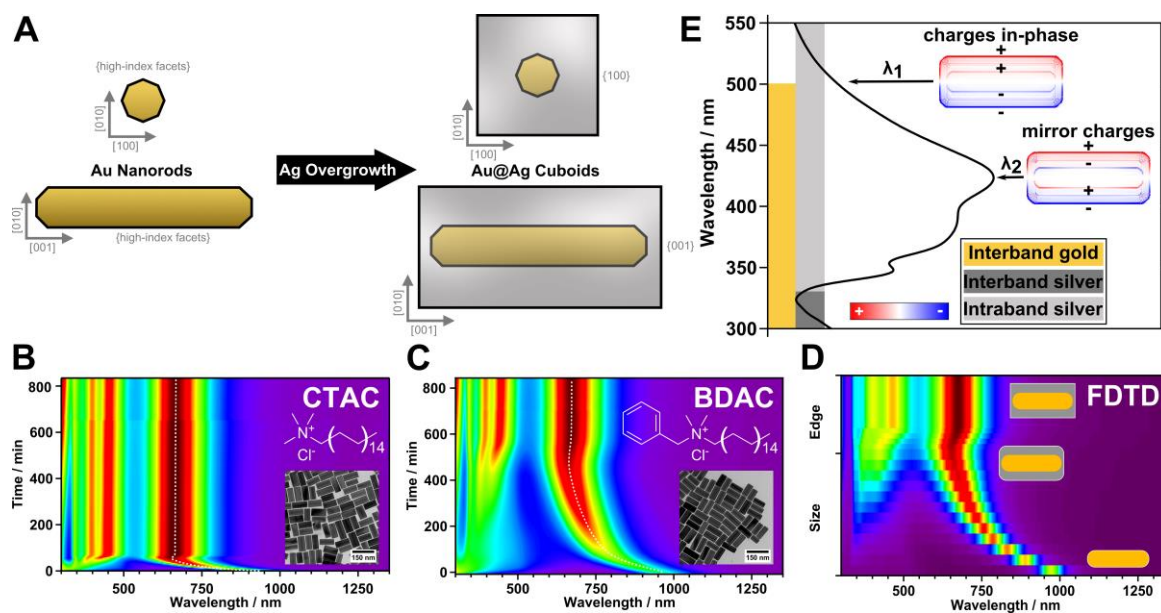


**Figure 2.1.** (A) Anisotropic silver overgrowth of gold nanorods into cuboids. Because of the selective stabilization of the  $\{100\}$  facets silver overgrowth takes place in lateral direction resulting in Au@Ag cuboids. (B/C) Normalized extinction spectra plotted as heat map vs. wavelength and time (peak maxima are dark red). The overgrowth was performed with CTAC (B) and BDAC (C) as surfactant molecule. (D) FDTD modeling revealed that the anisotropic growth period (size) is followed by edge sharpening (edge). (E) Excitation of Au@Ag cuboids in transversal polarization leads to mirror charges, if excited within the overlap region of the interband and intraband region of gold and silver, respectively. Adapted with permission from Tebbe *et al.*, *J Phys Chem C* **2015**, 119, 9513–9523, ©2015 American Chemical Society.

*In-situ* UV/vis/NIR monitoring revealed that the overgrowth proceeds much slower for benzyldimethylhexadecylammonium chloride (BDAC) ( $4 \pm 1 \text{ nm}^3/\text{s}$ ) compared to cetyltrimethylammonium chloride (CTAC) ( $48 \pm 5 \text{ nm}^3/\text{s}$ ) (see **Figure 2.1B/C**). Close correlation of static overgrowth experiments, performed by utilizing varying silver concentrations, with FDTD simulations evidenced that the overgrowth process is characterized by three different stages (see **Figure 2.1D**). In the first stage, the growth rate accelerates with time (BDAC 30 times slower than CTAC). In the second

stage, the growth rate stays constant and is 12 times higher for CTAC than for BDAC. This significant difference is caused by the substitution of one methyl group at the ammonium headgroup with an aromatic moiety. Since the micelles of both surfactants are of comparable size, diffusion is not rate determining. Thus, the difference is linked to processes at the nanocrystal surface, either transport across the bilayer or reduction of silver ions at the metal surface. The final stage is characterized by a red-shift of the longitudinal resonance mode, caused by edge sharpening effects.

In contrast to gold nanorods that are characterized by two resonance modes, the prepared Au@Ag cuboids display four modes that are blue-shifted. This is due to a decrease in symmetry for Au@Ag cuboids and a lower damping of silver compared to gold. The four resonance modes can be distinguished in two dipolar modes (longitudinal and transversal) and two higher dipolar transversal modes. FDTD modeling revealed that excitation within the overlap region of the intraband transition of silver and the interband transition of gold results in mirror charges at the gold-core silver-shell interface, as depicted in **Figure 2.1E**. In this frequency range the complex dielectric function of gold is similar to that of dielectrics, due to the high damping caused by interband transitions. Thus, the resulting mode pattern is similar to mode patterns observed for dielectric-core metal-shell particles. Because of the optical properties of the precisely tunable silver-shell, this effect is located within the visible frequency range of light.

The detailed knowledge of the overgrowth kinetics allowed tuning of the optical properties of prepared Au@Ag cuboids with exceptional precision. Furthermore, these anisotropic plasmonic core-shell nanoparticles exhibit mirror charges that potentially provide a closed current loop. Hence, they are interesting candidates as plasmonic building blocks for bottom-up fabrication of optical metamaterials.

## **Chapter 5**

### **Colloidally Stable and Surfactant-Free Protein-Coated Gold Nanorods in Biological Media**

In **Chapter 5**, I introduce an efficient exchange method of the stabilizing CTAB bilayer on gold nanorods with BSA. The BSA functionalized nanoparticles are colloidally stable under various conditions, *e.g.* high or low pH, high salt concentration, or in biological media. Furthermore, we successfully lyophilized the samples, which is

beneficial for storage and dosage purposes. The successful ligand exchange on the nanorod surface was proven *via* an elaborate SERS study.

The implementation of gold nanorods into bio-applications and into TASA processes is challenging. This is due to the cytotoxic but essential cationic surfactants that strongly affect the wetting properties of both templates and nanorods. Furthermore, the surfactant bilayer limits the interparticle distance in close-packed assemblies. Consequently, their exchange with ligands that provide biocompatibility, and render the nanorods colloidally stable and hydrophilic, is pivotal. Such a ligand represent well-defined macromolecular proteins that possess various different functional groups and can display high affinity towards metal surfaces. Thin protein shells render metal nanoparticles colloidally stable, due to electrosteric stabilization and, furthermore, allow tuning of their surface properties, *e.g.* charge inversion, by external stimuli.

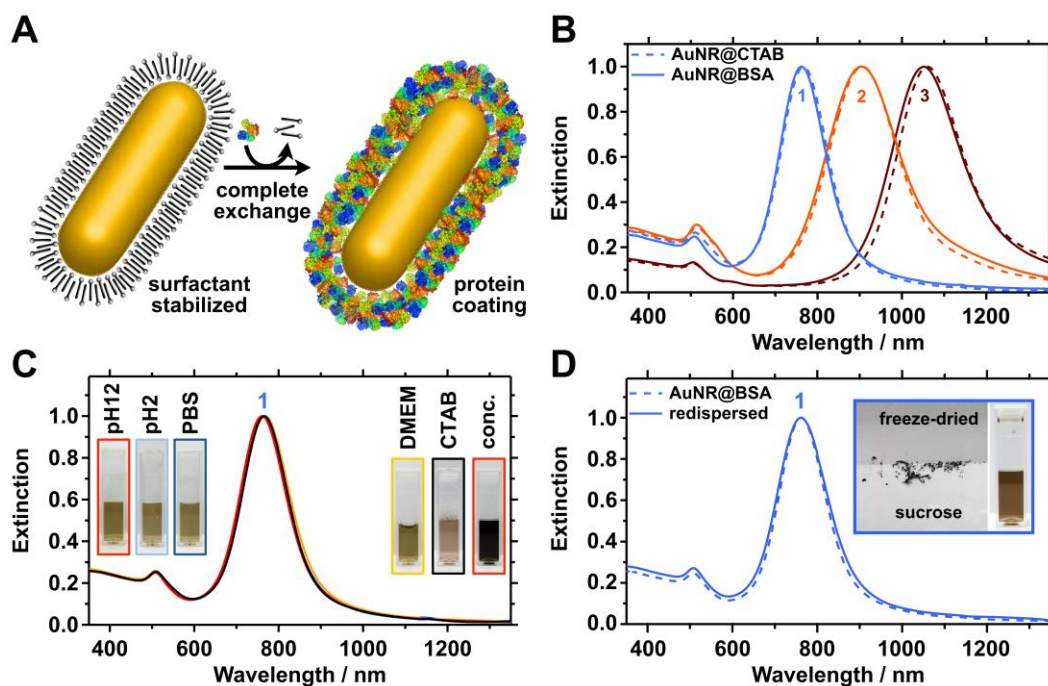


**Figure 2.2.** (A) Schematic depiction of the efficient exchange of the CTAB bilayer on gold nanorods with BSA. (B) Extinction spectra of three representative gold nanorod samples with varied aspect ratios stabilized with CTAB prior to the functionalization (intersected lines) and after functionalization with BSA (full lines). (C) Stability test of gold nanorods in different media (pH12, pH2, PBS, DMEM, CTAB and highly concentrated at pH12). (D) Gold nanorods functionalized with BSA and redispersed after lyophilization with sucrose as lyophilization agent. The inset shows the resulting powder and the redispersed gold nanorods (pH12). Adapted with permission from Tebbe *et al.*, *ACS Appl Mater Interfaces* **2015**, *7*, 5984-5991, ©2015 American Chemical Society.

Gold nanorods used within this study were either prepared following the method presented in **Chapter 4** (high aspect ratios (AR) >4.5) or with ascorbic acid as reducing agent (low AR). The protein functionalization (see **Figure 2.2A**) was accomplished by applying a modified method previously established for spherical nanoparticles. Fast destabilization of the CTAB bilayer *via* ultrasonication in combination with very low surfactant concentration (1/10 of the cmc), resulted in complete replacement of CTAB with BSA. Additionally, centrifugation with carefully adjusted parameters was crucial for preventing nanorods from aggregating. Successful coating without any agglomeration was proven utilizing UV/vis/NIR spectroscopy, indicated by the absence of significant peak shifts or broadening (see **Figure 2.2B**).

The functionalized gold nanorods were stable in various media such as high (pH 12) and low (pH 2) pH values, high salt concentrations (150 mM), Dulbecco's modified eagle's media (DMEM) and for high particle concentrations (>20 mg/mL) (see **Figure 2.2C**). This high stability is caused by electrosteric stabilization provided by different functionalities (amines, carboxylates) within the macromolecular protein corona.

Different lyophilizing agents that prevent proteins from denaturing during drying (sucrose, DMEM, DMEM with 10% new born calf serum (NCS) and BSA) were employed to lyophilize BSA coated particles. The best results with respect to stability and redispersibility were obtained for sucrose (see **Figure 2.2D**), DMEM with 10% NCS and 1 mg/mL BSA as lyophilizing agents. Solidification as powders significantly simplifies storage and dosage of protein coated gold nanorods.

The central question, whether CTAB molecules are completely exchanged or rather overcoated or incorporated within the protein corona during ligand exchange was addressed with SERS. The results obtained for gold nanorods and gold spheres clearly indicate that no CTAB is present in close proximity to the gold surface after the ligand exchange. This important result suggests that the prepared BSA coated nanorods are biocompatible. Furthermore, these functionalized negatively charged hydrophilic gold nanorods can be organized by TASA as presented in the following chapter.

## II. Controlled Alignment of Gold Nanorods

### **Chapter 6**

#### **Optically Anisotropic Substrates *via* Wrinkle-Assisted Convective Assembly of Gold Nanorods on Macroscopic Areas**

In **Chapter 6**, I present the directional template-assisted convective self-assembly of anisotropic BSA functionalized gold nanorods on wrinkle-templates. As a key parameter to switch between different assembly patterns, I identified the wrinkle amplitude. Optical characterization of ensembles of well-aligned single lines of gold nanorods on indium tin oxide (ITO) revealed the high optical anisotropy of the prepared array. Controlled self-assembly of anisotropic plasmonic building blocks is of paramount importance for the large-area bottom-up fabrication of metamaterials that operate within the optical frequency range. Organizations of single and double lines of gold nanorods represent common motifs that can provide negative electric permittivity and magnetic permeability, respectively. However, the requirements to achieve effective optical material properties are high, with respect to the quality of assembled building blocks, the periodicity (well below the wavelength of light) and the quality of the organizations.

In this context, plasma oxidized wrinkled poly(dimethylsiloxane) (PDMS) elastomers represent templates with precisely tunable nanoscale features and adjustable wetting properties. Additionally, this technique is scalable to macroscopic sample areas. Gold nanorods were functionalized with BSA, following the method presented in **Chapter 5**. The synthesized anisotropic plasmonic building blocks displayed a narrow size distribution, dimensions of 80 nm in length and 22 nm in width, and a longitudinal plasmon resonance at 836 nm. Subsequent BSA coating provides negatively charged, hydrophilic gold nanorods (pH 10) and the obtained nanoparticle suspensions exhibited compatible wetting properties on hydrophilic substrates indicated by a low contact angle ( $<10^\circ$ ). Crack-free wrinkle-templates with wavelengths ( $\sim 230$  nm) well-below the wavelength of light were prepared utilizing a modified version of the established wrinkle-preparation protocol. However, the key step for successful nanorod alignment was the ability to tune the amplitude (from 30 nm down to 5 nm) *via* controlled plasma post-treatment without changing the wavelength of the wrinkle-substrate. In combination with dip-coating parallel to the

desired rod orientation, providing slow and controlled motion of the contact-line, high quality assemblies on large sample areas were realized (see **Figure 2.3A-C**). Single lines of gold nanorods aligned in tip-to-tip configuration were obtained for amplitudes well-below the diameter of the assembled plasmonic building blocks. Furthermore, for increasing amplitudes different structure types, *e.g.* double and triple lines, were attained. Thus, tuning the amplitude of the wrinkle-substrates represents a simple means to control the structure type of anisotropic plasmonic building blocks within prepared surface-assemblies.

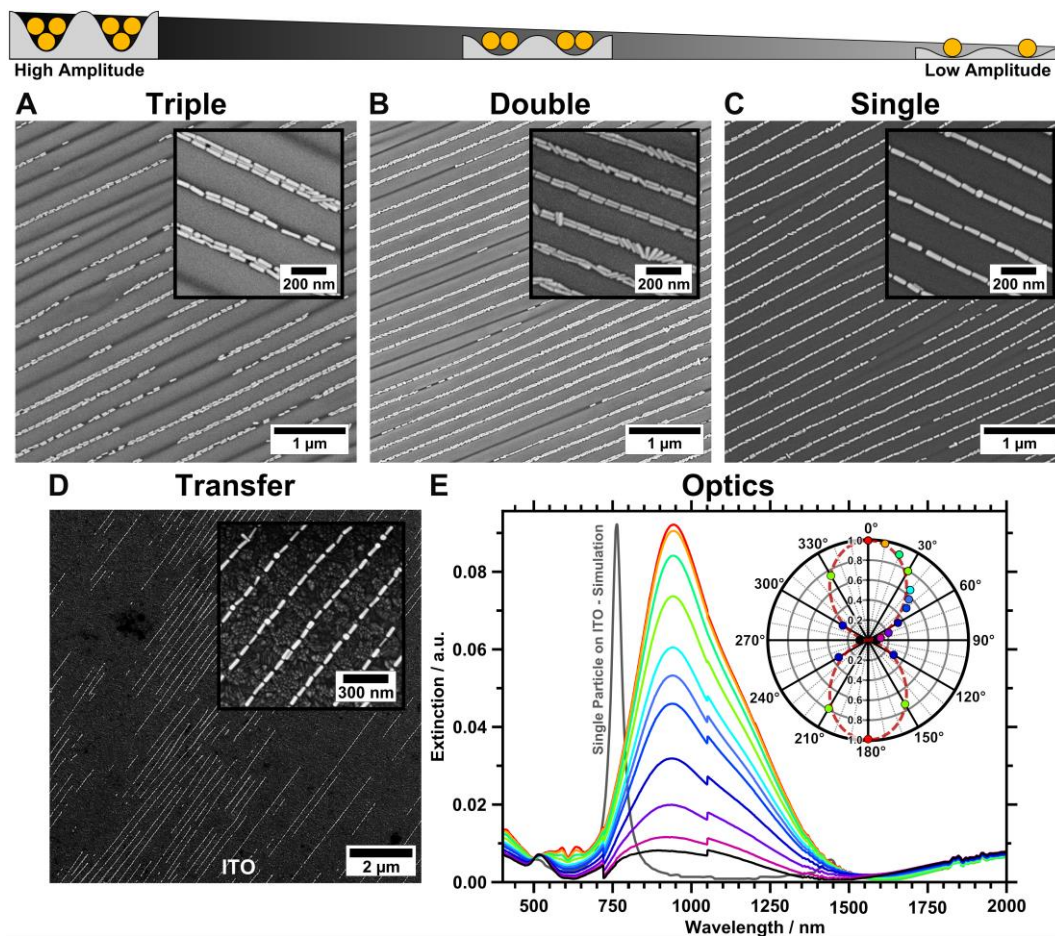


**Figure 2.3.** Different structure types obtained for convective self-assembly of gold nanorods on wrinkle-templates with decreasing amplitudes. Gold nanorods were assembled into (A) triple lines, (B) double lines and (C) single lines ( $[\text{Au}] = 1 \text{ mg/mL}$ ). (D) Single line gold nanorod organization after transfer onto an ITO substrate. (E) Polarization angle dependent extinction spectra of linear assembled gold nanorods on ITO substrates. The inset depicts a polar plot of the extinction maxima versus the polarization angle. Tebbe *et al.*, *Faraday Discuss* **2015**, *118*, 243-260. Adapted by permission of The Royal Society of Chemistry.

Careful statistical analysis of the single line surface-assemblies revealed that the averaged interparticle gap distance was within the limit of strong coupling ( $\sim 7.5 \text{ nm}$ )

for highly filled assemblies ( $\sim 90\%$ ). Furthermore, we determined the two-dimensional order parameter  $\langle S_{2D} \rangle$  to be as high as 0.97. These characteristic parameters indicate that the applied method provides excellent results with respect to selectivity, orientation and quality of gold nanorod surface-assemblies on wrinkle-substrates.

Optical characterization was performed after capillary force driven transfer of uniaxially aligned gold nanorods onto ITO substrates (**Figure 2.3D**). The organized films were subject to polarization dependent far-field UV/Vis/NIR measurements (see **Figure 2.3E**). Because of the small interparticle gap sizes, the organized rods couple and the longitudinal resonance mode is red-shifted compared to individual nanorods. Furthermore, the longitudinal peak intensity scales with the angle of polarization and decreases from parallel ( $0^\circ$ ) to perpendicular polarization ( $90^\circ$ ). This result gives clear evidence that uniaxially aligned gold nanorods render the sample highly optically anisotropic. We determined the optical order parameter  $S_{\text{optical}}$  to be as high as 0.91, in good agreement with the statistical evaluation.

The methods developed in this chapter will potentially pave the road towards bottom-up large-area self-assembly of optical metamaterials.

## **Chapter 7**

### **Reversible Gold Nanorod Alignment in Mechano-Responsive Elastomers**

The publication presented in **Chapter 7** aimed on the preparation of highly filled nanocomposites that change their optical properties upon external mechanical stimulation. This was achieved by phase transfer of CTAB stabilized gold nanorods into a hydrophobic polymer matrix *via* functionalization with a  $\alpha,\omega$ -dithiol functionalized ABA triblock co-oligomer and subsequent incorporation into an elastomeric polymer matrix.

In contrast to static two-dimensional surface-assemblies incorporation of anisotropic nanoparticles into elastomeric polymers provides materials with mechano-responsive optical properties. Such materials might find application as strain sensors, tunable optical filters, or flexible conductors. However, homogeneous incorporation of nanoparticles prepared *via* wet-chemical approaches into hydrophobic polymers stays challenging, due to phase separation and agglomeration upon phase transfer.

To overcome these challenges, we functionalized CTAB stabilized gold nanorods prepared as described in **Chapter 4-6** with a thiol-isoprene-styrene-isoprene-thiol

(TISIT) triblock co-oligomer. The functionalization was performed *via* a simple phase transfer reaction within a toluene/water microemulsion using the thiolated triblock oligomer as phase transfer agent (see **Figure 2.4A**). After isolation of the co-oligomer nanorod composite the highly filled (1.9 wt%) and CTAB free material was subject to mechanical tests. Even though the homogeneous incorporation of gold nanorods significantly enhanced the mechanical properties of the nanocomposite, due to physically cross-linking, the overall filling fraction was not high enough to yield a fully cross-linked elastomeric material.

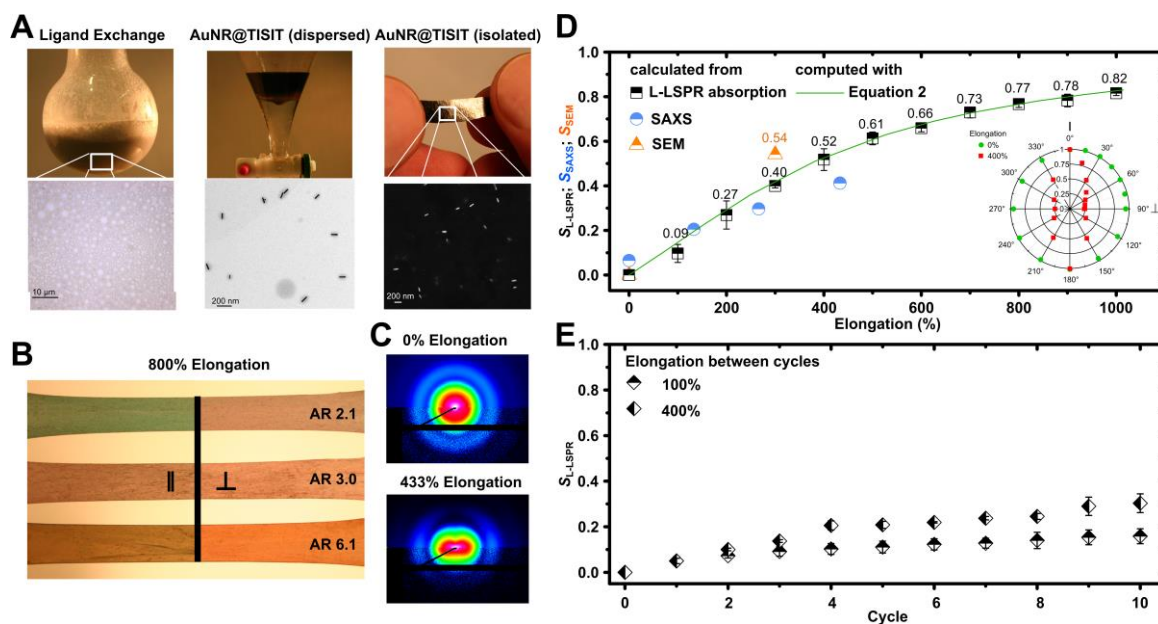


**Figure 2.4.** (A) Images of the microemulsion (photo/microscope), phase separated solutions after phase transfer (photo/TEM) and isolated nanocomposite (photo/SEM). (B) Polarized optical images from nanocomposites blended with Kraton® and filled with nanorods of varied aspect ratios. (C) SAXS patterns obtained for elongations of 0% and 433%. (D) Determined order parameters  $S_{SAXS}$  (blue circles),  $S_{L-LSPR}$  (black squares) and  $S_{TEM}$  (orange triangles) plotted versus elongation. The inset shows the polarization dependent peak intensity for 0% (green) and 400% (red) elongation plotted as polar plot. (E) The reversibility was tested *via* cyclic elongation of the elastomeric nanocomposite up to 100% and 400% elongation, respectively. Adapted from publication title, *Polymer*, 66, 2015, Holger Pletsch *et al.*, Reversible gold nanorod alignment in mechano-responsive elastomers, 167-172, ©2015, with permission from Elsevier.

In order to introduce elasticity we followed two different routes: (I) *in-situ* reduction of silver ions which provides a high cross-linking density within the TISIT matrix, and (II) blending the nanocomposite into Kraton®, a commercial thermoplastic elastomer. (I) yielded a thermoplastic elastomer, but due to the high extinction cross-section of

the highly filled material, optical characterization was not possible; (II) significantly enhanced the mechanical properties and successfully reduced the optical density of our nanocomposites (see **Figure 2.4B**).

Reversible mechano-responsive alignment of well-dispersed and isolated gold nanorods within the polymer matrix (see **Figure 2.4A**) was confirmed by SEM, SAXS and UV/vis/NIR transmission spectroscopy measurements. SAXS and UV/vis/NIR measurements performed with a fixed polarization angle perpendicular to the stretching direction proved that the alignment of incorporated nanorods parallel to the stretching direction directly scales with elongation. For an effective elongation of 433% the calculated SAXS order parameter  $S_{\text{SAXS}}$  was 0.41 (see **Figure 2.4C/D**). Optical characterization revealed an optical order parameter  $S_{\text{Optical}}$  of 0.82 for an elongation of 1000% (see **Figure 2.4D**). In consistency with these results the peak intensity directly scales with the polarization angle for a fixed elongation (see **Figure 2.4D** inset). The reversibility of the alignment was probed *via* cyclic elongation tests, revealing only minor memory effects (see **Figure 2.4E**).

The prepared nanocomposites exhibited reversible and stepless mechano-responsive alignment of incorporated gold nanorods, which gave rise to reversible anisotropic optical properties.

### III. Close-Packed Nanoparticle Assemblies as SERS Platforms

#### **Chapter 8**

#### **Organized Solid Thin Films of Gold Nanorods with Different Sizes for Surface-Enhanced Raman Scattering Applications**

In **Chapter 8**, I studied the enhancing effect of cleaning methods, for removing excess CTAB within gold nanorod solutions and present at the surface of gold nanorod organizations, on the SERS intensity. Furthermore, we found that varying the aspect ratio of gold nanorods organized into close-packed assemblies, affects the obtained overall SERS efficiency.

SERS spectroscopy relies on strong localized electromagnetic field enhancement in combination with close proximity of the target analyte to the region of highest field

intensity. Gold nanorods provide localized field enhancement at their tips if excited at their longitudinal resonance frequency. Furthermore, electromagnetic coupling between metal nanoparticles in close-packed assemblies can provide additional strong localized field enhancement (“hot spots”) for resonant excitation.

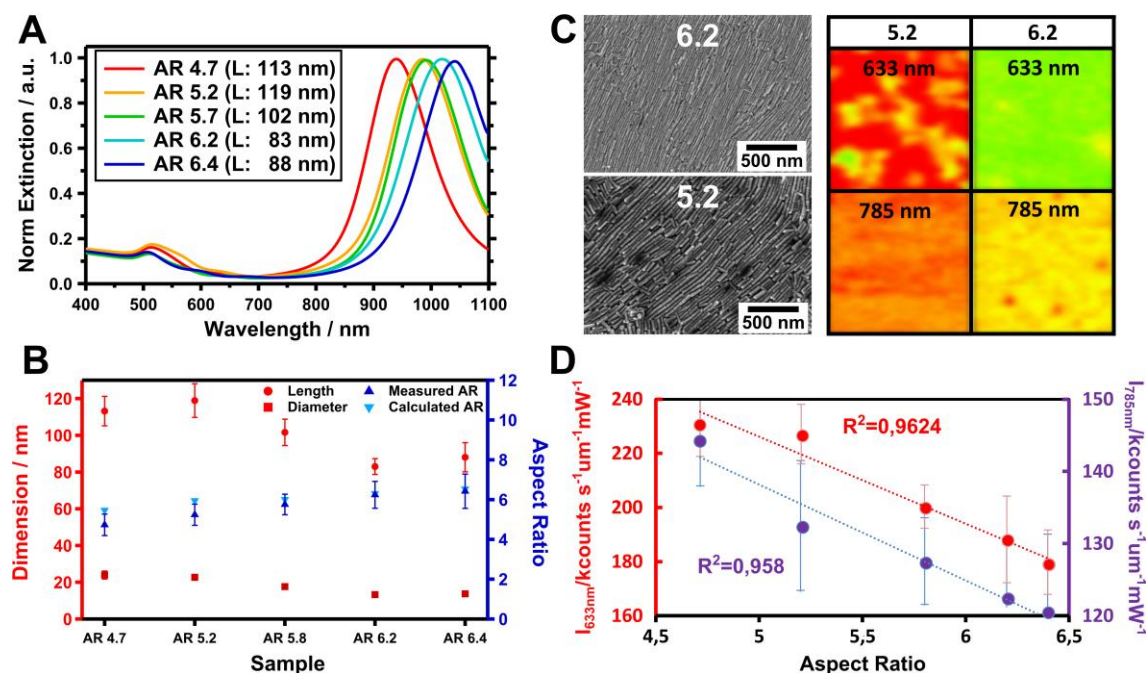


**Figure 2.5** (A) UV/vis/NIR spectra of gold nanorods with varied aspect ratios. (B) Dimensions and aspect ratios of individual gold nanorod samples. (C) SEM images of gold nanorods, self-assembled into close-packed lying-down superlattices after plasma cleaning and SERS intensity maps obtained for benzenethiol with different laser lines (633 nm and 785 nm). (D) Averaged SERS intensities plotted versus the aspect ratio of the self-assembled gold nanorods for two different laser lines (633 nm and 785 nm). Adapted with permission from Tebbe *et al.*, *J Phys Chem C* **2014**, 118, 28095 – 28100, ©2014 American Chemical Society.

Low polydispersity of plasmonic particles is a fundamental requirement to facilitate the preparation of well-organized, close-packed superlattices. For this purpose gold nanorods with narrow size distributions and varied aspect ratios (4.7-6.4) were prepared following a procedure introduced in previous chapters employing the seed amount as tuning parameter (see **Figure 2.5A/B**). The longitudinal plasmon resonances of the prepared gold nanorods were located within the NIR frequency range (940 to 1040 nm). For particles in solution only moderate SERS intensities were obtained for benzenethiol and off-resonant excitation (NIR laser line 785 nm). Furthermore, the signal intensities decayed with increasing aspect ratio, due to less efficient excitation. Applying multiple washing steps to remove excess CTAB gave rise to four-fold higher SERS intensities.

The obtained gold nanorods were self-assembled *via* droplet evaporation into close-packed films on cleaned glass slides. For the chosen self-assembly parameters, *e.g.* slow evaporation rates and low particle concentrations, the CTAB stabilized gold nanorods spontaneously self-assembled into close-packed lying-down superlattices (see **Figure 2.5C**). In this configuration near-field coupling of both, the transversal and longitudinal modes will result in the formation of homogeneously distributed side-by-side and tip-to-tip hot spots and these organizations will display a complex absorption and scattering behavior.

Plasma cleaning was applied to remove excess of CTAB and resulted in a significant increase in homogeneity and overall SERS intensity measured for benzenethiol, due to an increase in accessibility of the metal surface. For increasing aspect ratios of gold nanorods within prepared organizations the measured SERS intensities consistently decreased. Furthermore, the red-laser line (633 nm) exhibited higher SERS intensities compared to the NIR-laser line (785 nm) (see **Figure 2.5D**). The strong coupling responsible for hot-spot formation presumably lead to a significant broadening and red-shift of both the transversal and longitudinal mode. Higher SERS intensities obtained for the red-laser line indicate side-by-side rather than tip-to-tip coupling being responsible for field enhancement. Furthermore, the linear decrease for increasing aspect ratios obtained for both laser lines indicates that the coupled resonance modes red-shifted for higher aspect ratios and, thus, are less efficiently excited by the applied laser light.

In this study, I presented a fast and simple method for the fabrication of efficient SERS platforms *via* self-assembly of gold nanorods with varied aspect ratios into close-packed lying-down superlattices. Furthermore, I studied the impact of cleaning procedures and aspect ratios on the obtained SERS intensities.

## **Chapter 9**

### **Macroscale Plasmonic Substrates for Highly Sensitive Surface-Enhanced Raman Scattering**

In **Chapter 9**, I present a reversible and highly efficient optical sensor platform for the detection of carbon monoxide. Such SERS platforms were prepared *via* template-assisted self-assembly of gold nanospheres into close-packed pyramidal organizations that provide strong field enhancement at their pyramidal apex. Subsequent surface functionalization of the organized gold nanoparticles with a

thiolated ferro-complex that reversibly traps carbon monoxide provided a highly sensitive optical sensor platform, which can be used in cyclic fashion.

Besides close-packed surface-assemblies of metal nanoparticles that provide homogeneous and high SERS intensities over the entire substrate, particles organized into macroscale superstructures can possess areas with additional localized high field enhancement. This is due to collective coupling effects within the assembled structures that provide additional field enhancement at the nanoscale apex of the topographic features, ideally consisting of a single nanoparticle. In this context, especially pyramidal superstructures of close-packed nanoparticles are promising as they represent macroscopic organizations with nanoscale, highly curved tips.

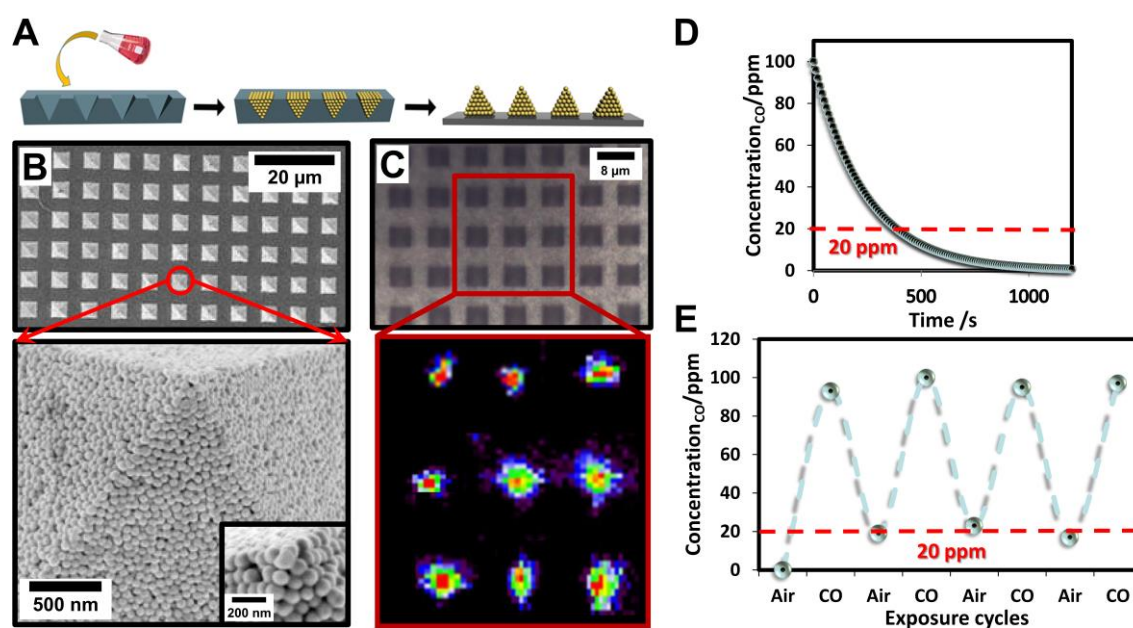


**Figure 2.6.** (A) Schematic depiction of the sample preparation method. Monodisperse gold nanospheres were cast on a silicon wafer with inverse pyramidal structures. The structures were dried under controlled conditions and subsequently transferred to a flat target substrate. (B) SEM micrographs of the resulting close-packed pyramidal assemblies. (C) Optical image of pyramidal structures and high resolution SERS map obtained for 1-naphthalenethiol. (D) Time dependent recovery of the carbon monoxide sensor. (E) Response of the optical sensor platform to cyclic carbon monoxide exposure. Adapted with permission from Macroscale Plasmonic Substrates for Highly Sensitive Surface-Enhanced Raman Scattering, Alba *et al.*, *Angew Chem, Int Ed*, **2013**, 52, 6459 - 6463. ©2015 The authors.

Spherical gold colloids with diameters of 80 nm were prepared *via* wet-chemical seed-mediated synthesis, utilizing CTAB as surfactant. For the template-assisted self-assembly into periodic macroscale pyramidal organizations, silicone substrates with an inverse pyramidal structure were employed. These substrates were prepared *via*

direct laser writing lithography followed by chemical etching. Slow evaporation under controlled environmental conditions of drop-cast, highly concentrated gold colloid solutions yielded well-organized, close-packed superlattices with micrometer sized pyramidal topography (see **Figure 2.6A**). The prepared pyramidal assemblies were transferred to flat target substrates (see **Figure 2.6B**). Strong interparticle coupling was indicated by the appearance of a pronounced broad resonance mode within the near-infrared region. As a proof of concept, the pyramidal arrays were functionalized with 1-naphthalenethiol and the SERS intensity was mapped (see **Figure 2.6C**). Indeed, the SERS intensities obtained at the nanoscale apex of the pyramids were about two-orders of magnitude higher compared to the surrounding flat, close-packed assemblies. This result was further validated by high-resolution confocal SERS measurements, performed at a single pyramid. Even though strong interparticle coupling gave rise to high SERS intensities across the whole substrate, the additional field enhancement at the pyramidal tips allowed single-molecule detection, as confirmed for crystal-violet at a surface concentration of 0.06 molecules/ $\mu\text{m}^2$ .

However, for the preparation of an ultrafast and reversible optical sensor for carbon monoxide detection, the surface of the nanostructured pyramidal array was functionalized with a thiolated iron porphyrin. Iron porphyrin mimics the structure of myoglobin and hemoglobin that are known for their high affinity and reversible binding to oxygen and carbon monoxide. This highly active SERS molecule acts as secondary probe that changes its characteristic Raman signature upon reversible binding with carbon monoxide. Because of the covalent character of the thiol group the secondary probe was fixed in close proximity to the metal surface within the spatial volume, providing high field enhancement. This allows detection of trace amounts of toxic carbon monoxide within the environmental atmosphere well-below the critical limit of 20 ppm. Furthermore, due to the reversible binding, the sensor platform recovers and can be used in a cyclic fashion for online-monitoring of the carbon monoxide concentration (see **Figure 2.6D/E**).

The presented design approach based on close-packed gold nanoparticles self-assembled into macroscopic pyramidal organizations in combination with appropriate surface modification provided an ultrafast and reversible optical sensor platform for the effective monitoring of toxic carbon monoxide. Such highly sensitive and reusable SERS platforms hold great potential for the routine detection of trace

amounts of toxic or harmful compounds within the environmental atmosphere utilizing portable Raman spectrometers.

## **Chapter 10**

### **SERS Platforms of Plasmonic Hydrophobic Surfaces for Analyte Concentration: Hierarchically Assembled Gold Nanorods on Anodized Aluminum**

In **Chapter 10**, I present a SERS platform, based on self-assembly of gold nanorods into linear close-packed chains. Anodized aluminum oxide (AAO) substrates with linear surface corrugations served as templates for the directed self-assembly of CTAB stabilized gold nanorods. The obtained well-aligned gold nanorod chains facilitated tip-to-tip hot spot formation and, consequently, provided homogeneous, high SERS intensities.

As described in **Chapter 6**, organization of gold nanorods into well-defined linear surface-assemblies is highly challenging. However, such assemblies have great potential as efficient and homogeneous SERS substrates, due to the high-field enhancement caused by hot-spot formation in between adjacent nanorods in tip-to-tip configuration. The topographic surface patterns directing the self-assembly process need to precisely match the building block dimensions within a very limited acceptable range of deviation. This renders bottom-up large-area template fabrication a key challenge in nanoscience.

Hence, to address this problem, we utilized controlled electrochemical oxidation (galvanostatic anodization) of aluminum in phosphoric acid solutions to prepare AAO substrates with periodic grooves exhibiting a mean groove width of 36 nm (see **Figure 2.7A**). The underlying competing mechanisms, dissolution of aluminum and creation of aluminum oxide, enable the fabrication of a variety of different porous AAO morphologies. However, surface corrugations with dimensions ideally suitable for the organization of nanorods were obtained for a 90 s treatment. Subsequently, CTAB stabilized gold nanorods were self-assembled onto the AAO templates *via* spin coating of concentrated gold nanorod solutions (length = 42 nm; width = 15 nm, longitudinal plasmon mode = 703 nm) (**Figure 2.7B-E**). The AAO templates exhibited a hydrophobic wetting behavior with a contact angle of 104° for water, which is highly unfavorable for the capillary force driven self-assembly of gold nanorods. In this case, the surfactant CTAB, present within the gold nanorod suspensions at a concentration

close to the cmc (1 mM), was beneficial, as the surface active molecule enhanced the wettability of the AAO templates and reduced the contact angle to 52°.

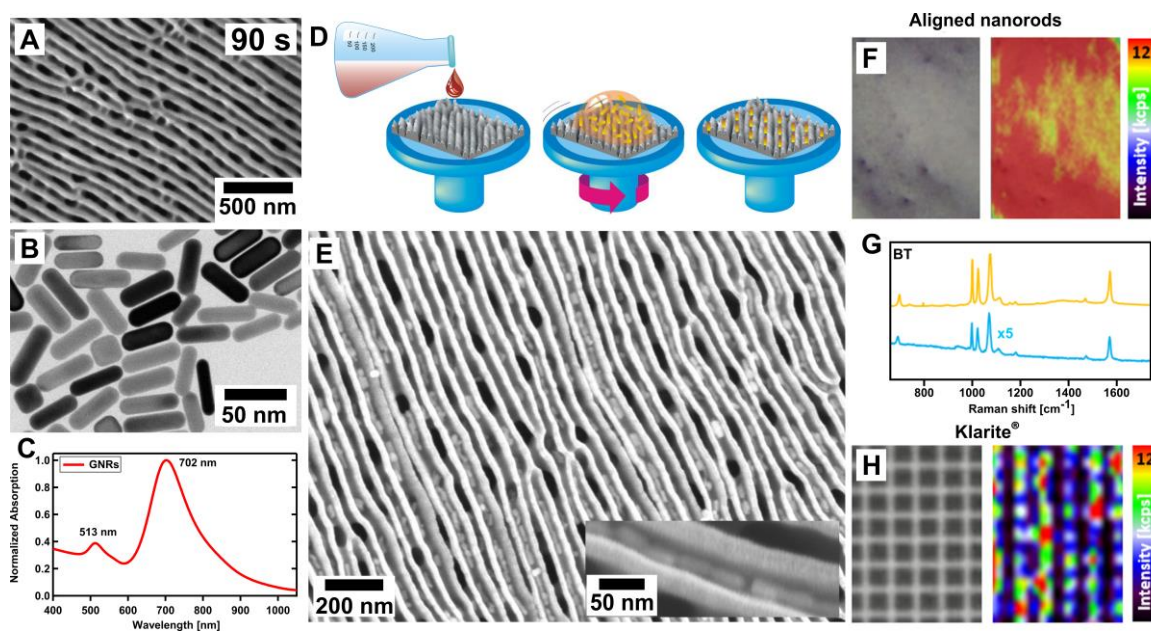


**Figure 2.7** (A) AAO substrate with linear and parallel surface corrugations. (B) TEM image of CTAB stabilized gold nanorods. (C) UV/vis/NIR extinction spectra of gold nanorods. (D) Schematic depiction of the assembly process of gold nanorods on the AAO template. (E) SEM image of the resulting well-aligned gold nanorod assemblies. (F) Micrograph and SERS map obtained for benzenethiol (785 nm NIR laser line). (G) SERS spectra for benzenethiol on aligned nanorods on AAO templates (yellow) and Klarite® as reference (blue). (H) Micrograph and SERS map obtained for benzenethiol on Klarite®. Adapted with permission from Tebbe *et al.*, SERS Platforms of Plasmonic Hydrophobic Surfaces for Analyte Concentration: Hierarchically Assembled Gold Nanorods on Anodized Aluminum, *Part Part Syst Charact* **2014**, *31*, 1134–1140, ©2014 WILEY-VCH Verlag GmbH & Co. KGaA, Weinheim.

This approach enabled the preparation of close-packed surface-assemblies of linear aligned chains of gold nanorods in tip-to tip configuration (**Figure 2.7E**). The increase in environmental refractive index for substrate supported gold nanorods and the longitudinal mode coupling give rise to a red-shift of the resonance modes. Consequently, the NIR laser light source (785 nm) resulted in efficient excitation and provided homogeneous SERS signals. In order to test the SERS efficiency of the prepared SERS platforms, they were functionalized with benzenethiol and 1-naphthoic acid, both characterized by high SERS cross-sections.

Benzenethiol was applied *via* gas phase deposition. The resulting SERS measurements on AAO substrates revealed a five-fold higher averaged SERS signal intensity and significantly higher homogeneity compared to the commercially available standard

substrate Klarite® (**Figure 2.7F-G**). 1-naphthoic acid was applied *via* dropcasting. Because of the high contact angle ( $\sim 105^\circ$ ) obtained after plasma activation of these SERS platforms the analyte could be concentrated within a small spot on the substrate surface upon solvent evaporation. For Klarite® with a lower contact angle ( $\sim 68^\circ$ ) the analyte was distributed on a larger sample area and being, consequently, less concentrated. Hence, SERS measurements for 1-naphthoic acid gave rise to a homogeneous distributed and 40-fold higher signal intensity compared to Klarite®. The presented approach is a facile and scalable method for the preparation of highly efficient SERS substrates *via* bottom-up self-assembly of anisotropic plasmonic nanoparticles on tailored AAO templates.

## Contribution to joint publications

The publications and results presented in this thesis were prepared within collaborative research projects. Thus, various researchers were involved at different stages of research and publication process. In the following, the contribution of all authors to joint publications is addressed chapter-wise. (#) Denotes authors that contributed equally to the publication. (\*) Denotes the corresponding authors.

### Chapter 4

#### **Silver-Overgrowth-Induced Changes in Intrinsic Optical Properties of Gold Nanorods: From Non-Invasive Monitoring of Growth Kinetics to Tailoring Internal Mirror Charges**

*By Moritz Tebbe, Christian Kuttner, Martin Mayer, Max Männel, Nicolas Pazos-Perez, Tobias A.F. König,\* and Andreas Fery\**

I performed the experimental work, carried out data analysis, prepared the figures and wrote the manuscript. Christian Kuttner was involved in scientific discussion, performed data analysis and wrote parts of the manuscript. Martin Mayer performed some of the silver overgrowth experiments under my guidance, was involved in data analysis as well as scientific discussion and proof read the manuscript. Max Männel was involved in the synthesis of gold nanorods within his bachelor thesis under my guidance and corresponding data analysis. Nicolas Pazos-Perez was involved in scientific discussion and proof read the manuscript. Tobias A.F. König performed FDTD modeling and data analysis, was involved in scientific discussion and wrote parts of the manuscript. Andreas Fery supervised the project, was involved in scientific discussion and proof read the manuscript.

### Chapter 5

#### **Colloidally Stable and Surfactant-Free Protein-Coated Gold Nanorods in Biological Media**

*By Moritz Tebbe,# Christian Kuttner,# Max Männel, Andreas Fery, and Munish Chanana\**

I performed all synthetic experiments, carried out data analysis and wrote the manuscript. Christian Kuttner performed all SERS measurements, evaluated the corresponding data and wrote parts of the manuscript. Max Männel performed some of the experiments under my guidance. Andreas Fery was involved in scientific discussion and proof read the manuscript. Munish Chanana supervised the project, was involved in scientific discussion and wrote parts of the manuscript.

## Chapter 6

### **Optically Anisotropic Substrates *via* Wrinkle-Assisted Convective Assembly of Gold Nanorods on Macroscopic Areas**

*By Moritz Tebbe, Martin Mayer, Bernhard A. Glatz, Christoph Hanske, Patrick T. Probst, Mareen B. Müller, Matthias Karg, Munish Chanana, Tobias A. F. König, Christian Kuttner, and Andreas Fery\**

I synthesized the nanorods, functionalized the nanoparticles with BSA, organized the nanostructures and carried out all SEM and UV/vis/NIR measurements. Furthermore, I performed the analysis of the data and wrote the manuscript along with preparation of included figures. Martin Mayer and Patrick T. Probst were strongly involved in lab-work on all stages but mainly related to nanoparticle synthesis and assembly along with data analysis and the preparation of the figures under my guidance and proof read the manuscript. Additionally, Martin Mayer performed TEM measurements. Bernhard A. Glatz developed the presented wrinkling procedure, prepared the wrinkle-substrates and proof read the manuscript. Christoph Hanske and Mareen B. Müller developed the underlying general assembly and printing process, carried out capillary printing and proof read the manuscript. Munish Chanana developed the protein functionalization of nanorods and proof read the manuscript. Tobias A. F. König performed FDTD simulations, performed interpretation of optical data and wrote the corresponding parts of the manuscript. Christian Kuttner developed some of the procedures for data analysis, performed parts of the data analysis and wrote the corresponding parts of the manuscript. Andreas Fery and Matthias Karg developed the concept for the presented work, supervised the whole project including scientific discussion and proof read the manuscript.

## Chapter 7

### **Reversible Gold Nanorod Alignment in Mechano-Responsive Elastomers**

*By Holger Pletsch,<sup>#</sup> Moritz Tebbe,<sup>#</sup> Martin Dulle, Beate Förster, Andreas Fery, Stephan Förster, Andreas Greiner and Seema Agarwal\**

I synthesized the gold nanorods, carried out angle dependent UV/vis/NIR measurements and data analysis and wrote the manuscript. Furthermore, I developed the phase transfer reaction together with Holger Pletsch. Holger Pletsch synthesized the polymers, carried out the phase transfer reactions and polymer blending as well as mechanical tests. Furthermore, he measured strain dependent UV/vis/NIR and wrote the manuscript. Martin Dulle carried out SAXS experiments, data analysis and wrote the corresponding parts of the manuscript. Beate Förster carried out the *in-situ* strain dependent SEM measurements of the nanocomposites. Andreas Fery was involved in scientific discussions and proof read the manuscript. Stephan Förster was involved in SAXS data interpretation, scientific discussion and wrote parts of the manuscript. Andreas Greiner was involved in scientific discussion and proof read the manuscript. Seema Agarwal supervised the project, was involved in scientific discussion and proof read the manuscript.

## Chapter 8

### **Organized Solid Thin Films of Gold Nanorods with Different Sizes for Surface-Enhanced Raman Scattering Applications**

*By Moritz Tebbe, Max Maennel, Andreas Fery, Nicolas Pazos-Perez\* and Ramon A. Alvarez-Puebla\**

I carried out the experimental work, parts of the data analysis and wrote parts of the manuscript. Max Männel performed some of the gold nanorod syntheses within his bachelor thesis under my guidance. Andreas Fery was involved in scientific discussion and proof read the manuscript. Nicolas Pazos-Perez supervised the project, performed SERS measurements, was involved in scientific discussion and wrote parts of the manuscript. Ramon A. Alvarez-Puebla supervised the project, was involved in scientific discussion, carried out data analysis and wrote parts of the manuscript.

## Chapter 9

### **Macroscale Plasmonic Substrates for Highly Sensitive Surface-Enhanced Raman Scattering**

*By Maria Alba, Nicolas Pazos-Perez, Belen Vaz, Pilar Formentin, Moritz Tebbe, Miguel A. Correa-Duarte, Pedro Granero, Josep Ferre-Borrull, Rosana Alvarez, Josep Pallares, Andreas Fery,\* Angel R. de Lera,\* Lluís F. Marsal,\* and Ramón A. Alvarez-Puebla\**

I synthesized the spherical nanoparticles, performed the assembly experiments and characterized the assembled structures *via* SEM and AFM. Maria Alba prepared the inverted pyramidal templates by direct laser writing lithography and chemical etching on silicon substrates. Nicolas Pazos-Perez supervised the project and experiments, performed assembly and functionalization experiments, characterized the particles and assembled structures *via* TEM and SEM. Furthermore, he was involved in scientific discussion and wrote the manuscript. Belen Vaz synthesized the porphyrin molecule with a single thiol group at just one location of its periphery and performed the CO experiments. Pilar Formentin helped with the preparation of the inverted pyramidal templates. Miguel A. Correra-Duarte performed the optical characterization of the pyramidal assemblies, was involved in scientific discussion and proof read the manuscript. Pedro Granero and Josep Ferre-Borrull calculated the distribution of the near electric field in a pyramid composed of particles and proof read the manuscript. Rosana Alvarez helped during the synthesis of the thiolated porphyrin. Josep Pallares was involved in scientific discussion and proof read the manuscript. Andreas Fery was involved in scientific discussion and proof read the manuscript. Angel R. de Lera designed the synthesis of the thiolated porphyrin, was involved in scientific discussion and proof read the manuscript. Lluís F. Marsal was involved in scientific discussion and proof read the manuscript. Ramon A. Alvarez-Puebla supervised the project, performed the SERS measurements, carried out data analysis, was involved in scientific discussion and wrote the manuscript.

## Chapter 10

### **SERS Platforms of Plasmonic Hydrophobic Surfaces for Analyte Concentration: Hierarchically Assembled Gold Nanorods on Anodized Aluminum**

*By Moritz Tebbe,<sup>#</sup> Pavel Cherepanov,<sup>#</sup> Ekaterina V. Skorb, Sergey K. Poznyak, Javier Garcia de Abajo, Andreas Fery, Daria V. Andreeva, Ramon A. Alvarez-Puebla, and Nicolas Pazos-Perez\**

I carried out nanoparticle synthesis and performed the assembly and wetting experiments. Additionally, I characterized the resulting samples *via* SEM and AFM, performed data analysis and wrote parts of the manuscript. Pavel Cherepanov prepared the AAO templates, performed SEM, AFM, and data analysis and wrote parts of the manuscript. Ekaterina V. Skorb and Sergey K. Poznyak assisted with preparation of AAO, were involved in scientific discussion and proof read the manuscript. Andreas Fery was involved in scientific discussion and proof read the manuscript. Javier Garcia de Abajo performed FDTD simulations, prepared the corresponding figure and proof read the manuscript. Daria V. Andreeva supervised the project, was involved in scientific discussion and proof read the manuscript. Ramon A. Alvarez-Puebla was involved in scientific discussion and proof read the manuscript. Nicolas Pazos-Perez supervised the project, performed the SERS experiments as well as data analysis and wrote the manuscript.



# 3

## Theory and Status of the Field



### 3.1 Plasmonics

The interaction of electromagnetic radiation with metals can be described in a classical picture as a local polarization induced by external driving fields.<sup>1</sup> Knowing the dielectric function and using Maxwell's set of equations, allows determining the optical response of metals.<sup>1</sup> For an isotropic material the displacement field  $\mathbf{D}$  that responds to free charges is linked to the total electric field  $\mathbf{E}$  as described in equation 1. A similar expression is obtained for the magnetic displacement  $\mathbf{B}$  and the magnetic field  $\mathbf{H}$ .<sup>1,2</sup>

$$\mathbf{D} = \varepsilon \mathbf{E} \quad (1)$$

$$\mathbf{B} = \mu \mathbf{H} \quad (2)$$

Where,  $\varepsilon$  and  $\mu$  are the dielectric constant or dielectric permittivity and magnetic permeability, respectively. In conventional materials the coupling of the magnetic field component of light to the atoms is weak at optical frequencies and the magnetic permeability  $\mu$  becomes close to unity.<sup>2</sup> The equation implies an instantaneous response of the displacement field  $\mathbf{D}$  on the electric field  $\mathbf{E}$ .<sup>1</sup> To account for the finite response time, we have to include the frequency dependency. Thus, we obtain the dispersive dielectric function  $\varepsilon(\omega)$  for linear media that represents a complete description of the interaction of matter with light in the classical picture.<sup>1</sup>

$$\mathbf{D}(\omega) = \varepsilon(\omega) \mathbf{E}(\omega) \quad (3)$$

The intriguing plasmonic response of noble metals is only due to the unique properties of the highly dispersive dielectric function, which is characterized by a negative real part  $\varepsilon'$  for a broad frequency range (see **Figure 1B**).<sup>1</sup> For metals, the dielectric function can be described by the Drude free-electron model, considering the conduction electrons to be a freely movable, non-self-interacting gas while the metal lattice is fixed.<sup>1</sup> Thus, only the collective time variant oscillations of the electrons within the metal, driven by the external applied field, are considered. Taking contributions from the bound electrons into account (*e.g.* interband transitions) we can define the extended Drude or Lorentz-Drude model as:<sup>1-3</sup>

$$\varepsilon(\omega) = \varepsilon' + i\varepsilon'' = \varepsilon_b(\omega) - \frac{\omega_p^2}{(\omega^2 + \gamma^2)} + i \frac{\omega_p^2 \gamma}{\omega(\omega^2 + \gamma^2)} \quad (4)$$

Where,  $\varepsilon_b(\omega)$  is the contribution of the core electrons (background permittivity) modeled as Lorentz-oscillators,  $\omega_p$  is the volume plasma frequency and  $\gamma$  is the

damping constant or Drude relaxation rate.<sup>1-3</sup> For small frequencies, the contribution of  $\epsilon_b(\omega)$  can be considered to be a constant offset value.<sup>2</sup>

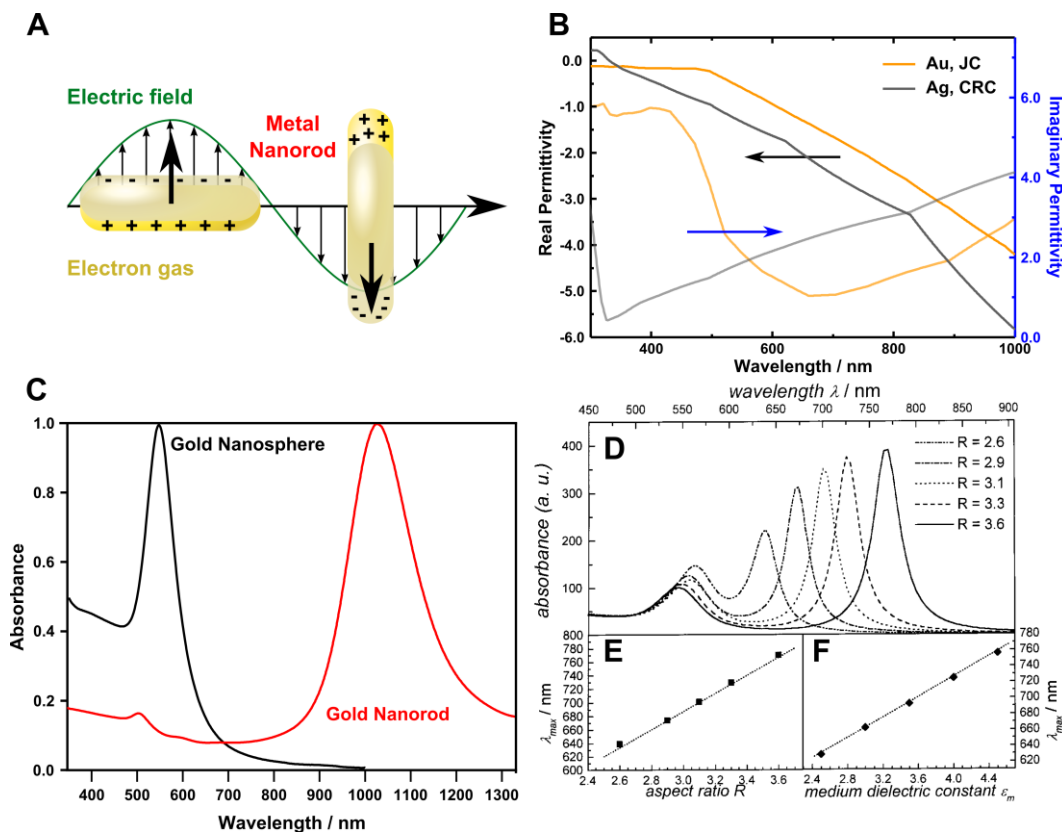


**Figure 3.1.** (A) Schematic depiction of the collective displacement of the conduction electrons in a metal nanorod coupled to an external driving electromagnetic field. (B) Dielectric function of gold and silver. Data taken from Ref 4 (Johnson and Christy, Gold), and Ref 5 (CRC, Silver). (C) Normalized LSPRs spectra, obtained for gold spheres (80 nm) and gold nanorods (13 x 80 nm, AR = 6.1). Reprinted with permission from Ref. 6, ©2014 American Chemical Society, and Ref. 7, ©2015 Elsevier Ltd. (D) Simulated surface plasmon absorption of gold nanorods with varied aspect ratios (2.6-3.6) using Gans theory.<sup>8</sup> (E) Longitudinal LSPR plotted vs. aspect ratio. (F) Longitudinal LSPR plotted vs. the surrounding medium dielectric constant. The obtained red-shift of the longitudinal LSPR follows a linear trend for both, increasing aspect ratio and increasing medium dielectric constant. Reprinted with permission from Ref. 8, ©1999 American Chemical Society.

Damping provides the imaginary part  $\epsilon''$  of the dielectric function and is due to collisions of electrons with the atomic lattice or other scattering events.<sup>1</sup> Consequently, it is directly linked to the electron mean free path  $l$  and the Fermi velocity  $v_F$  via  $\gamma = v_F/l$ .<sup>2</sup> The volume plasma frequency  $\omega_p$  can be expressed as shown in equation 5.

$$\omega_p = \sqrt{\frac{ne^2}{\epsilon_0 m}} \quad (5)$$

Where,  $n$  is the charge carrier or conduction electron density,  $e$  is the elementary charge,  $\epsilon_0$  is the vacuum permittivity, and  $m$  is the electron effective mass, respectively.<sup>2</sup>

Generally, plasmons (*e.g.* volume, surface, and localized surface plasmons) are electron density oscillations and have a longitudinal wave character. Consequently, they can only be excited by transverse electromagnetic waves, if the electric field component is in plane with the electron density oscillation.<sup>1</sup>

The above discussed considerations were made for bulk metals/infinite surfaces. However, the situation changes dramatically for metal structures with finite dimensions close to or smaller than the exciting wavelength. Coupling of the external time variant electromagnetic field and the confined conduction electrons within the metal nanostructure results in a coherent motion of the conduction electrons, as schematically depicted in **Figure 3.1A**.<sup>1,9</sup> Because of the displacement of the electrons negative and positive excess charge densities develop at opposite sides, which in turn results in a net restoring force.<sup>1,10</sup> The strength of this restoring force defines the resonant, collective oscillation frequency of the conduction electrons.<sup>1,10</sup> These discrete localized surface plasmon resonances (LSPRs) are responsible for the strong absorption and scattering of noble metal nanoparticle dispersions within the optical frequency range, as shown in **Figure 3.1C** for gold spheres and nanorods, and provide their bright colors.<sup>1,9,10</sup>

In 1908, Mie presented his exact theoretical description of the LSPRs obtained for spherical metal nanoparticles by solving Maxwell's equations in spherical coordinates, including linear optical effects such as scattering and extinction.<sup>1,9-11</sup> This multipolar approach fully accounts for phase retardation effects present in larger metal nanoparticles (>20 nm), which give rise to higher order resonance modes, such as quadrupolar modes.<sup>1,10,11</sup> Retardation effects are responsible for the extrinsic size effect becoming manifest in the red-shift of the LSPRs with increasing nanoparticle diameter.<sup>1,9,10</sup> Furthermore, Mie's theory can be expanded to account for different shapes of nanoparticles.<sup>1,9,12</sup>

For particles, which are significantly smaller than the excitation wavelength (<20 nm) retardation effects can be neglected and the electric field can be considered to be

constant across the metal nanoparticle.<sup>1,9,10</sup> As a consequence, Mie's theory can be approximated *via* the quasistatic approximation for a metal nanoparticle in an electrostatic field and the complex polarizability  $\alpha$  obtained for a homogeneous isotropic sphere can be expressed as shown in equation 6.<sup>1,9</sup>

$$\alpha = 4\pi a^3 \frac{\varepsilon - \varepsilon_m}{\varepsilon + 2\varepsilon_m} \quad (6)$$

Where  $a$  is the particle diameter,  $\varepsilon$  the dielectric function of the metal and  $\varepsilon_m$  the dielectric constant of the environment, respectively. For a frequency dependent dielectric function  $\varepsilon(\omega)$  of the metal, following the Drude form, the polarizability  $\alpha$  expresses a resonance at the minimum of the denominator ( $\varepsilon + 2\varepsilon_m$ ).<sup>9</sup> For a small or invariant imaginary part  $Im[\varepsilon(\omega)]$  this expression simplifies to the Fröhlich condition that is  $Re[\varepsilon(\omega)] = -2\varepsilon_m$  for the real part and the resonance condition for a metal sphere in air ( $\varepsilon_m = 1$ ) is met for  $\omega_0 = \omega_p/\sqrt{3}$ .<sup>9</sup> This fundamental mode is the dipolar surface plasmon of the metal nanoparticle.<sup>9</sup> Apparently, the resonance frequency  $\omega_0$  is size independent, within the quasistatic approximation, but strongly dependent on the dielectric environment and red-shifts for increasing  $\varepsilon_m$ , as depicted in **Figure 3.1F** for gold nanorods.<sup>1,8,9</sup> This effect is exploited in numerous applications to detect changes in the environmental refractive index  $n = \sqrt{\varepsilon_m}$ .<sup>13</sup>

Furthermore, the far field scattering  $\sigma_{sca}$  and absorption  $\sigma_{abs}$  cross-sections can be directly calculated from the polarizability  $\alpha$  *via* equations 7 and 8.<sup>1</sup>

$$\sigma_{sca} = \frac{k^4}{6\pi} |\alpha|^2 = \frac{8\pi}{3} k^4 a^6 \left| \frac{\varepsilon - \varepsilon_m}{\varepsilon + 2\varepsilon_m} \right|^2 \quad (7)$$

$$\sigma_{abs} = k Im[\alpha] = 4\pi k a^3 Im \left[ \frac{\varepsilon - \varepsilon_m}{\varepsilon + 2\varepsilon_m} \right] \quad (8)$$

Where the wave vector  $k = 2\pi/\lambda$ . Consequently, both, the scattering and absorption intensity, strongly scale with nanoparticle size and for large particle diameters (>80 nm) the scattering cross-section will dominate the extinction.<sup>14</sup> The analytical quasistatic approximation can be extended to ellipsoids and the orientation dependent polarizability  $\alpha_i$  obtained is shown in equation 9.<sup>1,9</sup>

$$\alpha_i = 4\pi a_1 a_2 a_3 \frac{\varepsilon - \varepsilon_m}{3\varepsilon_m + 3L_i(\varepsilon - \varepsilon_m)} \quad (9)$$

Where  $a_1 \leq a_2 \leq a_3$  are the semi axes of the ellipsoid and  $L_i$  is the geometrical factor that is:

$$L_i = \frac{a_1 a_2 a_3}{2} \int_0^\infty \frac{dq}{(d_i^2 + q)f(q)} \quad (10)$$

with  $f(q) = \sqrt{(q + a_1^2)(q + a_2^2)(q + a_3^2)}$ .<sup>9</sup> For a sphere, the geometrical factor becomes unity and  $a_1 = a_2 = a_3 = 1/3$  and, thus, equations 6-8 are recovered.<sup>1</sup> The general resonance condition is satisfied for  $\omega_i = \omega_p \sqrt{L_i}$ .<sup>1</sup> For a prolate spheroid, that is an elongated, rod-like particle, the two minor axes become equal ( $a_2 = a_3$ ) and, consequently,  $1/3 \leq L_x = L_y \leq 1/2$  and  $L_z \rightarrow 0$ .<sup>1,9</sup> Hence, the conduction electrons, which oscillate along the minor and major axes, exhibit different polarizabilities and give rise to two separate plasmon resonance modes.<sup>1,9</sup> These modes are referred to as transversal and longitudinal mode, respectively.<sup>1</sup> The transversal mode is slightly blue-shifted, whereas the longitudinal mode is strongly red-shifted (see **Figure 3.1C/D**) compared to the mode obtained for a spherical particle. This red-shift scales almost linearly with increasing aspect ratio, due to an increase in charge separation and, thus, a decrease in the net restoring force. Consequently, varying the aspect ratio of noble metal nanorods allows to tune their plasmon resonances across the entire visible into the NIR wavelength range, as shown in **Figure 3.1C-E**.<sup>1,8,10</sup> In general, the number of resonance modes obtained for metal nanostructures increases with decreasing symmetry.<sup>15</sup>

The strongly size and shape dependent LSPRs of isolated metal nanoparticles,<sup>16-18</sup> especially of gold nanorods, are used in a wide range of applications, *e.g.* as refractive index sensors,<sup>13,19</sup> for hyperthermia,<sup>20</sup> and as labels, due to their high scattering and absorption cross-sections and the absence of photo-bleaching effects.<sup>13,20</sup>

LSPRs of metal nanostructures placed in close proximity to each other undergo plasmon coupling. Plasmon coupling results in significant spectral shifts of the overlapping plasmon resonances<sup>21</sup> and gives rise to complex optical responses.<sup>6</sup> Furthermore, near-field coupling results in highly localized fields and facilitates the propagation of light below the limit of diffraction.<sup>22-24</sup>

Near-field dipolar coupling efficiency scales exponentially for small particle separations and drops off for separations exceeding approx. 2.5 times the particle diameter.<sup>25</sup> The strong distance dependency is exploited for instance in “plasmon ruler” applications, as a measure of the interparticle distance.<sup>26,27</sup>

The dipolar near-field coupling between plasmon resonances of two spherical nanoparticles can be described according to the quasistatic plasmon hybridization model in close analogy to the hybridization model applied to overlapping orbitals in molecules.<sup>1,28,29</sup> Two excited dipoles that oscillate in-phase along their major axis

hybridize into a symmetric “bonding” mode. This bonding mode is characterized by a net dipole moment that can be excited by an incident plane wave and, thus, is referred to as “bright” mode.<sup>1</sup> The resonance frequency of the bonding mode is shifted to energetically lower values. Out-of-phase oscillation of the coupled dipoles gives rise to an antisymmetric “antibonding” mode without a net dipole moment.<sup>1</sup> Therefore, this mode cannot be excited by an incident plane wave and is referred to as “dark” mode with a characteristic resonance frequency shifted to energetically higher values.<sup>1</sup> Because of the versatility of the plasmon hybridization model, it can be applied to more complex geometries such as nano-shells,<sup>28</sup> nanostars<sup>30</sup> or nanorods.<sup>20,31</sup>

For dimers of gold nanorods, a huge variance of relative orientations exist.<sup>31</sup> Four hybridized modes are obtained for the symmetric tip-to-tip and side-by-side alignment and longitudinal excitation, as depicted in **Figure 3.2A**.<sup>31,32</sup> The bright mode with the lowest energy is the bonding mode obtained for tip-to-tip geometry, whereas the bright mode with the highest energy is the antibonding mode obtained for side-by-side assembled rods.<sup>31-33</sup> Two modes can be classified as dark modes without a net dipole moment, the bonding side-by-side and antibonding tip-to-tip mode.<sup>31</sup> The dark bonding mode, obtained for the side-by-side dimer configuration is of central importance for metamaterials, to be discussed in detail in **Section 3.3**.

Breaking of the symmetry, due to small variations in size,<sup>20,34,35</sup> position<sup>20,35-37</sup> or dielectric environment,<sup>20</sup> allows bright and dark modes to couple and indirectly excite dark modes. Consequently, such dark modes can be referred to as “grey” modes, which are characterized by a low coupling efficiency and a small net dipole moment.<sup>38</sup> Since dark modes are “non-radiant” and are, thus, generally characterized by low radiative loss and narrow linewidths,<sup>38</sup> they can be utilized for efficient wave guiding in strongly coupling nanoparticle chains.<sup>39,40</sup>

Interference between parallel excited broad bright and narrow dark modes gives rise to Fano resonances, characterized by an asymmetric linewidth and a narrow spectral transparency window.<sup>41</sup> The effect of symmetry-breaking, which enables excitation of dark modes, and the ability to tune the spectral position of both bright and dark modes independently in coupled plasmonic nanostructures can give rise to strong, tunable Fano resonances with steep dispersion.<sup>36,41</sup> Because of their strong sensitivity towards the local dielectric environment Fano resonances are of particular interest

for different applications, *e.g.* for plasmon rulers,<sup>37</sup> for optical switches,<sup>42</sup> non-linear optics<sup>43</sup> and metamaterials.<sup>32</sup>

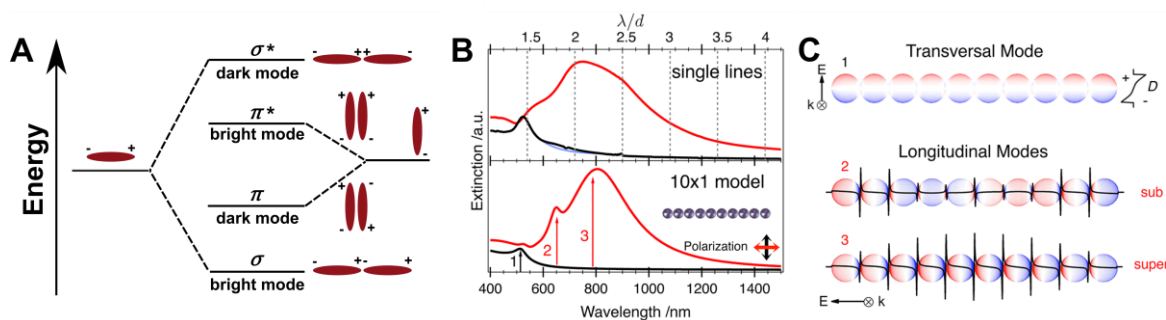


**Figure 3.2.** (A) Hybridization model obtained for different geometric arrangements of gold nanorod dimers for longitudinal excitation (\* denotes antibonding modes). Adapted with permission from Ref. 32, ©2006 American Chemical Society. (B) Polarization dependent optical far-field spectra obtained experimentally for centimeter-squared assemblies of close-packed single lines of gold nanospheres and simulated for ten particles *via* generalized multisphere Mie theory. (C) Obtained transversal, sub- and super-radiant modes for single particle chains. Reprinted with permission from Ref. 6, ©2014 American Chemical Society.

Strong collective plasmon coupling within ensembles of close-packed chains of plasmonic nanoparticles gained increasing attention recently, owing to their potential for efficient wave guiding below the diffraction limit.<sup>6,21,39,40,44,45</sup> Such surface-assemblies are characterized by a strong anisotropic optical response<sup>6,21,44,46,47</sup> and can be produced on centimeter-square areas with small (1-2 nm) interparticle distances utilizing bottom-up self-assembly strategies, as depicted in **Figure 3.2B**.<sup>6</sup> Increasing the chain length results in a significant red-shift of the dominant longitudinal dipolar super-radiant mode,<sup>21</sup> accompanied by the emergence of higher order dipolar sub-radiant and quadrupolar modes (see **Figure 3.2C**).<sup>6,44,45</sup> Eventually, the shift converges and becomes independent of the chain-length above a critical threshold, called the “infinite chain limit”, typically reached for ten particles in a single particle chain.<sup>6,45</sup>

To gain detailed information about the far-field as well as the near-field response of arbitrarily shaped particles, either isolated or in complex arrangements, various numerical approaches have been developed for computational modelling, such as for instance the finite-difference time-domain (FDTD) method,<sup>1,48</sup> the discrete dipole approximation (DDA),<sup>1,29</sup> the multiple multipole (MMP) methods,<sup>1,6,29</sup> and the boundary element method (BEM).<sup>1,29,49</sup>

In conclusion, the ability to confine electromagnetic radiation below the limit of diffraction and to precisely tune plasmonic structures down to the nanoscale, to tailor their optical properties renders the field of plasmonics a fascinating research topic with high potential for the design of optical devices and metamaterials. The phenomena of surface-enhanced Raman scattering (SERS) and optical metamaterials will be discussed in more detail in the following sections as they are of central importance for this thesis.

## 3.2 Surface-Enhanced Raman Scattering Spectroscopy

Raman scattering is an inelastic scattering process, which is in contrast to elastic scattering (Rayleigh scattering) accompanied by a change in energy of the scattered photon, first discovered by Chandrasekhara Venkata Raman in 1928.<sup>50,51</sup> The difference in energy between the incoming and scattered photon corresponds to different vibrational states of the molecule and, therefore, the Raman spectrum represents a unique fingerprint of the molecule.<sup>51</sup> Surface-enhanced Raman scattering (SERS) is a phenomenon allowing for highly sensitive structural detection of low concentrated analytes and was first reported in the mid 70's for pyridine adsorbed on roughened silver electrodes.<sup>52-54</sup> SERS relies on amplification of the normal Raman scattering cross-section of the probe molecule adsorbed on or in close vicinity to nanostructured metal surfaces by many orders of magnitude.<sup>51,55-57</sup> This is based on the strong localized enhancement of the electromagnetic (EM) field, which arises from the localized surface plasmon resonances, antennae effects and plasmon coupling obtained for nanostructured metal surfaces.<sup>51,55-57</sup> For a linear response approximation and using complex notations to account for the harmonic time dependency, a simple proportionality between the modified Raman polarizability  $\alpha^R$ , the modified electromagnetic field  $\vec{E}_{Loc}$  at the molecule position and the excited Raman dipole  $\vec{p}$  that oscillates at the shifted Raman-frequency  $\omega_R$  is obtained under SERS conditions:<sup>56</sup>

$$\vec{p}(\omega_R) = \alpha^R(\omega_R, \omega_L) \vec{E}_{Loc}(\omega_L) \quad (11)$$

Where  $\omega_L$  is the exciting laser frequency. Consequently, the radiated power of the Raman dipole that is proportional to  $|\vec{p}|^2$  can be enhanced by two effects either by

increasing  $\vec{E}_{Loc}$ , referred to electromagnetic enhancement or by increasing  $\alpha^R$ , referred to as chemical enhancement.<sup>56</sup>

The chemical enhancement effect is analyte specific and based on perturbations of the electron density of the probe molecules, due to weak or strong electronic (covalent) interactions with the metal substrate and charge transfer effects changing their optical polarizability.<sup>56</sup> However, chemical enhancement only results in enhancement factors (EF) of around one order of magnitude and, thus, contributes insignificantly to the overall SERS EF.<sup>56,58</sup>

Consequently, the main effect that boosts the SERS EF is the strongly amplified magnitude of the localized electromagnetic field at the surface of plasmonic metal nanostructures that can exceed the magnitude of the incoming electromagnetic field by many orders of magnitude, when excited close to its resonance frequency (see **Section 3.1**).<sup>56</sup> These spatially localized regions providing high field enhancement are called hot spots.<sup>55,57</sup>

The contribution of the local field enhancement to the SERS EF can be estimated by considering two effects. (1) The contribution of the scattered light at the laser excitation frequency  $\omega_L$  affecting the excitation of the Raman dipole (incoming light) and (2) at the shifted Raman frequency  $\omega_R$  affecting the emission of the Raman dipole (outgoing light).<sup>56,57</sup> Both effects are directly proportional to the magnitude of the local field enhancement  $|\vec{E}(\omega)|^2$  and, thus, the EM enhancement factor can be expressed as the so called  $|E|^4$  approximation, ignoring the Raman shift and considering that  $\omega_L \sim \omega_R$ :<sup>56</sup>

$$EF_{EM} \approx M_{Loc}(\omega_L)M_{Loc}(\omega_R) \approx \frac{|\vec{E}(\omega_L)|^4}{|\vec{E}_0(\omega_L)|^4} \quad (12)$$

Where  $M_{Loc}(\omega) = |\vec{E}(\omega)|^2 / |\vec{E}_0(\omega)|^2$ . Maximum EM field enhancement obtained at hot spots can be predicted from EM calculations to be as high as  $5 \cdot 10^4$  for spheres and  $3 \cdot 10^7$  for ellipsoids.<sup>55</sup> Furthermore, plasmon coupling can result in further amplification of the field intensities within the gap of coupling nanostructures, due to strongly constrained fields providing field enhancement of  $5 \cdot 10^9$  or larger.<sup>55,57</sup>

In addition to the simplified estimations discussed above, several considerations need to be taken into account for the determination of SERS EF in real systems and for the tailored nanofabrication of SERS substrates. Since the magnitude of field enhancement drops off very quickly, the amplification of the Raman signal strongly

scales with the distance ( $I_{SERS} \propto r^{-10}$  for a sphere) of the analyte to the surface.<sup>57,59</sup> Furthermore, the overall concentration and distribution of the probe molecule at the substrate surface is a crucial parameter when determining single molecule (SM)<sup>55</sup> or averaged SERS EF.<sup>56</sup> The highest SERS EF reported are within the range of  $\sim 10^{10}$ - $10^{11}$ , in good agreement with predictions based on electromagnetic calculations.<sup>56,58</sup>

Since almost every molecule is Raman active SERS is a powerful, non-destructive method that is used in various disciplines including polymer and materials science, biosensing, biochemistry, catalysis and electrochemistry, amongst others.<sup>57,58</sup>

The ideal SERS substrate is chemically stable, provides high, homogeneous and reproducible SERS enhancement and is easy to prepare.<sup>57</sup> Consequently, most often nanostructured noble metals such as gold or silver with optimized plasmon resonances are employed as SERS platforms.<sup>57,58</sup> Thus, recent advances in SERS are intimately linked to the field of plasmonics and nanofabrication.<sup>57,58</sup>

Since SERS requires the analyte to be in close proximity to the hot spot, either probe molecules with high affinity towards metal surfaces such as thiolated compounds or smart surfaces that trap the molecule of interest in close proximity to the metal surface are required. The latter can be realized utilizing host-guest interactions, *e.g.* highly specific antigen to antibody coupling,<sup>60,61</sup> or DNA hybridization,<sup>62</sup> and shells of SERS encoded silica<sup>63</sup> or polymers such as pNIPAM.<sup>64,65</sup>

Nanosphere lithography (NSL) is a simple and reproducible method to prepare highly regular nanostructured SERS substrates.<sup>57</sup> Monolayers of self-assembled hexagonally close-packed colloids are either coated with metal films (film over nanosphere, FON)<sup>66</sup> or used as masks for metal nanostructure fabrication.<sup>67</sup>

Recent development in wet-chemical synthesis approaches provides a huge variety of nanoscopic metal building-blocks,<sup>68</sup> *e.g.* gold nanorods and nanostars that provide high EM field enhancement at their tips. Capillary force driven self-assembly of vertically-aligned hexagonally close-packed nanorod films provides high densities of homogeneously distributed hot spots with high SERS EF, due to the antenna effect.<sup>69,70</sup> Another level of hierarchy can be achieved utilizing nanostructured templates that allow for spatially controlling hot spot positions and further increase the substrate homogeneity, which is a prerequisites for analytical SERS.<sup>65,71-73</sup>

Self-assembly of metal nanoparticles into dimers, trimers and clusters provides individual SERS platforms both in solution and on substrates.<sup>74,75</sup> Selective cluster

formation can either be realized *via* DNA hybridization<sup>46,68,75,76</sup>, employing pickering emulsions<sup>74</sup> or *via* template-assisted self-assembly (see **Section 3.6**).<sup>77</sup>

### 3.3 Optical Metamaterials

Optical metamaterials are artificial mesostructured materials with effective optical properties that are determined by the mesostructure rather than by the properties of the constituent components only. Thus, they allow tailoring of effective medium constants in the visible frequency range, like the index of refraction by design.<sup>2</sup> Such materials with unusual optical properties can be prepared from rationally designed building blocks, so-called “meta-atoms” with subwavelength dimensions, organized into structured composites with periodicities well-below the wavelength of interest.<sup>2</sup> A special class of metamaterials represent materials with negative index of refraction (NIMs). As proposed by Veselago *et al.*<sup>78</sup> in 1968, such a material can be realized if both the electric permittivity  $\epsilon$  and magnetic permeability  $\mu$  are negative within the same frequency range. Following Snell’s law, such materials refract the incoming light beam to the same side of the interface normal when crossing the boundary between positive and negative index of refraction.<sup>79,80</sup> Furthermore, the flow of energy (Poynting vector) and the phase velocity (wave vector) are pointing in opposite directions for light traveling in a material with negative index of refraction.<sup>2,81,82</sup> Based on the concept of NIMs, various intriguing applications have been proposed, such as subdiffraction limit imaging (super lenses),<sup>81,83</sup> optical cloaking,<sup>84</sup> and nonlinear optics.<sup>85</sup>

Whereas metals provide a negative permittivity below their plasma frequency, the interaction of matter with the magnetic field component of light is weak and the permeability for natural materials is, thus, close to unity.<sup>86,87</sup> To overcome this limitation, magnetic meta-atoms providing negative permeability can be designed from nonmagnetic conducting materials.<sup>88,89</sup> The basic concept for magnetic meta-atoms is a pair of split ring resonators (SRR), which was first described theoretically by Pendry *et al.*<sup>88</sup> Following this concept Smith *et al.*<sup>89</sup> were the first to experimentally demonstrate effective negative index of refraction within the GHz frequency range. The magnetic response of the engineered, artificial meta-atoms arises from its interaction with impinging electromagnetic radiation. Either, the magnetic or electric field component, excites a current flow within a circular metallic ring, purely inductive

$L$  in nature and non-resonant.<sup>2</sup> To enhance the magnetic response and introduce a resonance, the ring is intersected at one side resulting in a capacitance  $C$ .<sup>2</sup> Consequently, the SRR acts as a LC oscillator with a resonance frequency  $\omega_0$  of  $1/\sqrt{LC}$ . This gives rise to a negative permeability  $\mu$  close to the high frequency range of the resonance.<sup>2,89</sup>

Scaling the dimension of the SRR allows for tuning the resonance to higher frequencies close to the spectral range of visible light.<sup>90-92</sup> However, there are several challenges accompanied with scaling of planar SRR. Close to their plasma frequency the properties of metals strongly deviate from ideal conductors, characterized by increased losses and finite charge carrier velocity, which inherently limits the scalability of SRR.<sup>2,93,94</sup> Furthermore, scaling is also limited from a technical point of view as for nanometer sized features expensive and time consuming nanofabrication techniques, *e.g.* e-beam lithography, need to be applied.<sup>92</sup>

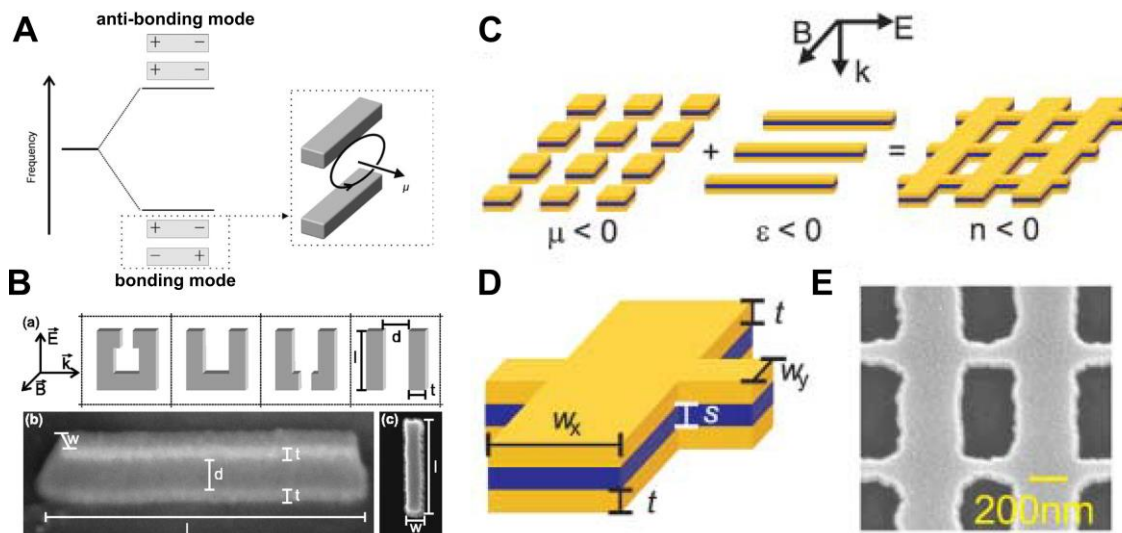


**Figure 3.3.** (A) Transverse coupling of two parallel metal nanowires according to the hybridization model. Resonant excitation of the antisymmetric bonding mode provides a current loop with a magnetic dipole moment that acts as magnetic “atom”. Reprinted with permission from Ref. 95, ©2010 Wiley-VCH Verlag GmbH & Co. KGaA, Weinheim. (B) Evolution of the split Ring resonator (SRR) towards a parallel rod arrangement and lithographically prepared parallel metal nanorods. Reprinted with permission from Ref. 98, ©2005 Optical Society of America. (C/D) Schematic depiction of the double-fishnet structure consisting of parallel metal rods ( $\mu < 0$ ) and metal wires ( $\epsilon < 0$ ). (E) Lithographically prepared double-fishnet structure, which provides an effective negative index of refraction. Reprinted with permission from Ref. 100, ©2006 by the American Association for the Advancement of Science.

To partly overcome these limitations and to push the magnetic resonance into the visible frequency range, the design of meta-atoms has been adjusted.<sup>87,94</sup> Dipolar coupling of side-by-side aligned metal wires gives rise to two distinct hybridized modes, an antibonding bright mode and a bonding dark mode (see **Section 3.1**).<sup>38,95</sup> The antisymmetric surface charge pattern of the dark bonding mode results in a current loop and represents a fundamental design approach for plasmonic metamaterials with negative permeability (see **Figure 3.3A**).<sup>38,95</sup> Breaking of the symmetry allows to excite the dark mode and can result in a magnetic response in the visible frequency range (see **Figure 3.3B**).<sup>96-98</sup>

Resonantly excited metal nanoparticles, placed in close proximity to a metal film give rise to induced mirror charges, which are characterized by an antisymmetric charge pattern. Thus, they are equivalent to the dark bonding modes within the hybridization model (see **Section 3.1**). Consequently, such mirror charges can result in magnetic modes that can provide negative permeability.<sup>99</sup>

Combining these meta-atoms with effective negative permittivity at the same frequency range can result in materials with effective negative index of refraction within the visible frequency range.<sup>87,94</sup> In this context, especially the so called “double-fishnet” structure proved efficiency within the visible frequency range, as depicted in **Figure 3.3C-E**.<sup>100-104</sup> This metal nanostructure design combines metal nanobars separated by a dielectric spacer and metal wires, which provide negative permeability and negative permittivity, respectively.

Whereas the above discussed metamaterial designs are two-dimensional metasurfaces, several attempts towards three-dimensional designs have been reported.<sup>105,106</sup> These approaches, which provide materials with negative permeability and negative index of refraction within the visible frequency range, rely on hierarchical stacking of several meta-layers prepared *via* elaborate nanofabrication methods.<sup>95,103,107,108</sup>

Here, the discussion is limited to optical metamaterial concepts closely related to negative index of refraction. However, the field of optical metamaterials is impressively wide and still evolving quickly.<sup>38,105,109</sup>

Three key concepts will significantly contribute to overcome the challenges related to optical losses of metals and nanofabrication methods limiting today’s applicability of optical metamaterials. (I) further development of the already widely used concept of two-dimensional optical metasurfaces will enable the reduction of losses, the

implementation into nanophotonic chip devices and reduce the challenges associated with elaborate nanofabrication processes.<sup>38,105</sup> (II) introducing alternative plasmonic materials that operate in the visible frequency range such as intermetallics will reduce losses, allow to tune the resonance frequencies over a wide range and enhance the compatibility with silicon based chip technology.<sup>3,105</sup> (III) the application of bottom-up nanofabrication methods, such as self-assembly on all levels of hierarchy, *e.g.* individual meta-atoms and periodic metasurfaces/metamaterials, will pave the road towards scalability and cost-efficient mass production (see **Section 3.6**).<sup>110</sup>

### 3.4 Synthesis of Gold Nanorods

Metal nanocrystals are particles having at least one-dimension with a length-scale in the nanometer range (1-100 nm).<sup>15</sup> They have been used for centuries to stain glass windows, owing to their unique optical properties arising from localized surface plasmon resonances (see **Section 3.1**).<sup>10</sup> Faraday was the first who reported on a protocol for the preparation of spherical gold nanoparticles by reducing a gold precursor solution with phosphorous in water.<sup>111</sup> However, the wet-chemical synthesis of anisotropic one-dimensional metal nanoparticles, *e.g.* gold nanorods (AuNRs), was only achieved within the last few decades.<sup>112</sup> Since then, the field of nanocrystal synthesis has witnessed a tremendous development and, today, scientists are able to prepare high quality metal nanoparticles in large-quantities, with precise control over composition, shape, and size and with tailored optical properties.<sup>10,15,112,113</sup> In this context, the wet-chemical seed-mediated synthesis of AuNRs, is by far the most efficient and reliable protocol for the large-scale preparation of one-dimensional plasmonic building blocks with tailored optical properties and narrow size distribution.<sup>112,114,115</sup> In the following, the fundamental mechanisms and recent developments in the controlled wet-chemical synthesis of single-crystalline AuNRs will be discussed.

For the wet-chemical seed-mediated synthesis of AuNRs several key parameters are of central importance. The crystallinity and size distribution of the employed seeds is crucial, as they dictate the final crystallinity and polydispersity of the prepared AuNRs.<sup>112,114</sup> Furthermore, shape directed nanorod growth is only facilitated in the presence of growth directing agents, *e.g.* cetyltrimethylammonium bromide (CTAB), selectively stabilizing certain crystallographic facets.<sup>112,114-116</sup> Additionally, control

over growth kinetics and impurities plays a central role as they affect the overall gold nanorod quality and the amount of byproducts.<sup>112</sup>

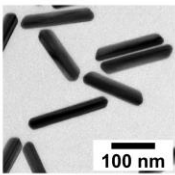
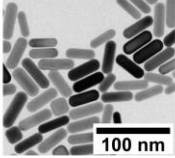
For gold, which preferentially packs in a face centered cubic (fcc) lattice, the surface energies of the low-index facets follow the energetic sequence of  $\gamma_{\{111\}} < \gamma_{\{100\}} < \gamma_{\{110\}}$ .<sup>15</sup> Halide anions and their complexes have a pronounced affinity towards the low index facets of gold nanocrystals and their binding affinity follows the sequence  $\text{Cl}^- < \text{Br}^- < \text{I}^-$ .<sup>113,117,118</sup> Several studies claim that bromide ions have a higher affinity towards the more open, higher energy  $\{100\}$ <sup>119,120</sup> or  $\{110\}$ <sup>121</sup> facets, whereas iodide ions have a strong affinity towards the  $\{111\}$ <sup>122,123</sup> facets. However, the role of halides as shape-directing agents in nanocrystal growths is complex and still under debate.<sup>113,118,124</sup>

The key step for large-scale synthesis of AuNRs with high yields was the separation of the fast seed preparation step, which provides seeds with desired crystallinity and narrow size distribution, from the subsequent slow and directed gold nanorod growth step.<sup>112</sup>

Small gold nanoparticle seeds are prepared *via* a fast nucleation step under oversaturated chemical conditions with a strong reducing agent, such as sodium borohydride.<sup>114</sup> Within the size regime of the seed particles (<10 nm) the minimum free energy structures are multiply-twinned particles such as icosahedra or decahedra, bound by  $\{111\}$  facets.<sup>15,125</sup> However, seed crystallinity and size strongly depends on the employed stabilizing agent. Citrate-capped seeds express a multiply-twinned crystal structure.<sup>114,126</sup> In contrast, CTAB stabilized seeds are single-crystalline and have a truncated octahedron (Wulff's polyhedron) shape balancing the expression of  $\{111\}$  and  $\{100\}$  facets with the nearly spherical shape.<sup>127</sup> This is the thermodynamically most stable form for a fcc metal nanocrystal.<sup>15</sup>

The cationic surfactant CTAB is by far the most widely used surfactant for uniaxial gold nanorod growth.<sup>112,115</sup> Above its critical micelle concentration of 0.8 mM, CTAB micelles with an aggregation number of 60 are obtained.<sup>130</sup> CTAB micelles and metal ions present in solution form stable micelle- $\text{Au}^{3+}$  complexes with one CTAB- $\text{Au}^{3+}$  molecule solubilized in each micelle.<sup>130</sup> Furthermore, CTAB forms a stable close-packed bilayer at the gold nanocrystal surface above the critical micelle concentration.<sup>131-133</sup> The positively charged ammonium headgroups are bound to bromide ions that cover the gold surface. The hydrophobic tails point towards the environment and the second CTAB layer is adsorbed onto the surface layer *via*

hydrophobic tail-to-tail interactions.<sup>131</sup> Thus, a positively charged CTAB bilayer is formed, which provides electrostatic stabilization of gold nanocrystals in water and provides a zeta potential of up to +90 mV.<sup>116</sup>

Seed	Growth solution	AuNR Properties/Structure	Notes
(I) 3.5 nm Citrate AuNP	HAuCl <sub>4</sub> , CTAB, Ascorbic Acid	 Dimensions ~ 400 x 25 nm	- 5% rod yield (by shape) - AR 6-20 - Penta-twinned crystals
(II) 1.3 nm CTAB AuNP	HAuCl <sub>4</sub> , CTAB, AgNO <sub>3</sub> , Ascorbic Acid	 Dimensions ~ 60 x 12 nm	- 95% rod yield (by shape) - 15% rod yield (total gold) - AR 1.5-5.0 - Single-crystals

**Figure 3.4.** (A) Comparison of the two fundamental seed-mediated AuNR growth approaches. (I) The three-step seeded growth approach based on citrate-capped seeds which provides penta-twinned nanorods with aspect ratios in the range from 6-20, as proposed by Jana *et al.*<sup>128,129</sup> in 2001. (II) The silver-assisted seeded growth based on CTAB-capped seeds, which provides single-crystalline AuNRs with aspect ratios in the range from 1-5, as published by Nikoobakht *et al.*<sup>121</sup> in 2003. Adapted with permission from Ref. 112, ©2013 American Chemical Society. TEM figures are unpublished data. TEM of penta-twinned AuNRs reprinted with permission from Martin Mayer.

### 3.4.1 Synthesis of Penta-Twinned Gold Nanorods

The first protocol for the wet-chemical synthesis of AuNRs with reasonable yield was reported in 2001 by Jana *et al.*<sup>128,129</sup> who introduced the seed-mediated approach (see **Figure 3.4**). Citrate-capped penta-twinned seeds ( $d = 3.5$  nm) were overgrown in a growth solution containing tetrachloroauric(III) acid (HAuCl<sub>4</sub>) as metal precursor, ascorbic acid as reducing agent and the surfactant CTAB in high concentration (0.1 M).<sup>127,129</sup> Ascorbic acid is a mild reducing agent, which is not able to directly reduce the CTAB micelle-Au<sup>3+</sup> complex to Au<sup>0</sup> in acidic conditions, without the presence of metal seeds.<sup>115,116,129</sup> The obtained CTAB micelle-Au<sup>+</sup> complexes are reduced to Au<sup>0</sup> in a surface catalyzed reduction step at the seed surface.<sup>115,129</sup> This is crucial to suppress secondary nucleation.<sup>129</sup> By varying the seed to metal precursor ratio the aspect ratio could be adjusted in the range from 1 to 10.<sup>129</sup> The obtained AuNRs have a pentagonal cross-section with {111} facets at their tips and {100} facets at their sides.<sup>120</sup> Multiple subsequent overgrowth steps allow to tune the aspect ratio of the penta-twinned AuNRs in the range of 6 to 20 with dimensions up to

400 x 25 nm.<sup>128</sup> Even though the first protocol comprised silver as additive, silver is not essential for the shape-directed synthesis of penta-twinned AuNRs.<sup>128,130,134</sup>

Since the overall yield of desired shapes (AuNRs) compared to byproducts (spherical particles) is moderate, subsequent cleaning procedures, such as centrifugation<sup>128</sup> or size selective precipitation<sup>126</sup> need to be applied to increase the shape yield. Especially, depletion forces are a very powerful tool in this regard since they enable selective precipitation of specific nanoparticle shapes by adjusting the surfactant concentration.<sup>126,135,136</sup> The overall shape yield and reproducibility of the synthesis was increased by careful adjustment of the seed preparation method (~50%)<sup>116,130</sup> and pH of the solution (~90%).<sup>137</sup>

Different mechanisms have been proposed to explain the uniaxial growth of penta-twinned nanorods. Murphy's group suggested, specific CTAB binding at the longitudinal {100} facets in combination with a "zipping" mechanism of the CTAB molecules fosters metal ion reduction at the nanorod tips.<sup>120,138</sup> Mulvaney's group proposed an electric-field directed growth that gives rise to an increased collision probability and, thus, an increased reduction rate of the micelle-metal ion complex at the highly curved nanorod tips.<sup>116,130</sup> However, the initial step that results in symmetry breaking of the seed is not addressed by either models and is often attributed to the twinned structure of the seeds.<sup>130</sup>

### 3.4.2 Synthesis of Single-Crystalline Gold Nanorods

Based on the above discussed, seed-mediated protocol for pentagonal nanorods Nikoobakht *et al.*<sup>121</sup> developed the silver-assisted seed-mediated synthesis of single-crystalline AuNRs (see **Figure 3.4**). Single-crystalline CTAB-capped seeds ( $d = 1.5$  nm) and the addition of aliquots of silver nitrate to the growth solution, give rise to single-crystalline AuNRs with aspect ratios in the range of 1 to 5.<sup>121,127</sup> Changing the amount of silver ions in solution or the seed to gold ion ratio allow to tune the aspect ratio and size of AuNRs.<sup>115,121,139</sup> For increasing amounts of silver ions or gold precursor the aspect ratio increases.<sup>121,139</sup> However, above a certain silver ion concentration, the aspect ratio decreases again.<sup>121</sup> Addition of benzyldimethylhexadecylammonium chloride (BDAC) as co-surfactant, significantly reduces the reaction kinetics and results in nanorods with aspect ratios of up to 10.<sup>121</sup>

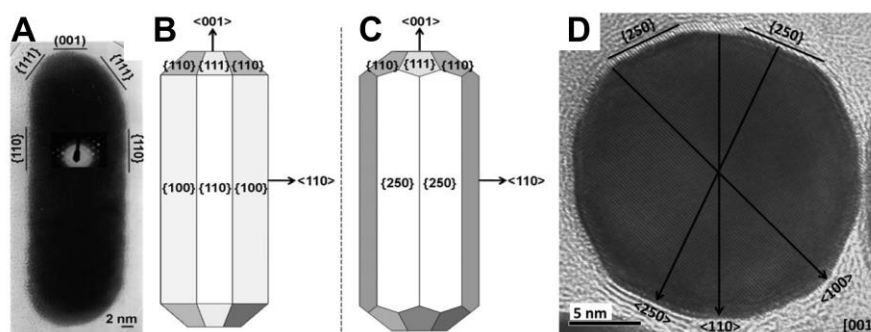


**Figure 3.5.** Comparison of the models for single-crystalline AuNRs proposed by Wang *et al.*<sup>140</sup> and Carbó-Argibal *et al.*<sup>141</sup> (A) Side-view with assigned low index facets  $\{110\}$ ,  $\{111\}$  and  $\{100\}$ . (B) Model proposed by Wang *et al.* (C) Model proposed by Carbó-Argibal *et al.* (D) Top-view with assigned high-index facets  $\{250\}$ . Both models clearly indicate an octagonal cross-section with growth direction in  $[001]$ . Adapted with permission from Ref. 140, ©1999 Elsevier Science B.V. and Ref. 141, ©2010 Wiley-VCH Verlag GmbH & Co. KGaA, Weinheim.

The high nanorod shape yield ( $> 95\%$ ), the low polydispersity and the aspect ratio range from 1 to 5, which provides tunable LSPRs within the optical frequency range, are the reasons why this protocol and its variations are the most widely used method to prepare AuNRs.<sup>112,115,139</sup> The obtained single-crystalline AuNRs have an octagonal cross-section. But the facet indexing is still controversially discussed and single-crystalline gold-nanorods have been reported to be bound by alternating  $\{100\}$  and  $\{110\}$  low-index facets<sup>127,142</sup> or in other cases by high index facets (see **Figure 3.5**).<sup>141,143</sup>

The growth kinetics of single-crystalline AuNRs have been addressed with optical spectroscopy methods<sup>139,144,145</sup> and X-ray scattering methods.<sup>146-148</sup> These studies indicate that a short initial one-dimensional growth period, which leads to high aspect ratios, is followed by three-dimensional AuNR growth, which reduces the overall aspect ratio.

The uniaxial growth of single-crystalline AuNRs proceeds in  $[001]$  direction (see **Figure 3.5**).<sup>115,127,141</sup> Consequently, the growth process is inherently linked to facet selective stabilization of the more open, higher energy longitudinal facets ( $\{100\}/\{110\}$  or  $\{520\}$ ), to efficiently reduce the deposition rate of gold onto the side facets.<sup>112,115</sup> However, the role of silver and bromide ions and the underlying growth mechanism of single-crystalline AuNRs is still under debate.<sup>112,115</sup>

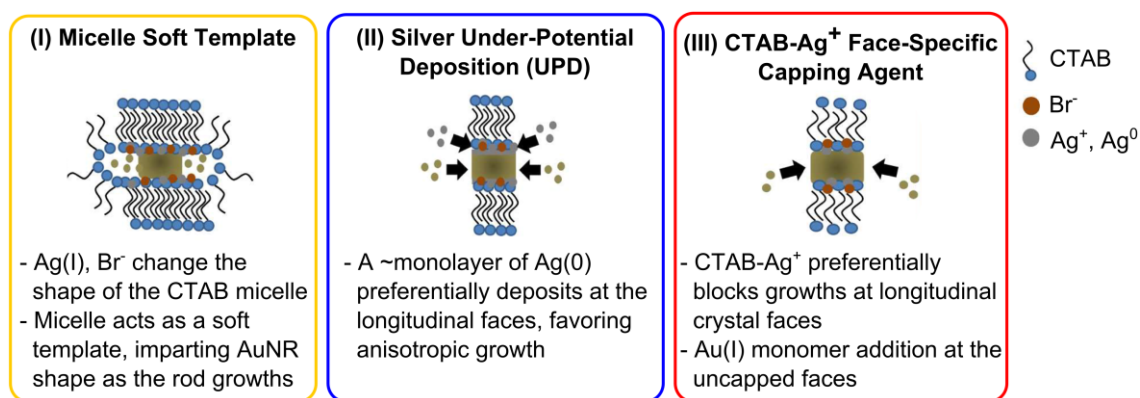


**Figure 3.6.** Three different growth mechanisms were proposed for the silver-assisted seed-mediated growth of single-crystalline AuNRs (I) Micelle Soft Template, (II) Silver Under-Potential Deposition (UPD), and (III) CTAB-Ag<sup>+</sup> Face-Specific Capping Agent. Adapted with permission from Ref. 112, ©2013 American Chemical Society.

Three different mechanism have been proposed, which potentially induce uniaxial growth of single-crystalline AuNRs (see **Figure 3.6**):<sup>112</sup> (I) the soft-templating mechanism of rod-like CTAB micelles, where silver ions induce a spherical to cylindrical transition of the micelles,<sup>149-151</sup> (II) deposition of a silver monolayer at the {110} facets of the nanorods (silver under-potential deposition (UPD)), where the UPD shift for silver on different gold facets follows the sequence {110}>{100}>{111},<sup>127,152</sup> (III) the strong binding of an unspecified CTAB-Ag<sup>+</sup> complex at the more open higher energy {110} or {520} facets.<sup>118,129,153,154</sup>

Various groups found evidence that at least a small amount (1 to 10%) of silver or silver ions are incorporated or in close proximity to the AuNR surface utilizing different analytical methods.<sup>139,154-157</sup> However, the challenge is to distinguish between elementary Ag<sup>0</sup> and Ag<sup>+</sup> ions and to identify their position at the AuNR surface to give clear evidence for one of the proposed growth mechanisms.<sup>112</sup> Furthermore, because of synergistic effects of the used reagents clear assignment of the specific role of a single component is challenging.<sup>112</sup>

Recently, the group of Liz-Marzán revisited the role of the unspecified CTAB-Ag<sup>+</sup> complex for the growth process of single-crystalline AuNRs *via* detailed simulations.<sup>118</sup> They found the formation of a CTA<sup>+</sup>[Br-Ag-Br]<sup>-</sup> being accompanied by a strong energy gain indicating that this complex is present in the growth solution. This complex adsorbs preferentially at the high index {520} facets and reduces their surface energy significantly compared to the {110} and {100} facets. Thus, the facet-selective binding of this complex can induce anisotropic growth in [100] direction.

Furthermore, they explain the important initial symmetry breaking event of the seeds by selective adsorption of  $\text{CTA}^+[\text{Br-Ag-Br}]^-$  onto the  $\{100\}$  facets of the Wulff structure.

The embryonic stages of the AuNRs growth were investigated by Walsh *et al.*<sup>125</sup> via HR-TEM, recently. Indeed, they found evidence that without  $\text{Ag}^+$  no symmetry breaking event takes place. In the presence of  $\text{Ag}^+$  single-crystalline seed particles grow isotropically until facet truncations are observed. The authors claim selective stabilization of the higher index facet truncations initiating the anisotropic growth of AuNRs.

Since the underlying growth mechanism is not fully understood and the effect of different ingredients is strongly interrelated, recent improvements made in the synthesis of the single-crystalline AuNRs are based on empirical studies.<sup>112,115</sup>

Because of the high affinity of the iodide ions towards the crystallographic facets of AuNRs already minute amounts ( $\sim 50$  ppm) have been reported to block AuNRs growth completely, due to a facet poisoning effect.<sup>117,158-160</sup> Thus, especially lot-by-lot variations of purchased CTAB batches need to be considered.<sup>158-160</sup>

Even though the stabilization of certain facets accompanied by changes in their surface energy points at a thermodynamically driven AuNRs growth process, reaction kinetics are of central importance. Generally, reducing the reaction kinetics results in enhanced shape yields and narrower size distributions, as well as higher aspect ratios, presumably due to a more epitaxial deposition of gold.

Reducing the pH value in the growth solution reduces the concentration of ascorbate monoanion that is the gold reducing species ( $\text{pK}_a^1$  of ascorbic acid is 4.1).<sup>161</sup> Consequently, lower pH values give rise to a more controlled AuNRs growth process. This results in higher aspect ratios, narrower size distributions and higher yields of AuNRs.

Alvarez-Publa *et al.*<sup>69</sup> reported on significant increase in the yield of AuNRs (1000-fold) with narrow size distribution. This was achieved by a significant increase in the seed amount applied to the growth solution and a subsequent controlled overgrowth of AuNRs *via* slow reduction of the residual gold ions in solution.

Ye *et al.* reported on binary surfactant mixtures<sup>162</sup> (CTAB/sodium-oleate (NaOL)) and aromatic additives<sup>163</sup> (salicylic acid derivatives) significantly improving the size distribution and dimensional tunability of AuNRs prepared *via* the silver-assisted synthesis. Both NaOL and salicylic acid derivatives are weak reducing agents.<sup>162,163</sup>

Pre-reduction of gold ions allows the adjustment of the amount of ascorbic acid to lower values.<sup>162</sup> Furthermore, these compounds will interact with the CTAB bilayer and alter its properties, such as packing density, its affinity towards certain facets and the stability of the complex formed with metal ions.<sup>162,163</sup> Both effects strongly influence the reaction kinetics and the overall growths process. Scarabelli *et al.*<sup>164</sup> further investigated the effect of 5-bromo salicylic acid and identified the pre-reduction time of gold ions to be the most critical reaction parameter.

Vigdmerman *et al.*<sup>144</sup> exchanged the reducing agent ascorbic acid with a large excess of hydroquinone. This results in a significant increase in aspect ratios (5 to 8) and dimensions of prepared AuNRs, as well as narrow size distributions and high shape yields (byproducts <1%). Hydroquinone is a mild reducing agent, thus, the reaction kinetics are significantly reduced compared to ascorbic acid. Furthermore, hydroquinone has a similar molecular structure as the aromatic additives discussed earlier and, hence, might interact with the CTAB bilayer or the metal complex in a similar manner. Furthermore, due to the large excess of hydroquinone gold conversion rates of almost 100% can be achieved.

### 3.5 Surface Functionalization of Gold Nanorods

The previously discussed synthetic protocols provide gold nanorods (AuNRs) with tunable optical properties, in large-quantities and with low polydispersity.<sup>115</sup> However, most often the as-synthesized AuNRs cannot be used directly for the targeted application and surface functionalization is essential to tune the properties of AuNRs and introduce additional functionality.<sup>115,165</sup>

Especially, the widely used surfactant cetyltrimethylammonium bromide (CTAB) comes along with several drawbacks, such as cytotoxicity,<sup>166</sup> poor colloidal stability for low CTAB and high salt concentrations or in organic media,<sup>115</sup> strong interactions with charged molecules,<sup>115</sup> limited interparticle spacing within close-packed arrangements,<sup>6,71</sup> and strong effects on the overall wetting properties. Consequently, surface modification of CTAB stabilized AuNRs is essential for many applications.<sup>115,165</sup> In the following, several key concepts for the surface modification of AuNRs with organic and inorganic coatings will be discussed.

Chemisorption of low molecular weight compounds and polymers utilizing thiol chemistry is a powerful tool to functionalize gold nanorod surfaces that provides

stable coatings, due to the covalent nature of the gold-sulfur bond.<sup>115,165</sup> Especially, end-tethering of thiol functionalized polyethylene glycol (PEG), often referred to as PEGylation, is widely used to exchange CTAB and stabilize AuNRs.<sup>167-172</sup> PEG brushes provide sterically stabilized AuNRs that can be solubilized in water and several organic solvents, rendering AuNRs biocompatible.

The group of Kumacheva selectively functionalized gold nanorod tips with thiolated-polystyrene chains.<sup>173-175</sup> Selective tip functionalization with polymer brushes is facilitated by the high surface curvature and a less densely packed CTAB bilayer. Changing the solvent quality induces self-assembly of AuNRs into polymer-like chains. Vigderman *et al.*<sup>176</sup> reported on quantitative replacement of CTAB with a thiol-functionalized CTAB derivative. Cell tests proved the biocompatibility of the functionalized AuNRs and samples could even be lyophilized.

Because of strong ionic interactions it is not straight forward to replace CTAB with negatively charged compounds.<sup>115</sup> Wijaya *et al.*<sup>177</sup> developed a two-step process, referred to as round-trip functionalization, to overcome this issue. AuNRs were first functionalized with dodecanethiol and transferred to acetone, followed by functionalization with negatively charged thiolated compounds, *e.g.* mercaptoundecanoic acid, PEGs, or DNA. The group of Bach successfully functionalized CTAB stabilized AuNRs with negatively charged thiol-PEG-carboxylates in a single-step utilizing buffer solutions and a nonionic surfactant.<sup>72,172,178</sup> The functionalized AuNRs can be self-assembled into close-packed vertically aligned crystals, precipitated in a size selective manner and are biocompatible.

The group of Murphy adopted the standard layer-by-layer (LBL) method to build-up stable polyelectrolyte multilayers on AuNRs.<sup>166,179-181</sup> This method allows to prepare multilayers with well-defined shell thicknesses and surface charges *via* alternating functionalization steps. The obtained AuNRs are colloidally stable and biocompatible.<sup>166</sup> Furthermore, this approach allows to introduce functional groups that can be selectively addressed, *e.g. via* click- or carbodiimide chemistry.<sup>180,181</sup> However, due to the multistep approach this technique is highly time consuming and poorly scalable.

The same group reported on a polymerizable CTAB derivative that is used to stabilize the surfactant bilayer.<sup>182</sup> In this way, excess of CTAB can be removed from solution and the colloidally stable AuNRs exhibited significantly reduced cytotoxicity.

Besides synthetic polymers, highly monodisperse natural bio-macromolecules such as proteins can be used to functionalize CTAB stabilized gold nanoparticles as well.<sup>165</sup> Proteins are multivalent, charged macromolecules possessing a high affinity towards gold surfaces and exhibit sensitivity towards pH and ionic strength depending on their molecular structure.<sup>165</sup> Strozyk *et al.*<sup>183</sup> reported on functionalization of CTAB stabilized gold nanoparticles with bovine serum albumin (BSA) *via* chemisorption, owing to the covalent thiol/disulfide-gold bonds of the cysteine groups of BSA. The coated nanoparticles revealed excellent colloidal stability for high pH values (pH>7), due to electrosteric stabilization. Furthermore, they exhibited strong bidirectional pH-sensitivity and underwent reversible aggregation, because of surface charge inversion from negative to positive.

Silica coating of AuNRs *via* the well-known Stöber process is another approach to functionalize gold nanorod surfaces.<sup>184</sup> This procedure allows to incorporate functional molecules within the silica-shell, *e.g.* dyes, drugs or SERS tags<sup>185-187</sup> and post-modification *via* the versatile silane-chemistry.<sup>188,189</sup> Homogeneous silica-shells with tunable thickness are commonly prepared in a two-step procedure. First, AuNRs are functionalized with a silane coupling agent such as (3-mercaptopropyl)-trimethoxysilane (MPTMS),<sup>188,190</sup> PEGylated,<sup>185</sup> or coated with polyelectrolyte multilayers<sup>189</sup> to provide affinity of the metal surface towards silica and grant colloidal stability of AuNRs upon transfer into ethanol. Second, as functionalized AuNRs are coated with a silica-shell *via* hydrolysis and subsequent condensation of silica precursor molecules. Direct coating of CTAB stabilized AuNRs in aqueous environment results in porous silica-shells that might find application in drug delivery.<sup>186,187,191</sup>

### 3.6 Colloidal Surface-Assemblies

So far, the discussion focused on the synthesis of anisotropic metal building blocks and the fundamental physics and concepts of plasmonic nanostructures. In this context, precise control over the spatial position and orientation of individual anisotropic plasmonic building blocks within the nanostructured arrangements is a prerequisite to tune their near-field coupling and gain control over the macroscopic optical properties of the organizations.<sup>31-33,35,38,95,192-194</sup>

Various strategies have been developed to prepare nanostructured organizations of anisotropic metal nanostructures at surfaces. Top-down nanofabrication methods such as e-beam and focused ion beam lithography, are the most widely used techniques to prepare well-defined nanoscopic metal structures, due to their versatility and precision.<sup>1</sup> Thus, these techniques greatly enhanced our fundamental understanding of plasmonics.<sup>1</sup> But top-down methods inherently suffer from limited scalability, resolution, and throughput directly related to high costs.<sup>1,6,40</sup> Furthermore, they are not compatible with silicon manufacturing techniques and the polycrystalline nature of prepared metal nanostructures results in additional damping effects.<sup>3,40</sup> Consequently, there is a great demand for the development of alternative approaches that can be scaled on large-areas while overcoming aforementioned limitations. In this context, template-assisted self-assembly of anisotropic colloidal metal nanoparticles obtained in large quantities and with narrow size distributions from wet-chemical synthesis holds great potential.<sup>15,114,115</sup> This bottom-up technique enables the fabrication of complex plasmonic surface-assemblies on large sample areas with spatial precision on the nanoscale and tunable collective optical properties.<sup>6,39,40,44,77,192-201</sup>

In general, self-assembly is a spontaneous process that takes place under non-equilibrium conditions and gives rise to the organization of mobile components into ordered structures.<sup>202,203</sup> This process is driven by the tendency of the system to minimize its Gibbs free energy and balance the attractive and repulsive interaction forces.<sup>202,203</sup> In static self-assembly, the system is in its global or local thermodynamic equilibrium after structure formation.<sup>202</sup> In contrast to self-organization processes, *e.g.* in living cells, self-assembly does not dissipate energy.<sup>202</sup> Self-assembly can take place on all length-scales, *e.g.* the molecular-level or the colloidal length-scale, typically ranging from 1 nm to 1  $\mu\text{m}$ .<sup>196,202,203</sup> Spherical colloids with repulsive interaction forces spontaneously self-assemble into cubic close-packed crystals if the free volume of the suspension is reduced below a certain threshold.<sup>204</sup> Such organizations exhibit unusual optical properties, *e.g.* optical bandgaps caused by the long-range order of the periodic colloidal lattices, referred to as photonic crystals.<sup>205,206</sup>

Consequently, in order to understand and eventually control self-assembly of anisotropic metal colloids into spatially periodic organizations we need to discuss the different fundamental interaction forces present in colloidal suspensions.<sup>203</sup>

### 3.6.1 The Forces at Work in Colloidal Self-Assembly

The dynamics and interaction forces present in colloidal systems span multiple time- and length-scales as well as magnitudes and act simultaneously between different constituents of the system, *e.g.* colloid-colloid, colloid-solvent and colloid-substrate.<sup>203</sup> The review of Li *et al.*<sup>203</sup> provides a thorough overview of the forces that are relevant for colloidal self-assembly, which will be discussed briefly in the following.

Brownian motion of colloids in solution is a random diffusion process, driven by thermal energy.<sup>203</sup> The relation between the particle radius  $R$  and the particle diffusion coefficient  $D$  is described by the Stokes-Einstein equation and the particle diffusion scales as  $D \propto 1/R$ .<sup>203</sup> Brownian motion counteracts any directional force that is of comparable order, *e.g.* gravitational forces for small colloids. Additionally, this motion is responsible for collisions in colloidal systems and, thus, intrinsically affects the self-assembly process.<sup>203</sup>

According to the well-known DLVO theory, named after Derjaguin-Landau-Verwey and Overbeek, colloidal stability is granted by the electrostatic repulsion that compensates the van der Waals (vdW) attraction at large separations and, thus, prevents colloids from aggregating.<sup>203,207</sup>

Attractive vdW interaction forces are always present between two interacting particles. They are caused by cooperative dislocations of partial charges giving rise to induced transient and permanent dipoles on the molecular level.<sup>203</sup> On the colloidal length-scale, the geometry-dependent vdW interaction potential  $W_{(vdW)}$  can span up to several hundreds of nanometers according to the Hamaker constant and typically scales with particle size  $R$  and distance  $d$  as  $W_{(vdW)} \propto -R/d$ .<sup>203</sup>

The repulsive electrostatic interaction potential is caused by the electric double-layer (EDL) present at the surface of colloids in aqueous solutions.<sup>203</sup> According to the Guoy-Chapman-Stern model the EDL consists of the Stern-layer that is characterized by immobilized charges and a linearly decaying potential and a diffusive-layer that consists of weakly attracted, thermally diffusing ions, characterized by an exponentially decaying potential (see **Figure 3.7A**).<sup>203</sup> The long-range repulsive electrostatic double-layer potential can span hundreds of nanometers for low ionic strength and can be described by the Poisson-Boltzmann equation.<sup>203</sup> The

electrostatic interaction potential typically scales as  $W_{(EDL)} \propto Re^{-\kappa d}$ , where  $\kappa$  is the inverse Debye length.<sup>203</sup>

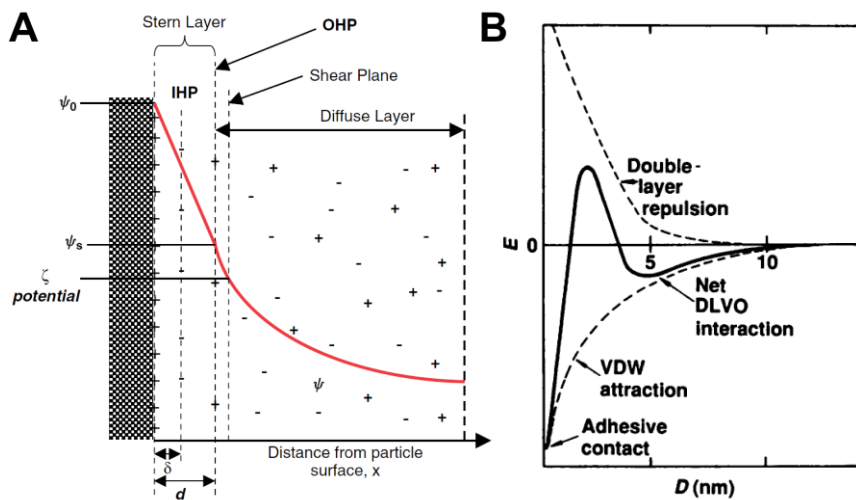


**Figure 3.7.** (A) Schematic representation of the electric double-layer (EDL) according to the Guoy-Chapman-Stern model. Reprinted with permission from Ref. 203, ©2008 Curtin University of Technology and John Wiley & Sons, Ltd. (B) Classical DLVO potential for two interacting flat surfaces ( $W_{(EDL)} \propto e^{-\kappa d}$ ,  $W_{(vdW)} \propto -1/d^2$ ). Adapted with permission from Ref. 207, ©1988 by the American Association for the Advancement of Science.

The DLVO theory considers the contributing interaction potentials to be additive  $W_{DLVO} = W_{(EDL)} + W_{(vdW)}$  and the obtained DLVO potential is characterized by a primary global minimum for short-distances, caused by the dominating attractive vdW interaction and an energy barrier that prevents particles from aggregation at intermediate distances, due to the dominating repulsive electrostatic interaction (see **Figure 3.7B**).<sup>203,207</sup>

Capillary forces are strong long-range forces that can cover distances of several millimeters, depending on the surface tension, the contact angle, and the particle size and distance.<sup>203</sup> They are mediated by the fluid interface and act at the triple phase boundary between the liquid medium (water), the protruding colloidal particle and a third mobile medium most often air.<sup>203</sup> The physical origin of the capillary force is the surface tension  $\gamma$  of the suspending liquid that arises from the tendency of the suspending liquid to minimize its total interfacial energy.<sup>203</sup> Curvature of liquid surfaces gives rise to the Laplace pressure and the resulting capillary force can be calculated based on the Laplace equation.<sup>203</sup>

The capillary forces that act on partially wetted colloids supported by a substrate can either act in normal or in lateral direction, with respect to the substrate surface as

depicted schematically in **Figure 3.8**.<sup>203,208</sup> Liquid bridges with a concave shape give rise to attractive normal capillary forces between the substrate and the particle that scale as  $F_{c_l} \propto -\gamma R$ .<sup>203,209</sup> The attractive lateral capillary forces (immersion forces) between two protruding colloids are relevant down to particle radii of few nanometers and scale as  $F_{c_-} \propto -\gamma R^2/d$ .<sup>203,208</sup>

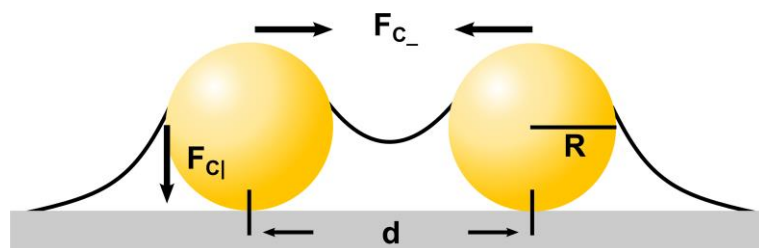


**Figure 3.8.** Schematic depiction of the normal ( $F_{c_l}$ ) and lateral (immersion) ( $F_{c_-}$ ) capillary forces obtained for liquid bridges with concave shapes that act on a partially wetted spherical particle supported by a substrate and in between two protruding spherical particles, respectively. Adapted with permission from Ref. 203, ©2008 Curtin University of Technology and John Wiley & Sons, Ltd.

In a liquid with directed flow pattern, the convective or hydrodynamic drag force that acts on the suspended colloids will result in a motion of the colloids with a trajectory pointing into the direction of the flux.<sup>210</sup> For Stokes flow, the hydrodynamic drag force that acts on a spherical colloid is  $F_D = 6\pi\eta Rv$ , where  $\eta$  is the viscosity of the medium and  $v$  is the relative velocity.<sup>203</sup>

For the sake of simplicity, the above discussion focused on isotropic colloids. However, the anisotropy of the building blocks strongly influences the forces that act on the colloidal length-scales, to be discussed in the following in more detail.

### 3.6.2. Self-Assembly Methods

In general, evaporation induced self-assembly is most often employed as a bottom-up method to prepare well-defined close-packed colloidal surface-assemblies with varied dimensionality (see **Figure 3.9A**). Capillary forces that exceed the other forces on the colloidal length-scale by several orders of magnitude, facilitate nucleation, as well as close-packing of the growing colloidal crystal at the contact line.<sup>203,211-214</sup> The evaporation induced convective flow of particles towards the contact line results in accumulation of colloids and drives the epitaxial crystal growths.<sup>203,211-214</sup> Brownian motion and electrostatic repulsion are essential as they keep the colloids mobile during the self-assembly process until the particles get locked in their minimum free

energy configuration, due to attractive vdW interaction forces in the final stage of the self-assembly process.<sup>203,214</sup>

In the following, different methods that have been applied to self-assemble colloids will be discussed, with a special emphasis on anisotropic metal nanocrystals and template-assisted self-assembly approaches.

Drop casting on wettable substrates is by far the simplest method to self-assemble colloids into close-packed two- or three- dimensional colloidal crystals.<sup>211-213</sup> However, to enhance the reproducibility and the surface coverage and to gain control over spatial placement and orientation within the arrangements of colloids, different self-assembly methods have been developed.<sup>199,214,215</sup> In particular, the concentration of colloids and additives, their polydispersity, the rate of evaporation, the contact angle, and the contact line movement across the substrate are key parameters for colloidal self-assembly.<sup>196,213-215</sup> Furthermore, adding a physical constraint, *e.g.* a topographically patterned template, to direct the self-assembly process of colloids facilitates precise assembly of colloidal building blocks into one-, two- or three-dimensional arrays.<sup>195-197</sup>

For the preparation of colloidal crystals at surfaces, various methods can be applied. Spin-coating is a rapid process allowing to apply thin, densely packed particle layers onto large substrate areas by fast rotation of a spread suspension.<sup>16,216</sup> In contrast, dip-coating allows to precisely control the contact line movement across the substrate.<sup>214</sup> Tuning the withdrawal speed to exactly balance the velocity of crystal growth enables the preparation of two-dimensional hexagonally close-packed particle arrays with low defect rates and large domain sizes.<sup>214</sup>

As an alternative, trapping a colloidal suspension droplet in between two plates and dragging the droplet across the substrate, enables precise control over the contact line movement.<sup>215</sup> This technique is named capillary force (contact angle  $\theta > 20^\circ$ ) or convective (contact angle  $\theta < 20^\circ$ ) force assembly (CFA) depending on the slope of the contact line, which affects the underlying process of self-assembly (see **Figure 3.9A-D**).<sup>217</sup> CFA allows very precise spatial organization of colloidal building blocks into close- and non-close packed (using a topographically structured template) surface-assemblies.<sup>194,200,215,217-221</sup>

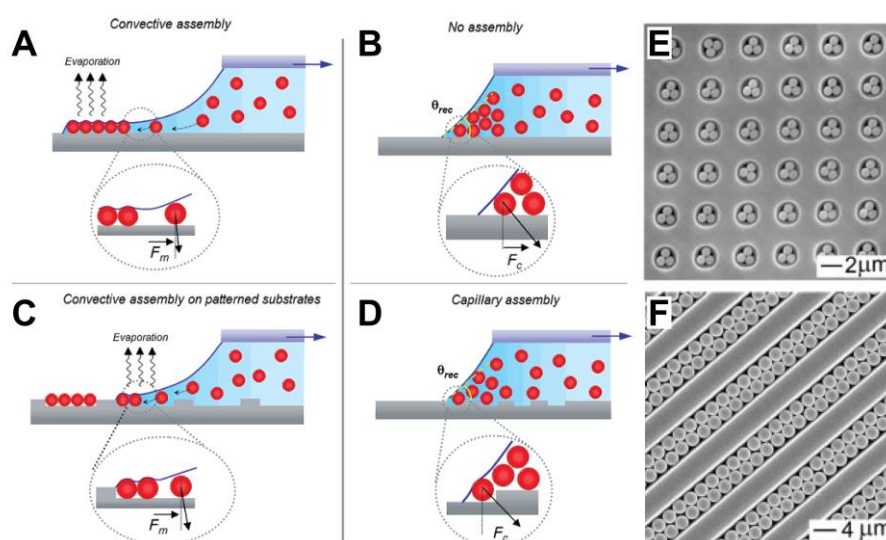


**Figure 3.9.** Different assembly processes based on a colloidal suspension trapped between a substrate (flat/topographic template) and a plate. The droplet is moved relative to the substrate surface. (A/C) Convective self-assembly (contact angle  $<20^\circ$ ). (B/D) Capillary self-assembly only obtained on topographic templates (contact angle  $>20^\circ$ ). Reprinted with permission from Ref. 217, ©2007 American Chemical Society. (E) Polystyrene latex particles (0.9  $\mu\text{m}$  in diameter) self-assembled into trimers within 2  $\mu\text{m}$  holes (F) Polystyrene latex particles (2.5  $\mu\text{m}$  in diameter) self-assembled into close-packed double lines within channels with a width of 5  $\mu\text{m}$ . Reprinted with permission from Ref. 196, ©2003 WILEY-VCH Verlag GmbH & Co. KGaA, Weinheim.

Template-assisted self-assembly (TASA) relies on structured substrates that direct the colloidal self-assembly (see **Figure 3.9C-F**).<sup>193,196,197</sup> The site, structure and orientation selective assembly of colloids can be either assisted by a geometric constraint or by contrast in physical interaction forces.<sup>193,196,197</sup> Templates enable the fabrication of complex, spatially defined one-, two-, and three-dimensional surface-assemblies of colloidal building blocks with properties, *e.g.* size and orientation of aggregates, and periodicities that are pre-determined by the template geometry.<sup>196</sup> **Figure 3.9** shows spherical polystyrene colloids that were self-assembled into trimers within holes and hexagonally close-packed dimer chains within trenches.<sup>196</sup> The structure type can be precisely tuned by adjusting the ratio of the particle dimension and the dimension of the topographic template feature. Topographically structured templates are most often prepared *via* conventional lithography and are either used directly as templates or replicated *via* soft imprint lithography prior use.<sup>196,222</sup> Chemically patterned substrates can be manufactured for instance *via* micro-contact printing.<sup>222,223</sup> If lithography is applied for template preparation, the

formation of colloidal surface-assemblies can be described as hybrid technique, which comprises both top-down (template) and bottom-up (self-assembly) fabrication steps.

### 3.6.3 Self-Assembly of Gold Nanorods

The self-assembly of one-dimensional rod-like metal nanocrystals is significantly more complex compared to isotropic colloids, owing to the shape dependency of the interaction forces and the decreased symmetry of the building blocks.<sup>192,193</sup> Various different types of structures can be obtained in one-, two- or three- dimensional long-range ordered organizations of nanorods, *e.g.* close-packed and non-close-packed arrangements, alignment into end-to-end or side-by-side configuration, orientation in horizontal or vertical direction or ordering in nematic or smectic phases.<sup>192,193</sup>

The evaporation-induced self-assembly of gold nanorods into ordered structures has been extensively studied.<sup>69,70,163,192,193,224-228</sup> Nikoobakht *et al.*<sup>226</sup> argued that the preferential side-to-side assembly of gold nanorods within horizontal oriented nanorod assemblies is due to the higher lateral immersion capillary force, acting along the particle major axis, compared to the minor axis. However, in highly concentrated gold nanorod suspensions self-assembly into liquid-crystalline phases is thermodynamically favored, due to the gain in translational entropy that overcompensates the loss in orientation entropy, according to Onsager's theory.<sup>20,163</sup> Furthermore, attractive depletion forces can induce parallel alignment of gold nanorods and close-packed vertical or horizontal oriented superlattices of gold nanorods are obtained after solvent evaporation.<sup>69,135,193,224,229</sup> Ye *et al.*<sup>163</sup> obtained horizontally organized smectic phases of self-assembled gold nanorods synthesized with aromatic additives. Gomez-Grana *et al.*<sup>70</sup> reported on hexagonally close-packed vertically oriented gold nanorod crystals, which were self-assembled utilizing a gemini surfactant. Similar results were presented by Thai *et al.*<sup>72</sup> for gold nanorods functionalized with a negatively charged PEG.

As outlined earlier well-defined one- and two-dimensional close- and non-close-packed surface assemblies of anisotropic metal nanocrystals can be obtained utilizing template-assisted self-assembly.<sup>193</sup>

Nepal *et al.*<sup>230</sup> reported on the site selective adsorption of negatively charged gold nanorods on positively charged nanopatterned templates. Changing the interaction

forces (Debye-length) and adjustment of the width of pattern enabled tuning of the interparticle distances and the local orientation.

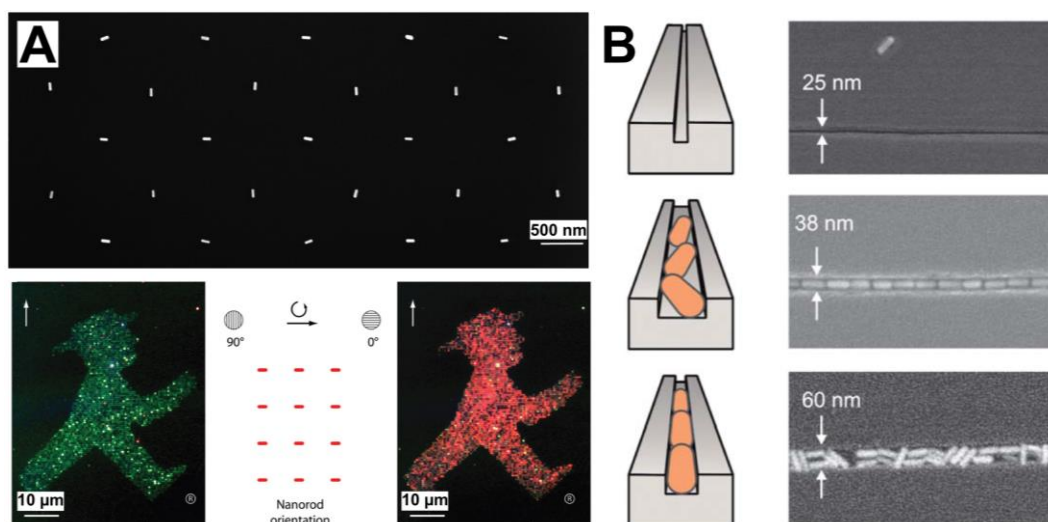


**Figure 3.10.** (A) Gold nanorods with dimensions of 25 x 80 nm are co-assembled with two orientations on a template with anisotropic line-lets of 50 x 140 nm in dimension and 40 nm in depth. Aligned gold nanorods are illuminated in dark-field configuration with perpendicular (green) or parallel (red) polarized light with respect to the gold nanorod orientation. Pixels were separated by 500 nm. (The AMPELMANN is a registered trademark of the AMPELMANN GmbH.) Reprinted with permission from Ref. 194, © 2012 WILEY-VCH Verlag GmbH & Co. KGaA, Weinheim. (B) Different assembly qualities obtained for varied template geometries and gold nanorod dimensions of 24 x 64 nm. Highly deterministic self-assembly gold nanorods in end-to-end orientation are obtained for a channel width of 40 nm and depth of 60 nm. Reprinted with permission from Ref. 201, ©2013 The Royal Society of Chemistry.

Kuemin *et al.*<sup>194,200</sup> self-assembled gold nanorods with single particle resolution and determined orientation on large-substrate areas. They utilized capillary force assembly and PDMS templates with periodic anisotropic holes that were replicated from a silicon substrate prepared *via* e-beam lithography. The gold nanorods formed crystalline phases within the accumulation zone that were preferentially oriented parallel to the contact line. Nevertheless, the final gold nanorod orientation was determined by the orientation of the anisotropic topographic pattern of the substrate, due to reorientation of the particles, caused by capillary forces. The obtained gold nanorod organizations exhibited polarization dependent optical properties (see **Figure 3.10A**).

Rey *et al.*<sup>201</sup> reported on the deterministic assembly of gold nanorods into close-packed end-to-end aligned nanoparticle single chains utilizing a similar technique as Kuemin *et al.* (see **Figure 3.10B**). They systematically varied the channel dimensions and assembly temperature identifying optimal assembly parameters based on quantitative and qualitative criteria. As expected, end-to-end alignment is only obtained if the template dimensions precisely match the particle width. Channels with too small dimensions are not filled at all, whereas too large channel dimensions result in high filling fractions but undefined particle orientation. Furthermore, deterministic self-assembly is only observed for assembly temperatures that are well-above the dew point ( $\Delta T > 25^\circ$ ).

### 3.6.4 Lithography-free Templates

Self-assembled block copolymers can serve as lithography-free templates for metal nanocrystal organization.<sup>231,232</sup> Liu *et al.*<sup>232</sup> used plasma etched lamellar block copolymers as topographic templates for self-assembly of gold nanorods *via* spin-coating. By variation of the block lengths they were able to adjust the lamellar periods in the range of 50-80 nm and tune the resulting nanorod structures from double to single lines.

Wrinkle-templates represent another class of lithography-free prepared substrates with tunable, well-defined periodic topographic patterns that have been successfully employed for the template-assisted self-assembly of colloids within our group.<sup>6,65,71,73,233-239</sup> Applying a thin stiff film, *e.g.* metal,<sup>240,241</sup> polymer<sup>242,243</sup> or silica,<sup>244,245</sup> onto a stretched elastomeric substrate results in the formation of permanent wrinkles upon relaxation. This is due to the buckling instability, which minimizes the stress within the surface layer of the two-layer system.<sup>246</sup> For the simplest case of an uniaxial strain the obtained wrinkles will be oriented perpendicular to the strain direction.<sup>243-246</sup> Because of the ability to directly cross-link the surface of poly(dimethylsiloxane) (PDMS) *via* plasma oxidation into a glassy-like, hard thin film, PDMS is most often used as elastomeric substrate.<sup>244</sup>

The periodicity  $\lambda$  and the amplitude  $A$  of the obtained wrinkles, both linearly depending on the film thickness  $h$  ( $\lambda, A \propto h$ ), can be tuned down to wavelengths of 150 nm and amplitudes of 5 nm, respectively.<sup>241,246</sup> Above the critical onset strain for wrinkle formation, the amplitude is always strain dependent and for large strains the wavelength becomes strain dependent, too.<sup>246,247</sup> Furthermore, the wavelength has a

cube root dependency on the ratio of the elastic modulus of the applied film  $E_f$  and the substrate  $E_s$  ( $\lambda \propto \sqrt[3]{E_f/E_s}$ ).<sup>242,248</sup> Since buckling is a mechanical process, wrinkling is scalable to large substrate areas.<sup>246</sup> Complex wrinkle patterns can be obtained by variation of the applied strain pattern or by introducing sharp lateral transitions in the elastomeric modulus of the substrate.<sup>246,249</sup>

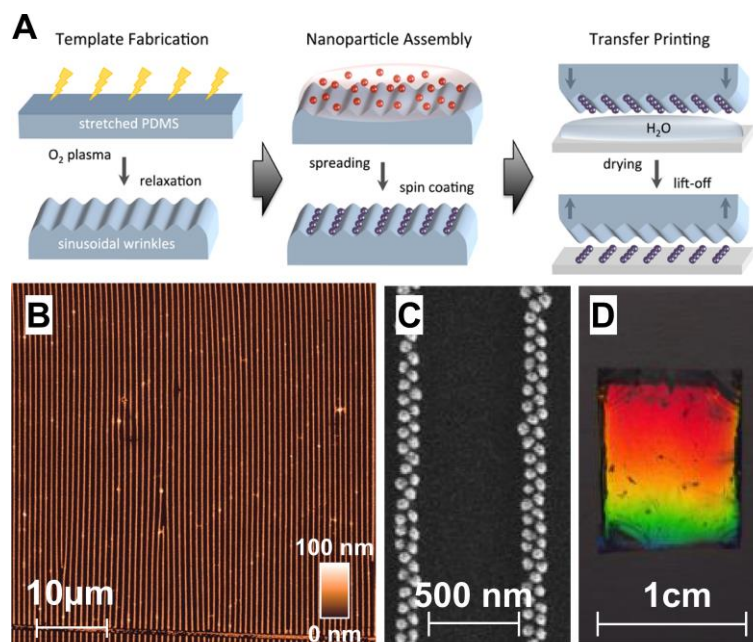


**Figure 3.11.** (A) Schematic depiction of the preparation process of close-packed linear assemblies of spherical gold nanoparticles into single particle chains, dimer chains and trimer chains on centimeter-squared-areas based on template-assisted self-assembly on wrinkle-templates: (I) Wrinkle-templates are prepared *via* relaxation of stretched plasma treated PDMS substrates. (II) Gold nanoparticles with diameters of 80 nm are assembled *via* spin coating from concentrated solutions. (III) Aligned gold nanoparticles are transferred onto flat hydrophilic substrate *via* wet contact printing. (B) AFM, (C) SEM and (D) optical micrographs of obtained periodic close-packed dimer chains. Reprinted with permission from Ref. 6, ©2014 American Chemical Society.

In 2007, Lu *et al.*<sup>239</sup> published the first proof-of-concept for template-assisted self-assembly of colloidal particles on wrinkle-substrates. Spherical polystyrene particles were organized on wrinkle-substrates *via* dip-coating. Since then, the technique underwent a tremendous development and has been applied to a broad variety of colloidal building blocks, *e.g.* spherical polymer particles,<sup>235</sup> core-shell particles,<sup>65,234</sup> spherical gold particles<sup>6,71,73</sup> and anisotropic tobacco mosaic viruses.<sup>237,238</sup> For spherical particles spin-coating proved to be very efficient.<sup>6,65,234,235</sup> The obtained structures have been successfully transferred to planar hydrophilic surfaces *via* wet

contact printing.<sup>65,234,235</sup> Tuning the wettability of the target substrate by chemical patterning and multiple printing provides complex hierarchical assembly patterns.<sup>235</sup> Only recently, Hanske *et al.*<sup>6</sup> reported on the wrinkle-assisted self-assembly of protein stabilized spherical gold nanoparticles into periodic close-packed single particle chains, dimer chains and trimer chains on centimeter-square areas as shown in **Figure 3.11**. Because of the thin BSA-layer, the average interparticle distance is in the range of 1-2 nm. Thus, strong plasmonic coupling results in significant peak shifts and provides unique optical properties on the macroscopic scale (see **Section 3.1**).

Consequently, wrinkle-substrates represent lithography-free, scalable and precisely tunable templates that are the ideal means for the directed self-assembly of spherical and anisotropic plasmonic building blocks into close-packed strongly coupled chains with subwavelength periodicities and on macroscopic sample-areas. Such surface-assemblies might find application in various fields, *e.g.* for surface-enhanced spectroscopy methods, for subdiffraction limit waveguiding or for the design of metamaterials, amongst others.

## References

- (1) Pelton, M.; Bryant, G., *Introduction to Metal-Nanoparticle Plasmonics*. John Wiley & Sons: United States of America, New Jersey, 2013; p 275.
- (2) Cai, W.; Shalaev, V. M., *Optical Metamaterials: Fundamentals and Applications*. Springer Science + Business Media: United States of America, New York, 2010; p 200.
- (3) Naik, G. V.; Shalaev, V. M.; Boltasseva, A., Alternative Plasmonic Materials: Beyond Gold and Silver. *Adv Mater* **2013**, *25*, 3264-3294.
- (4) Johnson, P. B.; Christy, R. W., Optical Constants of the Noble Metals. *Phys Rev B: Condens Matter Mater Phys* **1972**, *6*, 4370-4379.
- (5) Hagemann, H. J.; Gudat, W.; Kunz, C., Optical constants from the far infrared to the x-ray region: Mg, Al, Cu, Ag, Au, Bi, C, and Al<sub>2</sub>O<sub>3</sub>. *J Opt Soc Am* **1975**, *65*, 742-744.
- (6) Hanske, C.; Tebbe, M.; Kuttner, C.; Bieber, V.; Tsukruk, V. V.; Chanana, M.; König, T. A. F.; Fery, A., Strongly Coupled Plasmonic Modes on Macroscopic Areas via Template-Assisted Colloidal Self-Assembly. *Nano Lett* **2014**, *14*, 6863-6871.
- (7) Pletsch, H.; Tebbe, M.; Dulle, M.; Förster, B.; Fery, A.; Förster, S.; Greiner, A.; Agarwal, S., Reversible gold nanorod alignment in mechano-responsive elastomers. *Polymer* **2015**, *66*, 167-172.
- (8) Link, S.; El-Sayed, M. A., Spectral Properties and Relaxation Dynamics of Surface Plasmon Electronic Oscillations in Gold and Silver Nanodots and Nanorods. *J Phys Chem B* **1999**, *103*, 8410-8426.
- (9) Maier, S. A., *Plasmonics: Fundamentals and Application*. Springer Science + Business Media: United States of America, New York, 2007; p 223.
- (10) Burda, C.; Chen, X.; Narayanan, R.; El-Sayed, M. A., Chemistry and Properties of Nanocrystals of Different Shapes. *Chem Rev* **2005**, *105*, 1025-1102.

- (11) Mie, G., Beiträge zur Optik trüber Medien, speziell kolloidaler Metallösungen. *Ann Phys* **1908**, *330*, 377-445.
- (12) Gans, R., Über die Form ultramikroskopischer Goldteilchen. *Ann Phys* **1912**, *342*, 881-900.
- (13) Dreaden, E. C.; Alkilany, A. M.; Huang, X.; Murphy, C. J.; El-Sayed, M. A., The golden age: gold nanoparticles for biomedicine. *Chem Soc Rev* **2012**, *41*, 2740-2779.
- (14) Karg, M.; König, T. A. F.; Retsch, M.; Stelling, C.; Reichstein, P. M.; Honold, T.; Thelakkat, M.; Fery, A., Colloidal self-assembly concepts for light management in photovoltaics. *Mater Today* **2015**, *18*, 185-205.
- (15) Xia, Y.; Xiong, Y.; Lim, B.; Skrabalak, S. E., Shape-Controlled Synthesis of Metal Nanocrystals: Simple Chemistry Meets Complex Physics? *Angew Chem, Int Ed* **2009**, *48*, 60-103.
- (16) Müller, M. B.; Kuttner, C.; König, T. A. F.; Tsukruk, V. V.; Förster, S.; Karg, M.; Fery, A., Plasmonic Library Based on Substrate-Supported Gradienial Plasmonic Arrays. *ACS Nano* **2014**, *8*, 9410-9421.
- (17) Kuwata, H.; Tamaru, H.; Esumi, K.; Miyano, K., Resonant light scattering from metal nanoparticles: Practical analysis beyond Rayleigh approximation. *Appl Phys Lett* **2003**, *83*, 4625-4627.
- (18) Novo, C.; Funston, A. M.; Pastoriza-Santos, I.; Liz-Marzán, L. M.; Mulvaney, P., Spectroscopy and High-Resolution Microscopy of Single Nanocrystals by a Focused Ion Beam Registration Method. *Angew Chem, Int Ed* **2007**, *46*, 3517-3520.
- (19) Zijlstra, P.; Paulo, P. M. R.; Orrit, M., Optical detection of single non-absorbing molecules using the surface plasmon resonance of a gold nanorod. *Nat Nanotechnol* **2012**, *7*, 379-382.
- (20) Chen, H.; Shao, L.; Li, Q.; Wang, J., Gold nanorods and their plasmonic properties. *Chem Soc Rev* **2013**, *42*, 2679-2724.

- (21) Barrow, S. J.; Funston, A. M.; Gómez, D. E.; Davis, T. J.; Mulvaney, P., Surface Plasmon Resonances in Strongly Coupled Gold Nanosphere Chains from Monomer to Hexamer. *Nano Lett* **2011**, *11*, 4180-4187.
- (22) Maier, S. A.; Kik, P. G.; Atwater, H. A., Observation of coupled plasmon-polariton modes in Au nanoparticle chain waveguides of different lengths: Estimation of waveguide loss. *Appl Phys Lett* **2002**, *81*, 1714-1716.
- (23) Maier, S. A.; Kik, P. G.; Atwater, H. A.; Meltzer, S.; Harel, E.; Koel, B. E.; Requicha, A. A. G., Local detection of electromagnetic energy transport below the diffraction limit in metal nanoparticle plasmon waveguides. *Nat Mater* **2003**, *2*, 229-232.
- (24) Maier, S. A.; Brongersma, M. L.; Kik, P. G.; Atwater, H. A., Observation of near-field coupling in metal nanoparticle chains using far-field polarization spectroscopy. *Phys Rev B: Condens Matter Mater Phys* **2002**, *65*, 193408.
- (25) Su, K. H.; Wei, Q. H.; Zhang, X.; Mock, J. J.; Smith, D. R.; Schultz, S., Interparticle Coupling Effects on Plasmon Resonances of Nanogold Particles. *Nano Lett* **2003**, *3*, 1087-1090.
- (26) Sönnichsen, C.; Reinhard, B. M.; Liphardt, J.; Alivisatos, A. P., A molecular ruler based on plasmon coupling of single gold and silver nanoparticles. *Nat Biotechnol* **2005**, *23*, 741-745.
- (27) Zubritskaya, I.; Lodewijks, K.; Maccaferri, N.; Mekonnen, A.; Dumas, R. K.; Åkerman, J.; Vavassori, P.; Dmitriev, A., Active Magnetoplasmonic Ruler. *Nano Lett* **2015**, *15*, 3204-3211.
- (28) Prodan, E.; Radloff, C.; Halas, N. J.; Nordlander, P., A Hybridization Model for the Plasmon Response of Complex Nanostructures. *Science* **2003**, *302*, 419-422.
- (29) Myroshnychenko, V.; Rodriguez-Fernandez, J.; Pastoriza-Santos, I.; Funston, A. M.; Novo, C.; Mulvaney, P.; Liz-Marzan, L. M.; Garcia de Abajo, F. J., Modelling the optical response of gold nanoparticles. *Chem Soc Rev* **2008**, *37*, 1792-1805.

- (30) Hao, F.; Nehl, C. L.; Hafner, J. H.; Nordlander, P., Plasmon Resonances of a Gold Nanostar. *Nano Lett* **2007**, *7*, 729-732.
- (31) Funston, A. M.; Novo, C.; Davis, T. J.; Mulvaney, P., Plasmon Coupling of Gold Nanorods at Short Distances and in Different Geometries. *Nano Lett* **2009**, *9*, 1651-1658.
- (32) Jain, P. K.; Eustis, S.; El-Sayed, M. A., Plasmon Coupling in Nanorod Assemblies: Optical Absorption, Discrete Dipole Approximation Simulation, and Exciton-Coupling Model. *J Phys Chem B* **2006**, *110*, 18243-18253.
- (33) Osberg, K. D.; Harris, N.; Ozel, T.; Ku, J. C.; Schatz, G. C.; Mirkin, C. A., Systematic Study of Antibonding Modes in Gold Nanorod Dimers and Trimers. *Nano Lett* **2014**, *14*, 6949-6954.
- (34) Brown, L. V.; Sobhani, H.; Lassiter, J. B.; Nordlander, P.; Halas, N. J., Heterodimers: Plasmonic Properties of Mismatched Nanoparticle Pairs. *ACS Nano* **2010**, *4*, 819-832.
- (35) Slaughter, L. S.; Wu, Y.; Willingham, B. A.; Nordlander, P.; Link, S., Effects of Symmetry Breaking and Conductive Contact on the Plasmon Coupling in Gold Nanorod Dimers. *ACS Nano* **2010**, *4*, 4657-4666.
- (36) Hao, F.; Sonnefraud, Y.; Dorpe, P. V.; Maier, S. A.; Halas, N. J.; Nordlander, P., Symmetry Breaking in Plasmonic Nanocavities: Subradiant LSPR Sensing and a Tunable Fano Resonance. *Nano Lett* **2008**, *8*, 3983-3988.
- (37) Liu, N.; Hentschel, M.; Weiss, T.; Alivisatos, A. P.; Giessen, H., Three-Dimensional Plasmon Rulers. *Science* **2011**, *332*, 1407-1410.
- (38) Meinzer, N.; Barnes, W. L.; Hooper, I. R., Plasmonic meta-atoms and metasurfaces. *Nat Photonics* **2014**, *8*, 889-898.
- (39) Solis, D.; Paul, A.; Olson, J.; Slaughter, L. S.; Swanglap, P.; Chang, W.-S.; Link, S., Turning the Corner: Efficient Energy Transfer in Bent Plasmonic Nanoparticle Chain Waveguides. *Nano Lett* **2013**, *13*, 4779-4784.

- (40) Solis, D.; Willingham, B.; Nauert, S. L.; Slaughter, L. S.; Olson, J.; Swanglap, P.; Paul, A.; Chang, W.-S.; Link, S., Electromagnetic Energy Transport in Nanoparticle Chains via Dark Plasmon Modes. *Nano Lett* **2012**, *12*, 1349-1353.
- (41) Luk'yanchuk, B.; Zheludev, N. I.; Maier, S. A.; Halas, N. J.; Nordlander, P.; Giessen, H.; Chong, C. T., The Fano resonance in plasmonic nanostructures and metamaterials. *Nat Mater* **2010**, *9*, 707-715.
- (42) Chang, W.-S.; Lassiter, J. B.; Swanglap, P.; Sobhani, H.; Khatua, S.; Nordlander, P.; Halas, N. J.; Link, S., A Plasmonic Fano Switch. *Nano Lett* **2012**, *12*, 4977-4982.
- (43) Metzger, B.; Schumacher, T.; Hentschel, M.; Lippitz, M.; Giessen, H., Third Harmonic Mechanism in Complex Plasmonic Fano Structures. *ACS Photonics* **2014**, *1*, 471-476.
- (44) Slaughter, L. S.; Willingham, B. A.; Chang, W.-S.; Chester, M. H.; Ogden, N.; Link, S., Toward Plasmonic Polymers. *Nano Lett* **2012**, *12*, 3967-3972.
- (45) Willingham, B.; Link, S., Energy transport in metal nanoparticle chains via sub-radiant plasmon modes. *Opt Express* **2011**, *19*, 6450-6461.
- (46) Barrow, S. J.; Wei, X.; Baldauf, J. S.; Funston, A. M.; Mulvaney, P., The surface plasmon modes of self-assembled gold nanocrystals. *Nat Commun* **2012**, *3*: 1275, 1-9.
- (47) Chang, W.-S.; Willingham, B. A.; Slaughter, L. S.; Khanal, B. P.; Vigderman, L.; Zubarev, E. R.; Link, S., Low absorption losses of strongly coupled surface plasmons in nanoparticle assemblies. *Proc Natl Acad Sci U S A* **2011**, *108*, 19879-19884.
- (48) Tebbe, M.; Kuttner, C.; Mayer, M.; Maennel, M.; Pazos-Perez, N.; König, T. A. F.; Fery, A., Silver-Overgrowth-Induced Changes in Intrinsic Optical Properties of Gold Nanorods: From Noninvasive Monitoring of Growth Kinetics to Tailoring Internal Mirror Charges. *J Phys Chem C* **2015**, *119*, 9513-9523.

- (49) García de Abajo, F. J.; Howie, A., Relativistic Electron Energy Loss and Electron-Induced Photon Emission in Inhomogeneous Dielectrics. *Phys Rev Lett* **1998**, *80*, 5180-5183.
- (50) Raman, C. V.; Krishnan, K. S., A New Type of Secondary Radiation. *Nature* **1928**, *121*, 501-502.
- (51) Ru, E. L.; Etchegoin, P., *Principles of Surface Enhanced Raman Spectroscopy and related plasmonis effects*. Elsevier: United Kingdom, Oxford, 2009; p 663.
- (52) Fleischmann, M.; Hendra, P. J.; McQuillan, A. J., Raman spectra of pyridine adsorbed at a silver electrode. *Chem Phys Lett* **1974**, *26*, 163-166.
- (53) Jeanmaire, D. L.; Van Duyne, R. P., Surface raman spectroelectrochemistry: Part I. Heterocyclic, aromatic, and aliphatic amines adsorbed on the anodized silver electrode. *J Electroanal Chem Interfacial Electrochem* **1977**, *84*, 1-20.
- (54) Albrecht, M. G.; Creighton, J. A., Anomalously intense Raman spectra of pyridine at a silver electrode. *J Am Chem Soc* **1977**, *99*, 5215-5217.
- (55) Le Ru, E. C.; Etchegoin, P. G., Single-Molecule Surface-Enhanced Raman Spectroscopy. *Annu Rev Phys Chem* **2012**, *63*, 65-87.
- (56) Le Ru, E. C.; Etchegoin, P. G., Quantifying SERS enhancements. *MRS Bull* **2013**, *38*, 631-640.
- (57) Schlücker, S., Surface-Enhanced Raman Spectroscopy: Concepts and Chemical Applications. *Angew Chem, Int Ed* **2014**, *53*, 4756-4795.
- (58) Sharma, B.; Frontiera, R. R.; Henry, A.-I.; Ringe, E.; Van Duyne, R. P., SERS: Materials, applications, and the future. *Mater Today* **2012**, *15*, 16-25.
- (59) Stiles, P. L.; Dieringer, J. A.; Shah, N. C.; Van Duyne, R. R., Surface-Enhanced Raman Spectroscopy. *Annu Rev Anal Chem* **2008**, *1*, 601-626.
- (60) Grubisha, D. S.; Lipert, R. J.; Park, H.-Y.; Driskell, J.; Porter, M. D., Femtomolar Detection of Prostate-Specific Antigen: An Immunoassay Based on Surface-

- Enhanced Raman Scattering and Immunogold Labels. *Anal Chem* **2003**, *75*, 5936-5943.
- (61) Alba, M.; Pazos-Perez, N.; Vaz, B.; Formentin, P.; Tebbe, M.; Correa-Duarte, M. A.; Granero, P.; Ferré-Borrull, J.; Alvarez, R.; Pallares, J.; Fery, A.; de Lera, A. R.; Marsal, L. F.; Alvarez-Puebla, R. A., Macroscale Plasmonic Substrates for Highly Sensitive Surface-Enhanced Raman Scattering. *Angew Chem, Int Ed* **2013**, *52*, 6459-6463.
- (62) Cao, Y. C.; Jin, R.; Mirkin, C. A., Nanoparticles with Raman Spectroscopic Fingerprints for DNA and RNA Detection. *Science* **2002**, *297*, 1536-1540.
- (63) Mir-Simon, B.; Reche-Perez, I.; Guerrini, L.; Pazos-Perez, N.; Alvarez-Puebla, R. A., Universal One-Pot and Scalable Synthesis of SERS Encoded Nanoparticles. *Chem Mater* **2015**, *27*, 950-958.
- (64) Álvarez-Puebla, R. A.; Contreras-Cáceres, R.; Pastoriza-Santos, I.; Pérez-Juste, J.; Liz-Marzán, L. M., Au@pNIPAM Colloids as Molecular Traps for Surface-Enhanced, Spectroscopic, Ultra-Sensitive Analysis. *Angew Chem, Int Ed* **2009**, *48*, 138-143.
- (65) Müller, M.; Tebbe, M.; Andreeva, D. V.; Karg, M.; Alvarez Puebla, R. A.; Pazos Perez, N.; Fery, A., Large-Area Organization of pNIPAM-Coated Nanostars as SERS Platforms for Polycyclic Aromatic Hydrocarbons Sensing in Gas Phase. *Langmuir* **2012**, *28*, 9168-9173.
- (66) Shafer-Peltier, K. E.; Haynes, C. L.; Glucksberg, M. R.; Van Duyne, R. P., Toward a Glucose Biosensor Based on Surface-Enhanced Raman Scattering. *J Am Chem Soc* **2003**, *125*, 588-593.
- (67) Hulteen, J. C.; Van Duyne, R. P., Nanosphere lithography: A materials general fabrication process for periodic particle array surfaces. *J Vac Sci Technol A* **1995**, *13*, 1553-1558.
- (68) Tan, S. J.; Campolongo, M. J.; Luo, D.; Cheng, W., Building plasmonic nanostructures with DNA. *Nat Nanotechnol* **2011**, *6*, 268-276.

- (69) Alvarez-Puebla, R. A.; Agarwal, A.; Manna, P.; Khanal, B. P.; Aldeanueva-Potel, P.; Carbó-Argibay, E.; Pazos-Pérez, N.; Vigderman, L.; Zubarev, E. R.; Kotov, N. A.; Liz-Marzán, L. M., Gold nanorods 3D-supercrystals as surface enhanced Raman scattering spectroscopy substrates for the rapid detection of scrambled prions. *Proc Natl Acad Sci U S A* **2011**, *108*, 8157-8161.
- (70) Gómez-Graña, S.; Pérez-Juste, J.; Alvarez-Puebla, R. A.; Guerrero-Martínez, A.; Liz-Marzán, L. M., Self-Assembly of Au@Ag Nanorods Mediated by Gemini Surfactants for Highly Efficient SERS-Active Supercrystals. *Adv Opt Mater* **2013**, *1*, 477-481.
- (71) Pazos-Perez, N.; Ni, W.; Schweikart, A.; Alvarez-Puebla, R. A.; Fery, A.; Liz-Marzan, L. M., Highly uniform SERS substrates formed by wrinkle-confined drying of gold colloids. *Chem Sci* **2010**, *1*, 174-178.
- (72) Thai, T.; Zheng, Y.; Ng, S. H.; Mudie, S.; Altissimo, M.; Bach, U., Self-Assembly of Vertically Aligned Gold Nanorod Arrays on Patterned Substrates. *Angew Chem, Int Ed* **2012**, *51*, 8732-8735.
- (73) Schweikart, A.; Pazos-Perez, N.; Alvarez-Puebla, R. A.; Fery, A., Controlling inter-nanoparticle coupling by wrinkle-assisted assembly. *Soft Matter* **2011**, *7*, 4093-4100.
- (74) Pazos-Perez, N.; Wagner, C. S.; Romo-Herrera, J. M.; Liz-Marzán, L. M.; García de Abajo, F. J.; Wittemann, A.; Fery, A.; Alvarez-Puebla, R. A., Organized Plasmonic Clusters with High Coordination Number and Extraordinary Enhancement in Surface-Enhanced Raman Scattering (SERS). *Angew Chem, Int Ed* **2012**, *51*, 12688-12693.
- (75) Zheng, Y.; Thai, T.; Reineck, P.; Qiu, L.; Guo, Y.; Bach, U., DNA-Directed Self-Assembly of Core-Satellite Plasmonic Nanostructures: A Highly Sensitive and Reproducible Near-IR SERS Sensor. *Adv Funct Mater* **2013**, *23*, 1519-1526.
- (76) Mirkin, C. A.; Letsinger, R. L.; Mucic, R. C.; Storhoff, J. J., A DNA-based method for rationally assembling nanoparticles into macroscopic materials. *Nature* **1996**, *382*, 607-609.

- (77) Fan, J. A.; Bao, K.; Sun, L.; Bao, J.; Manoharan, V. N.; Nordlander, P.; Capasso, F., Plasmonic Mode Engineering with Templated Self-Assembled Nanoclusters. *Nano Lett* **2012**, *12*, 5318-5324.
- (78) Veselago, V. G., Electrodynamics of Substances with Simultaneously Negative Values of  $\epsilon$  and  $\mu$ . *Sov Phys Usp* **1968**, *10*, 509-514.
- (79) Lezec, H. J.; Dionne, J. A.; Atwater, H. A., Negative refraction at visible frequencies. *Science* **2007**, *316*, 430-432.
- (80) Smith, D. R.; Pendry, J. B.; Wiltshire, M. C. K., Metamaterials and negative refractive index. *Science* **2004**, *305*, 788-792.
- (81) Pendry, J. B., Negative refraction makes a perfect lens. *Phys Rev Lett* **2000**, *85*, 3966-3969.
- (82) Veselago, V. G.; Narimanov, E. E., The left hand of brightness: past, present and future of negative index materials. *Nat Mater* **2006**, *5*, 759-762.
- (83) Zhang, X.; Liu, Z., Superlenses to overcome the diffraction limit. *Nat Mater* **2008**, *7*, 435-441.
- (84) Schurig, D.; Mock, J. J.; Justice, B. J.; Cummer, S. A.; Pendry, J. B.; Starr, A. F.; Smith, D. R., Metamaterial electromagnetic cloak at microwave frequencies. *Science* **2006**, *314*, 977-980.
- (85) Segal, N.; Keren-Zur, S.; Hendler, N.; Ellenbogen, T., Controlling light with metamaterial-based nonlinear photonic crystals. *Nat Photonics* **2015**, *9*, 180-184.
- (86) Pendry, J. B.; Holden, A. J.; Stewart, W. J.; Youngs, I., Extremely Low Frequency Plasmons in Metallic Mesostructures. *Phys Rev Lett* **1996**, *76*, 4773-4776.
- (87) Shalaev, V. M., Optical negative-index metamaterials. *Nat Photonics* **2007**, *1*, 41-48.

- (88) Pendry, J. B.; Holden, A. J.; Robbins, D. J.; Stewart, W. J., Magnetism from conductors and enhanced nonlinear phenomena. *IEEE Trans Microw Theory Techn* **1999**, *47*, 2075-2084.
- (89) Smith, D. R.; Padilla, W. J.; Vier, D. C.; Nemat-Nasser, S. C.; Schultz, S., Composite medium with simultaneously negative permeability and permittivity. *Phys Rev Lett* **2000**, *84*, 4184-4187.
- (90) Linden, S.; Enkrich, C.; Wegener, M.; Zhou, J. F.; Koschny, T.; Soukoulis, C. M., Magnetic response of metamaterials at 100 terahertz. *Science* **2004**, *306*, 1351-1353.
- (91) Yen, T. J.; Padilla, W. J.; Fang, N.; Vier, D. C.; Smith, D. R.; Pendry, J. B.; Basov, D. N.; Zhang, X., Terahertz Magnetic Response from Artificial Materials. *Science* **2004**, *303*, 1494-1496.
- (92) Enkrich, C.; Wegener, M.; Linden, S.; Burger, S.; Zschiedrich, L.; Schmidt, F.; Zhou, J. F.; Koschny, T.; Soukoulis, C. M., Magnetic Metamaterials at Telecommunication and Visible Frequencies. *Phys Rev Lett* **2005**, *95*, 203901.
- (93) Zhou, J.; Koschny, T.; Kafesaki, M.; Economou, E. N.; Pendry, J. B.; Soukoulis, C. M., Saturation of the Magnetic Response of Split-Ring Resonators at Optical Frequencies. *Phys Rev Lett* **2005**, *95*, 223902-1-4.
- (94) Soukoulis, C. M.; Linden, S.; Wegener, M., Negative refractive index at optical wavelengths. *Science* **2007**, *315*, 47-49.
- (95) Liu, N.; Giessen, H., Coupling Effects in Optical Metamaterials. *Angew Chem, Int Ed* **2010**, *49*, 9838-9852.
- (96) Cai, W.; Chettiar, U. K.; Yuan, H.-K.; de Silva, V. C.; Kildishev, A. V.; Drachev, V. P.; Shalaev, V. M., Metamagnetics with rainbow colors. *Opt Express* **2007**, *15*, 3333-3341.
- (97) Shalaev, V. M.; Cai, W.; Chettiar, U. K.; Yuan, H.-K.; Sarychev, A. K.; Drachev, V. P.; Kildishev, A. V., Negative index of refraction in optical metamaterials. *Opt Lett* **2005**, *30*, 3356-3358.

- (98) Dolling, G.; Enkrich, C.; Wegener, M.; Zhou, J. F.; Soukoulis, C. M.; Linden, S., Cut-wire pairs and plate pairs as magnetic atoms for optical metamaterials. *Opt Lett* **2005**, *30*, 3198-3200.
- (99) Wang, H.; O'Dea, K.; Wang, L., Selective absorption of visible light in film-coupled nanoparticles by exciting magnetic resonance. *Opt Lett* **2014**, *39*, 1457-1460.
- (100) Dolling, G.; Enkrich, C.; Wegener, M.; Soukoulis, C. M.; Linden, S., Simultaneous Negative Phase and Group Velocity of Light in a Metamaterial. *Science* **2006**, *312*, 892-894.
- (101) Xiao, S.; Chettiar, U. K.; Kildishev, A. V.; Drachev, V. P.; Shalaev, V. M., Yellow-light negative-index metamaterials. *Opt Lett* **2009**, *34*, 3478-3480.
- (102) García-Meca, C.; Ortuño, R.; Rodríguez-Fortuño, F. J.; Martí, J.; Martínez, A., Double-negative polarization-independent fishnet metamaterial in the visible spectrum. *Opt Lett* **2009**, *34*, 1603-1605.
- (103) Valentine, J.; Zhang, S.; Zentgraf, T.; Ulin-Avila, E.; Genov, D. A.; Bartal, G.; Zhang, X., Three-dimensional optical metamaterial with a negative refractive index. *Nature* **2008**, *455*, 376-379.
- (104) Dolling, G.; Wegener, M.; Soukoulis, C. M.; Linden, S., Negative-index metamaterial at 780 nm wavelength. *Opt Lett* **2007**, *32*, 53-55.
- (105) Kildishev, A. V.; Boltasseva, A.; Shalaev, V. M., Planar Photonics with Metasurfaces. *Science* **2013**, *339*.
- (106) Holloway, C. L.; Kuester, E. F.; Gordon, J. A.; O'Hara, J.; Booth, J.; Smith, D. R., An Overview of the Theory and Applications of Metasurfaces: The Two-Dimensional Equivalents of Metamaterials. *IEEE Antennas Propag Mag* **2012**, *54*, 10-35.
- (107) Liu, N.; Guo, H.; Fu, L.; Kaiser, S.; Schweizer, H.; Giessen, H., Three-dimensional photonic metamaterials at optical frequencies. *Nat Mater* **2008**, *7*, 31-37.

- (108) Soukoulis, C. M.; Wegener, M., Past achievements and future challenges in the development of three-dimensional photonic metamaterials. *Nat Photonics* **2011**, *5*, 523-530.
- (109) Zheludev, N. I.; Kivshar, Y. S., From metamaterials to metadevices. *Nat Mater* **2012**, *11*, 917-924.
- (110) Mühligh, S.; Cunningham, A.; Dintinger, J.; Scharf, T.; Bürgi, T.; Lederer, F.; Rockstuhl, C., Self-assembled plasmonic metamaterials. *Nanophotonics* **2013**, *2*, 211-240.
- (111) Faraday, M., The Bakerian Lecture: Experimental Relations of Gold (and Other Metals) to Light *Philos Trans R Soc London* **1857**, *147*, 145–181.
- (112) Lohse, S. E.; Murphy, C. J., The Quest for Shape Control: A History of Gold Nanorod Synthesis. *Chem Mater* **2013**, *25*, 1250-1261.
- (113) Lohse, S. E.; Burrows, N. D.; Scarabelli, L.; Liz-Marzán, L. M.; Murphy, C. J., Anisotropic Noble Metal Nanocrystal Growth: The Role of Halides. *Chem Mater* **2014**, *26*, 34-43.
- (114) Grzelczak, M.; Perez-Juste, J.; Mulvaney, P.; Liz-Marzán, L. M., Shape control in gold nanoparticle synthesis. *Chem Soc Rev* **2008**, *37*, 1783-1791.
- (115) Vigdeman, L.; Khanal, B. P.; Zubarev, E. R., Functional Gold Nanorods: Synthesis, Self-Assembly, and Sensing Applications. *Adv Mater* **2012**, *24*, 4811-4841.
- (116) Pérez-Juste, J.; Pastoriza-Santos, I.; Liz-Marzán, L. M.; Mulvaney, P., Gold nanorods: Synthesis, characterization and applications. *Coord Chem Rev* **2005**, *249*, 1870-1901.
- (117) DuChene, J. S.; Niu, W.; Abendroth, J. M.; Sun, Q.; Zhao, W.; Huo, F.; Wei, W. D., Halide Anions as Shape-Directing Agents for Obtaining High-Quality Anisotropic Gold Nanostructures. *Chem Mater* **2013**, *25*, 1392-1399.

- (118) Almora-Barrios, N.; Novell-Leruth, G.; Whiting, P.; Liz-Marzán, L. M.; López, N., Theoretical Description of the Role of Halides, Silver, and Surfactants on the Structure of Gold Nanorods. *Nano Lett* **2014**, *14*, 871-875.
- (119) Sau, T. K.; Murphy, C. J., Room Temperature, High-Yield Synthesis of Multiple Shapes of Gold Nanoparticles in Aqueous Solution. *J Am Chem Soc* **2004**, *126*, 8648-8649.
- (120) Johnson, C. J.; Dujardin, E.; Davis, S. A.; Murphy, C. J.; Mann, S., Growth and form of gold nanorods prepared by seed-mediated, surfactant-directed synthesis. *J Mater Chem* **2002**, *12*, 1765-1770.
- (121) Nikoobakht, B.; El-Sayed, M. A., Preparation and Growth Mechanism of Gold Nanorods (NRs) Using Seed-Mediated Growth Method. *Chem Mater* **2003**, *15*, 1957-1962.
- (122) Ha, T. H.; Koo, H.-J.; Chung, B. H., Shape-Controlled Syntheses of Gold Nanoprisms and Nanorods Influenced by Specific Adsorption of Halide Ions. *J Phys Chem C* **2007**, *111*, 1123-1130.
- (123) Millstone, J. E.; Wei, W.; Jones, M. R.; Yoo, H.; Mirkin, C. A., Iodide Ions Control Seed-Mediated Growth of Anisotropic Gold Nanoparticles. *Nano Lett* **2008**, *8*, 2526-2529.
- (124) Langille, M. R.; Personick, M. L.; Zhang, J.; Mirkin, C. A., Defining Rules for the Shape Evolution of Gold Nanoparticles. *J Am Chem Soc* **2012**, *134*, 14542-14554.
- (125) Walsh, M. J.; Barrow, S. J.; Tong, W.; Funston, A. M.; Etheridge, J., Symmetry Breaking and Silver in Gold Nanorod Growth. *ACS Nano* **2015**, *9*, 715-724.
- (126) Jana, N. R., Nanorod shape separation using surfactant assisted self-assembly. *Chem Commun* **2003**, 1950-1951.
- (127) Liu, M.; Guyot-Sionnest, P., Mechanism of Silver(I)-Assisted Growth of Gold Nanorods and Bipyramids. *J Phys Chem B* **2005**, *109*, 22192-22200.

- (128) Jana, N. R.; Gearheart, L.; Murphy, C. J., Wet Chemical Synthesis of High Aspect Ratio Cylindrical Gold Nanorods. *J Phys Chem B* **2001**, *105*, 4065-4067.
- (129) Jana, N. R.; Gearheart, L.; Murphy, C. J., Seed-Mediated Growth Approach for Shape-Controlled Synthesis of Spheroidal and Rod-like Gold Nanoparticles Using a Surfactant Template. *Adv Mater* **2001**, *13*, 1389-1393.
- (130) Pérez-Juste, J.; Liz-Marzán, L. M.; Carnie, S.; Chan, D. Y. C.; Mulvaney, P., Electric-Field-Directed Growth of Gold Nanorods in Aqueous Surfactant Solutions. *Adv Funct Mater* **2004**, *14*, 571-579.
- (131) Nikoobakht, B.; El-Sayed, M. A., Evidence for Bilayer Assembly of Cationic Surfactants on the Surface of Gold Nanorods. *Langmuir* **2001**, *17*, 6368-6374.
- (132) Lee, S.; Anderson, L. J. E.; Payne, C. M.; Hafner, J. H., Structural Transition in the Surfactant Layer that Surrounds Gold Nanorods as Observed by Analytical Surface-Enhanced Raman Spectroscopy. *Langmuir* **2011**, *27*, 14748-14756.
- (133) Gómez-Graña, S.; Hubert, F.; Testard, F.; Guerrero-Martínez, A.; Grillo, I.; Liz-Marzán, L. M.; Spalla, O., Surfactant (Bi)Layers on Gold Nanorods. *Langmuir* **2012**, *28*, 1453-1459.
- (134) Jana, N. R.; Gearheart, L.; Murphy, C. J., Wet chemical synthesis of silver nanorods and nanowires of controllable aspect ratio. *Chem Commun* **2001**, 617-618.
- (135) Park, K.; Koerner, H.; Vaia, R. A., Depletion-Induced Shape and Size Selection of Gold Nanoparticles. *Nano Lett* **2010**, *10*, 1433-1439.
- (136) Scarabelli, L.; Coronado-Puchau, M.; Giner-Casares, J. J.; Langer, J.; Liz-Marzán, L. M., Monodisperse Gold Nanotriangles: Size Control, Large-Scale Self-Assembly, and Performance in Surface-Enhanced Raman Scattering. *ACS Nano* **2014**, *8*, 5833-5842.
- (137) Busbee, B. D.; Obare, S. O.; Murphy, C. J., An Improved Synthesis of High-Aspect-Ratio Gold Nanorods. *Adv Mater* **2003**, *15*, 414-416.

- (138) Gao, J.; Bender, C. M.; Murphy, C. J., Dependence of the Gold Nanorod Aspect Ratio on the Nature of the Directing Surfactant in Aqueous Solution. *Langmuir* **2003**, *19*, 9065-9070.
- (139) Sau, T. K.; Murphy, C. J., Seeded High Yield Synthesis of Short Au Nanorods in Aqueous Solution. *Langmuir* **2004**, *20*, 6414-6420.
- (140) Wang, Z. L.; Mohamed, M. B.; Link, S.; El-Sayed, M. A., Crystallographic facets and shapes of gold nanorods of different aspect ratios. *Surf Sci* **1999**, *440*, L809-L814.
- (141) Carbó-Argibay, E.; Rodríguez-González, B.; Gómez-Graña, S.; Guerrero-Martínez, A.; Pastoriza-Santos, I.; Pérez-Juste, J.; Liz-Marzán, L. M., The Crystalline Structure of Gold Nanorods Revisited: Evidence for Higher-Index Lateral Facets. *Angew Chem, Int Ed* **2010**, *49*, 9397-9400.
- (142) Goris, B.; Bals, S.; Van den Broek, W.; Carbó-Argibay, E.; Gómez-Graña, S.; Liz-Marzán, L. M.; Van Tendeloo, G., Atomic-scale determination of surface facets in gold nanorods. *Nat Mater* **2012**, *11*, 930-935.
- (143) Katz-Boon, H.; Rossouw, C. J.; Weyland, M.; Funston, A. M.; Mulvaney, P.; Etheridge, J., Three-Dimensional Morphology and Crystallography of Gold Nanorods. *Nano Lett* **2011**, *11*, 273-278.
- (144) Vigderman, L.; Zubarev, E. R., High-Yield Synthesis of Gold Nanorods with Longitudinal SPR Peak Greater than 1200 nm Using Hydroquinone as a Reducing Agent. *Chem Mater* **2013**, *25*, 1450-1457.
- (145) Yang, J.; Lohse, S.; Boulos, S.; Murphy, C., The Early Life of Gold Nanorods: Temporal Separation of Anisotropic and Isotropic Growth Modes. *J Cluster Sci* **2012**, *23*, 799-809.
- (146) Hubert, F.; Testard, F.; Thill, A.; Kong, Q.; Tache, O.; Spalla, O., Growth and Overgrowth of Concentrated Gold Nanorods: Time Resolved SAXS and XANES. *Cryst Growth Des* **2012**, *12*, 1548-1555.
- (147) Henkel, A.; Schubert, O.; Plech, A.; Sönnichsen, C., Growth Kinetic of a Rod-Shaped Metal Nanocrystal. *J Phys Chem C* **2009**, *113*, 10390-10394.

- (148) Morita, T.; Tanaka, E.; Inagaki, Y.; Hotta, H.; Shingai, R.; Hatakeyama, Y.; Nishikawa, K.; Murai, H.; Nakano, H.; Hino, K., Aspect-Ratio Dependence on Formation Process of Gold Nanorods Studied by Time-Resolved Distance Distribution Functions. *J Phys Chem C* **2010**, *114*, 3804-3810.
- (149) Wadams, R. C.; Fabris, L.; Vaia, R. A.; Park, K., Time-Dependent Susceptibility of the Growth of Gold Nanorods to the Addition of a Cosurfactant. *Chem Mater* **2013**, *25*, 4772-4780.
- (150) Park, K.; Drummy, L. F.; Wadams, R. C.; Koerner, H.; Nepal, D.; Fabris, L.; Vaia, R. A., Growth Mechanism of Gold Nanorods. *Chem Mater* **2013**, *25*, 555-563.
- (151) Jana, N. R., Gram-Scale Synthesis of Soluble, Near-Monodisperse Gold Nanorods and Other Anisotropic Nanoparticles. *Small* **2005**, *1*, 875-882.
- (152) Personick, M. L.; Langille, M. R.; Zhang, J.; Mirkin, C. A., Shape Control of Gold Nanoparticles by Silver Underpotential Deposition. *Nano Lett* **2011**, *11*, 3394-3398.
- (153) Hubert, F.; Testard, F.; Spalla, O., Cetyltrimethylammonium Bromide Silver Bromide Complex as the Capping Agent of Gold Nanorods. *Langmuir* **2008**, *24*, 9219-9222.
- (154) Niidome, Y.; Nakamura, Y.; Honda, K.; Akiyama, Y.; Nishioka, K.; Kawasaki, H.; Nakashima, N., Characterization of silver ions adsorbed on gold nanorods: surface analysis by using surface-assisted laser desorption/ionization time-of-flight mass spectrometry. *Chem Commun* **2009**, 1754-1756.
- (155) Jackson, S. R.; McBride, J. R.; Rosenthal, S. J.; Wright, D. W., Where's the Silver? Imaging Trace Silver Coverage on the Surface of Gold Nanorods. *J Am Chem Soc* **2014**, *136*, 5261-5263.
- (156) Grzelczak, M.; Sánchez-Iglesias, A.; Rodríguez-González, B.; Alvarez-Puebla, R.; Pérez-Juste, J.; Liz-Marzán, L. M., Influence of Iodide Ions on the Growth of Gold Nanorods: Tuning Tip Curvature and Surface Plasmon Resonance. *Adv Funct Mater* **2008**, *18*, 3780-3786.

- (157) Orendorff, C. J.; Murphy, C. J., Quantitation of Metal Content in the Silver-Assisted Growth of Gold Nanorods. *J Phys Chem B* **2006**, *110*, 3990-3994.
- (158) Rayavarapu, R. G.; Ungureanu, C.; Krystek, P.; van Leeuwen, T. G.; Manohar, S., Iodide Impurities in Hexadecyltrimethylammonium Bromide (CTAB) Products: Lot-Lot Variations and Influence on Gold Nanorod Synthesis. *Langmuir* **2010**, *26*, 5050-5055.
- (159) Smith, D. K.; Miller, N. R.; Korgel, B. A., Iodide in CTAB Prevents Gold Nanorod Formation. *Langmuir* **2009**, *25*, 9518-9524.
- (160) Smith, D. K.; Korgel, B. A., The Importance of the CTAB Surfactant on the Colloidal Seed-Mediated Synthesis of Gold Nanorods. *Langmuir* **2008**, *24*, 644-649.
- (161) Bullen, C.; Zijlstra, P.; Bakker, E.; Gu, M.; Raston, C., Chemical Kinetics of Gold Nanorod Growth in Aqueous CTAB Solutions. *Cryst Growth Des* **2011**, *11*, 3375-3380.
- (162) Ye, X.; Zheng, C.; Chen, J.; Gao, Y.; Murray, C. B., Using Binary Surfactant Mixtures To Simultaneously Improve the Dimensional Tunability and Monodispersity in the Seeded Growth of Gold Nanorods. *Nano Lett* **2013**, *13*, 765-771.
- (163) Ye, X.; Jin, L.; Caglayan, H.; Chen, J.; Xing, G.; Zheng, C.; Doan-Nguyen, V.; Kang, Y.; Engheta, N.; Kagan, C. R.; Murray, C. B., Improved Size-Tunable Synthesis of Monodisperse Gold Nanorods through the Use of Aromatic Additives. *ACS Nano* **2012**, *6*, 2804-2817.
- (164) Scarabelli, L.; Grzelczak, M.; Liz-Marzán, L. M., Tuning Gold Nanorod Synthesis through Prereduction with Salicylic Acid. *Chem Mater* **2013**, *25*, 4232-4238.
- (165) Chanana, M.; Liz-Marzán Luis, M., Coating matters: the influence of coating materials on the optical properties of gold nanoparticles. *Nanophotonics* **2012**, *1*, 199.

- (166) Alkilany, A. M.; Nagaria, P. K.; Hexel, C. R.; Shaw, T. J.; Murphy, C. J.; Wyatt, M. D., Cellular Uptake and Cytotoxicity of Gold Nanorods: Molecular Origin of Cytotoxicity and Surface Effects. *Small* **2009**, *5*, 701-708.
- (167) Raja, G. R.; Wilma, P.; Liesbeth, H.; Patrick, C.; Hans, J.; Fijs, W. B. v. L.; Cees, O.; Srirang, M.; Ton, G. v. L., In vitro toxicity studies of polymer-coated gold nanorods. *Nanotechnology* **2010**, *21*, 145101-1-10.
- (168) Liao, H.; Hafner, J. H., Gold Nanorod Bioconjugates. *Chem Mater* **2005**, *17*, 4636-4641.
- (169) Zubarev, E. R.; Xu, J.; Sayyad, A.; Gibson, J. D., Amphiphilic Gold Nanoparticles with V-Shaped Arms. *J Am Chem Soc* **2006**, *128*, 4958-4959.
- (170) Xia, X.; Yang, M.; Wang, Y.; Zheng, Y.; Li, Q.; Chen, J.; Xia, Y., Quantifying the Coverage Density of Poly(ethylene glycol) Chains on the Surface of Gold Nanostructures. *ACS Nano* **2012**, *6*, 512-522.
- (171) Kinnear, C.; Dietsch, H.; Clift, M. J. D.; Endes, C.; Rothen-Rutishauser, B.; Petri-Fink, A., Gold Nanorods: Controlling Their Surface Chemistry and Complete Detoxification by a Two-Step Place Exchange. *Angew Chem, Int Ed* **2013**, *52*, 1934-1938.
- (172) Liu, K.; Zheng, Y.; Lu, X.; Thai, T.; Lee, N. A.; Bach, U.; Gooding, J. J., Biocompatible Gold Nanorods: One-Step Surface Functionalization, Highly Colloidal Stability, and Low Cytotoxicity. *Langmuir* **2015**, *31*, 4973-4980.
- (173) Lukach, A.; Liu, K.; Therien-Aubin, H.; Kumacheva, E., Controlling the Degree of Polymerization, Bond Lengths, and Bond Angles of Plasmonic Polymers. *J Am Chem Soc* **2012**, *134*, 18853-18859.
- (174) Liu, K.; Nie, Z.; Zhao, N.; Li, W.; Rubinstein, M.; Kumacheva, E., Step-Growth Polymerization of Inorganic Nanoparticles. *Science* **2010**, *329*, 197-200.
- (175) Liu, K.; Lukach, A.; Sugikawa, K.; Chung, S.; Vickery, J.; Therien-Aubin, H.; Yang, B.; Rubinstein, M.; Kumacheva, E., Copolymerization of Metal Nanoparticles: A Route to Colloidal Plasmonic Copolymers. *Angew Chem* **2014**, *126*, 2686-2691.

- (176) Vigderman, L.; Manna, P.; Zubarev, E. R., Quantitative Replacement of Cetyl Trimethylammonium Bromide by Cationic Thiol Ligands on the Surface of Gold Nanorods and Their Extremely Large Uptake by Cancer Cells. *Angew Chem, Int Ed* **2012**, *51*, 636-641.
- (177) Wijaya, A.; Hamad-Schifferli, K., Ligand Customization and DNA Functionalization of Gold Nanorods via Round-Trip Phase Transfer Ligand Exchange. *Langmuir* **2008**, *24*, 9966-9969.
- (178) Thai, T.; Zheng, Y.; Ng, S. H.; Ohshima, H.; Altissimo, M.; Bach, U., Facile gold nanorod purification by fractionated precipitation. *Nanoscale* **2014**, *6*, 6515-6520.
- (179) Gole, A.; Murphy, C. J., Polyelectrolyte-Coated Gold Nanorods: Synthesis, Characterization and Immobilization. *Chem Mater* **2005**, *17*, 1325-1330.
- (180) Gole, A.; Murphy, C. J., Azide-Derivatized Gold Nanorods: Functional Materials for "Click" Chemistry. *Langmuir* **2008**, *24*, 266-272.
- (181) Gole, A.; Murphy, C. J., Biotin–Streptavidin-Induced Aggregation of Gold Nanorods: Tuning Rod–Rod Orientation. *Langmuir* **2005**, *21*, 10756-10762.
- (182) Alkilany, A. M.; Nagaria, P. K.; Wyatt, M. D.; Murphy, C. J., Cation Exchange on the Surface of Gold Nanorods with a Polymerizable Surfactant: Polymerization, Stability, and Toxicity Evaluation. *Langmuir* **2010**, *26*, 9328-9333.
- (183) Strozyk, M. S.; Chanana, M.; Pastoriza-Santos, I.; Pérez-Juste, J.; Liz-Marzán, L. M., Protein/Polymer-Based Dual-Responsive Gold Nanoparticles with pH-Dependent Thermal Sensitivity. *Adv Funct Mater* **2012**, *22*, 1436-1444.
- (184) Stöber, W.; Fink, A.; Bohn, E., Controlled growth of monodisperse silica spheres in the micron size range. *J Colloid Interface Sci* **1968**, *26*, 62-69.
- (185) Fernández-López, C.; Mateo-Mateo, C.; Álvarez-Puebla, R. A.; Pérez-Juste, J.; Pastoriza-Santos, I.; Liz-Marzán, L. M., Highly Controlled Silica Coating of PEG-Capped Metal Nanoparticles and Preparation of SERS-Encoded Particles. *Langmuir* **2009**, *25*, 13894-13899.

- (186) Liu, J.; Detrembleur, C.; De Pauw-Gillet, M.-C.; Mornet, S.; Jérôme, C.; Duguet, E., Gold Nanorods Coated with Mesoporous Silica Shell as Drug Delivery System for Remote Near Infrared Light-Activated Release and Potential Phototherapy. *Small* **2015**, *11*, 2323-2332.
- (187) Zhang, Z.; Wang, L.; Wang, J.; Jiang, X.; Li, X.; Hu, Z.; Ji, Y.; Wu, X.; Chen, C., Mesoporous Silica-Coated Gold Nanorods as a Light-Mediated Multifunctional Theranostic Platform for Cancer Treatment. *Adv Mater* **2012**, *24*, 1418-1423.
- (188) Sendroiu, I. E.; Warner, M. E.; Corn, R. M., Fabrication of Silica-Coated Gold Nanorods Functionalized with DNA for Enhanced Surface Plasmon Resonance Imaging Biosensing Applications. *Langmuir* **2009**, *25*, 11282-11284.
- (189) Pastoriza-Santos, I.; Pérez-Juste, J.; Liz-Marzán, L. M., Silica-Coating and Hydrophobation of CTAB-Stabilized Gold Nanorods. *Chem Mater* **2006**, *18*, 2465-2467.
- (190) Obare, S. O.; Jana, N. R.; Murphy, C. J., Preparation of Polystyrene- and Silica-Coated Gold Nanorods and Their Use as Templates for the Synthesis of Hollow Nanotubes. *Nano Lett* **2001**, *1*, 601-603.
- (191) Gorelikov, I.; Matsuura, N., Single-Step Coating of Mesoporous Silica on Cetyltrimethyl Ammonium Bromide-Capped Nanoparticles. *Nano Lett* **2008**, *8*, 369-373.
- (192) Thorkelsson, K.; Bai, P.; Xu, T., Self-assembly and applications of anisotropic nanomaterials: A review. *Nano Today* **2015**, *10*, 48-66.
- (193) Zhang, S.-Y.; Regulacio, M. D.; Han, M.-Y., Self-assembly of colloidal one-dimensional nanocrystals. *Chem Soc Rev* **2014**, *43*, 2301-2323.
- (194) Kuemin, C.; Nowack, L.; Bozano, L.; Spencer, N. D.; Wolf, H., Oriented Assembly of Gold Nanorods on the Single-Particle Level. *Adv Funct Mater* **2012**, *22*, 702-708.

- (195) Yin, Y.; Lu, Y.; Gates, B.; Xia, Y., Template-Assisted Self-Assembly: A Practical Route to Complex Aggregates of Monodispersed Colloids with Well-Defined Sizes, Shapes, and Structures. *J Am Chem Soc* **2001**, *123*, 8718-8729.
- (196) Xia, Y.; Yin, Y.; Lu, Y.; McLellan, J., Template-Assisted Self-Assembly of Spherical Colloids into Complex and Controllable Structures. *Adv Funct Mater* **2003**, *13*, 907-918.
- (197) Velev, O. D.; Gupta, S., Materials Fabricated by Micro- and Nanoparticle Assembly – The Challenging Path from Science to Engineering. *Adv Mater* **2009**, *21*, 1897-1905.
- (198) Slaughter, L. S.; Wang, L.-Y.; Willingham, B. A.; Olson, J. M.; Swanglap, P.; Dominguez-Medina, S.; Link, S., Plasmonic polymers unraveled through single particle spectroscopy. *Nanoscale* **2014**, *6*, 11451-11461.
- (199) Kraus, T.; Malaquin, L.; Schmid, H.; Riess, W.; Spencer, N. D.; Wolf, H., Nanoparticle printing with single-particle resolution. *Nat Nanotechnol* **2007**, *2*, 570-576.
- (200) Kuemin, C.; Stutz, R.; Spencer, N. D.; Wolf, H., Precise Placement of Gold Nanorods by Capillary Assembly. *Langmuir* **2011**, *27*, 6305-6310.
- (201) Rey, A.; Billardon, G.; Lortscher, E.; Moth-Poulsen, K.; Stuhr-Hansen, N.; Wolf, H.; Bjornholm, T.; Stemmer, A.; Riel, H., Deterministic assembly of linear gold nanorod chains as a platform for nanoscale applications. *Nanoscale* **2013**, *5*, 8680-8688.
- (202) Whitesides, G. M.; Grzybowski, B., Self-Assembly at All Scales. *Science* **2002**, *295*, 2418-2421.
- (203) Li, Q.; Jonas, U.; Zhao, X. S.; Kappl, M., The forces at work in colloidal self-assembly: a review on fundamental interactions between colloidal particles. *Asia-Pac J Chem Eng* **2008**, *3*, 255-268.
- (204) Velev, O. D., Self-Assembly of Unusual Nanoparticle Crystals. *Science* **2006**, *312*, 376-377.

- (205) Xia, Y.; Gates, B.; Yin, Y.; Lu, Y., Monodispersed Colloidal Spheres: Old Materials with New Applications. *Adv Mater* **2000**, *12*, 693-713.
- (206) Kim, S.-H.; Lee, S. Y.; Yang, S.-M.; Yi, G.-R., Self-assembled colloidal structures for photonics. *NPG Asia Mater* **2011**, *3*, 25-33.
- (207) Israelachvili, J. N.; McGuiggan, P. M., Forces Between Surfaces in Liquids. *Science* **1988**, *241*, 795-800.
- (208) Kralchevsky, P. A.; Nagayama, K., Capillary forces between colloidal particles. *Langmuir* **1994**, *10*, 23-36.
- (209) Butt, H.-J.; Kappl, M., Normal capillary forces. *Adv Colloid Interface Sci* **2009**, *146*, 48-60.
- (210) Min, Y.; Akbulut, M.; Kristiansen, K.; Golan, Y.; Israelachvili, J., The role of interparticle and external forces in nanoparticle assembly. *Nat Mater* **2008**, *7*, 527-538.
- (211) Deegan, R. D.; Bakajin, O.; Dupont, T. F.; Huber, G.; Nagel, S. R.; Witten, T. A., Capillary flow as the cause of ring stains from dried liquid drops. *Nature* **1997**, *389*, 827-829.
- (212) Denkov, N. D.; Velev, O. D.; Kralchevsky, P. A.; Ivanov, I. B.; Yoshimura, H.; Nagayama, K., Two-dimensional crystallization. *Nature* **1993**, *361*, 26-26.
- (213) Denkov, N.; Velev, O.; Kralchevski, P.; Ivanov, I.; Yoshimura, H.; Nagayama, K., Mechanism of formation of two-dimensional crystals from latex particles on substrates. *Langmuir* **1992**, *8*, 3183-3190.
- (214) Dimitrov, A. S.; Nagayama, K., Continuous Convective Assembling of Fine Particles into Two-Dimensional Arrays on Solid Surfaces. *Langmuir* **1996**, *12*, 1303-1311.
- (215) Prevo, B. G.; Velev, O. D., Controlled, Rapid Deposition of Structured Coatings from Micro- and Nanoparticle Suspensions. *Langmuir* **2004**, *20*, 2099-2107.

- (216) Colson, P.; Cloots, R.; Henrist, C., Experimental Design Applied to Spin Coating of 2D Colloidal Crystal Masks: A Relevant Method? *Langmuir* **2011**, *27*, 12800-12806.
- (217) Malaquin, L.; Kraus, T.; Schmid, H.; Delamarche, E.; Wolf, H., Controlled Particle Placement through Convective and Capillary Assembly. *Langmuir* **2007**, *23*, 11513-11521.
- (218) Prevo, B. G.; Kuncicky, D. M.; Velev, O. D., Engineered deposition of coatings from nano- and micro-particles: A brief review of convective assembly at high volume fraction. *Colloids Surf A* **2007**, *311*, 2-10.
- (219) Born, P.; Blum, S.; Munoz, A.; Kraus, T., Role of the Meniscus Shape in Large-Area Convective Particle Assembly. *Langmuir* **2011**, *27*, 8621-8633.
- (220) Born, P.; Munoz, A.; Cavelius, C.; Kraus, T., Crystallization Mechanisms in Convective Particle Assembly. *Langmuir* **2012**, *28*, 8300-8308.
- (221) Ni, S.; Leemann, J.; Wolf, H.; Isa, L., Insights into mechanisms of capillary assembly. *Faraday Discuss* **2015**.
- (222) Xia, Y.; Whitesides, G. M., Soft Lithography. *Annu Rev Mater Sci* **1998**, *28*, 153-184.
- (223) Pretzl, M.; Schweikart, A.; Hanske, C.; Chiche, A.; Zettl, U.; Horn, A.; Böker, A.; Fery, A., A Lithography-Free Pathway for Chemical Microstructuring of Macromolecules from Aqueous Solution Based on Wrinkling. *Langmuir* **2008**, *24*, 12748-12753.
- (224) Jana, N. R., Shape Effect in Nanoparticle Self-Assembly. *Angew Chem, Int Ed* **2004**, *43*, 1536-1540.
- (225) Ming, T.; Kou, X.; Chen, H.; Wang, T.; Tam, H.-L.; Cheah, K.-W.; Chen, J.-Y.; Wang, J., Ordered Gold Nanostructure Assemblies Formed By Droplet Evaporation. *Angew Chem, Int Ed* **2008**, *47*, 9685-9690.
- (226) Nikoobakht, B.; Wang, Z. L.; El-Sayed, M. A., Self-Assembly of Gold Nanorods. *J Phys Chem B* **2000**, *104*, 8635-8640.

- (227) Sau, T. K.; Murphy, C. J., Self-Assembly Patterns Formed upon Solvent Evaporation of Aqueous Cetyltrimethylammonium Bromide-Coated Gold Nanoparticles of Various Shapes. *Langmuir* **2005**, *21*, 2923-2929.
- (228) Xiao, J.; Li, Z.; Ye, X.; Ma, Y.; Qi, L., Self-assembly of gold nanorods into vertically aligned, rectangular microplates with a supercrystalline structure. *Nanoscale* **2014**, *6*, 996-1004.
- (229) Jana, N. R.; Gearheart, L. A.; Obare, S. O.; Johnson, C. J.; Edler, K. J.; Mann, S.; Murphy, C. J., Liquid crystalline assemblies of ordered gold nanorods. *J Mater Chem* **2002**, *12*, 2909-2912.
- (230) Nepal, D.; Onses, M. S.; Park, K.; Jespersen, M.; Thode, C. J.; Nealey, P. F.; Vaia, R. A., Control over Position, Orientation, and Spacing of Arrays of Gold Nanorods Using Chemically Nanopatterned Surfaces and Tailored Particle–Particle–Surface Interactions. *ACS Nano* **2012**, *6*, 5693-5701.
- (231) Tong, Q.; Malachosky, E. W.; Raybin, J.; Guyot-Sionnest, P.; Sibener, S. J., End-to-End Alignment of Gold Nanorods on Topographically Enhanced, Cylinder Forming Diblock Copolymer Templates and Their Surface Enhanced Raman Scattering Properties. *J Phys Chem C* **2014**, *118*, 19259-19265.
- (232) Liu, Z.; Huang, H.; He, T., Large-Area 2D Gold Nanorod Arrays Assembled on Block Copolymer Templates. *Small* **2013**, *9*, 505-510.
- (233) Lee, J.; Seo, J.; Kim, D.; Shin, S.; Lee, S.; Mahata, C.; Lee, H.-S.; Min, B.-W.; Lee, T., Capillary Force-Induced Glue-Free Printing of Ag Nanoparticle Arrays for Highly Sensitive SERS Substrates. *ACS Appl Mater Interfaces* **2014**, *6*, 9053-9060.
- (234) Müller, M.; Karg, M.; Fortini, A.; Hellweg, T.; Fery, A., Wrinkle-assisted linear assembly of hard-core/soft-shell particles: impact of the soft shell on the local structure. *Nanoscale* **2012**, *4*, 2491-2499.
- (235) Hanske, C.; Müller, M. B.; Bieber, V.; Tebbe, M.; Jessl, S.; Wittemann, A.; Fery, A., The Role of Substrate Wettability in Nanoparticle Transfer from Wrinkled

Elastomers: Fundamentals and Application toward Hierarchical Patterning. *Langmuir* **2012**, *28*, 16745-16750.

- (236) Schweikart, A.; Fortini, A.; Wittemann, A.; Schmidt, M.; Fery, A., Nanoparticle assembly by confinement in wrinkles: experiment and simulations. *Soft Matter* **2010**, *6*, 5860-5863.
- (237) Horn, A.; Hiltl, S.; Fery, A.; Böker, A., Ordering and Printing Virus Arrays: A Straightforward Way to Functionalize Surfaces. *Small* **2010**, *6*, 2122-2125.
- (238) Horn, A.; Schoberth, H. G.; Hiltl, S.; Chiche, A.; Wang, Q.; Schweikart, A.; Fery, A.; Boeker, A., Nanostructured wrinkled surfaces for templating bionanoparticles-controlling and quantifying the degree of order. *Faraday Discuss* **2009**, *143*, 143-150.
- (239) Lu, C.; Mohwald, H.; Fery, A., A lithography-free method for directed colloidal crystal assembly based on wrinkling. *Soft Matter* **2007**, *3*, 1530-1536.
- (240) Bowden, N.; Brittain, S.; Evans, A. G.; Hutchinson, J. W.; Whitesides, G. M., Spontaneous formation of ordered structures in thin films of metals supported on an elastomeric polymer. *Nature* **1998**, *393*, 146-149.
- (241) Volynskii, A. L.; Bazhenov, S.; Lebedeva, O. V.; Bakeev, N. F., Mechanical buckling instability of thin coatings deposited on soft polymer substrates. *J Mater Sci* **2000**, *35*, 547-554.
- (242) Trenkenschuh, K.; Erath, J.; Kuznetsov, V.; Gensel, J.; Boulmedais, F.; Schaaf, P.; Papastavrou, G.; Fery, A., Tuning of the Elastic Modulus of Polyelectrolyte Multilayer Films built up from Polyanions Mixture. *Macromolecules* **2011**, *44*, 8954-8961.
- (243) Stafford, C. M.; Harrison, C.; Beers, K. L.; Karim, A.; Amis, E. J.; VanLandingham, M. R.; Kim, H.-C.; Volksen, W.; Miller, R. D.; Simonyi, E. E., A buckling-based metrology for measuring the elastic moduli of polymeric thin films. *Nat Mater* **2004**, *3*, 545-550.

- (244) Bowden, N.; Huck, W. T. S.; Paul, K. E.; Whitesides, G. M., The controlled formation of ordered, sinusoidal structures by plasma oxidation of an elastomeric polymer. *Appl Phys Lett* **1999**, *75*, 2557-2559.
- (245) Efimenko, K.; Rackaitis, M.; Manias, E.; Vaziri, A.; Mahadevan, L.; Genzer, J., Nested self-similar wrinkling patterns in skins. *Nat Mater* **2005**, *4*, 293-297.
- (246) Schweikart, A.; Fery, A., Controlled wrinkling as a novel method for the fabrication of patterned surfaces. *Microchim Acta* **2009**, *165*, 249-263.
- (247) Jiang, H.; Khang, D.-Y.; Song, J.; Sun, Y.; Huang, Y.; Rogers, J. A., Finite deformation mechanics in buckled thin films on compliant supports. *Proc Natl Acad Sci U S A* **2007**, *104*, 15607-15612.
- (248) Claussen, K. U.; Tebbe, M.; Giesa, R.; Schweikart, A.; Fery, A.; Schmidt, H.-W., Towards tailored topography: facile preparation of surface-wrinkled gradient poly(dimethyl siloxane) with continuously changing wavelength. *RSC Adv* **2012**, *2*, 10185-10188.
- (249) Glatz, B. A.; Tebbe, M.; Kaoui, B.; Aichele, R.; Kuttner, C.; Schedl, A. E.; Schmidt, H.-W.; Zimmermann, W.; Fery, A., Hierarchical line-defect patterns in wrinkled surfaces. *Soft Matter* **2015**, *11*, 3332-3339.

***I***

Synthesis of Plasmonic  
Building Blocks



# 4

## Silver-Overgrowth-Induced Changes in Intrinsic Optical Properties of Gold Nanorods: From Noninvasive Monitoring of Growth Kinetics to Tailoring Internal Mirror Charges

Moritz Tebbe, Christian Kuttner, Martin Mayer, Max Maennel, Nicolas Pazos-Perez, Tobias A.F. König, and Andreas Fery

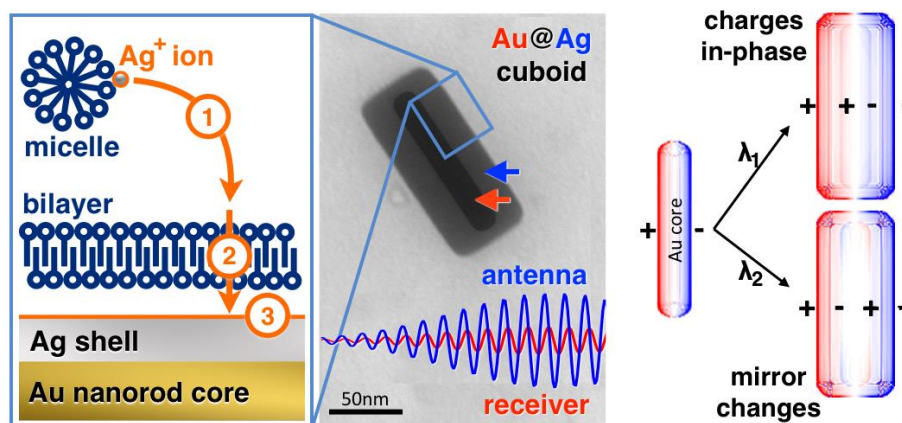


Figure 4.1. Table of Contents Figure.

Published in **The Journal of Physical Chemistry C**.

Reprinted with permission from Tebbe *et al.*, *J Phys Chem C* **2015**, 119, 9513–9523.

©2015 American Chemical Society.



## Abstract

We investigate the effect of surfactant-mediated, asymmetric silver overgrowth of gold nanorods on their intrinsic optical properties. From concentration-dependent experiments, we established a close correlation of the extinction in the UV/vis/NIR frequency range and the morphological transition from gold nanorods to Au@Ag cuboids. Based on this correlation, a generic methodology for *in situ* monitoring of the evolution of the cuboid morphology was developed and applied in time-dependent experiments. We find that growth rates are sensitive to the substitution of the surfactant headgroup by comparison of benzylhexadecyldimethylammonium chloride (BDAC) with hexadecyltrimethylammonium chloride (CTAC). The time-dependent overgrowth in BDAC proceeds about 1 order of magnitude slower than in CTAC, which allows for higher control during silver overgrowth. Furthermore, silver overgrowth results in a qualitatively novel optical feature: Upon excitation inside the overlap region of the interband transition of gold and intraband of silver, the gold core acts as a retarding element. The much higher damping of the gold core compared to the silver shell in Au@Ag cuboids induces mirror charges at the core/shell interface as shown by electromagnetic simulations. Full control over the kinetic growth process consequently allows for precise tailoring of the resonance wavelengths of both modes. Tailored and asymmetric silver-overgrown gold nanorods are of particular interest for large-scale fabrication of nanoparticles with intrinsic metamaterial properties. These building blocks could furthermore find application in optical sensor technology, light harvesting, and information technology.

## Introduction

Control over metallic nanoparticle morphology and composition gained increasing significance with respect to tailoring localized surface plasmon resonances (LSPRs). That makes noble metal nanoparticles excellent candidates for potential application as building blocks for metamaterial applications,<sup>1,2</sup> in optical sensing,<sup>3,4</sup> information technology,<sup>5,6</sup> and energy harvesting.<sup>7,8</sup> In optical metamaterials, a negative index of refraction can be produced combining a negative electric permittivity with a negative magnetic permeability at the same wavelength for building blocks (meta-atoms) much smaller than the used wavelength.<sup>9</sup> Major efforts have been spent in designing

resonator structures (*e.g.*, split ring resonators), which consist of an inductor-capacitor loop, a fundamental building block for fabrication of metamaterials with negative index of refraction.<sup>10,11</sup> These structures are restricted by small scale and expensive top-down methods such as electron beam lithography or focused ion beam milling.<sup>12</sup> To make widespread applications feasible, bottom-up methods are necessary, such as template-assisted self-assembly.<sup>13,14</sup> For bottom-up assembly a redesign of the applied plasmonic nanoparticle is crucial.<sup>15</sup> Stacked nanoparticle pairs or substrate-supported mirror charges are promising approaches for meta-atoms with so called extrinsic metamaterial properties, only present when assembled in distinct geometrical configurations.<sup>16,17</sup>

An alternative approach is the assembly of preformed metaatoms with intrinsic metamaterial properties.<sup>18</sup> Such metaatoms can be achieved by amorphous metal overgrowth of dielectric core particles<sup>19,20</sup> or by tailored synthesis of metal-core/metal-shell particles<sup>21-24</sup> with a clear signature of mirror charges at the core/shell interface. These mirror charges can be excited with an antenna particle into a receiver particle as it has been shown for pairs of nanoparticles<sup>17</sup> or metallic film-coupled nanoparticles.<sup>16</sup> Core/shell particles could be realized by high-precision asymmetric overgrowth and subsequent facet-selective etching.<sup>25-27</sup> Mirror charges at metal-/metal interfaces are induced by excitation inside the overlap region of the interband of gold (core) and intraband of silver (shell) between 326 and 515 nm wavelengths. Below its interband transition, gold acts as a retarding element because of the much higher damping compared to silver at the same wavelength. This asymmetry facilitates induction of mirror charges at the core/shell interface, which transforms gold-core/silver-shell nanoparticles (Au@Ag cuboids) into potential meta-atoms.

Well-defined gold/silver core/shell particles with a cuboidal morphology can be synthesized in large quantities in a three-step process based on surfactant-mediated seeded-growth approach.<sup>28,29</sup> First single-crystalline seed nanoparticles are formed and in a second step grown into single-crystalline gold nanorods.<sup>30</sup> These nanorods are subsequently overgrown with silver to form Au@Ag cuboids.<sup>22</sup> In general, fine-tuning of nanoparticle morphology requires to adjust parameters like seed crystallinity,<sup>31,32</sup> metal ion feed,<sup>33</sup> type and amount of reducing agent and surfactants, and application of ancillary additives.<sup>30,34-37</sup> Especially, the choice of the counterion of the surfactant is crucial owing to preferential adsorption to specific crystallographic

facets.<sup>24,38-40</sup> Differences in adsorption affinity are attributed to changes in surface energy which can be utilized to direct nanoparticle growth.<sup>24,41,42</sup> Gold-core/silver-shell nanoparticles in various morphologies can be prepared with high spatial precision from gold seeds exhibiting well-defined crystallinity by epitaxial overgrowth with silver.<sup>22-26,43-48</sup> In the presence of chloride ions, silver overgrowth takes place preferentially at crystal planes of higher index facets such as {110}, {111}, and {520}.<sup>22</sup> Single-crystalline gold nanorods with an octagonal cross-section are initially covered by eight lateral high-index facets.<sup>49</sup> Such nanocrystals grow into Au@Ag cuboids enclosed by six well-defined thermodynamically stable low-index {100} facets (see **Figure 4.2**).<sup>22,25,48</sup> After the transition from octagonal to rectangular cross-section, the system tends to reduce the free surface energy.<sup>27</sup> Thus, silver deposition preferentially takes place on its lateral facets.<sup>22,48</sup>

Consequently, it is evident that the choice of surfactant, apart from stabilizing the nanoparticles, is crucial for particle shape and monodispersity.<sup>28,36,37,50</sup> Three main contributions have been assigned to the surfactant: growth direction, complex formation with metal ions, and bilayer formation at the nanocrystal surface.<sup>32,51-54</sup> Aromatic compounds can be exploited in order to reduce the amount of impurities and reduce size dispersity in gold nanorod synthesis.<sup>28,30,31,34,35,55</sup> Benzyl-substituted surfactants like benzylhexadecyldimethylammonium chloride (BDAC) or aromatic additives like 5-bromosalicylic acid strongly influence nanoparticle synthesis.<sup>28,34,35</sup> Derivatives of phenole, *e.g.* hydroquinone, can act as weak reducing agents and, thus, are able to reduce metal ions.<sup>30,34,35</sup> Furthermore, aromatic compounds have been reported to influence the bilayer formation owing to hydrophobic and attractive  $\pi$ - $\pi$  interactions.<sup>56,57</sup> As a consequence, aromatic surfactants may affect the micellar aggregation number and the critical micelle concentration and alter the packing density of the bilayer.<sup>50,58,59</sup> Even though there are several studies on growth kinetics of anisotropic nanoparticles reported in the literature,<sup>35,36,54,60-67</sup> little is reported on the specific influence of aromatic moieties at cationic surfactant headgroups.<sup>47</sup> The challenge is the fundamental understanding how aromatics influence the reaction kinetics and if their influence is more related to complex formation, bilayer formation, diffusion, or all three combined.

So far, studies on the kinetics of the growth processes were mainly performed on solid substrates by tracking the growth of individual nanoparticles with sophisticated spectroscopic methods.<sup>64-66,68</sup> Methods like small-angle X-ray scattering (SAXS) and

conventional UV/vis/NIR extinction spectroscopy were utilized to gain information about the kinetics of particle ensembles.<sup>35,36,42,47,60-62,67,69-71</sup> Especially, UV/vis/NIR spectroscopy is accessible to a broad scientific community and allows for noninvasive growth monitoring with a high temporal resolution. Deriving morphological features for complex objects like overgrown nanoparticles, however, requires a solid understanding of the correlation of the spectroscopic response and the morphological changes during growth. A better understanding of the overgrowth kinetics will allow for increased control within nanoparticle synthesis and lead to a more rational molecular design of suitable surfactants.

In this work, we present the surfactant-controlled overgrowth of gold nanorods into gold–core/silver–shell nanoparticles (Au@Ag cuboids) to gain low growth rates for full control of the kinetic process. We chose two surfactants with the same counterion, but with different headgroup substituents, *i.e.*, benzylhexadecyldimethylammonium chloride (BDAC) and hexadecyltrimethylammonium chloride (CTAC), to synthesize Au@Ag cuboids. While BDAC offers lower growth rates, which is favorable for nanoparticle synthesis, CTAC serves as a reference system to further enhance our understanding of the silver-shell growth kinetics. We link the results from electromagnetic simulation precisely with the UV/vis/NIR extinction to provide information about morphology at each step of the overgrowth process and uncover transient morphological changes. Furthermore, we evaluate the formation of intrinsic mirror charge signatures at the core/shell interface for potential application in metamaterials.

## Experimental Section

**Materials.** All chemicals were purchased from Sigma-Aldrich unless mentioned otherwise: sodium borohydride ( $\text{NaBH}_4$ ,  $\geq 99.99\%$ ), gold(III) chloride trihydrate ( $\text{HAuCl}_4 \cdot 3\text{H}_2\text{O}$ ,  $\geq 99.9\%$ ), silver(I) nitrate ( $\text{AgNO}_3$ ,  $\geq 99.9\%$ ), hexadecyltrimethylammonium bromide (CTAB, 99%, Merck), hexadecyltrimethylammonium chloride (CTAC, Molekula), benzyldimethylhexadecylammonium chloride (BDAC, Molekula), ascorbic acid (AA,  $\geq 99.0\%$ ), and hydroquinone (HQ,  $\geq 99\%$ ) were used as received without further purification. All solutions were freshly prepared except for gold stock solution and used without further purification. Water was purified using a Milli-Q system (Millipore). The final resistivity was  $18.2 \text{ M}\Omega \cdot \text{cm}$ .

**Characterization.** UV/vis/NIR spectra were recorded at a Jasco V-670 (US-MD) with a temperature control unit. Nanoparticle solutions were dissolved 10 times with the respective surfactant to reduce extinction. TEM images were obtained with a LEO CEM902 operating at an acceleration voltage of 80 kV and with a LEO 922 OMEGA EFTEM with an acceleration voltage of 200 kV from Zeiss (Germany). Zero-loss filtered images were recorded using a bottom mounted Ultrascan 1000 (Gatan) CCD camera system. Gatan Digital Micrograph 3.9 for GMS 1.4 software was used for image acquisition. For TEM analysis 1 mL of nanoparticle solutions were concentrated to 100  $\mu\text{L}$  *via* centrifugation and washed twice to adjust the surfactant concentration to 1 mM. 5  $\mu\text{L}$  of the as-prepared solution was dried on Quantifoil 300 mesh copper grid with carbon films. Measurements performed for edge sharpening evaluation (**Figure 4.5**) were prepared under a  $\text{N}_2$  environment. For size evaluation the software ImageJ (version 1.44p, U.S. National Institutes of Health) was used.

**Seed Synthesis.** Seeds were prepared as reported elsewhere with small variations.<sup>30</sup> Briefly, 5 mL of an aqueous 0.5 mM  $\text{HAuCl}_4$  solution was added to 5 mL of an aqueous 0.2 M CTAB solution and stirred for 10 min. The solution was vigorously stirred at 1200 rpm, and 600  $\mu\text{L}$  of a freshly prepared 0.01 M  $\text{NaBH}_4$  solution was added quickly. The solution was stirred for 2 min and aged for another 30 min.

**HQ-Based Synthesis of Gold Nanorods.** Nanorods with an AR of 5.5 were prepared following a procedure published recently by Vigderman and Zubarev.<sup>30</sup> Briefly, to 250 mL of an aqueous 0.1 M CTAB solution 1250  $\mu\text{L}$  of a 0.1 M  $\text{HAuCl}_4$  stock solution was added to yield a final concentration of 0.5 mM. Afterward, 1250  $\mu\text{L}$  of an aqueous 0.1 M  $\text{AgNO}_3$  solution was added, followed by the addition of 12.5 mL of an aqueous 0.1 M HQ solution. The solution was stirred at 600 rpm at 32  $^\circ\text{C}$ , yielding a colorless solution. To induce nanorod growth, 6 mL of the as-prepared seed solution was added followed by vigorous shaking. The solution was stored at 32  $^\circ\text{C}$  overnight.

**Silver Overgrowth.** Overgrowth was performed according to a protocol published recently by Gomez-Graña *et al.* and others.<sup>22,45,46,72</sup> Briefly, as-prepared seeds were centrifuged at 8500 rcf for 30 min and transferred to a 10 mM surfactant solution. Subsequently, they were washed six times with a 10 mM surfactant solution to ensure full surfactant exchange. To 5 mL of 0.25 mM nanorod seeds in 10 mM surfactant solution varied amounts (2.5-100  $\mu\text{L}$ ) of a 0.1 M  $\text{AgNO}_3$  solution were added to adjust

the final Ag concentration to a desired value (0.05-2 mM) (see also Table S2). The solution was heated to 60 °C and stirred at a constant rate of 600 rpm. To initiate the reduction, an aqueous 0.4 M AA solution was added. The amounts were the same as for AgNO<sub>3</sub> to ensure a 4 times molar AA excess. The reactions were allowed to proceed at 60 °C for 8 h.

**Kinetic Experiments.** Dynamic overgrowth experiments were performed similar to static overgrowth experiments. Briefly, as-prepared seed nanorods were transferred to a 10 mM surfactant solution by centrifugation at 8500 rcf for 30 min and washed six times with a 10 mM surfactant solution to ensure full surfactant exchange. To 5 mL of seed solution containing 0.25 mM gold 100 μL of a 0.1 M AgNO<sub>3</sub> solution was added to adjust the final silver concentration to 2 mM. The solutions were heated to 60 °C and stirred at a constant rate of 600 rpm. To initiate the reduction, 100 μL of a 0.4 M AA solution was added. The reactions performed within UV/vis/NIR cuvettes were diluted 5 times with the specific 10 mM surfactant solution and were allowed to proceed at 60 °C for 14 h.

**FDTD Simulations.** Extinction spectra were simulated using a commercial software from Lumerical Solutions, Inc. (FDTD Solutions, Version 8.7.3). First, we modeled the gold nanorods (82 nm times 15 nm) in water ( $n = 1.333$ ) with different amounts of cap rounding (**Figure 4.S2**), which is defined by an ellipsoid with fixed first radius (nanorod width) and a variable second radius. In agreement with experimental peak positions, we chose a cap radius of 5 nm. The nanorods dimensions were evaluated using TEM images (**Figure 4.S1**). For a broadband source simulation (total-field scattered-field source,  $\lambda = 300$ -1300 nm), the FDTD software approximates the refractive index of the materials by a polynomial function. For the optical constants of Au, a fitting of the experimental data by Johnson and Christy (JC) was applied (six coefficients, one imaginary weight: 0.211 RMS error).<sup>73</sup> Second, the pure Ag cuboid was modeled with an edge radius of 8% of the cuboid length. Third, the Au@Ag cuboid was modeled with dimensions (82-92 nm x 15-38 nm) as evaluated from TEM images (**Figure 4.S3**). For the Ag permittivity, material data from Hagemann *et al.* (CRC) were used (five coefficients, two imaginary weight: 0.187 RMS error).<sup>74</sup> The parameters for the simulation performed for the kinetic plot are summarized in Table S1. A mesh size of 0.5 nm was chosen, and the zero-conformal-variant mesh refinement was used. For the best simulation stability, the mesh area was chosen to be 50 nm larger than the

existing structure in all three principal directions. All simulations reached the auto shut-off level of  $10^{-5}$  before reaching 150 fs simulation time. Antisymmetric boundary conditions (BC) were used normal to the polarization plane, and symmetric BC were used parallel to the polarization plane. In radiation direction we used in both directions the perfect match layer BC. To determine the surface charge densities, we simulated the model at the plasmonic mode frequency at a pulse length of  $\sim 20$  fs (optimized for long pulse length).

## Results and Discussion

### Synthesis and Optical Properties of Au@Ag Cuboids

Au@Ag cuboids are prepared in two steps. Single-crystalline gold nanorods were synthesized followed by a subsequent overgrowth with silver (see **Figure 4.2**). The gold nanorod cores used for surfactant-controlled silver overgrowth were prepared following a protocol published recently by Vigderman and Zubarev.<sup>30</sup> This seed-mediated synthesis utilizes the surfactant CTAB and silver nitrate ( $\text{AgNO}_3$ ) as growth directing agents, similar to the preparation of single-crystalline gold nanorods (see **Figure 4.2**).<sup>28,29</sup>

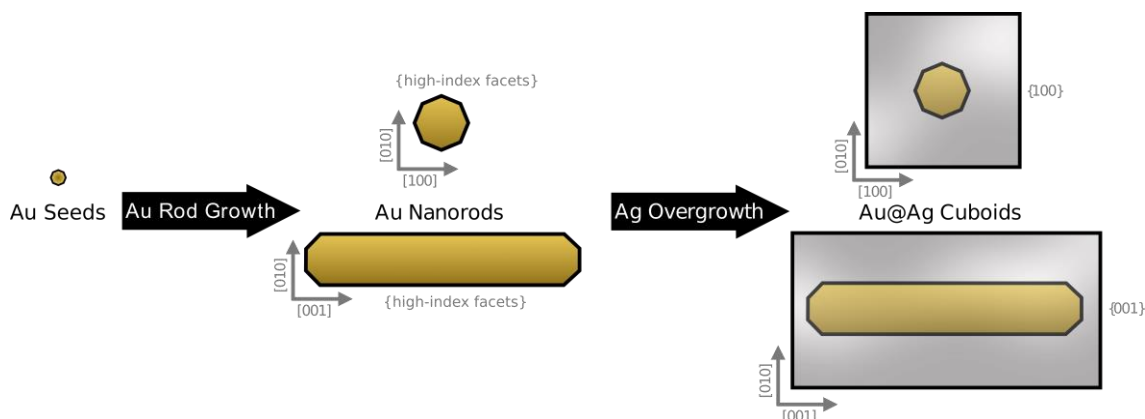


**Figure 4.2.** Schematic depiction of the synthetic pathway to Au@Ag cuboids: CTAB-stabilized spherical single-crystalline seed nanoparticles are grown into rods using CTAB and  $\text{AgNO}_3$  as directing agents and HQ as reducing agent. In a second, step the as-prepared gold nanorods are transferred to desired surfactants (BDAC, CTAC) and subsequently overgrown with silver into Au@Ag cuboids.<sup>22,48,49,75</sup>

In contrast to most widely used methods, ascorbic acid (AA) is replaced by an excess of hydroquinone (HQ).<sup>30,55</sup> This strongly influences the growth kinetics, since HQ is a weaker reducing agent and might also act similar to aromatic additives.<sup>34,35</sup> Thus,

applying HQ results in high gold ion conversions (up to 100%) and low amounts of impurities making further cleaning steps obsolete.<sup>30</sup> The concentration of AgNO<sub>3</sub> was optimized in order to yield high aspect ratios up to 5.5. So far, aspect ratios in this range have only been reported for synthesis routes using binary mixtures of surfactants.<sup>28,30</sup>

As-prepared gold nanorods were used to exchange CTAB against the respective surfactant (CTAC or BDAC) for subsequent anisotropic, controlled silver overgrowth (see **Figure 4.2**). Multiple centrifugation steps were performed to ensure complete replacement of counterions (bromide against chloride). The surfactants used in this work differ in the substitution of the ammonium headgroup with BDAC containing an aromatic benzyl group instead of a methyl group for CTAC (see **Figure 4.3**). Recently, Zhang and coworkers reported on the morphology of gold nanorods prepared with HQ and phenols to be single-crystalline.<sup>55</sup> This finding is consistent with our results as the gold nanorods prepared with HQ grow in highly anisotropic fashion. Consequently, the single-crystalline gold nanorods possess lateral high index facets and thus grow into well-defined Au@Ag cuboids with six {100} facets (see **Figure 4.2**). The final cuboidal morphology is expected for chloride as counterion stabilizing selectively the {100} facets due to a significantly reduced surface energy of these facets compared to others as a result of an increased packing density of ions.<sup>22</sup> Indeed, this manner is observed for both surfactants, giving evidence that the final crystalline structure and shape of the prepared cuboids and consequently the underlying growth process are strongly constrained to the counterion.<sup>22,25,45</sup> At acidic conditions the intermediate ascorbate anion is the dominant species present in solution and responsible for reducing silver ions.<sup>76,77</sup> Consequently, the reduction rate is significantly reduced compared to basic conditions. Thus, overgrowth was performed at elevated temperature of 60 °C to increase the reducing power of AA and ensure a consistent reduction of silver ions.<sup>22,26,72</sup>

The gold nanorods were characterized by UV/vis/NIR spectroscopy and transmission electron microscopy (TEM) as presented in **Figure 4.3**. The nanorods display a near-infrared longitudinal mode of 988 nm and a transversal mode of 510 nm (see **Figure 4.3a**). Nanorod dimensions were determined from TEM measurements to be 82 ± 8 nm in length and 15 ± 1 nm in diameter (see **Figure 4.S1**). The overall amount of impurities was below 1%, as suggested by the high intensity ratio of the longitudinal to transversal mode of 7.5.<sup>30,36</sup> Based on these results, finite-difference

time-domain (FDTD) modeling was performed.<sup>78</sup> By varying the rod dimensions and tip curvature, the best agreement with the experimental data was found for a gold nanorod of 82 nm in length, 15 nm in width, and a tip radius of 5 nm (compare **Figure 4.S2**). In modeling, a nanorod is constituted from a cylinder with two semiellipsoids as tips. The ellipsoid radius at the cylinder border is defined by the rod diameter while the radius in the geometric axis of the cylinder is defined as tip radius.

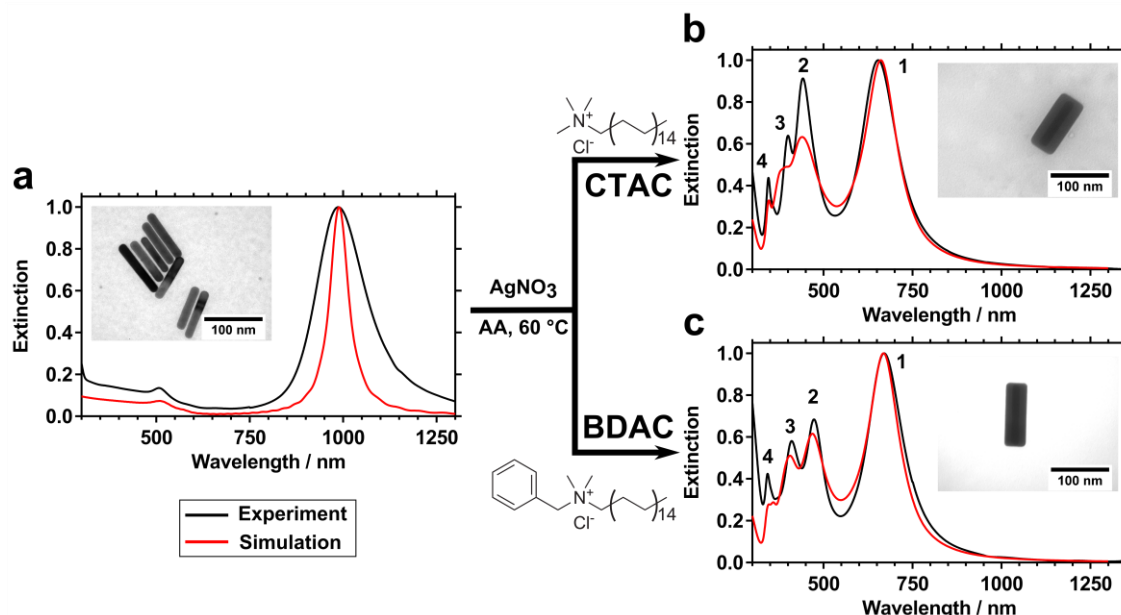


**Figure 4.3.** Normalized UV/vis/NIR extinction of (a) gold nanorod cores and Au@Ag cuboids prepared with (b) CTAC or (c) BDAC as surfactant. Simulated extinction spectra are included in red color. Insets show TEM images of the final nanoparticle morphology.

The UV/vis/NIR extinction spectra depicted in **Figure 4.3b,c** show syntheses performed with a molar Ag to Au ratio of 8 and either CTAC or BDAC as surfactant. The resulting spectra contain four resonance modes characteristic for cuboid or cubelike silver and gold–core/silver–shell nanoparticles.<sup>25,44–46,72</sup> The energetically lowest resonance mode is referred to the longitudinal mode ( $\sim 610$  nm), excited along the geometric axis. The energetically lowest resonance mode for a square cross section is attributed to the transversal mode ( $\sim 530$  nm), excited perpendicular to the geometric axis of the cuboid. The energetically highest resonance mode is just above the interband transition of silver (300 nm). Between the energetically highest and lowest plasmonic transverse mode two additional transversal modes are located (between 326 and 490 nm), which are characterized by a dominant dipolar mode and higher dipolar modes as a left shoulder. Generally, with increasing size of the particle the plasmonic modes shift toward lower energy because they are easier to

polarize.<sup>67,68</sup> Overgrowth of gold nanorods with a silver shell results in a significant narrowing of the longitudinal plasmonic mode due to lower amount of damping and better polarizability compared to gold. This effect is not related to changes in size distribution of nanoparticles and is referred to “plasmonic focusing”.<sup>65</sup>

The length and width of as-prepared Au@Ag cuboids were determined to be  $95 \pm 8$  and  $45 \pm 3$  nm for preparation with CTAC and  $92 \pm 8$  and  $39 \pm 2$  nm for BDAC (see **Figure 4.S3**), drastically altering the aspect ratio from 5.5 (gold nanorod cores) to around 2.1 and 2.4 for Au@Ag cuboids, respectively. The TEM images in **Figure 4.3b,c** clearly reveal that the epitaxial growth of the silver shell on gold nanorod seeds takes place almost exclusively at the lateral facets. Thus, the nanoparticles become thicker and ultimately grow into Au@Ag cuboids.<sup>22,27,44,45,72</sup> For the simulations presented in **Figure 4.3b,c** the best results were found for 0% and 2% edge rounding for BDAC and CTAC, respectively. We define the edge-rounding factor for a cuboid as the edge or corner radius, respectively, scaled by the length. As reported in the literature, the typical edge-rounding factor of cuboidal particles in an aqueous solution is between 8% and 16%.<sup>79-81</sup> The very low amount of edge rounding results in a large number of resonances and the significant red-shift of plasmonic modes (dipolar modes) compared to rounded nanostructures. Generally, the number of resonances increases as the symmetry of a structure decreases (see **Figure 4.S4**).<sup>80</sup> We found the best agreement between the simulated spectra and the experimental measured spectra when we assume sharp edges. Consequently, the edge rounding is a good indicator for the quality of Au@Ag cuboid syntheses.

### Noninvasive Monitoring of Silver Overgrowth

*In situ* monitoring by UV/vis/NIR spectroscopy allows for quantification of transient morphological changes (length, width, aspect ratio, edge rounding) during silver overgrowth, if quantitatively compared with detailed simulations. Therefore, we first performed static experiments (completed overgrowth at given Ag to Au ratios) to clearly correlate the morphology of Au@Ag cuboids with FDTD simulations. Second, we applied *in situ* monitoring in dynamic experiments for two surfactants with the same counterion, but with different headgroup substituents, *i.e.*, BDAC and CTAC. Third, we established a kinetic model to describe the overgrowth mechanism.

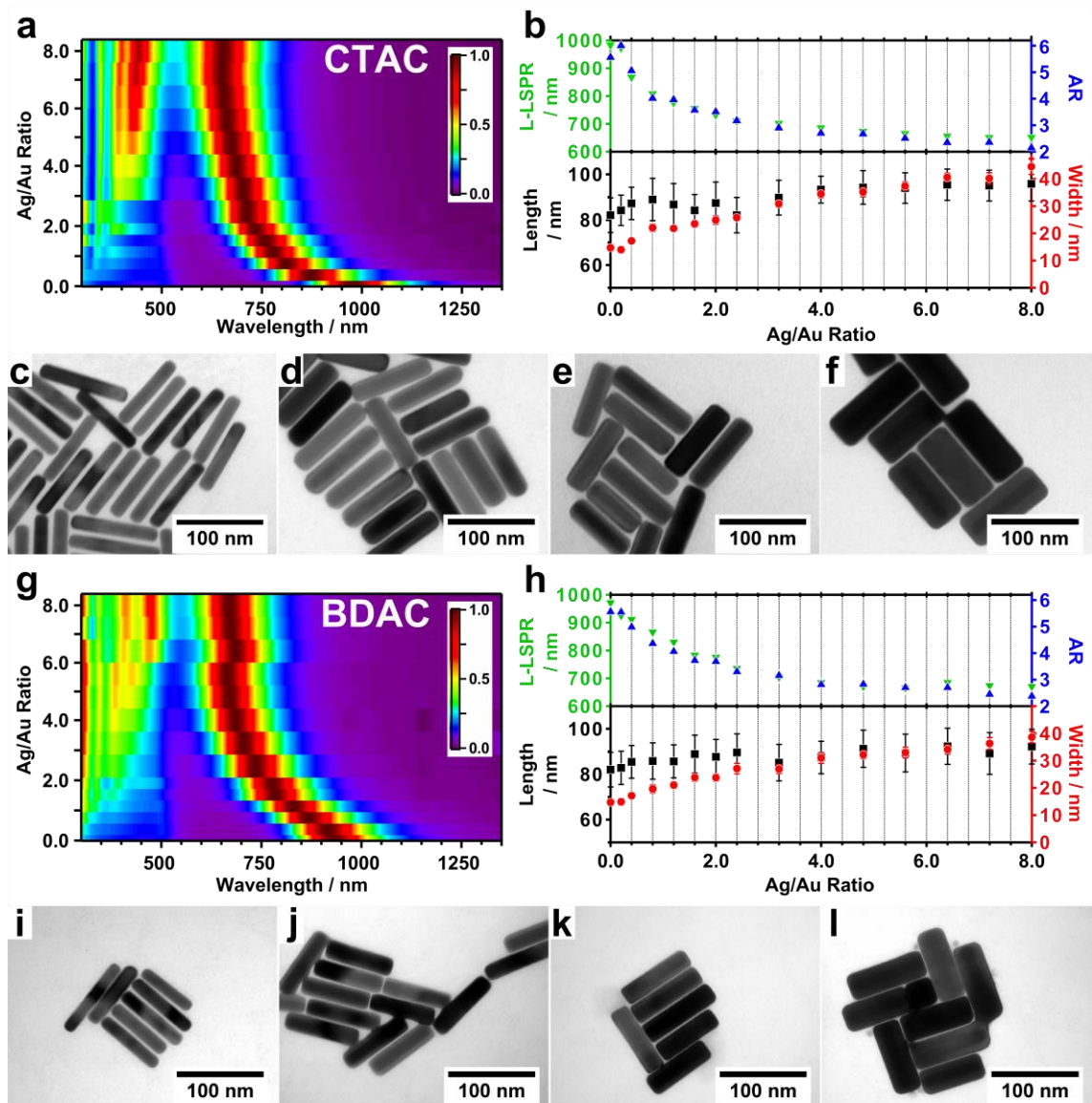


**Figure 4.4.** Au@Ag cuboid growth in static experiments: heat maps of the concentration-dependent evolution of plasmonic modes compiled from normalized UV/vis/NIR extinction spectra in (a) CTAC and (g) BDAC. Longitudinal modes (L-LSPR), length, width, and corresponding aspect ratio of Au@Ag cuboids synthesized in (b) CTAC and (h) BDAC plotted versus Ag to Au ratio. TEM micrographs of Au@Ag cuboids prepared with Ag to Au ratios of 0.2, 1.2, 2, and 6.4 for (c–f) CTAC and (i–l) BDAC.

**Figure 4.4** shows static experiments at different Ag to Au ratios (0 to 8). This ratio ultimately limits the amount of silver deposition leading to distinct thickness of the silver shell. The dimensions of resulting cuboids were evaluated with TEM (see **Figure 4.4** and **Figure 4.S5**). **Figure 4.4a–g** presents the spectral signatures for BDAC and CTAC in dependence on the Ag to Au ratio. The remarkable similarity of the observed plasmonic responses indicates that both surfactants yield Au@Ag cuboids of identical morphology. In particular, the blue-shift of the plasmonic mode (1) from

975 to 650 nm can be precisely tailored by variation of the Ag to Au ratio. The appearance of sharp transversal modes (*e.g.*, at ~450 nm (2)) indicates cuboids.

**Figure 4.4b–e** summarizes the morphological parameters (length, width, and aspect ratio) resulting from the choice of surfactant and Ag to Au ratio. The cuboids experience a change in aspect ratio from 6 down to 2 as they extend almost exclusively in width. The growth in length of about 10 nm is considerably below the lateral growth of up to 30 nm. Consequently, tailored overgrowth with defined Ag to Au ratio results in the identical Au@Ag cuboid morphologies, independent of the used surfactant. This intermediate result is crucial to link the spectral signature to morphological changes.

To study the influence of the surfactant on the kinetics of the overgrowth process, we conducted dynamic, *in situ* experiments at a fixed Ag to Au ratio of 8 at a temporal resolution of 5 min. **Figure 4.5a,b** shows the time-dependent UV/vis/NIR data using either CTAC or BDAC (see also **Figure 4.S6**). Qualitatively, it is obvious that the conversion with CTAC proceeds much faster than with BDAC but converges into almost identical mode structures *i.e.*, mode shifts and intensity distributions of all four modes. Therefore, we can conclude that both surfactants yield Au@Ag cuboids comparable in structure, size, and edge rounding (see **Figure 4.S7**).

The dynamic experiments revealed new transient spectral features, as we will discuss in the following. **Figure 4.5a,b** shows the longitudinal dipolar plasmonic mode (1), which experiences an initial shift toward blue up to a maximum value of about 652 nm for CTAC and 663 nm for BDAC. This blue-shift is followed by a significant red-shift of mode (1) of 15 nm for CTAC and 10 nm for BDAC. At the same time the transversal modes (2), (3), and (4) arise. Upon further overgrowth, these modes increase in intensity and shift toward red.

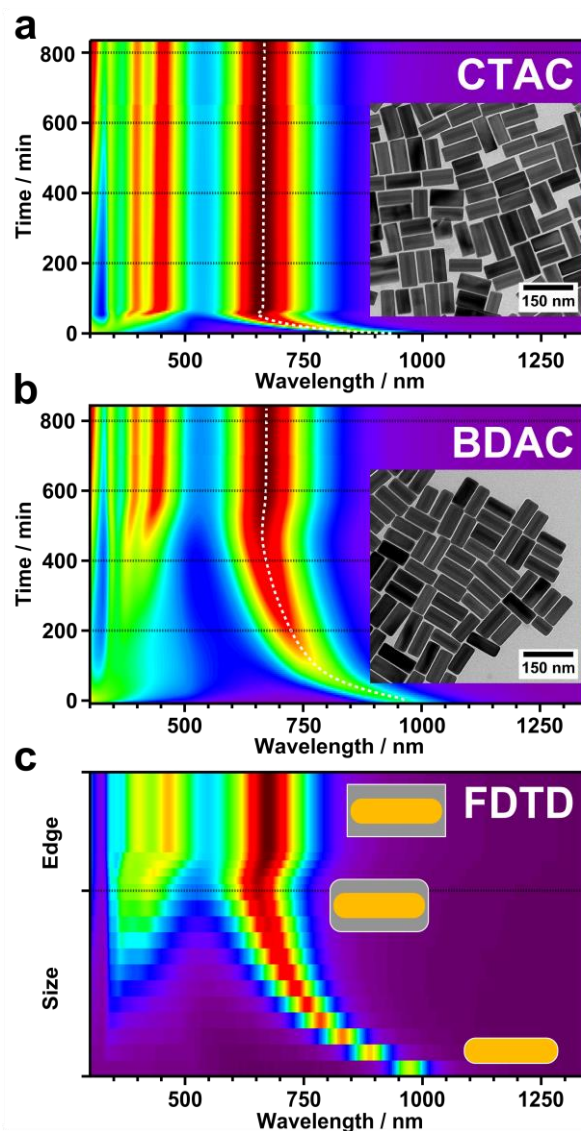


**Figure 4.5.** Au@Ag cuboid growth in dynamic experiments and compared to simulation: heat maps of time-dependent UV/vis/NIR extinction spectra of syntheses performed with (a) CTAC and (b) BDAC at Ag to Au ratio of 8 (also compare **Figure 4.S6**). Representative TEM insets show the final Au@Ag cuboids. The plasmonic mode (1) features an initial blue-shift followed by a slight red-shift as highlighted by the white dashed line. (c) Modeled evolution of the spectral signature considering both changes in dimension (size) and edge rounding (edge) (for simulation parameters see **Table 4.S1**).

Comparing FDTD simulation with above-mentioned results, the growth process can be divided in separated processes (see **Figure 4.5c**). The initial blue-shift of mode (1) can be attributed to the constant increase of the silver shell thickness, the corresponding change in aspect ratio, and the morphological transition from octagonal to square cross section. The subsequent significant red-shift cannot be explained by further overgrowth. We included an extended linear overgrowth (total

length 101 nm and total width 55 nm) in the Supporting Information (**Figure 4.S8a**). Theoretical modeling with an excellent match with the experimental observation assign this red-shift to a small change in the edge rounding, which is between 0% and 8% (**Figure 4.5c** and **Figure 4.S8b**). Taking this feature (so-called edge sharpening) into account, we can describe the overgrowth process in more detail: First, the Au@Ag cuboid extends stepwise both in length and in width, from its initial seed geometry (82 nm x 15 nm) up to 92 nm x 38 nm, keeping a constant edge rounding of 8%. After that, the edge rounding is decreased in order to emulate the red-shift. Finally, an ideal structure of an Au@Ag cuboid with sharp edges and final dimensions of 92 nm x 38 nm is formed and maintained. These results were evidenced by additional TEM measurements performed under inert gas conditions during sample preparation to suppress rapid oxidation/sulfidation of silver in air as observed for static experiments (see **Figure 4.4**). TEM micrographs shown in **Figure 4.5** as insets reveal sharp edges obtained for both surfactants, even though oxidation of the highly reactive sharp edges could not be completely avoided. However, the combination of UV/vis/NIR and theoretical modeling give strong evidence that the observed overgrowth can be clearly divided into completely separated processes: (I) growth and (II) edge sharpening.

### Quantitative Analysis of the Overgrowth Kinetics

In the following, we investigated the influence of the surfactant headgroup on the kinetics of overgrowth. Thus, we employed a master curve to evaluate the time-dependent volume change from the experimental UV/vis/NIR data (see **Figure 4.S9**). **Figure 4.6** shows the evolution of the particle volume over time for both surfactants. The volume change shows a sigmoidal behavior as expected for surface-controlled growth reactions.<sup>61,62</sup> The volume change over time is given by the number of silver ions ( $N_{Ag^+}$ ) reduced to elementary silver ( $N_{Ag^0}$ ) at the particle surface times the volume of a single silver atom  $V_{Ag^0}$  (0.0125 nm<sup>3</sup>).<sup>82</sup>

$$\frac{dV}{dt} = V_{Ag^0} \cdot \frac{dN_{Ag^0}}{dt} \text{ with } \frac{dN_{Ag^0}}{dt} = -\frac{dN_{Ag^+}}{dt}$$

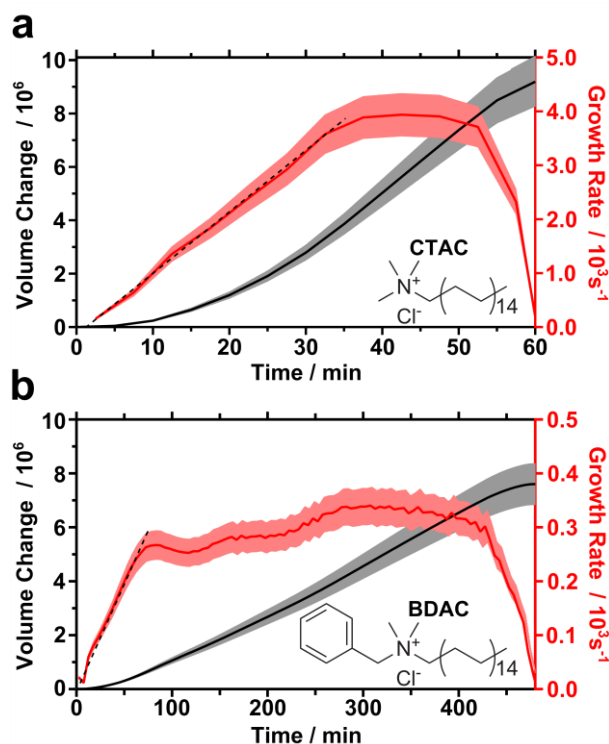


**Figure 4.6.** Surfactant-controlled overgrowth kinetics in (a) CTAC and (b) BDAC: volume change  $\Delta V/V_{Ag^0}$  (black), *i.e.*, the number of reduced ions  $N_{Ag^0}$ , over time. The corresponding growth rates (red), given by the first derivative  $dN_{Ag^0}/dt$ , exhibit three growth regimes: increasing growth rate, constant growth rate, and the cease of growth. Please note changes in scaling.

At first glance, it becomes apparent that the overgrowth proceeds in CTAC faster than in BDAC by a factor of 8. The respective maximum growth rates differ by about a single order of magnitude. Generally, the overgrowth proceeds similar for both surfactants: First, the growth rate increases linearly with time. The acceleration of the growth rate in BDAC ( $0.05 \pm 0.01 \text{ nm}^3/\text{s}^2$ ) is about 30 times slower than in CTAC ( $1.4 \pm 0.1 \text{ nm}^3/\text{s}^2$ ). Subsequently, the volume increases at nearly constant growth rates (CTAC,  $48 \pm 5 \text{ nm}^3/\text{s}$ ; BDAC,  $4 \pm 1 \text{ nm}^3/\text{s}$ ).<sup>61</sup> Finally, the growth rate decreases successively until the final volume is obtained. From the theoretical modeling, we can infer that late stages of the overgrowth process are dominated by shape changes of the particles, *i.e.*, edge sharpening. Consequently, the master curve is only valid within the actual growth regime (see **Figure 4.S9**). At this point, we can formulate a generalized silver overgrowth mechanism in the context of surfactant-controlled kinetics.

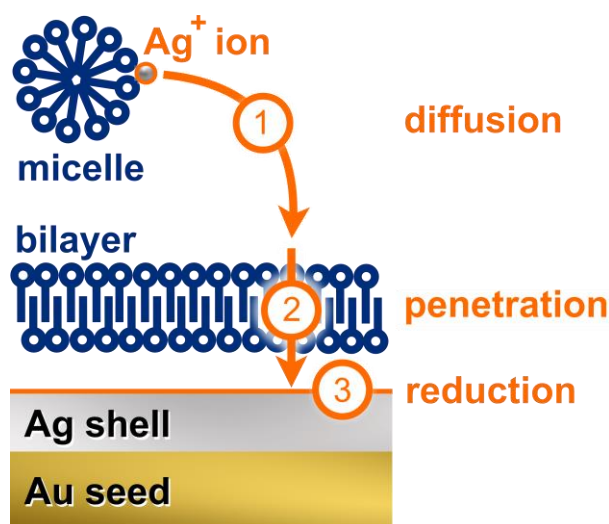


**Figure 4.7.** Schematic representation of the three-step silver overgrowth mechanism.

**Figure 4.7** gives a schematic representation of the generalized silver overgrowth mechanism, which involves three main processes: (1) the micellar diffusion of surfactant-stabilized Ag<sup>+</sup> ions (Ag<sup>+</sup>@micelle) in bulk solution, (2) the transport of ions across the fluid surfactant bilayer, and (3) the reduction of ions at the metal surface. In regard to the first process, both surfactants form micelles of different aggregation numbers (BDAC 62, CTAC 101)<sup>58</sup> but of comparable sizes (radius 3 nm, SAXS) in water.<sup>59</sup> Thus, similar diffusion rates can be expected in bulk solution above the critical micellar concentration. The resulting diffusion coefficient of  $7.6 \cdot 10^{-11} \text{ m}^2/\text{s}$  for such a micelle would result in much faster reaction kinetics for a purely diffusion-limited regime.<sup>61</sup> Thus, micellar diffusion (step 1) is not rate-limiting as it can be expected to allow for a steady supply of ions from solution indifferent of the surfactant. Therefore, the significant difference in reaction kinetics observed for BDAC and CTAC can be attributed to either the bilayer transition (surfactant–surfactant interactions; step 2) or the reduction at the surface (ion–surfactant interactions; step 3), or a balance of both.

In regard to step 2, the fluid surfactant bilayer at the particle surface acts as a stabilizing membrane. Hence, differences in membrane stiffness could significantly affect ion supply. The effective membrane stiffness not only arises from the molecular packing density and thermodynamics but also gains from distinct headgroup interactions. For BDAC, these are  $\pi$ – $\pi$  interactions of the benzyl substituents. However, a lower packing density (due to bulky headgroups) may be balanced by intermolecular interactions. In regard to step 3, Ag<sup>+</sup> exhibits higher binding affinity toward BDAC owing to cation– $\pi$  interactions of the electron-rich benzyl headgroup.<sup>83</sup>

The aromatic complexation might inhibit the reduction of  $\text{Ag}^+\text{@BDAC}$  compared to  $\text{Ag}^+\text{@CTAC}$ .

To solve the question whether the bilayer transition (step 2) or the reduction at the surface (step 3), or a balance of both, is rate determining requires further in-depth studies. Nevertheless, the presented approach can be used as a generic concept to determine growth rates of nanoparticle synthesis *in situ* even for complex morphologies. In addition, our results have great potential for tailoring of reaction rates by a rational choice of surfactants.

### **Plasmonic Modes of Au@Ag Cuboids.**

With an experimental control of the overgrowth process it is possible to fabricate tailored plasmonic Au@Ag cuboid modes. **Figure 4.8a** shows resonance frequencies of all dominant plasmonic modes during the overgrowth process and the corresponding changes in aspect ratio. Furthermore, we compared the plasmonic modes from the overgrowth process with a pure silver cuboid to emphasize the influence of the gold core. **Figure 4.8b** shows the surface charge distributions relative to their excited wavelength. The gold nanorod exhibits two dipolar modes, which are defined as zeroth-order modes (subscript 0) with respect to their exciting polarization (superscript L/T). The identical mode signatures are present for the pure silver cuboid of zeroth order. Because of sharper edges in comparison to the nanorod, we observe two further, higher dipolar modes (subscript 1-2). These so-called cubic plasmonic modes are well-known and described in more detail elsewhere.<sup>80,84</sup> As expected from the overgrowth process, the silver cuboid modes are dominating the gold nanorod mode, which results in a significant blue-shift of the gold nanorod mode. However, the resulting Au@Ag cuboid modes are different to the cuboid modes without gold core in respect to their excited polarization and wavelength. The longitudinal Au@Ag cuboid mode exhibits the same charge distribution at the gold nanorod core and the silver cuboid shell (in-phase charges). In contrast, all transversal Au@Ag cuboid modes exhibit opposite charges at the core in respect to the shell (mirror charges).

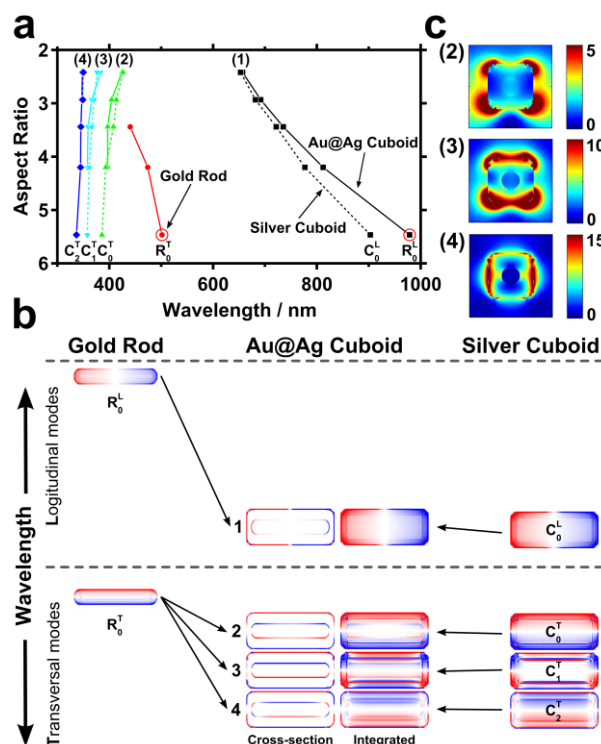


**Figure 4.8.** (a) Plasmonic modes evaluated from simulated extinction spectra for increasing aspect ratios for gold nanorod overgrowth with silver (solid lines) and pure silver cuboid (intersected lines). (b) Plasmonic modes (surface charge distribution) of the gold nanorod, Au@Ag cuboid, and pure silver cuboid relative to their excitation wavelength. (c) Electric field distribution of transversal modes of the Au@Ag cuboid. The edge rounding was fixed to 8%.

These induced mirror charges at the gold nanorod core in respect to the silver cuboid shell are correlated with the complex permittivity ( $\varepsilon = \varepsilon' + i\varepsilon''$ ) of the used materials (see **Figure 4.S10**). The induced mirror charges of the transversal Au@Ag cuboid modes occur between the band overlap of the intraband of silver (326 nm) and the interband of gold (515 nm). At this wavelength range the damping of gold is significantly higher compared to silver ( $\varepsilon''$ ), whereas the polarizability follows the same trend ( $\varepsilon'$ ). It is important to note that in the interband region of gold the real part of permittivity is at the limit for surface plasmon resonances (nonradiative condition) as described by Raether.<sup>85</sup> Briefly, for a non-radiative condition the real part of the metal must be negative and smaller as the permittivity of the environment ( $\varepsilon' < -\varepsilon_{\text{medium}}$ ), in our case water ( $\varepsilon_{\text{H}_2\text{O}} = 1.77$ ). In the interband of gold the permittivity falls below the non-radiative condition with increasing energy (see **Figure 4.S10**). Consequently, the induced mirror charges are getting stronger at lower wavelength (**Figure 4.8b,c**). More details of the transversal modes could be found in the Supporting Information (**Figures 4.S11–13** and **Text 4.S1**). This significant

difference in damping and polarizability at the overlap region renders the gold core a retarded plasmonic element compared to the silver shell. If this finding is transferred to an antenna-receiver model, the silver shell can be described as antenna, which transmits its electromagnetic field to the gold core (receiver). To the best of our knowledge, this antenna effect at the metal/metal interface of core/shell particles has not been reported in the literature so far.

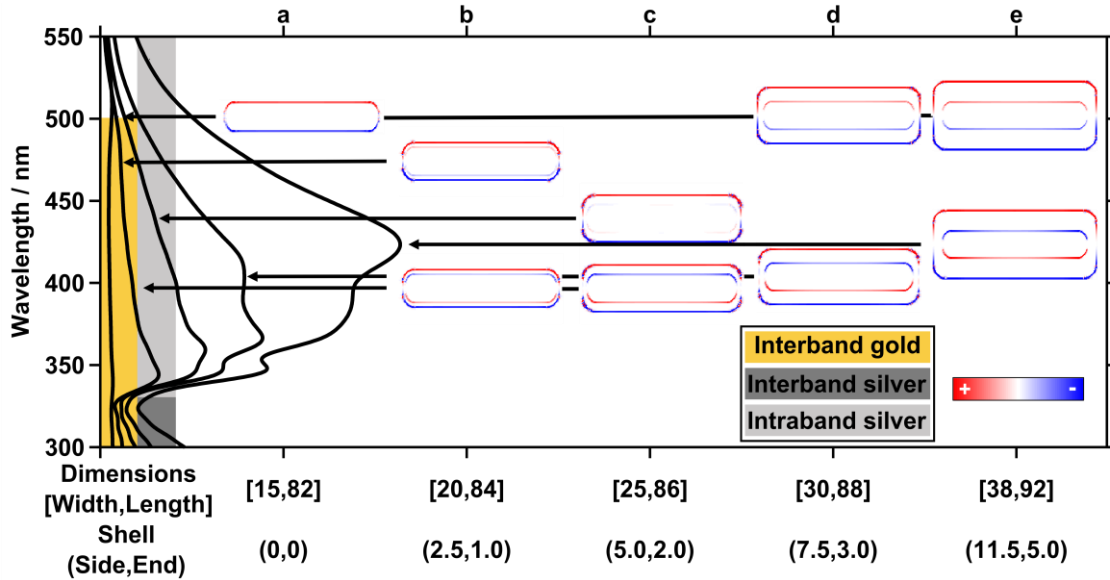


**Figure 4.9.** Evolution of plasmonic mode (2) during the tailored overgrowth process to emphasize the nature of in-phase and mirror charges. The mirror charges occur exclusively in the overlap region of interband and intraband of gold and silver, respectively. Surface charge distribution plots of (a) the gold nanorod core and (b–e) Au@Ag cuboids of different dimensions [width/length] and shell thicknesses (side/end). All units are in nanometers.

Following the plasmonic mode (2) during the overgrowth process reveals that the induced mirror charges already occur at a very thin silver layer (see **Figure 4.9**). These two modes at 474 nm (in-phase charged) and 397 nm (mirror charged) are also recognizable as peaks in the extinction cross section. With a further shell overgrowth only the mirror charged mode is visible in the extinction cross section (**Figure 4.9c–e**). To excite the inphase charge distribution (**Figure 4.9e**), the core must be excited at its resonance wavelength (502 nm) with a small bandwidth 33 THz (28 nm). The antenna effect has the same signature as the bonding and antibonding mode described by the hybridization model from Prodan *et al.*<sup>20</sup> Comparing the Au@Ag cuboid mirror charges with a hybridization model observed for stacked double crescents reveals two advantages:<sup>2</sup> All modes are in the optical visible spectrum, and the energetic difference between the modes is about a factor of 3

smaller. Consequently, with full control during the overgrowth the silver shell could be fine-tuned to the wavelength of interest. These building blocks with intrinsic metamaterial properties have potential for application in metamaterials, if self-assembled to clusters (trimer and heptamer assemblies) or modified by facet-selective etching to break the symmetry and form splitting-resonator-like structures. This paves the road for new strategies to develop cost-efficient syntheses of nanophotonic structures, which exhibit strong mirror-charge responses or Fano-like resonances, similar to metal/dielectric cluster assemblies.<sup>86</sup>

## Conclusion

The close correlation of transient morphological and optical changes during overgrowth of gold nanorods with a cuboidal silver shell is a straightforward approach to thoroughly explain *in situ* kinetics recorded with UV/vis/NIR spectroscopy. This approach enabled us to compare two different surfactants namely CTAC and BDAC with respect to their impact on nanoparticle growth behavior. Static experiments revealed almost no differences in nanoparticle quality for both surfactants since the overall growth mechanism and the final shape is dictated by the counterion chloride in combination with the Au to Ag ratio. Selective stabilization of {100} facets lead to nanoparticle overgrowth into Au@Ag cuboids as reported elsewhere.<sup>45,71</sup> However, the surfactants show significant differences in their overgrowth kinetics. The overgrowth rate of BDAC is about an order of magnitude lower compared to CTAC. This can be directly related to the headgroup structure as aromatics strongly influence the kinetics of nanoparticle syntheses. Detailed investigation revealed that the overgrowth kinetics can be divided in three stages: (I) accelerated growth, (II) constant growth rate, and (III) deceleration going along with edge sharpening. Furthermore, we found that edge rounding is a good indicator for quality of the performed synthesis. These results will help to further increase understanding of nanoparticle syntheses and overgrowth processes. In addition, this knowledge offers the possibility to fine-tune and enhance control for nanoparticle synthesis and overgrowth reactions. Investigation of the plasmonic modes revealed that the presence of the gold nanorod core inside the silver cuboid alters the resulting resonances. These Au@Ag cuboid modes feature in-phase and mirror-charged plasmonic modes. The latter might be of particular interest for metamaterial design

due to their induced mirror charge nature, which is a prerequisite for negative permeability.

## Associated Content

### Supporting Information

TEM characterization of gold nanorods and Au@Ag cuboids; 3D plots of the UV/vis/NIR data of the dynamic growth experiments; FDTD modeling of gold nanorods and Au@Ag cuboids, and their dynamic growth kinetics; systematic evaluation of the UV/vis/NIR data of the dynamic experiments based on the results of the static experiments; complex permittivity of Ag and Au; further information about mirror charges at the gold/silver interface of core/shell particles; electric field intensity cross sections and plane-plots; silver overgrowth synthesis parameters. This material is available free of charge *via* the Internet at <http://pubs.acs.org>.

## Acknowledgements

This work was funded by the European Research Council under grant ERC-2012-StG 306686 (METAMECH: Template-assisted assembly of METAmaterials using MECHanical instabilities) and PRIOSERS FP7MC-IEF-623527, and by the German Science Foundation within the SFB 840. M.T. was supported by the Elite Network Bavaria in the frame of the Elite Study Program “Macromolecular Science” and funded *via* a grant for Ph.D. candidates according to Bavarian elite promotion law (BayEFG). The authors thank C. Kunert for performing TEM measurements.

## Supporting Information

The following section provides further information about the experimental results and electromagnetic simulations of nanoparticle synthesis and silver overgrowth discussed in the main text. Additionally, information on performed kinetic experiments and corresponding data evaluation is provided.

## Gold Nanorod Characterization

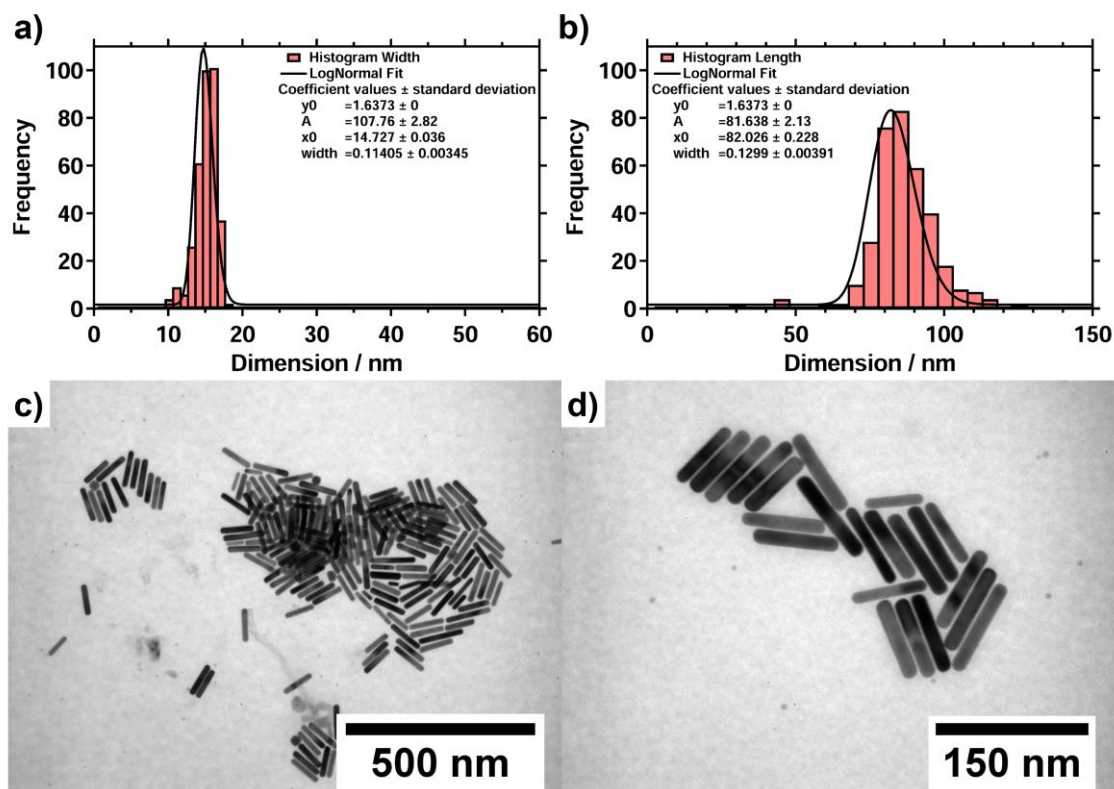


**Figure 4.S1.** CTAB-based gold nanorod synthesis with hydroquinone.<sup>30</sup> (a/b) Histograms of the width and length distribution of as prepared gold nanoparticles ( $n=150$ ). (c/d) Low- and high-magnification TEM images of as-prepared gold nanorods.

## FDTD Modeling of Gold Nanorods

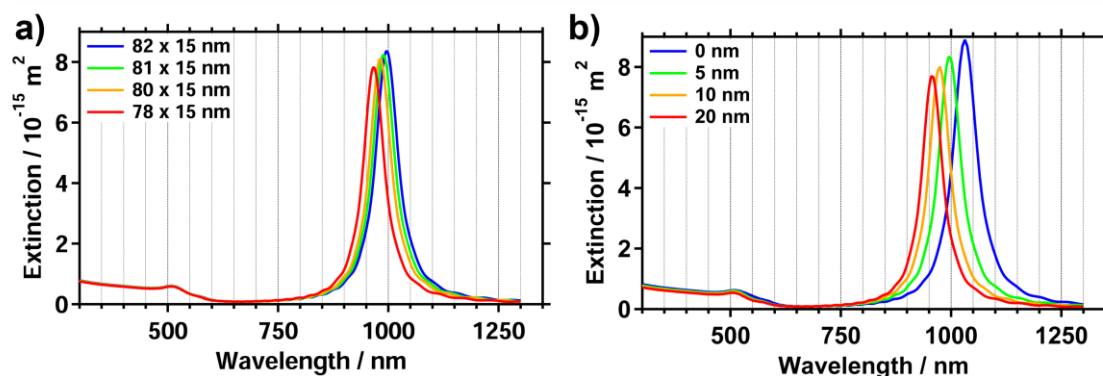


**Figure 4.S2.** Finite-difference time-domain (FDTD) modeling for gold nanorods performed on the basis of dielectric data taken from Johnson and Christy (JC).<sup>73</sup> (a) Modeled extinction spectra of gold nanorods with 5 nm tip rounding with fixed width and varied length (75-82 nm). (b) Modeled extinction spectra of gold nanorods for fixed length (82 nm) and width (15 nm) with varied tip rounding values (0-15 nm).

## Silver Overgrowth Characterization

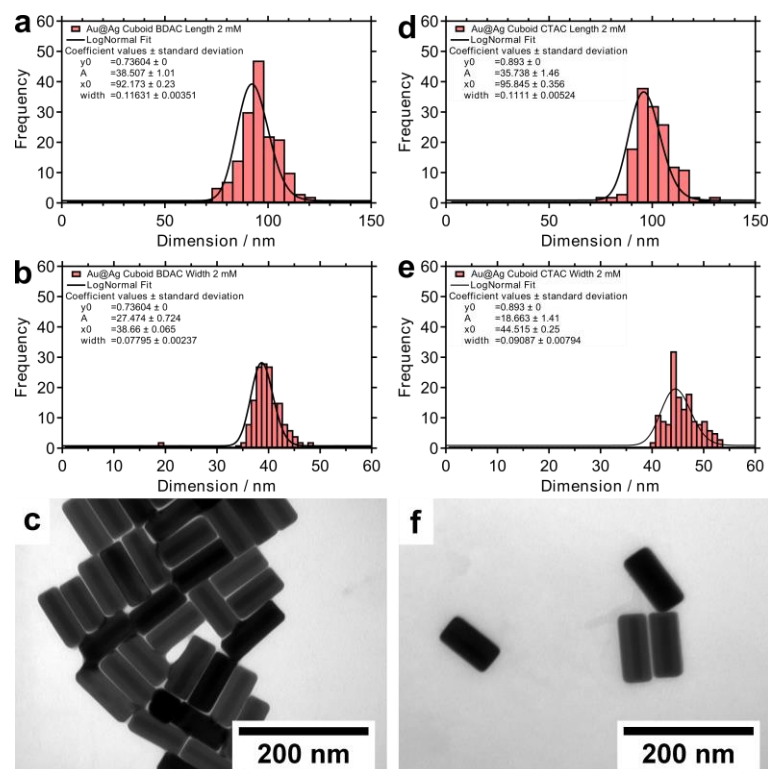


**Figure 4.S3.** Silver overgrowth of gold nanorods in 10 mM CTAC or BDAC at 60 °C and with a final Ag to Au ratio of 8 ([Ag] = 2 mM). (a/b) Distribution of the width and length of silver overgrowth performed with BDAC plotted as histograms. (c) TEM micrograph of as prepared cuboids in BDAC. (d/e) Distribution of the width and length of silver overgrowth performed with CTAC plotted as histograms. (f) TEM micrograph of as-prepared cuboids in CTAC.

## FDTD Modeling of Au@Ag Cuboids

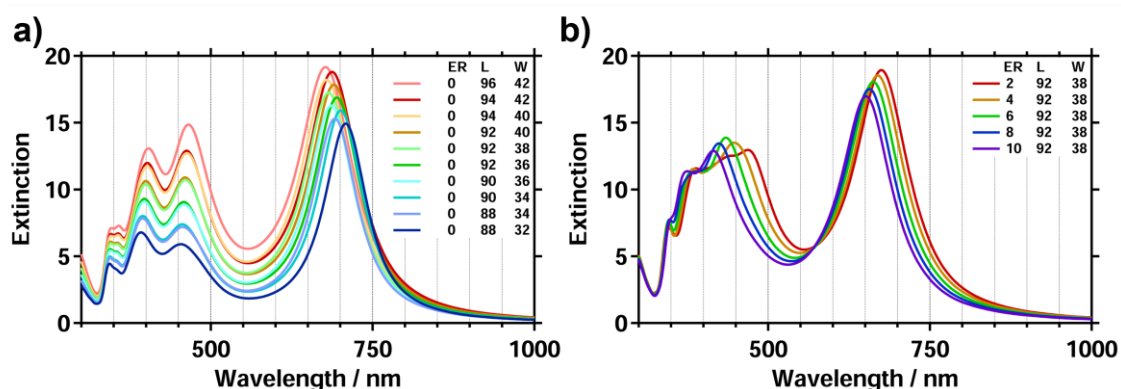


**Figure 4.S4.** FDTD modeling of Au@Ag cuboids, focused on small variations in dimension and edge rounding. (a) Modeled extinction spectra of Au@Ag cuboids with 0% edge rounding and varied width and length (88-96 nm and 32-42 nm). (b) Modeled extinction spectra of Au@Ag cuboids with fixed width and length (92 nm and 38 nm) and varied edge rounding values (2-10%).

## Evaluation of Static Overgrowth Experiments

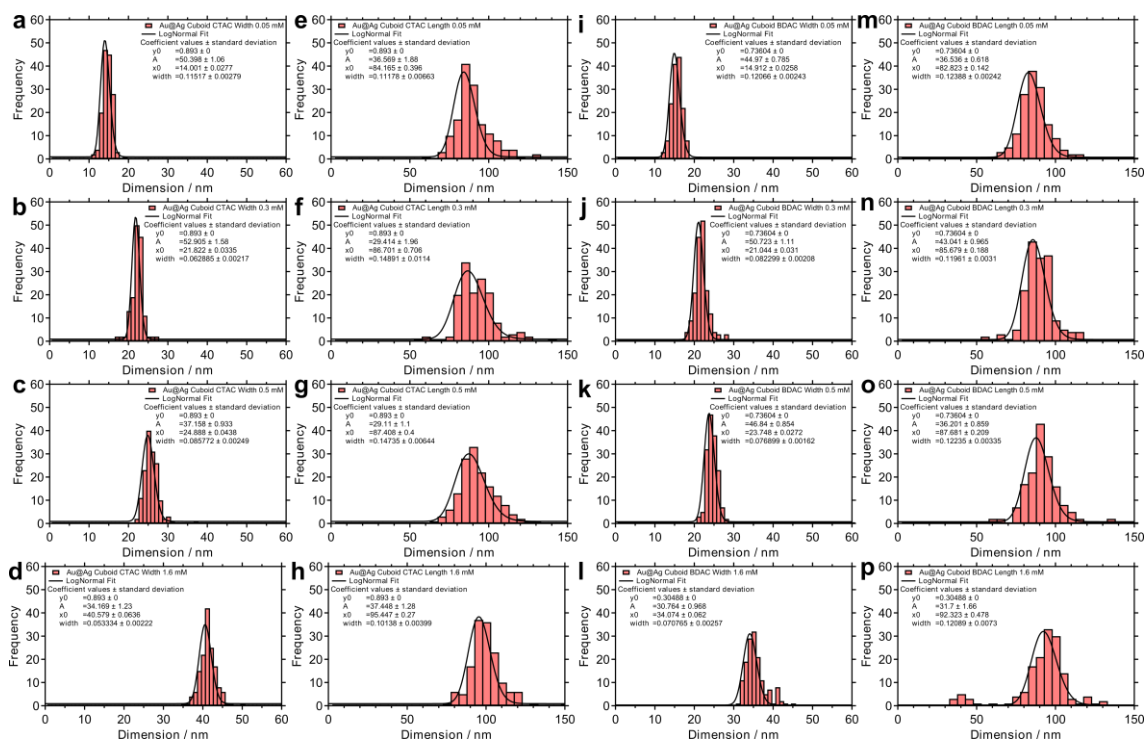


**Figure 4.S5.** Silver overgrowth of gold nanorods with 10 mM surfactant, at 60 °C for varied silver amounts. Distribution of the (a-d) width and (e-f) length of Au@Ag cuboids prepared with CTAC plotted as histograms ( $n = 150$ ). Distribution of the (i-l) width and (m-p) length of Au@Ag cuboids prepared with BDAC plotted as histograms ( $n = 150$ ). (Ag to Au ratio: (a/e/i/m) 0.2; (b/f/j/n) 1.2; (c/g/k/o) 2; (d/h/l/p) 6.4).

## Au@Ag Cuboid Growth Kinetics 3D Plots

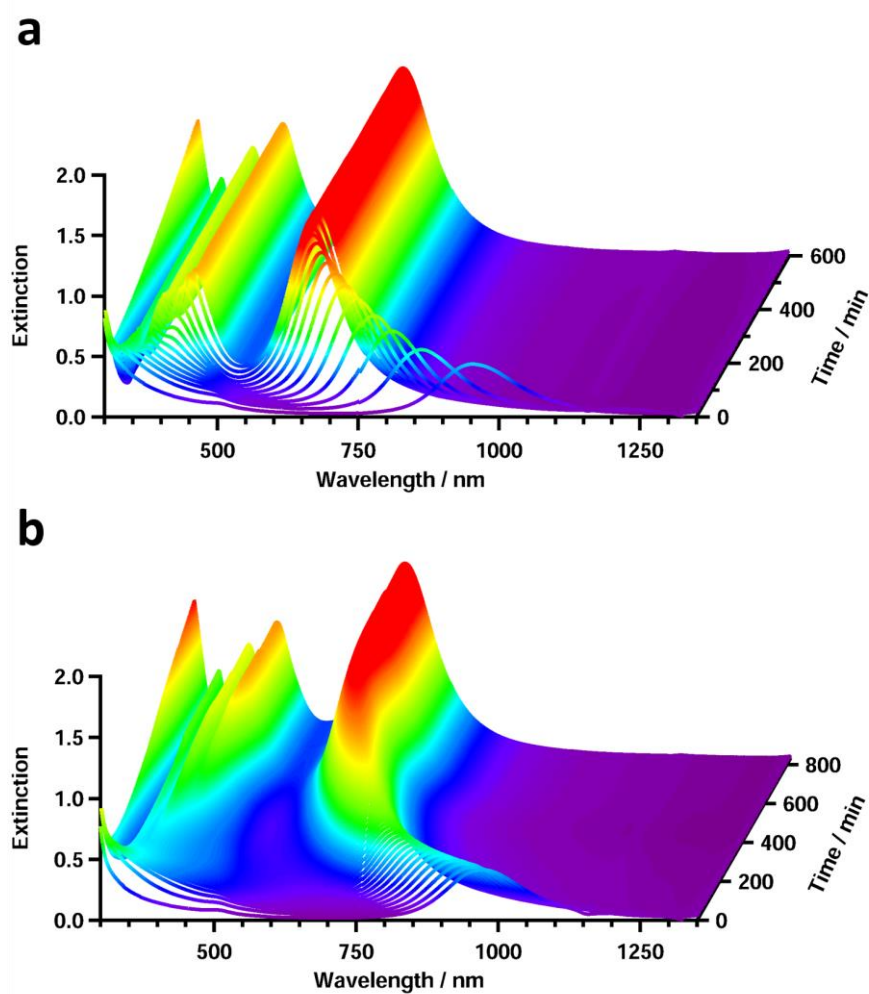


**Figure 4.S6.** Au@Ag cuboid growth in dynamic experiments: 3D representation of heat-maps (Figure 4a/b) of time-dependent UV/vis/NIR extinction spectra of synthesis performed with (a) CTAC and (b) BDAC at Ag to Au ratio of 8.

## Au@Ag Cuboid Growth Kinetics TEM Evaluation

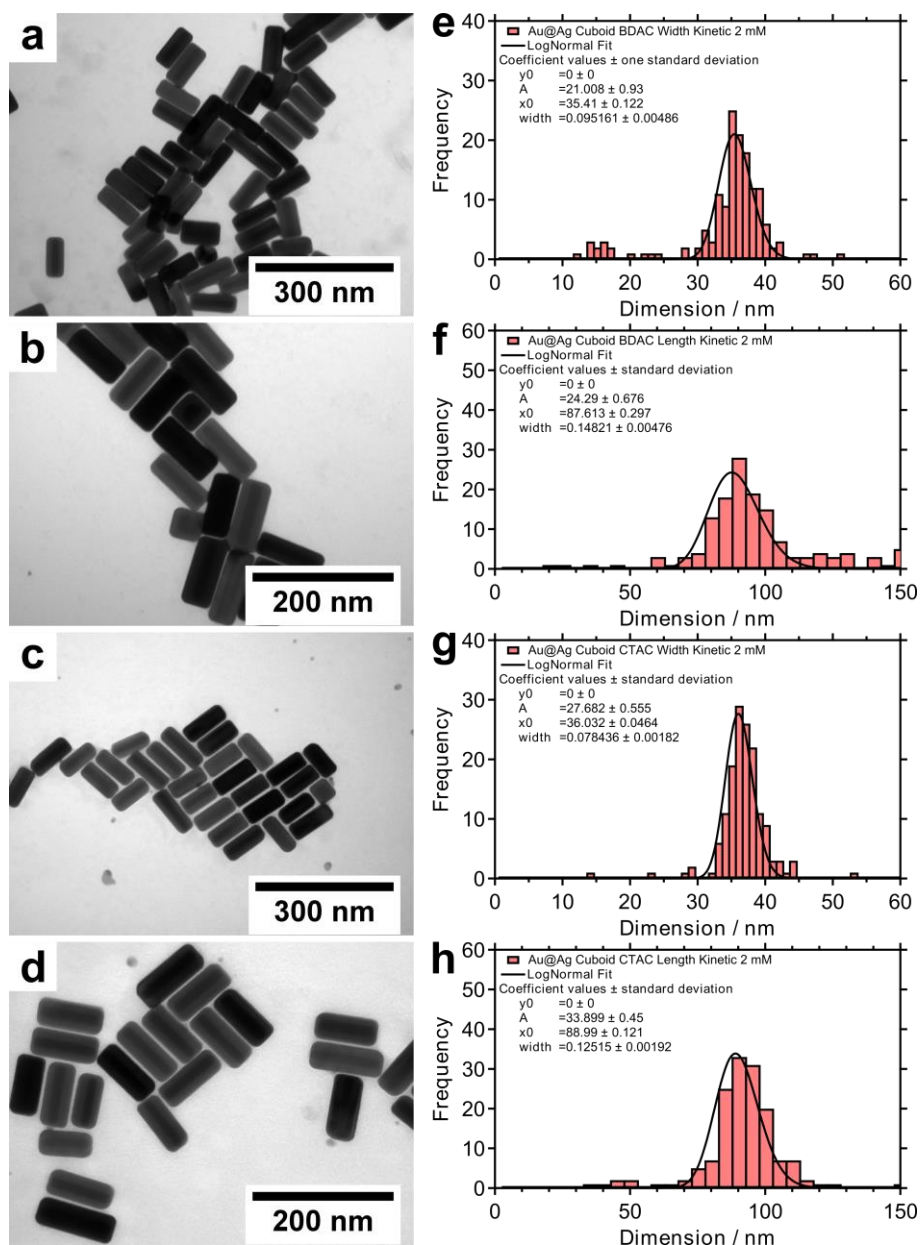


**Figure 4.S7.** TEM micrographs and histograms of as-prepared Au@Ag cuboid kinetic experiments. TEM images obtained for (a/b) BDAC and (c/d) CTAC. Histograms of the (e) width and (f) length of BDAC and for the (g) width and (h) length of CTAC obtained by measuring 150 nanoparticles.

## Modeling of Au@Ag Cuboid Growth Kinetics

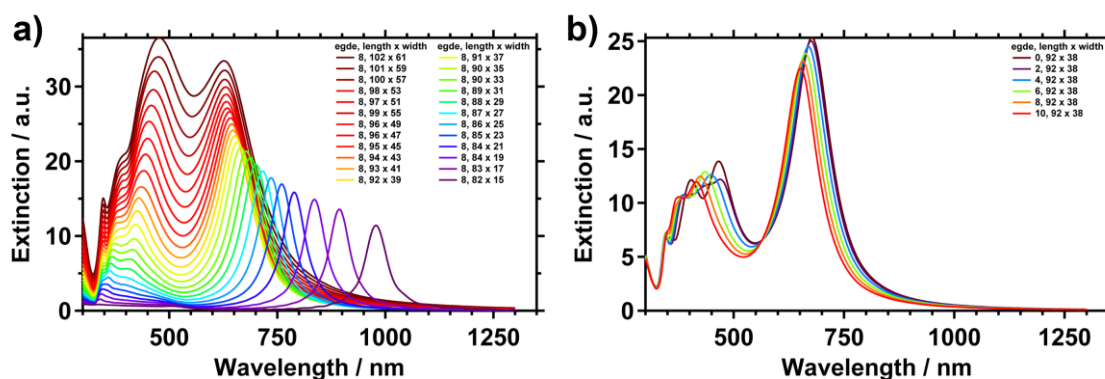


**Figure 4.S8.** (a) Extended plot of the FDTD modeling of Au@Ag cuboids performed including linear overgrowth up to 101 nm in length and 55 nm in width. (b) Modeled extinction spectra of cuboids with a fixed width and length (92 nm and 38 nm) and varied edge rounding values (0-10%).

**Table 4.S1.** FDTD simulation parameters as used for the kinetic plot in Figure 4.

Total length / nm	Total width / nm	Edge rounding / %
82	15	8
83	17	8
84	19	8
84	21	8
85	23	8
86	25	8
87	27	8
88	29	8
89	31	8
90	33	8
90	35	8
91	37	8
92	38	8
92	38	6
92	38	4
92	38	2
92	38	0

## Evaluation of Au@Ag Cuboid Growth Kinetics

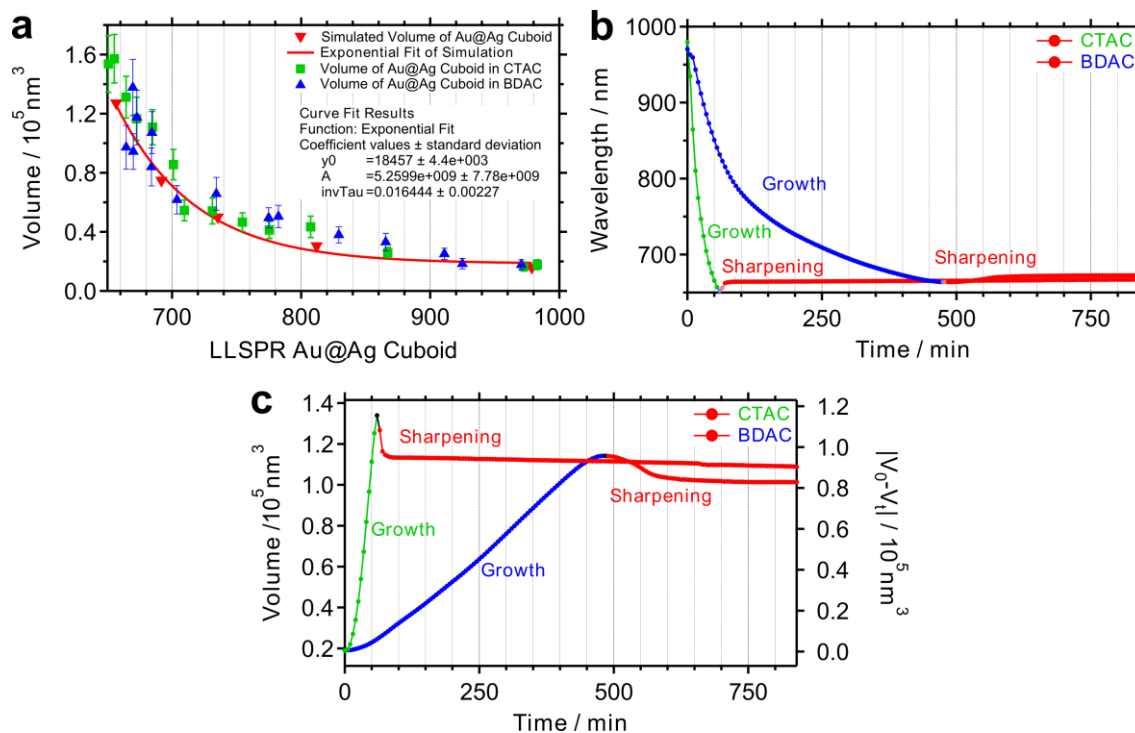


**Figure 4.S9.** Systematic evaluation of kinetic experiments based on results for static experiments. Experimentally determined (CTAC: green squares; BDAC: blue triangles) and modeled (red) Au@Ag cuboid volumes plotted versus their longitudinal resonance mode. (a) Modeled values were fitted with an exponential fit. (b) The longitudinal resonance mode of kinetic experiments performed with CTAC (green) and BDAC (blue) plotted versus reaction time. (c) Calculated volumes of kinetic experiments plotted versus time. Calculations were performed on the basis of the experimentally determined longitudinal resonance mode shift of the kinetic experiments and exponential fit of the modeled cuboid volumes. Please note that volumes determined on basis of spectral data after the maximum value of the longitudinal resonance mode are not representing real changes in volume but are caused by sharpening of Au@Ag cuboid edges.

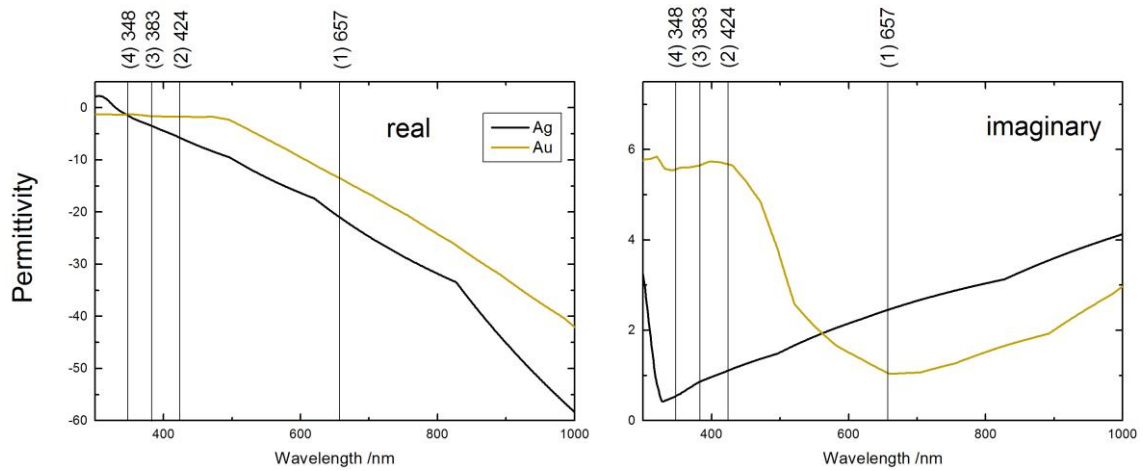


**Figure 4.S10.** Complex permittivity of silver (CRC) and gold (JC), which were used in the simulations. Labels (1-4) mark the wavelengths of the transversal and longitudinal modes.

#### **Text 4.S1. Mirror Charges at Au@Ag Gold-Core/Silver-Shell Nanoparticles**

We established a mirror charge model for Au@Ag gold-core/silver-shell cuboids based on the calculation of surface charge plots (normalized surface charge density,  $\rho_n = \text{Re}[\nabla \vec{E}]$ ). Figures S11-13 show the comparison of the plasmonic modes (gold nanorod, Au@Ag cuboid, and silver cuboid) with the help of the electric field intensity. As typically for a plasmonic resonance the field intensity is exponentially decaying into the dielectric environment. A significant lower intensity part decays into the metal core (receiver) and shows a resonance coupling with the shell (antenna). The Au@Ag cuboid shows the expected alteration of the plasmonic resonance in comparison to a silver cuboid, due to the refractive index change from silver to gold. In other words, the electric field of the Au@Ag cuboid mode (2) (dominant field at the edged/corner) is slightly modified due to the gold core (Figure S11). The electric field of the Au@Ag cuboid mode (3) (dominant field at the faces) is clearly modified due to the gold core (Figure S12). Mode (4), which shows a dominant field at the faces is also clearly modified due to the gold core and form a charge free area at the center (Figure S13).

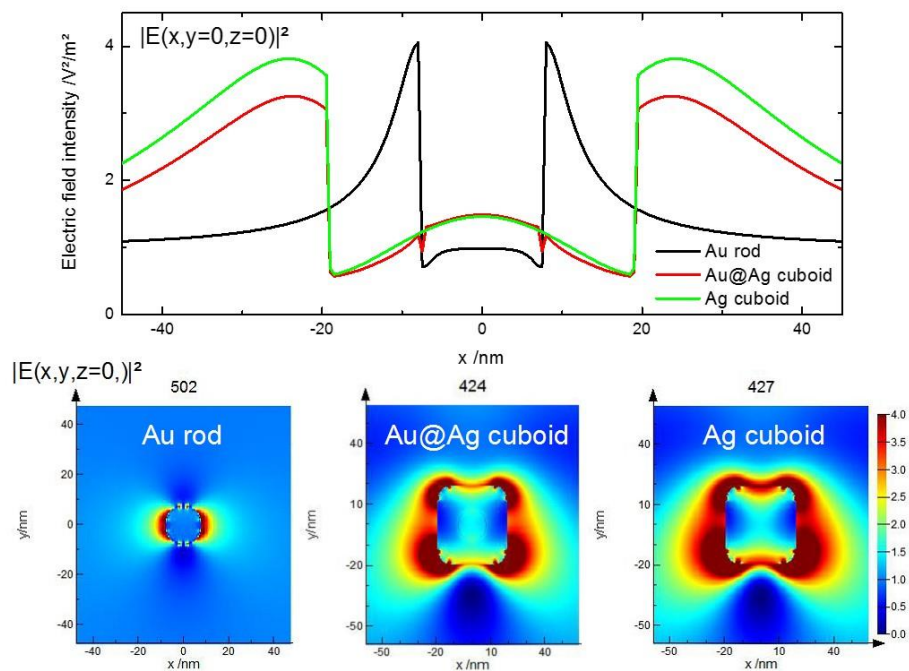


**Figure 4.S11.** Electric field intensity cross-section and plane-plot of the gold nanorod ( $R_0^T$ ), Au@Ag cuboid (2), and silver cuboid ( $C_0^T$ ) plasmonic mode at their specific resonance wavelengths. Plane-plots are imaged with identical scale bars.

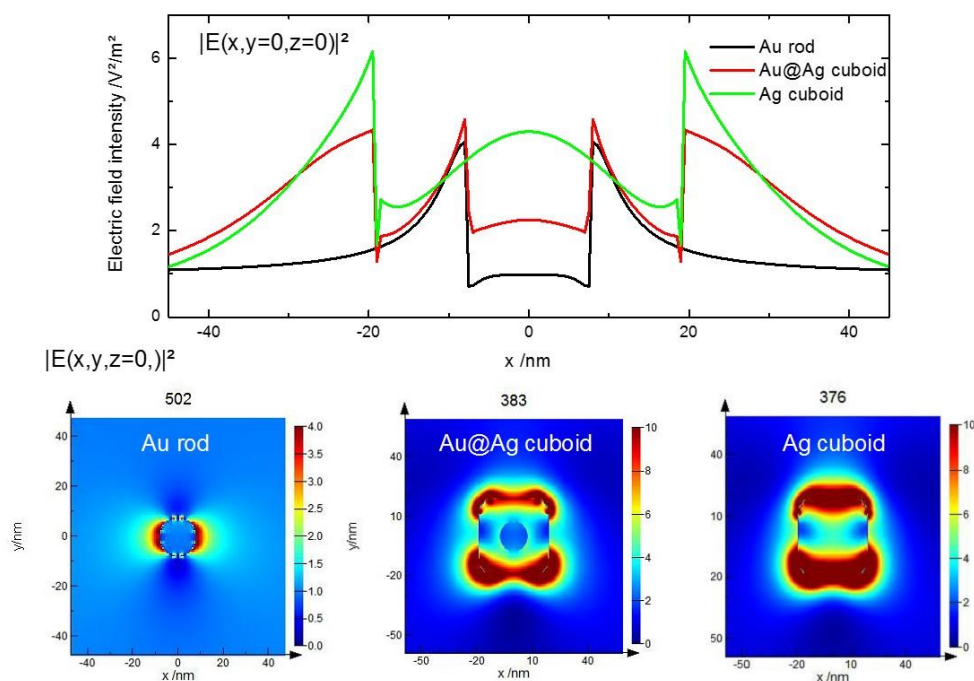


**Figure 4.S12.** Electric field intensity cross-section and plane-plot of the gold nanorod ( $R_0^T$ ), Au@Ag cuboid (3), and silver cuboid ( $C_1^T$ ) plasmonic mode at their specific resonance wavelengths. Plane-plots are imaged with identical scale bars.

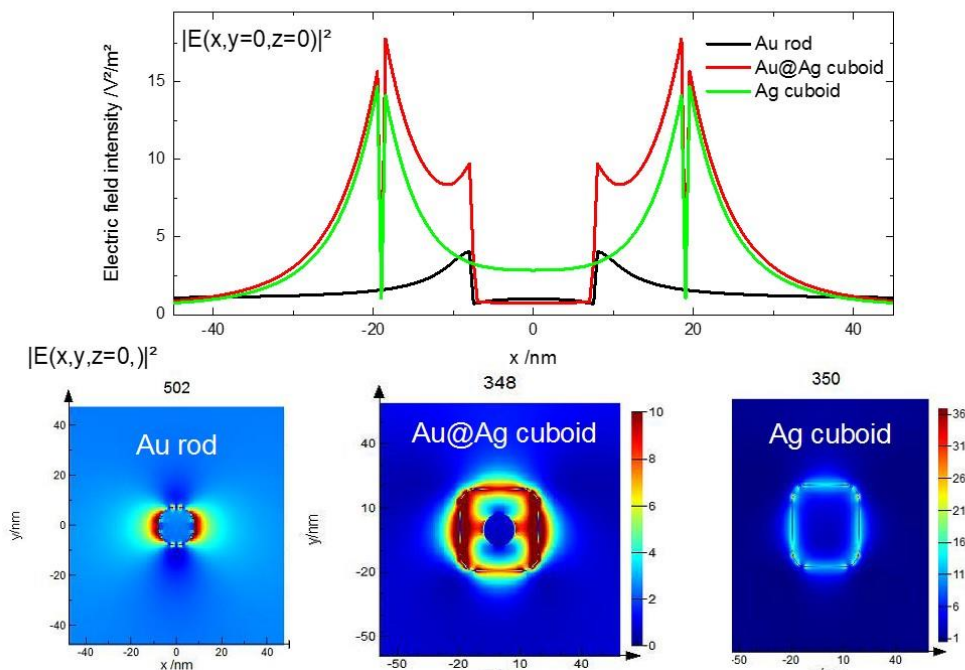


**Figure 4.S13.** Electric field intensity cross-section and plane-plot of the gold nanorod ( $R_0^T$ ), Au@Ag cuboid (4), and silver cuboid ( $C_2^T$ ) plasmonic mode at their specific resonance wavelengths. Plane-plots are imaged with identical scale bars.

**Table 4.S2.** Silver overgrowth synthesis parameters: Concentrations as used for static silver overgrowth experiments for both surfactants, BDAC and CTAC (10 mM) and at 60 °C. Parameters of synthesis #14 were also used for kinetic experiments.

<b>Experiment</b>	<b>Au / mM</b>	<b>AgNO<sub>3</sub> / mM</b>	<b>AA / mM</b>	<b>Ag/Au ratio</b>
<b>1</b>	0.25	0.05	0.2	<b>0.2</b>
<b>2</b>	0.25	0.1	0.4	<b>0.4</b>
<b>3</b>	0.25	0.2	0.8	<b>0.8</b>
<b>4</b>	0.25	0.3	1.2	<b>1.2</b>
<b>5</b>	0.25	0.4	1.6	<b>1.6</b>
<b>6</b>	0.25	0.5	2.0	<b>2.0</b>
<b>7</b>	0.25	0.6	2.4	<b>2.4</b>
<b>8</b>	0.25	0.8	3.2	<b>3.2</b>
<b>9</b>	0.25	1.0	4.0	<b>4.0</b>
<b>10</b>	0.25	1.2	5.0	<b>5.0</b>
<b>11</b>	0.25	1.4	5.6	<b>5.6</b>
<b>12</b>	0.25	1.6	6.4	<b>6.4</b>
<b>13</b>	0.25	1.8	7.2	<b>7.2</b>
<b>14</b>	<b>0.25</b>	<b>2.0</b>	<b>8.0</b>	<b>8.0</b>

## References

- (1) Liu, N.; Hentschel, M.; Weiss, T.; Alivisatos, A. P.; Giessen, H., Three-Dimensional Plasmon Rulers. *Science* **2011**, *332*, 1407-1410.
- (2) Liu, N.; Weiss, T.; Mesch, M.; Langguth, L.; Eigenthaler, U.; Hirscher, M.; Sönnichsen, C.; Giessen, H., Planar Metamaterial Analogue of Electromagnetically Induced Transparency for Plasmonic Sensing. *Nano Lett* **2009**, *10*, 1103-1107.
- (3) Hao, F.; Nordlander, P.; Sonnefraud, Y.; Dorpe, P. V.; Maier, S. A., Tunability of Subradiant Dipolar and Fano-Type Plasmon Resonances in Metallic Ring/Disk Cavities: Implications for Nanoscale Optical Sensing. *ACS Nano* **2009**, *3*, 643-652.
- (4) Anker, J. N.; Hall, W. P.; Lyandres, O.; Shah, N. C.; Zhao, J.; Van Duyne, R. P., Biosensing with plasmonic nanosensors. *Nat Mater* **2008**, *7*, 442-453.
- (5) Oulton, R. F.; Sorger, V. J.; Zentgraf, T.; Ma, R.-M.; Gladden, C.; Dai, L.; Bartal, G.; Zhang, X., Plasmon lasers at deep subwavelength scale. *Nature* **2009**, *461*, 629-632.
- (6) Pacifici, D.; Lezec, H. J.; Atwater, H. A., All-optical modulation by plasmonic excitation of CdSe quantum dots. *Nat Photonics* **2007**, *1*, 402-406.
- (7) Linic, S.; Christopher, P.; Ingram, D. B., Plasmonic-metal nanostructures for efficient conversion of solar to chemical energy. *Nat Mater* **2011**, *10*, 911-921.
- (8) Karg, M.; König, T. A. F.; Retsch, M.; Stelling, C.; Reichstein, P. M.; Honold, T.; Thelakkat, M.; Fery, A., Colloidal self-assembly concepts for light management in photovoltaics. *Mater Today* **2015**, *18*, 185-205.
- (9) Cai, W.; Shalaev, V., *Optical Metamaterials: Fundamentals and Applications*. Springer Science + Business Media: United States of America, New York, 2010; p 200.

- (10) Rockstuhl, C.; Lederer, F.; Etrich, C.; Zentgraf, T.; Kuhl, J.; Giessen, H., On the reinterpretation of resonances in split-ring-resonators at normal incidence. *Opt Express* **2006**, *14*, 8827-8836.
- (11) Shelby, R. A.; Smith, D. R.; Schultz, S., Experimental Verification of a Negative Index of Refraction. *Science* **2001**, *292*, 77-79.
- (12) Soukoulis, C. M.; Wegener, M., Past achievements and future challenges in the development of three-dimensional photonic metamaterials. *Nat Photonics* **2011**, *5*, 523-530.
- (13) Hanske, C.; Tebbe, M.; Kuttner, C.; Bieber, V.; Tsukruk, V. V.; Chanana, M.; König, T. A. F.; Fery, A., Strongly Coupled Plasmonic Modes on Macroscopic Areas via Template-Assisted Colloidal Self-Assembly. *Nano Lett* **2014**, *14*, 6863-6871.
- (14) Kraus, T.; Brodoceanu, D.; Pazos-Perez, N.; Fery, A., Colloidal Surface Assemblies: Nanotechnology Meets Bioinspiration. *Adv Funct Mater* **2013**, *23*, 4529-4541.
- (15) Nordlander, P., The Ring: A Leitmotif in Plasmonics. *ACS Nano* **2009**, *3*, 488-492.
- (16) Wang, H.; O'Dea, K.; Wang, L., Selective absorption of visible light in film-coupled nanoparticles by exciting magnetic resonance. *Opt Lett* **2014**, *39*, 1457-1460.
- (17) Dolling, G.; Enkrich, C.; Wegener, M.; Zhou, J. F.; Soukoulis, C. M.; Linden, S., Cut-wire pairs and plate pairs as magnetic atoms for optical metamaterials. *Opt Lett* **2005**, *30*, 3198-3200.
- (18) Kuznetsov, A. I.; Miroshnichenko, A. E.; Fu, Y. H.; Zhang, J.; Luk'yanchuk, B., Magnetic light. *Sci Rep* **2012**, *2*:492, 1-6.
- (19) Wang, H.; Brandl, D. W.; Le, F.; Nordlander, P.; Halas, N. J., Nanorice: A Hybrid Plasmonic Nanostructure. *Nano Lett* **2006**, *6*, 827-832.

- (20) Prodan, E.; Radloff, C.; Halas, N. J.; Nordlander, P., A Hybridization Model for the Plasmon Response of Complex Nanostructures. *Science* **2003**, *302*, 419-422.
- (21) Chen, H.; Shao, L.; Li, Q.; Wang, J., Gold nanorods and their plasmonic properties. *Chem Soc Rev* **2013**, *42*, 2679-2724.
- (22) Gómez-Graña, S.; Goris, B.; Altantzis, T.; Fernández-López, C.; Carbó-Argibay, E.; Guerrero-Martínez, A.; Almora-Barrios, N.; López, N.; Pastoriza-Santos, I.; Pérez-Juste, J.; Bals, S.; Van Tendeloo, G.; Liz-Marzán, L. M., Au@Ag Nanoparticles: Halides Stabilize {100} Facets. *J Phys Chem Lett* **2013**, *4*, 2209-2216.
- (23) Hou, S.; Hu, X.; Wen, T.; Liu, W.; Wu, X., Core–Shell Noble Metal Nanostructures Templated by Gold Nanorods. *Adv Mater* **2013**, *25*, 3857-3862.
- (24) Lohse, S. E.; Burrows, N. D.; Scarabelli, L.; Liz-Marzán, L. M.; Murphy, C. J., Anisotropic Noble Metal Nanocrystal Growth: The Role of Halides. *Chem Mater* **2013**, *26*, 34-43.
- (25) Hao, J.; Qingfeng, Z.; Nicolas, L.; Chunmei, Y.; Douglas, A. B.; Peter, N.; Hui, W., Tunable Plasmonic Nanoparticles with Catalytically Active High-Index Facets. *Nano Lett* **2014**, *14*, 3674-3682.
- (26) Park, K.; Drummy, L. F.; Vaia, R. A., Ag shell morphology on Au nanorod core: role of Ag precursor complex. *J Mater Chem* **2011**, *21*, 15608-15618.
- (27) Xia, Y.; Xiong, Y.; Lim, B.; Skrabalak, S. E., Shape-Controlled Synthesis of Metal Nanocrystals: Simple Chemistry Meets Complex Physics? *Angew Chem, Int Ed* **2009**, *48*, 60-103.
- (28) Nikoobakht, B.; El-Sayed, M. A., Preparation and growth mechanism of gold nanorods (NRs) using seed-mediated growth method. *Chem Mater* **2003**, *15*, 1957-1962.
- (29) Jana, N. R.; Gearheart, L.; Murphy, C. J., Seed-Mediated Growth Approach for Shape-Controlled Synthesis of Spheroidal and Rod-like Gold Nanoparticles Using a Surfactant Template. *Adv Mater* **2001**, *13*, 1389-1393.

- (30) Vigderman, L.; Zubarev, E. R., High-Yield Synthesis of Gold Nanorods with Longitudinal SPR Peak Greater than 1200 nm Using Hydroquinone as a Reducing Agent. *Chem Mater* **2013**, *25*, 1450-1457.
- (31) Vigderman, L.; P. Khanal, B.; R. Zubarev, E., Functional gold nanorods: synthesis, self-assembly, and sensing applications. *Adv Mater* **2012**, *24*, 4811-4841.
- (32) Grzelczak, M.; Perez-Juste, J.; Mulvaney, P.; Liz-Marzan, L. M., Shape control in gold nanoparticle synthesis. *Chem Soc Rev* **2008**, *37*, 1783-1791.
- (33) Müller, M. B.; Kuttner, C.; König, T. A. F.; Tsukruk, V. V.; Förster, S.; Karg, M.; Fery, A., Plasmonic Library Based on Substrate-Supported Gradiational Plasmonic Arrays. *ACS Nano* **2014**, *8*, 9410-9421.
- (34) Ye, X.; Jin, L.; Caglayan, H.; Chen, J.; Xing, G.; Zheng, C.; Doan-Nguyen, V.; Kang, Y.; Engheta, N.; R. Kagan, C.; B. Murray, C., Improved size-tunable synthesis of monodisperse gold nanorods through the use of aromatic additives. *ACS Nano* **2012**, *6*, 2804-2817.
- (35) Scarabelli, L.; Grzelczak, M.; Liz-Marzán, L., M., Tuning Gold Nanorod Synthesis through Prereduction with Salicylic Acid. *Chem Mater* **2013**, *25*, 4232-4238.
- (36) Khlebtsov, B. N.; Khanadeev, V. A.; Ye, J.; Sukhorukov, G. B.; Khlebtsov, N. G., Overgrowth of Gold Nanorods by Using a Binary Surfactant Mixture. *Langmuir* **2014**, *30*, 1696-1703.
- (37) Ye, X.; Zheng, C.; Chen, J.; Gao, Y.; Murray, C. B., Using Binary Surfactant Mixtures To Simultaneously Improve the Dimensional Tunability and Monodispersity in the Seeded Growth of Gold Nanorods. *Nano Lett* **2013**, *13*, 765-771.
- (38) DuChene, J. S.; Niu, W.; Abendroth, J. M.; Sun, Q.; Zhao, W.; Huo, F.; Wei, W. D., Halide Anions as Shape-Directing Agents for Obtaining High-Quality Anisotropic Gold Nanostructures. *Chem Mater* **2012**, *25*, 1392-1399.

- (39) Grzelczak, M.; Sánchez-Iglesias, A.; Rodríguez-González, B.; Alvarez-Puebla, R.; Pérez-Juste, J.; Liz-Marzán, L. M., Influence of Iodide Ions on the Growth of Gold Nanorods: Tuning Tip Curvature and Surface Plasmon Resonance. *Adv Funct Mater* **2008**, *18*, 3780-3786.
- (40) Millstone, J. E.; Wei, W.; Jones, M. R.; Yoo, H.; Mirkin, C. A., Iodide Ions Control Seed-Mediated Growth of Anisotropic Gold Nanoparticles. *Nano Lett* **2008**, *8*, 2526-2529.
- (41) Almora-Barrios, N.; Novell-Leruth, G.; Whiting, P.; Liz-Marzán, L. M.; López, N., Theoretical Description of the Role of Halides, Silver, and Surfactants on the Structure of Gold Nanorods. *Nano Lett* **2014**, *14*, 871-875.
- (42) Si, S.; Leduc, C.; Delville, M.-H.; Lounis, B., Short Gold Nanorod Growth Revisited: The Critical Role of the Bromide Counterion. *ChemPhysChem* **2012**, *13*, 193-202.
- (43) Xu, D.; Jianfeng, Z.; Xiaoyun, L.; Danli, L.; Liusheng, Z., Preparation of monodisperse bimetallic nanorods with gold nanorod core and silver shell and their plasmonic property and SERS efficiency. *J Raman Spectrosc* **2014**, *45*, 431-437.
- (44) Gómez-Graña, S.; Pérez-Juste, J.; Alvarez-Puebla, R. A.; Guerrero-Martínez, A.; Liz-Marzán, L. M., Self-Assembly of Au@Ag Nanorods Mediated by Gemini Surfactants for Highly Efficient SERS-Active Supercrystals. *Adv Opt Mater* **2013**, *1*, 477-481.
- (45) Jiang, R.; Chen, H.; Shao, L.; Li, Q.; Wang, J., Unraveling the Evolution and Nature of the Plasmons in (Au Core)-(Ag Shell) Nanorods. *Adv Mater* **2012**, *24*, 200-207.
- (46) Gong, J.; Zhou, F.; Li, Z.; Tang, Z., Synthesis of Au@Ag Core-Shell Nanocubes Containing Varying Shaped Cores and Their Localized Surface Plasmon Resonances. *Langmuir* **2012**, *28*, 8959-8964.
- (47) Yoshifumi, O.; Koji, N.; Ayaka, K.; Naotoshi, N.; Ayumu, I.; Yasuro, N., Uniform and controllable preparation of Au-Ag core-shell nanorods using anisotropic silver shell formation on gold nanorods. *Nanoscale* **2010**, *2*, 1489-1493.

- (48) Goris, B.; De Backer, A.; Van Aert, S.; Gómez-Graña, S.; Liz-Marzán, L. M.; Van Tendeloo, G.; Bals, S., Three-Dimensional Elemental Mapping at the Atomic Scale in Bimetallic Nanocrystals. *Nano Lett* **2013**, *13*, 4236-4241.
- (49) Carbó-Argibay, E.; Rodríguez-González, B.; Gómez-Graña, S.; Guerrero-Martínez, A.; Pastoriza-Santos, I.; Pérez-Juste, J.; Liz-Marzán, L. M., The Crystalline Structure of Gold Nanorods Revisited: Evidence for Higher-Index Lateral Facets. *Angew Chem, Int Ed* **2010**, *49*, 9397-9400.
- (50) Kou, X.; Zhang, S.; Tsung, C.-K.; Yang, Z.; Yeung, M. H.; Stucky, G. D.; Sun, L.; Wang, J.; Yan, C., One-Step Synthesis of Large-Aspect-Ratio Single-Crystalline Gold Nanorods by Using CTPAB and CTBAB Surfactants. *Chem - Eur J* **2007**, *13*, 2929-2936.
- (51) Gómez-Graña, S.; Hubert, F.; Testard, F.; Guerrero-Martínez, A.; Grillo, I.; Liz-Marzán, L. M.; Spalla, O., Surfactant (Bi)Layers on Gold Nanorods. *Langmuir* **2011**, *28*, 1453-1459.
- (52) Nikoobakht, B.; El-Sayed, M. A., Evidence for Bilayer Assembly of Cationic Surfactants on the Surface of Gold Nanorods. *Langmuir* **2001**, *17*, 6368-6374.
- (53) Murphy, C. J.; Thompson, L. B.; Alkilany, A. M.; Sisco, P. N.; Boulos, S. P.; Sivapalan, S. T.; Yang, J. A.; Chernak, D. J.; Huang, J., The Many Faces of Gold Nanorods. *J Phys Chem Lett* **2010**, *1*, 2867-2875.
- (54) Lohse, S. E.; Murphy, C. J., The Quest for Shape Control: A History of Gold Nanorod Synthesis. *Chem Mater* **2013**, *25*, 1250-1261.
- (55) Zhang, L.; Xia, K.; Lu, Z.; Li, G.; Chen, J.; Deng, Y.; Li, S.; Zhou, F.; He, N., Efficient and facile synthesis of gold nanorods with finely tunable plasmonic peaks from visible to near-IR range. *Chem Mater* **2014**, *26*, 1794-1798.
- (56) Sinnokrot, M. O.; Sherrill, C. D., High-Accuracy Quantum Mechanical Studies of  $\pi$ - $\pi$  Interactions in Benzene Dimers. *J Phys Chem A* **2006**, *110*, 10656-10668.
- (57) Sinnokrot, M. O.; Sherrill, C. D., Unexpected Substituent Effects in Face-to-Face  $\pi$ -Stacking Interactions. *J Phys Chem A* **2003**, *107*, 8377-8379.

- (58) Alargova, R. G.; Kochijashky, I. I.; Zana, R., Fluorescence Study of the Aggregation Behavior of Different Surfactants in Aqueous Solutions in the Presence and in the Absence of Gas. *Langmuir* **1998**, *14*, 1575-1579.
- (59) Park, K.; Koerner, H.; Vaia, R. A., Depletion-Induced Shape and Size Selection of Gold Nanoparticles. *Nano Lett* **2010**, *10*, 1433-1439.
- (60) Pérez-Juste, J.; Liz-Marzán, L. M.; Carnie, S.; Chan, D. Y. C.; Mulvaney, P., Electric-Field-Directed Growth of Gold Nanorods in Aqueous Surfactant Solutions. *Adv Funct Mater* **2004**, *14*, 571-579.
- (61) Henkel, A.; Schubert, O.; Plech, A.; Sonnichsen, C., Growth Kinetic of a Rod-Shaped Metal Nanocrystal. *J Phys Chem C* **2009**, *113*, 10390-10394.
- (62) Zijlstra, P.; Bullen, C.; Chon, J. W. M.; Gu, M., High-temperature seedless synthesis of gold nanorods. *J Phys Chem B* **2006**, *110*, 19315-19318.
- (63) Gulati, A.; Liao, H.; Hafner, J. H., Monitoring gold nanorod synthesis by localized surface plasmon resonance. *J Phys Chem B* **2006**, *110*, 22323-22327.
- (64) Novo, C.; Funston, A. M.; Mulvaney, P., Direct observation of chemical reactions on single gold nanocrystals using surface plasmon spectroscopy. *Nat Nanotechnol* **2008**, *3*, 598-602.
- (65) Becker, J.; Zins, I.; Jakab, A.; Khalavka, Y.; Schubert, O.; Sönnichsen, C., Plasmonic Focusing Reduces Ensemble Linewidth of Silver-Coated Gold Nanorods. *Nano Lett* **2008**, *8*, 1719-1723.
- (66) Becker, J.; Schubert, O.; Sönnichsen, C., Gold Nanoparticle Growth Monitored in situ Using a Novel Fast Optical Single-Particle Spectroscopy Method. *Nano Lett* **2007**, *7*, 1664-1669.
- (67) Sau, T. K.; Murphy, C. J., Seeded High Yield Synthesis of Short Au Nanorods in Aqueous Solution. *Langmuir* **2004**, *20*, 6414-6420.
- (68) Herrmann, L. O.; Baumberg, J. J., Watching Single Nanoparticles Grow in Real Time through Supercontinuum Spectroscopy. *Small* **2013**, *9*, 3743-3747.

- (69) Morita, T.; Tanaka, E.; Inagaki, Y.; Hotta, H.; Shingai, R.; Hatakeyama, Y.; Nishikawa, K.; Murai, H.; Nakano, H.; Hino, K., Aspect-Ratio Dependence on Formation Process of Gold Nanorods Studied by Time-Resolved Distance Distribution Functions. *J Phys Chem C* **2010**, *114*, 3804-3810.
- (70) Edgar, J. A.; McDonagh, A. M.; Cortie, M. B., Formation of Gold Nanorods by a Stochastic “Popcorn” Mechanism. *ACS Nano* **2012**, *6*, 1116-1125.
- (71) Hubert, F.; Testard, F.; Thill, A.; Kong, Q.; Tache, O.; Spalla, O., Growth and Overgrowth of Concentrated Gold Nanorods: Time Resolved SAXS and XANES. *Cryst Growth Des* **2012**, *12*, 1548-1555.
- (72) Okuno, Y.; Nishioka, K.; Kiya, A.; Nakashima, N.; Ishibashi, A.; Niidome, Y., Uniform and controllable preparation of Au-Ag core-shell nanorods using anisotropic silver shell formation on gold nanorods. *Nanoscale* **2010**, *2*, 1489-1493.
- (73) Johnson, P. B.; Christy, R. W., Optical Constants of the Noble Metals. *Phys Rev B: Condens Matter Mater Phys* **1972**, *6*, 4370-4379.
- (74) Hagemann, H. J.; Gudat, W.; Kunz, C., Optical constants from the far infrared to the x-ray region: Mg, Al, Cu, Ag, Au, Bi, C, and A1203. *J Opt Soc Am A* **1975**, *65*, 742-744.
- (75) Goris, B.; Bals, S.; Van den Broek, W.; Carbó-Argibay, E.; Gómez-Graña, S.; Liz-Marzán, L. M.; Van Tendeloo, G., Atomic-scale determination of surface facets in gold nanorods. *Nat Mater* **2012**, *11*, 930-935.
- (76) Huang, C.-C.; Yang, Z.; Chang, H.-T., Synthesis of Dumbbell-Shaped Au–Ag Core–Shell Nanorods by Seed-Mediated Growth under Alkaline Conditions. *Langmuir* **2004**, *20*, 6089-6092.
- (77) Mushran, S. P.; Agrawal, M. C.; Mehrotra, R. M.; Sanehi, R., Kinetics and mechanism of reduction of silver (I) by ascorbic-acid. *J Chem Soc, Dalton Trans* **1974**, 1460-1462.
- (78) Gupta, M. K.; König, T.; Near, R.; Nepal, D.; Drummy, L. F.; Biswas, S.; Naik, S.; Vaia, R. A.; El-Sayed, M. A.; Tsukruk, V. V., Surface Assembly and Plasmonic

- Properties in Strongly Coupled Segmented Gold Nanorods. *Small* **2013**, *9*, 2979-2990.
- (79) Im, S. H.; Lee, Y. T.; Wiley, B.; Xia, Y., Large-Scale Synthesis of Silver Nanocubes: The Role of HCl in Promoting Cube Perfection and Monodispersity. *Angew Chem, Int Ed* **2005**, *44*, 2154-2157.
- (80) Kodyath, R.; Malak, S. T.; Combs, Z. A.; Koenig, T.; Mahmoud, M. A.; El-Sayed, M. A.; Tsukruk, V. V., Assemblies of silver nanocubes for highly sensitive SERS chemical vapor detection. *J Mater Chem A* **2013**, *1*, 2777-2788.
- (81) König, T.; Kodyath, R.; Combs, Z. A.; Mahmoud, M. A.; El-Sayed, M. A.; Tsukruk, V. V., Silver Nanocube Aggregates in Cylindrical Pores for Higher Refractive Index Plasmonic Sensing. *Part Part Syst Charact* **2014**, *31*, 274-283.
- (82) Aylward, G. H., Findlay, Tristan J. V., *Datensammlung Chemie in SI Einheiten*. Wiley-VCH: Germany, Weinheim, 1999; p.188.
- (83) Ma, J. C.; Dougherty, D. A., The Cation- $\pi$  Interaction. *Chem Rev* **1997**, *97*, 1303-1324.
- (84) Zhang, S.; Bao, K.; Halas, N. J.; Xu, H.; Nordlander, P., Substrate-Induced Fano Resonances of a Plasmonic Nanocube: A Route to Increased-Sensitivity Localized Surface Plasmon Resonance Sensors Revealed. *Nano Lett* **2011**, *11*, 1657-1663.
- (85) Raether, H., *Surface Plasmons on Smooth and Rough Surfaces and on Gratings*. Springer: Germany, Berlin, 1988; p 117.
- (86) Fan, J. A.; Wu, C.; Bao, K.; Bao, J.; Bardhan, R.; Halas, N. J.; Manoharan, V. N.; Nordlander, P.; Shvets, G.; Capasso, F., Self-Assembled Plasmonic Nanoparticle Clusters. *Science* **2010**, *328*, 1135-1138.



# 5

## Colloidally Stable and Surfactant-Free Protein-Coated Gold Nanorods in Biological Media

Moritz Tebbe, Christian Kuttner, Max Männel, Andreas Fery, and Munish Chanana

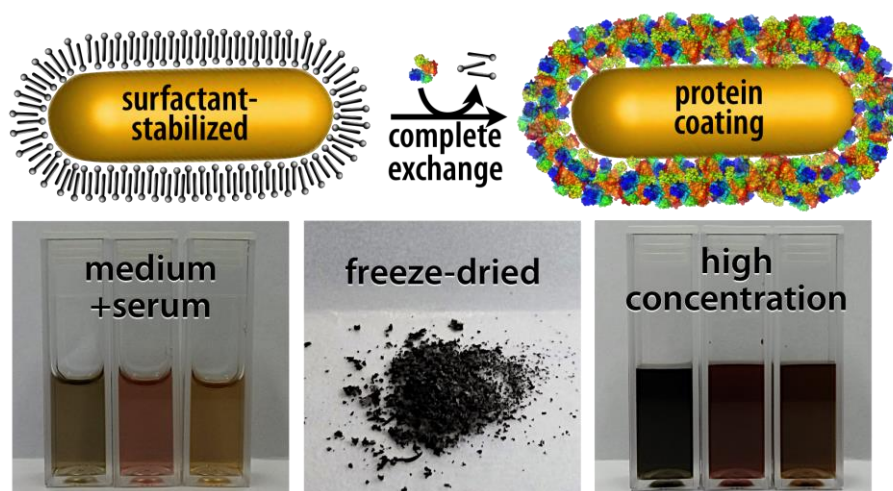


**Figure 5.1.** Figure of Table of Contents.

Published in **ACS Applied Materials & Interfaces**.

Reprinted with permission from Tebbe *et al.*, *ACS Appl Mater Interfaces* **2015**, *7*, 5984-5991. ©2015 American Chemical Society.



## Abstract

In this work, we investigate the ligand exchange of cetyltrimethylammonium bromide (CTAB) with bovine serum albumin for gold nanorods. We demonstrate by surface-enhanced Raman scattering measurements that CTAB, which is used as a shape-directing agent in the particle synthesis, is completely removed from solution and particle surface. Thus, the protein coated nanorods are suitable for bioapplications, where cationic surfactants must be avoided. At the same time, the colloidal stability of the system is significantly increased, as evidenced by spectroscopic investigation of the particle longitudinal surface plasmon resonance, which is sensitive to aggregation. Particles are stable at very high concentrations ( $C_{Au}$  20 mg/mL) in biological media such as phosphate buffer saline or Dulbecco's Modified Eagle's Medium and over a large pH range (2–12). Particles can even be freeze-dried (lyophilized) and redispersed. The protocol was applied to gold nanoparticles with a large range of aspect ratios and sizes with main absorption frequencies covering the visible and the near-IR spectral range from 600 to 1100 nm. Thus, these colloidally stable and surfactant-free protein-coated nanoparticles are of great interest for various plasmonic and biomedical applications.

## Keywords

ligand exchange, protein coating, colloidal stability, CTAB replacement, biocompatible, lyophilized

## Introduction

Gold nanorods (AuNRs) belong to a highly interesting class of nanosized objects used for a plethora of biomedical and biotechnological applications such as sensing,<sup>1</sup> imaging,<sup>2-4</sup> and others.<sup>5</sup> Their local surface plasmon resonances (LSPRs) strongly depend on their shape and dimensions (size, aspect ratio). Especially in the case of AuNRs with higher aspect ratios ( $AR > 4$ ), the longitudinal LSPR is located in the so-called “water transparency window” in the near-IR (NIR, 800–1300 nm), where absorption of biomatter is low, thus showing potential in a wide variety of biological applications (*e.g.*, biolabeling or hyperthermia). Along with some other additives, cetyltrimethylammonium bromide (CTAB) is the most widely used compound for the

precise synthesis of AuNRs with different lengths and aspect ratios. Even though such gold nanoparticles (AuNPs) exhibit optimal optical properties for biomedical applications, their application in biomedicine is restricted due to the presence of CTAB, which is cytotoxic above a concentration of 1–10  $\mu\text{M}$ .<sup>6</sup> In addition to this problem, CTAB-stabilized particles suffer from low colloidal stability in aqueous salt solutions, incompatibility with other solvents, and instability in long-term storage (which result in crystallization of CTAB and morphology loss upon reshaping).<sup>7</sup>

Many efforts have thus been made to replace CTAB in synthesis or to functionalize CTAB-coated AuNRs.<sup>8-14</sup> Various strategies have been developed to improve the stability and biocompatibility of AuNRs by using polymers,<sup>15-17</sup> peptides,<sup>18</sup> surfactants,<sup>19</sup> and lipids<sup>13,20,21</sup> to modify the NP surface. Most of these strategies use thiolated molecules or electrostatic interaction forces to bind to the gold surface. However, the majority of the applied coating materials are based on either simple surfactants, such as oleic acid or end-thiolated CTAB,<sup>14</sup> or on polymers, such as different polyelectrolytes,<sup>9</sup> PEG,<sup>22-25</sup> or polystyrene.<sup>26</sup> Also inorganic coatings such as silica shells have been used.<sup>22,27</sup> Current applications demand a combination of colloidal stability, biocompatibility, and access to further functionalization, and stimulus responsiveness. Even though many of the above-mentioned systems suffice some of these requirements, there is still a need for such multifunctional coatings.

In this context, proteins represent a promising class of multifunctional coating material.<sup>28-31</sup> Proteins offer a chemically well-defined structure with various chemical functionalities such as thiols, amines, and carboxylates that have high binding affinity toward metal surfaces.<sup>28,32</sup> Furthermore, they are high molecular-weight charged polymers, which provide electrosteric stabilization and pH-responsiveness to the particles.<sup>28-31</sup>

We recently reported on the protein coating of different spherical AuNPs with citrate and CTAB as stabilizing agents for their use as dual-responsive NPs. However, functionalization of nanorods with proteins is not straightforward, owing to destabilization and consequently strong irreversible aggregation of AuNRs during the functionalization process. In general, the functionalization of high aspect ratio NPs with polymers stays a challenge.<sup>1,33-35</sup> Because of the large side-to-tip area ratio and the large surface-to-volume ratio compared to spherical systems, functionalization of CTAB-stabilized AuNRs is more demanding.<sup>14</sup> CTAB binds relatively weakly on the tips of an AuNR and much stronger on the sides of the AuNR, since those expose

different crystallographic planes.<sup>36-38</sup> This fact, which is exploited in the synthesis for shape directing, is problematic within the exchange. The CTAB molecules on the tips are exchanged first, causing imbalance in the CTAB bilayer structure on the rod surface. Because of this two-step exchange process, bilayer structure breaks down and results in fast AuNR aggregation. Hence, it is important to exchange the whole CTAB bilayer at once, rather than in two steps, to overcome or avoid the aggregation process.<sup>1</sup>

Furthermore, considering the relevant bioapplications, CTAB must be removed completely both from the solution and particle surface. In our previous report, the question whether the negatively charged protein coating adsorbs on top of the positively charged CTAB bilayer *via* electrostatic interactions or replaces the CTAB molecules partially or completely remains unanswered.

Hence, in this work, we report on replacing CTAB completely from AuNRs of variable aspect ratios with bovine serum albumin (BSA) without affecting the colloidal stability of the AuNRs but rather enhancing it significantly. We show the complete removal of CTAB from the particle surface employing surface-enhanced Raman scattering (SERS) measurements. We analyze the impact of protein coating on colloidal stability using the characteristic spectroscopic features of the longitudinal localized surface plasmon resonance (L-LSPR), which is highly sensitive toward aggregation. Finally we investigate freeze-drying and redispersion properties of the BSA-coated AuNRs.

## Results and Discussion

**Figure 5.2** presents an overview of the spectroscopic properties and morphology of the nanorods synthesized in this study. The AuNRs were prepared following two synthetic approaches reported elsewhere.<sup>39-41</sup> Combining both synthesis methods allows for covering the visible and the NIR spectral range from 600 to 1100 nm with L-LSPR of the NRs (see **Figure 5.2a**).

For the coating of CTAB-stabilized AuNRs with BSA, we modified substantially our previously reported protein coating procedure for CTAB-stabilized gold nanospheres (AuNS).<sup>29</sup> Prior to the ligand exchange of AuNRs, the CTAB concentration of the dispersions was adjusted to 0.1 mM right before functionalization, which is by a factor of ten below the CMC of CTAB (1 mM). Please note, NP concentrations are kept the

same as in the original synthesis. The AuNRs are stable for short time at this CTAB concentration; therefore, it is crucial to adjust the CTAB concentration directly prior to exchange. The AuNR dispersions are added to a relatively highly concentrated protein solution (10 mg/mL) at pH 7 under vigorous stirring and sonication (BSA solution/NP dispersions, 3:1 v/v). The mixture was sonicated for another 30 min and then centrifuged. The supernatant was replaced by the same amount of a basic and less-concentrated protein solution (1 mg/mL, pH 12) and incubated for at least 24 h. Subsequently, the AuNR dispersions were washed with basic water (pH 11-12, at least three times) *via* centrifugation and concentrated to desired values.

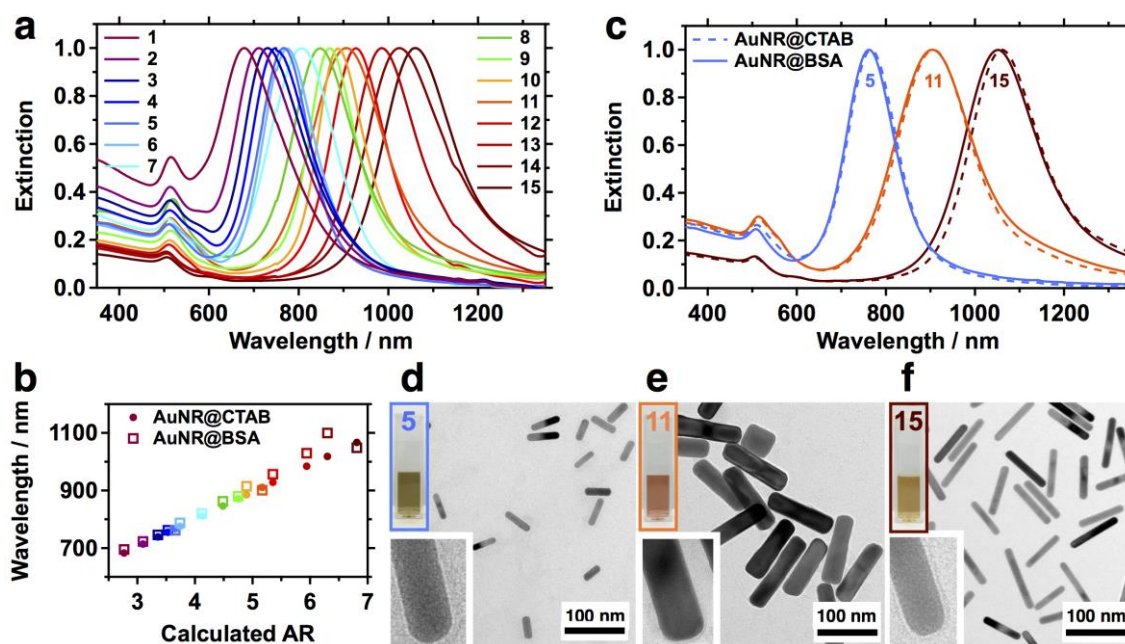


**Figure 5.2.** (a) UV-vis-NIR spectra of all AuNR@CTAB. (b) L-LSPRs of AuNR before and after BSA coating. (c) UV-vis-NIR spectra of three selected AuNR samples (Nos. 5, 11, and 15) before and after BSA coating. (d-f) TEM images of the AuNR@BSA from (c).

For a successful and aggregation-free BSA coating of AuNRs, CTAB must be replaced fast and completely from the surface. Hence, the ligand-exchange process on the surface must be fast and efficient. In the procedure presented here, this is presumably achieved by the interplay of intrinsic properties of the protein and the chosen experimental parameters. Hereby, three main aspects play an important role: First, the high BSA-to-CTAB ratio throughout the process results in a strong shift of equilibrium toward BSA-coated particles, which is in agreement with theory.<sup>42</sup> Second, BSA exhibits a higher binding affinity toward metal surfaces because BSA, as a protein, is a multivalent ligand compared to CTAB, which is a monovalent ligand. Third, the released CTAB (positively charged, hydrophobic tail) builds a complex with

the excess BSA (negatively charged, hydrophobic core) in the solution and is removed efficiently from the solution in the first centrifugation steps. Hence, by adjusting the CTAB concentration far below the CMC, using high BSA concentrations (10 mg/mL) and fast destabilization of CTAB bilayer by ultra-sonication in the presence of unbound BSA, a complete and aggregation-free BSA coating of AuNRs can be ensured. The colloidal stability after the different coating procedure steps was monitored *via* UV-vis-NIR spectroscopy. The functionalized nanorods were also characterized by transmission electron microscopy (TEM). **Figure 5.2b** shows the results for BSA-coating of all the different AuNR samples. For clarity, the extinction spectra (**Figure 5.2c**) and TEM images (**Figure 5.2d-f**) of three representative AuNR dispersions (**Figure 5.2d-f** insets) with increasing aspect ratios (ARs) are shown. By comparing the position of the L-LSPR (**Figure 5.2b**), the shape of the extinction spectra (**Figure 5.2c**), and the color of the dispersions (**Figure 5.2d-f** insets), the aggregation-free coating of the AuNRs with BSA can be confirmed. In the case of any aggregation, the LSPR peak of the plasmonic NPs would shift drastically toward higher wavelengths, and the whole LSPR band would broaden significantly along with a decrease in overall intensity.<sup>43</sup> The L-LSPR of the low AR AuNRs (**Figure 5.2b**, Nos. 1–7) exhibit a spectral shift of only few nanometers, attributed to the local refractive index changes in the vicinity of the gold surface. The LSPR band also does not change in shape, revealing no aggregation during the coating process. Thus, successful ligand exchange (coating) without aggregation of the AuNRs is demonstrated. In the case of the high AR AuNRs (**Figure 5.2b**, Nos. 8–15), the L-LSPR lies in the NIR range and is therefore more sensitive toward changes in refractive index.<sup>44-46</sup> Sample Nos. 12–14 exhibit a more pronounced red-shifted L-LSPR after BSA coating and purification, while sample Nos. 11 and 15 are slightly blue shifted. Changes in LSPR reflect changes in composition of AuNR ensembles. Consequently the purification of the AuNRs *via* centrifugation can have a huge impact on the final quality and therefore on the LSPR band of AuNRs ensembles. Harsh centrifugation can cause nanoparticle aggregation, which leads to a broadening and a red shift of the LSPR. At the same time gentle centrifugation can cause a narrowing of the dispersity and L-LSPR, owing to the size- and shape-dependent sedimentation coefficients of anisotropic NPs (centrifugation speeds can be found in Experimental Section). In our case aggregation of AuNRs can be excluded, since the shape and the overall peak width of the LSPR band is not changing significantly as it can be seen from **Figure 5.2c** and the full width half-

maximum (FWHM) values before and after functionalization (**Figure 5.S1** in the Supporting Information). The AuNR@BSA samples are remarkably stable over time (months), without any sign of aggregation (Supporting Information, **Figure 5.S3**).

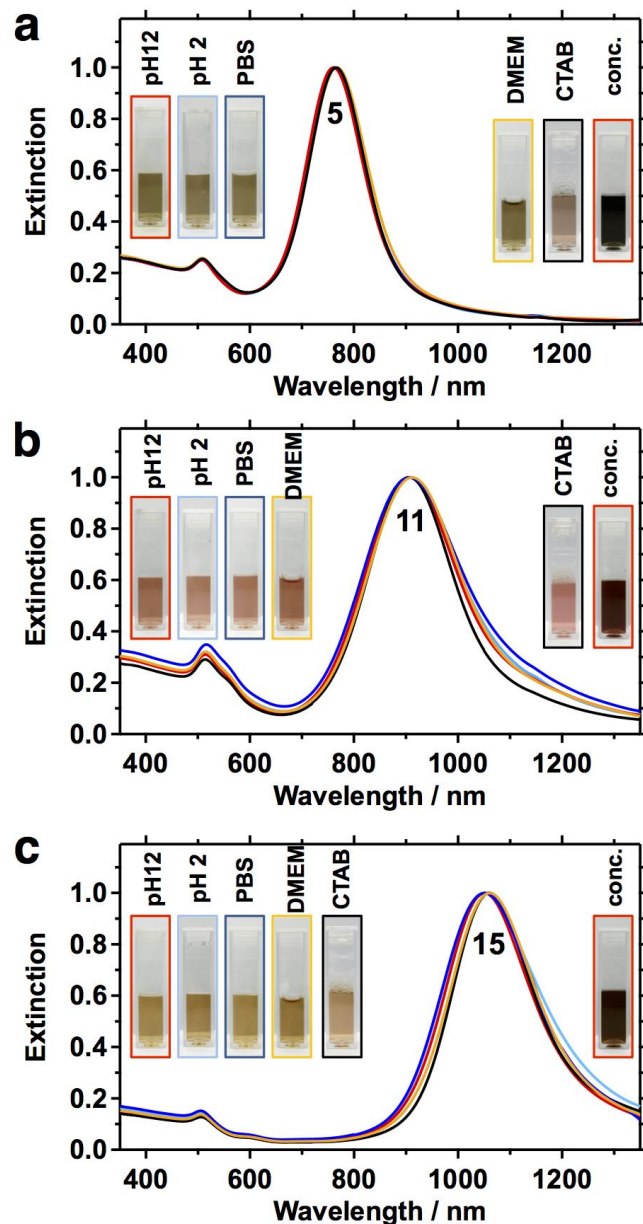


**Figure 5.3.** UV-vis-NIR spectra and photographs of three selected AuNRs, namely, (a) No. 5 at 760 nm, (b) No. 11 at 900 nm, and (c) No. 15 at 1050 nm dispersed in different media: AuNR@BSA samples ( $c_{\text{Au}} = 0.2 \text{ mM}$ ) were dissolved at different pH (12 and 2), in PBS buffer (150 mM, pH 7.5), in DMEM+10% NCS (pH 7.5), and highly concentrated (1 mM). AuNR@CTAB samples are included for comparison.

As mentioned in the Introduction, the prerequisite for any biomedical application of colloidal particles is their colloidal stability under physiological salt concentrations (equivalent to 150 mM NaCl) and in complex biofluids, which contain sugars and proteins. Hence, the colloidal stability of three selected AuNR samples (Nos. 5, 11, and

15) coated with BSA (**Figure 5.3a**) was investigated in aqueous solutions at different conditions, including phosphate-buffered saline (PBS) solutions and Dulbecco's Modified Eagle's Medium (DMEM) cell culture media with 10% newborn bovine calf serum (NCS). The colloidal stability of the AuNRs in medium was again monitored by UV-vis-NIR spectroscopy (**Figure 5.3**). Remarkably, the AuNR@BSA samples were highly stable in these media over time (Supporting Information, **Figure 5.S4**). Please note that such protein-coated NPs are even more stable in the presence of free protein in the solution.<sup>30</sup> The AuNR@BSA were also highly stable at pH values above, as well as below, the isoelectric point of BSA (pI<sub>BSA</sub> = 4.8).<sup>29</sup> They exhibited a negative surface charge ( $\zeta < -35$  mV) at pH 12 and a positive surface charge ( $\zeta > +20$  mV) at pH 1, consistent with the values reported for BSA-coated NPs previously.<sup>29</sup>

For dosage, storage, transportation, and material handling, a dry powder form is advantageous as compared to a solution. Particularly in biomedical applications, the dose of such nanoparticles must be precisely adjusted, which can be easily done by weighing the dry sample. Drying a nanomaterial to powder and redispersing it in desired media at desired concentrations, without inducing irreversible particle aggregation during the drying or redispersion process, is highly challenging. In our case, lyophilized powders of purified dispersions (free of unbound protein and other solutes) exhibited hydrophobic properties and did not redisperse in aqueous media (see Supporting Information, **Figure 5.S2**). The reason for this is that proteins pose intrinsically a demanding challenge to achieve successful lyophilization due to their denaturation during freeze-drying.<sup>47</sup> To avoid irreversible denaturation of proteins, hydrogen bond-forming stabilizers (lyoprotectors) such as sugars (sucrose, trehalose) or proteins such as albumins are employed. This also applies to the protein-coated nanoparticle systems. Thus, we freeze-dried our dispersions using different formulations and obtained dark brown lyophilized powders. In particular, we lyophilized purified NPs (washed 5×, pH 12), with and without lyoprotecting additives. We employed sucrose as a low-molecular-weight sugar-based additive and BSA itself as a high-molecular-weight protein-based additive. Furthermore, we also employed DMEM and DMEM containing 10% NCS as formulation media for the lyophilization. Depending on the formulation the AuNR@protein powders exhibited different solubility behavior upon redispersion in water, buffers, and medium.

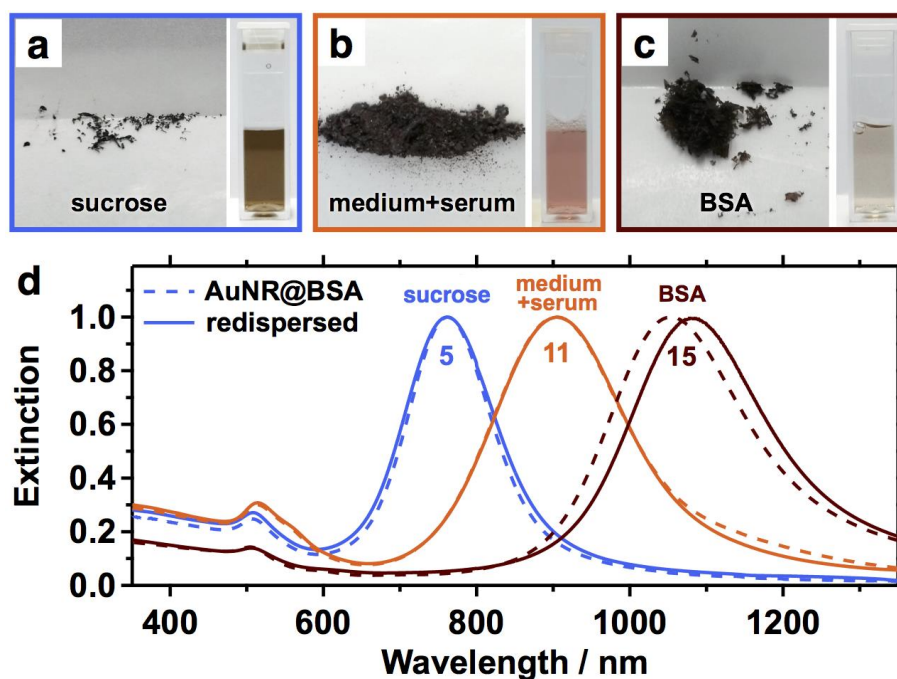


**Figure 5.4.** Redispersion behavior of different freeze-dried AuNR@BSA powders: (a) No. 5 with 1 mg/mL sucrose ( $c_{Au} = 0.34$  mM); (b) No. 11 from DMEM+10% NCS ( $c_{Au} = 0.12$  mM); and (c) No. 15 with 1 mg/mL BSA ( $c_{Au} = 0.16$  mM). All powders spontaneously redispersed in water at pH 12 (cuvettes). (d) UV-vis-NIR spectra of AuNR@ BSA samples before (dashed line) and after freeze-drying (full line).

Whereas the powders from the formulations that contained lyoprotectors redispersed readily in water (pH > 7) and buffers as well as cell culture media, the powders from the water formulation (pH 12), which contained no stabilizing additives, were not redispersible (see Supporting Information, **Figure 5.S2**). The powder from the water formulation remained as a clump at the air–water interface or rather stuck to the walls of the vial showing a hydrophobic character of the lyophilized protein coating. The powders containing lyoprotecting agents, on the other hand, exhibited remarkable redispersion behavior. Powders from the formulations containing sucrose (1 mg/mL) or BSA (1 mg/mL) both redispersed spontaneously in aqueous media. The redispersion behavior upon addition of Milli-Q water at pH 12 was documented in Videos V1 and V2, provided in the Supporting Information. These dispersions of the freeze-dried AuNR@BSA were also highly stable over time periods of weeks and months (Supporting Information, **Figure 5.S5**). Here, the dispersions were identical to the original AuNR@protein dispersions before lyophilization in terms of quality and colloidal stability (**Figure 5.4d**). The L-LSPR of the sucrose-lyoprotected sample matches perfectly before and after lyophilization. In

the case of the BSA-lyoprotected sample, there is a slight red shift after redispersion, which is presumably due to the incomplete redispersion of the dry AuNRs or changes in the local refractive index (changes in coating thickness or density). Furthermore, we lyophilized stable dispersions of AuNR@protein in pure DMEM and in DMEM containing 10% NCS. The powders were light brown in color, due to the high salt and high protein content. Both DMEM-based AuNR@BSA powders redispersed spontaneously upon addition of water (see Video V3 for redispersion behavior of DMEM+10% NCS). Although the pure DMEM dispersions of AuNR@protein were highly stable before lyophilization, the redispersed systems exhibited slight aggregation of the AuNRs. However, the DMEM formulation containing 10% NCS redispersed perfectly, and the AuNR@BSA samples showed the same quality and colloidal stability as before the lyophilization (see **Figure 5.4**). It is worth noting that such cell culture media-based dry formulations could directly be used in bioapplications simply by adding water to the readymade formulation.

Considering the growing interest in AuNRs for biomedical applications, it is highly important to remove CTAB (or CTAC) completely from the particle surface. By coating negatively charged proteins on surfactant-coated positively charged NPs, three possible scenarios can occur: (1) the proteins adsorb on top of the positively charged CTAB bilayer *via* electrostatic interactions and wrap the AuNR completely; (2) the protein replaces partially the CTAB molecules; and (3) the protein replaces all CTAB molecules completely from the AuNR surface. Hence, to answer the question whether CTAB is still present underneath or within the protein layer after functionalization we performed SERS. Analytical SERS allows for ultrasensitive detection of organic molecules in the vicinity of plasmonic nanostructures.<sup>48-52</sup> In analytical SERS the general notion dictates to aim for maximum enhancement factors by using excitation wavelengths matching the localized surface plasmon resonance of the applied NPs. Since the LSPR depends on particle size, shape, orientation, and aggregation, a broad assortment of excitation sources (lasers) would be required to flexibly adopt for the respective samples of interest.

**Figure 5.5** shows the SERS spectra of AuNR and AuNS with CTAB and BSA coating dispersed in water and compared with conventional Raman spectra of crystalline CTAB and dry solid BSA. In contrast to the reports in literature, where only selected signals (1070 and 1445  $\text{cm}^{-1}$ ) were used,<sup>53</sup> we evaluated an extended frequency regime to assert the complete replacement of CTAB by BSA. Furthermore, we decided

to include spherical NPs<sup>31</sup> in this SERS study providing further validation of the complete exchange of CTAB by BSA at the nanoparticle surface and answering the open question of the previous report.<sup>29</sup> Moreover, we show that also off-resonance measurements, using a standard HeNe laser at 633 nm, allow for the SERS characterization of the ligand shell of NPs. Off-resonance excitation inherently limits the local electromagnetic enhancement to surface-near distances. However, the loss in electromagnetic enhancement can be balanced by measuring at high NP concentrations (up to 20 mg/mL), which can be achieved with protein-coated NPs. At higher concentrations, the total number of scattering events is greatly increased. Additionally, measurements of dispersions take advantage of the continuous flow of NPs through the confocal excitation volume and therewith allow for efficient probing of the NP coating. The low-frequency domain (**Figure 5.5a**) is dominated by the halide counterion signal of surface-bound bromide ( $\text{AuBr}^-$ ) at  $176\text{ cm}^{-1}$ ,<sup>53</sup> indicating a surface-bound interlayer of halides between the cetylammmonium cation ( $\text{CTA}^+$ ) molecules and the NP gold surface. After BSA coating this signal completely vanished, as expected.

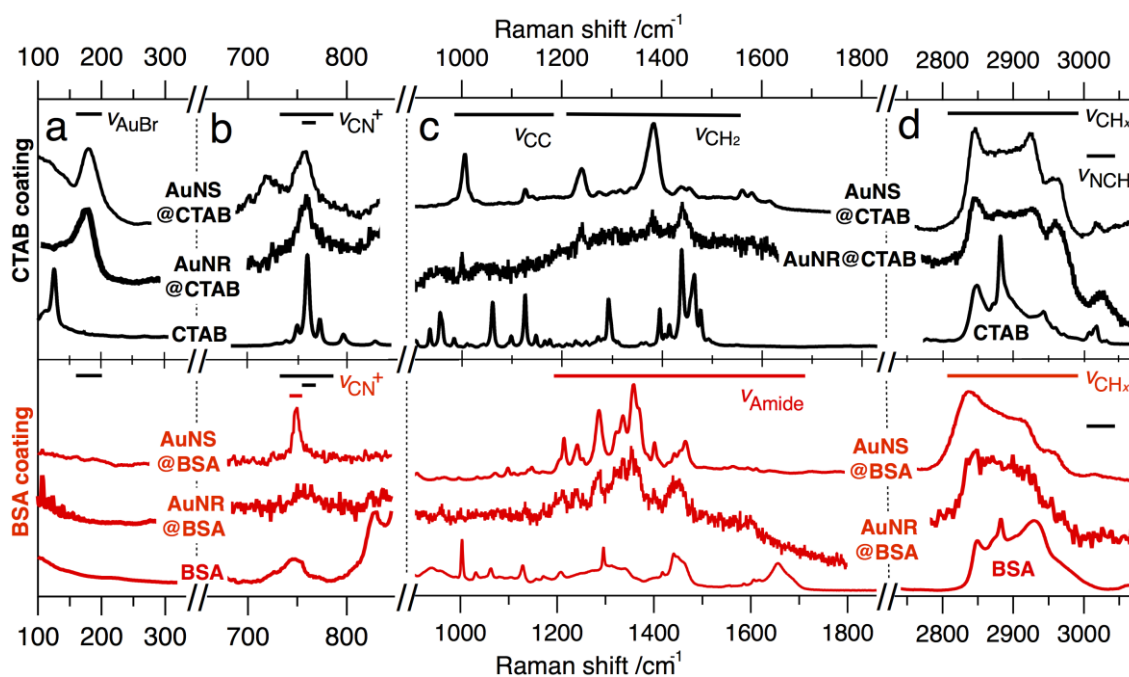


**Figure 5.5.** SERS of AuNPs (AuNS: spheres; AuNR: rods) with CTAB (black, upper) and BSA (red, lower) coating dispersed in water and compared with conventional Raman spectra of crystalline CTAB and dry BSA: (a) Counterion signals; (b) ammonium signals; (c) skeletal chain vibrations (upper) and amide bands (lower); (d) methyl/methylene “fingerprint”. The spectra are offset, scaled for clarity, and show raw data without background correction.

**Figure 5.5b** shows the frequency domain attributed to the CN<sup>+</sup> stretching of the trimethylammonium (TMA) headgroup. While crystalline CTAB features three distinct signals at 754, 763, and 774 cm<sup>-1</sup>,<sup>53</sup> the CTAB coatings only show the symmetric stretch at 763 cm<sup>-1</sup>.<sup>53,54</sup> For BSA-coated NPs this signal is lost, whereas another signal at 750 cm<sup>-1</sup> arises for the AuNS sample and solid BSA. This signal can be assigned to the aromatic amino acid tryptophan.<sup>55,56</sup> Even though this signal is not well-resolved for AuNR, it can be expected to differ from the distinct CN<sup>+</sup> vibration (TMA, 763 cm<sup>-1</sup>).

The mid-frequency domain (**Figure 5.5c**) of CTAB exhibits a couple of signals characteristic for molecules with long alkyl chains.<sup>53,57,58</sup> These so-called skeletal vibrations are mainly CC (*e.g.*, 1070 and 1144 cm<sup>-1</sup>) and CH<sub>2</sub> modes (*e.g.*, 1295, 1393, 1447, 1464, and 1481 cm<sup>-1</sup>). In wet state, as for the CTAB coated NPs, a reduced amount of signals can be resolved. Besides strong CC stretching vibrations at 1000 and 1144 cm<sup>-1</sup>, the CH<sub>2</sub> wagging motions at 1232 and 1374 cm<sup>-1</sup> are most pronounced. The latter signal is expected to partly overlap with strong CH<sub>3</sub> deformations of the headgroup, which would explain the broad peak appearance. The other motions like twisting (~1300 cm<sup>-1</sup>), scissoring (~1450 cm<sup>-1</sup>), and symmetric stretching (~1580 cm<sup>-1</sup>) are of much reduced intensity.<sup>58</sup>

At first glance, the BSA-coated NPs show more condensed mid frequency spectra with strong signals in the 1200 to 1500 cm<sup>-1</sup> range. Characteristic for proteins are the three amide bands, which reflect combinations of C=O, CN, and NH modes.<sup>55,59</sup> The BSA coating only exhibits the Amide III (CN, NH) at 1295 cm<sup>-1</sup>. The Amide I (mainly C=O, 1650 cm<sup>-1</sup>) cannot be resolved, and the Amide II (1550 cm<sup>-1</sup>) is not present for BSA.<sup>55</sup> Further signals are the CH<sub>2</sub> stretching (near 1450 cm<sup>-1</sup>)<sup>55</sup> and various functional groups of the protein. Though a complete deconvolution is beyond the scope of this analysis, the absence of the distinct skeletal vibrations clearly indicates the successful removal of CTAB from the NP surface.

The high-frequency multiplet of methyl/methylene CH<sub>x</sub> vibrations at 2800 to 3000 cm<sup>-1</sup> may serve as a fingerprint pattern (see **Figure 5.5d**). In contrast to earlier studies where these fingerprint modes could not be well-resolved,<sup>53,55,60</sup> we were able to well-resolve distinct patterns for both coatings. The fingerprint pattern consists of four CH stretching vibrations:<sup>54</sup> sym. CH<sub>2</sub> at 2850 cm<sup>-1</sup>, antisym. CH<sub>2</sub> at 2880 cm<sup>-1</sup>, sym. CH<sub>3</sub> at 2930 cm<sup>-1</sup>, and antisym. CH<sub>3</sub> at 2960 cm<sup>-1</sup>. Da Costa and co-workers showed that these modes are almost temperature-insensitive but are very sensitive

to environmental and conformational changes.<sup>54</sup> The fingerprint shape reflects the general order/disorder of alkyl chains (intensity ratio of 2880/2850 signals) as well as the polarity of the chain environment (2930/2850 ratio). A high chain order can be found for both crystalline CTAB and solid BSA based on the sharp antisym. methylene stretch ( $2880\text{ cm}^{-1}$ ) owing to close packing of planar zigzag chains.<sup>58</sup> The order at the NP surface is reduced owing to the higher mobility of the methylene groups. Furthermore, the sym. methyl stretch ( $2930\text{ cm}^{-1}$ ) is a sensor for the polarity at the particle/coating interface. Here, the  $\text{AuBr}^-$  interlayer of the CTAB-coated NPs exhibits higher polarity than the more hydrophobic gold surface, as seen for BSA-coated NPs. In addition, the absence of the NCH antisym. stretching mode at  $3040\text{ cm}^{-1}$  next to the multiplet, assigned to the  $\text{CTA}^+$  headgroup,<sup>58</sup> further suggests the complete removal of CTAB from the surface.

Consequently, both AuNS and AuNR give strong evidence for the complete exchange of CTAB by BSA throughout the studied frequency spectrum. The characteristic signals of CTAB and BSA are listed in Table 1. The protein coating resulted in a loss of the counterion ( $\text{AuBr}^-$ ), headgroup (CN, NCH), and skeletal chain (CC,  $\text{CH}_2$ ) signals characteristic for CTAB. In lieu of these, distinct signals of the amide bands could be found along with significant changes of the high-frequency fingerprint pattern, as expected.

**Table 5.1.** Overview of characteristic vibrational modes of CTAB and BSA used for analysis of the nanoparticle coatings (AuNS: nanospheres; AuNR: nanorods).

	$\nu\text{AuBr}^-$ (counterion)	$\nu\text{CN}^+$	$\nu\text{CC}$ skeletal (chain)	$\nu\text{CH}_2$	Amide bands (protein)	$\nu\text{CH}_x$	$\nu\text{NCH}$ (headgroup)
Raman shift / $\text{cm}^{-1}$	180	760	1000-1600	1200-1700	2800-3000	3040	
CTAB <sup>a</sup>	-	+	+	-	+	+	
AuNS@CTAB <sup>b</sup>	+	+	+	-	+	+	
AuNR@CTAB <sup>b</sup>	+	+	+	-	+	+	
BSA <sup>a</sup>	-	-	-	+	+	-	
AuNS@BSA <sup>b</sup>	-	-	-	+	+	-	
AuNR@BSA <sup>b</sup>	-	-	-	+	+	-	

<sup>a</sup> Conventional Raman measurements of crystalline solids in dry state.

<sup>b</sup> SERS measurements of nanoparticles dispersed in water at high concentrations.

## Conclusion

In conclusion, we report on highly stable and surfactant-free protein-coated AuNRs. The colloidal stability is evidenced by UV–vis–NIR spectroscopic characterization of the samples, which show no changes in their LSPRs characteristic for aggregation. The high colloidal stability at very high particle concentrations is maintained at physiological salt concentrations and even in biological media such as DMEM. Moreover, owing to the robust protein coating, such NPs can be lyophilized to powder, similar to proteins. Strikingly, the optical and colloidal properties of the AuNRs are completely maintained upon redispersion. By freeze-drying such particles, long-term storage under ambient conditions and stability could be ensured. Furthermore, the protein-coated AuNRs can be directly freeze-dried in cell culture media containing serum, which can be then redispersed on desire. Such cell culture media-based dry formulations could be directly used in bioapplications simply by adding water to the ready-made formulations. Most importantly, we showed *via* SERS that the toxic surfactant CTAB is completely removed from the surface of AuNRs and AuNS. The complete removal of CTAB is a key step toward safe bioapplication of protein-coated NPs. In the context of biotoxicity, the cellular uptake of protein-coated AuNPs and the evolution of their protein corona will be the focus of subsequent studies.

## Experimental Section

### Materials

Silver nitrate ( $\text{AgNO}_3$ , 99.9999%), sodium borohydride ( $\text{NaBH}_4$ , 99%), hydroquinone (HQ, >99%), hydrogen tetrachloroaurate ( $\text{HAuCl}_4$ , >99.9%), ascorbic acid (AA, 99.0%), bovine serum albumin (BSA, 98%), Dulbecco's Modified Eagle's Medium (DMEM, sterile-filtered without phenol red, D5921), newborn calf serum (NCS, sterile-filtered), and sucrose (>99.0%) were purchased from Sigma-Aldrich. Citrate (99%) and 1 M HCl and NaOH solutions were supplied by Grüssing. Cetyltrimethylammonium bromide (CTAB, 99%, 364.45 g/mol, 0.359 mg/kg iodine) was received from Merck KGaA. All chemicals were used as received. Pure-grade solvents and Milli-Q-grade water were used in all preparations.

### **AuNR Seeds**

Seeds were prepared following a procedure published elsewhere.<sup>41</sup> Briefly, to 5 mL of an aqueous 0.2 mM CTAB solution, 5 mL of an aqueous 0.5 mM HAuCl<sub>4</sub> solution was added. To prevent CTAB from crystallization the solution was kept at 32 °C. Subsequently, Au ions were rapidly reduced by adding 0.6 mL of an aqueous 0.01 mM NaBH<sub>4</sub> under vigorous stirring. Seeds were aged for 30 min at 300 rpm stirring speed. For synthesis with volumes of 1 L seed preparations was scaled to 30 mL.

### **AuNRs of Low Aspect Ratio**

For preparing AuNRs of low aspect ratios a method by Nikoobakht and El-Sayed<sup>39,40</sup> was adopted with small variations. Aqueous solutions (30 mL) containing 0.1 M CTAB and 0.25 mM HAuCl<sub>4</sub> using an aqueous 0.1 M Au stock solution were prepared and kept at 32 °C. Subsequently, varied amounts of an aqueous 0.5 mM AgNO<sub>3</sub> stock solution were added to adjust the final silver ion concentration (AuNRs Nos. 1–4 and Nos. 6 and 7: 24, 25, 30, 35, 40, and 50 μM) followed by the addition of 195 μL of an aqueous 0.1 M HCl solution to adjust the pH. Next, 112.5 μL of a 0.1 M AA solution were added to reduce the Au<sup>3+</sup> to Au<sup>1+</sup> ions accompanied by a color change from yellow to colorless. In the last step, the AuNR growth was initiated by the addition of 300 μL of as prepared seed solution. The color changed within 10 min to a slight purple. After 24 h at 32 °C, growth was accomplished. Up-scaled synthesis was performed in a volume of 1 L with the same concentration of CTAB, HAuCl<sub>4</sub>, and AA, respectively, using a final Ag concentration of 40 μM (AuNR No. 5). Nanorod growth was induced with 7 mL of seed solution.

### **AuNRs of High Aspect Ratios**

Gold nanorods with larger AR values (>4) were prepared following a procedure developed by Vigdeman and Zubarev.<sup>41</sup> Aqueous 0.1 M CTAB solution (10 mL) containing 0.5 mM HAuCl<sub>4</sub> was prepared using an aqueous 0.1 M gold stock solution. Desired amounts of an aqueous 0.1 mM AgNO<sub>3</sub> were used to adjust the Ag ion concentration (AuNRs Nos. 8–10 and Nos. 12 and 13: 0.3, 0.6, 0.65, 0.5, 0.5, and 0.5 mM) followed by the addition of 150 μL of an aqueous 0.1 M HQ solution. Color change from yellow to colorless indicated successful reduction of gold ions. As-prepared seed solutions (AuNRs Nos. 1–4 and Nos. 6 and 7: 80, 80, 80, 40, 160, and 320 μL) were added under rapid stirring to induce rod growth. Color change to a slight purple could be observed after 5 h. The solutions were stored at 32 °C for 24 h. Up-

scaled syntheses with volumes of 1 L were performed using same concentrations of CTAB, HAuCl<sub>4</sub>, and HQ, respectively, and a final concentration of Ag of 0.5 mM (AuNRs No. 11) and 0.4 mM (AuNRs No. 15). Synthesis was induced using 24 mL (AuNRs No. 11) and 15 mL (AuNRs No. 15).

### **AuNS**

Spherical gold nanoparticles with a diameter of 80 nm were synthesized as a reference system for SERS studies following a procedure published previously.<sup>31</sup>

### **Functionalization with BSA**

Prior to the BSA coating of CTAB stabilized nanoparticles the CTAB concentration in dispersions must be adjusted to the CMC of CTAB, that is, 1 mM (NP concentrations were kept identical to the original synthesis). Then, the NP dispersions with adjusted CTAB concentrations were added slowly to the BSA solution under ultrasonication (BSA solution/NP dispersions, 1:1 v/v). The BSA solution contains: BSA (10 mg/mL), 0.02% citrate, pH 7. The NPs were sonicated for 30 min and then centrifuged. Centrifugation parameters need to be adjusted, that is, sample No. 5 at 7000–8000 rcf, No. 11 at 1500–3500 rcf, and No. 15 at 5000–6000 rcf. The supernatant is replaced by the 10× diluted BSA solution, that is, 1 mg/mL BSA, 0.02% citrate, pH 12, and stirred for at least 24 h. Then the particles were washed with basic water (pH 11–12, >4×) *via* centrifugation and concentrated as desired.

### **Freeze-Drying**

AuNR@BSA samples (3.5 mL) were freeze-dried using sucrose, BSA, DEMEM, or DMEM+10%NCS as lyoprotecting agents. The concentrations were 1 mg/mL for sucrose and BSA. DEMEM and DMEM+10%NCS were used as obtained. The nanorods were centrifuged, and the precipitate was redispersed in the respective media. The Au contents of the resulting powders were 42 wt % for sucrose, 5.6 wt % for BSA, and 5.6 wt % for DMEM+10%NCS.

### **Characterization**

UV–vis–NIR spectra were measured with an Agilent Cary 5000 spectrophotometer with an attached Cary Universal Measurement Accessory (UMA). TEM measurements were done on a Zeiss 922 OMEGA EFTEM at a voltage of 200 kV. Zero-loss filtered images were recorded using a bottom-mounted Ultrascan 1000 (Gatan) CCD camera system. Gatan Digital Micrograph 3.9 for GMS 1.4 software was used for image

acquisition. SERS. Surface-enhanced Raman scattering was measured with a confocal Raman microscope (LabRAM Division, HORIBA Jobin Yvon) equipped with a high-resolution grating (1800 grooves/mm), a Peltier-cooled CCD camera ( $-70\text{ }^{\circ}\text{C}$ , Synapse) and a HeNe laser as excitation line at 633 nm. Spectra were collected by focusing the laser spot at the air/liquid interface of a sessile drop of liquid (100  $\mu\text{L}$  of each solution cast on a glass slide) by using a 100 $\times$  objective (Olympus, NA 0.9), providing a spatial resolution of  $\sim 1\text{ }\mu\text{m}^2$ . Each sample was measured at least three times at positions more than 300  $\mu\text{m}$  apart from each other.

## Acknowledgements

This study was funded by the European Research Council under Grant No. ERC-2012-StG 306686 (METAMECH: Template-assisted assembly of METAmaterials using MECHANical instabilities) and by the German Research Foundation (DFG) within the collaborative research center SFB 840. M.T. was supported by the Univ. of Bayreuth graduate school and by the Elite Network Bavaria in the framework of the Elite Study Program “Macromolecular Science” and funded *via* a grant for Ph.D. candidates according to Bavarian elite promotion law (BayEFG). The authors would like to thank C. Kunert for TEM measurements. C.K. would like to acknowledge fruitful discussions with Dr. W. Häfner.

## Supporting Information

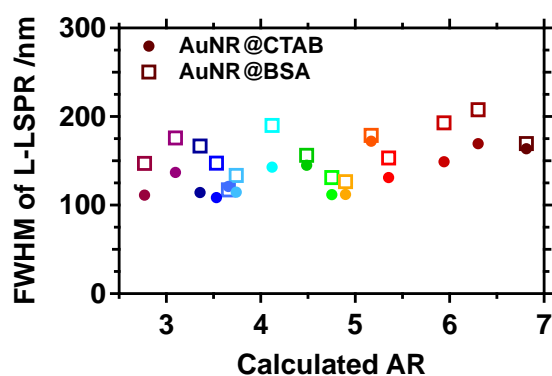


**Figure 5.S1.** AuNRs before and after functionalization with BSA (compare **Figure 5.2**).

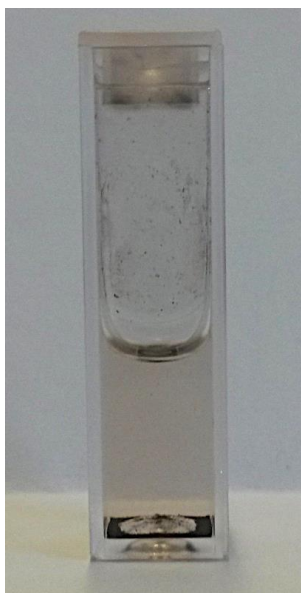


**Figure S2.** Redispersion behavior of lyophilized powder of BSA-coated AuNR #15 without additional lyoprotecting agents. The powder did not redisperse spontaneously in Milli-Q water at pH 12.

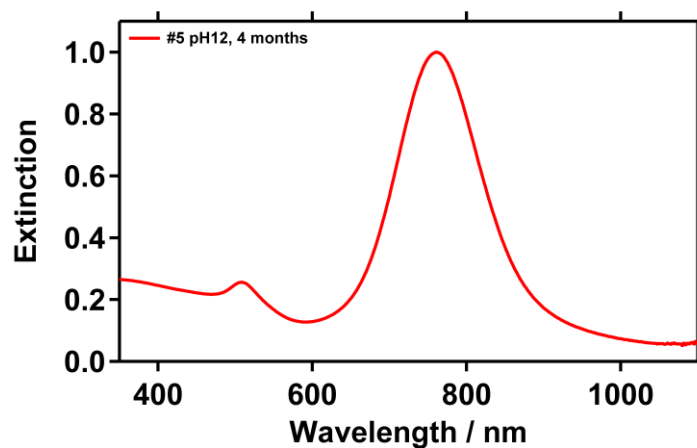


**Figure 5.S3.** UV-vis-NIR extinction of a dispersion of BSA-coated AuNR #5 (non-freeze-dried) in Milli-Q water at pH 12 after 4 months of storage at 4 °C. The longitudinal LSPR peak is at 760 nm.

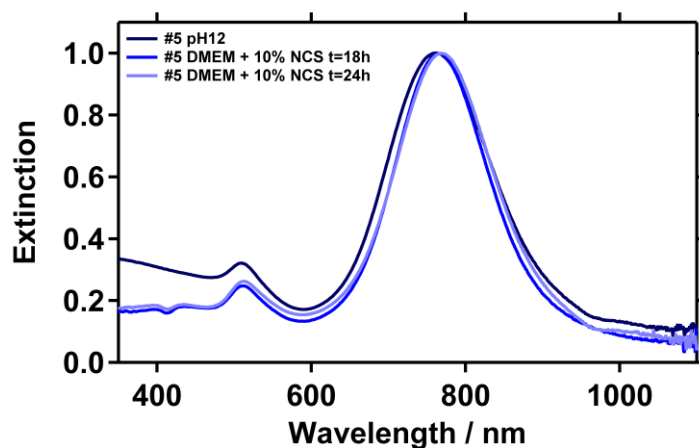


**Figure 5.S4.** UV-vis-NIR extinction of freeze-dried powder of AuNR@BSA #5 (with sucrose as lyoprotecting agent), freshly redispersed in Milli-Q water at pH 12 (dark blue, L-LSPR 760 nm) and in DMEM + 10% NCS after 18 h (L-LSPR 765 nm) and 24 h (L-LSPR, 768 nm) at room temperature. The L-LSPR shift to changes in local refractive index owed to the adsorption of protein. The AuNRs do not sediment and the spectra do not broaden over time, proving the excellent stability of the system.

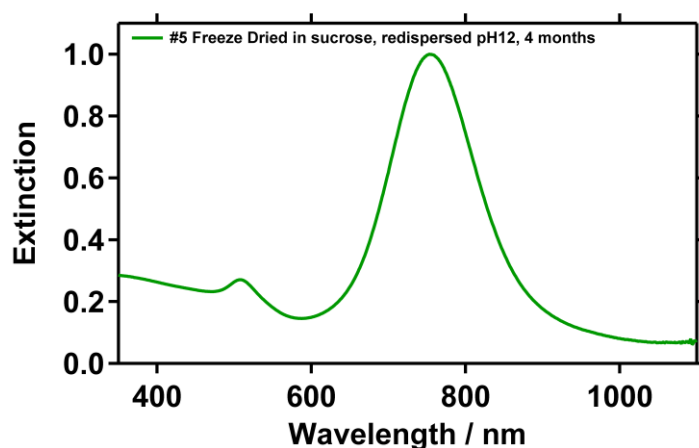
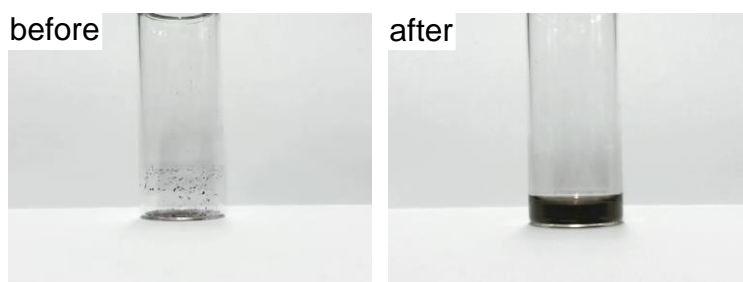


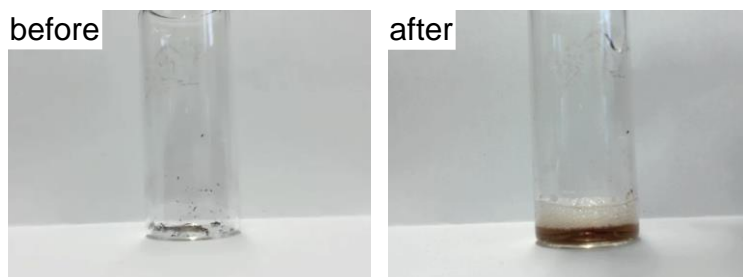
**Figure 5.S5.** UV-vis-NIR extinction of a redispersed powder of BSA-coated AuNR #5 (freeze-dried with sucrose as lyoprotecting agent) in Milli-Q water at pH 12 after 4 months of storage at 4 °C. The longitudinal LSPR peak is located at 753 nm.

### Further information on redispersion behavior of lyophilized AuNR@BSA powders.

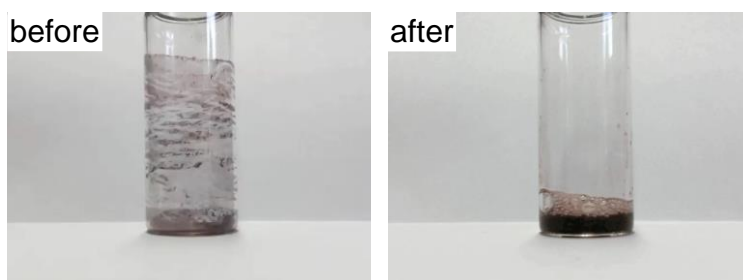
Videos V1, V2, and V3 show the spontaneous redispersion of freeze-dried AuNR@BSA powders with three different lyoprotecting agents. In the following, each video is represented by still images before and after redispersion with Milli-Q water at pH 12.



**Video 5.V1.** Redispersion of powder of freeze-dried AuNR@BSA #5 with sucrose (1 mg/mL,  $c_{\text{Au}} = 0.34$  mM) as lyoprotecting agents in Milli-Q water at pH 12.



**Video 5.V2.** Redispersion of powder of freeze-dried AuNR@BSA #15 with BSA (1 mg/mL,  $c_{\text{Au}} = 0.16$  mM) as lyoprotecting agents in Milli-Q water at pH 12.



**Video 5.V3.** Redispersion of powder of freeze-dried AuNR@BSA #11 with medium and serum (DMEM + 10% NCS;  $c_{\text{Au}} = 0.12$  mM) as lyoprotecting agents in Milli-Q water at pH 12.

### Surface-enhanced Raman spectroscopy.

In analytical SERS the general notion dictates to aim for maximum enhancement factors by using excitation wavelengths matching the localized surface plasmon resonance of the applied NPs. Since the LSPR depends on particle size, shape, orientation, and aggregation, a broad assortment of excitation sources (lasers) would be required to flexibly adopt for the respective samples of interest. Here, we showed that also off-resonance measurements, using a standard HeNe laser at 633 nm, allowed for the SERS characterization of the ligand shell of nanoparticles (NPs). Off-resonance excitation inherently limits the local electromagnetic enhancement to surface-near distances. However, the loss in electromagnetic enhancement can be

balanced by measuring at high NP concentrations (up to 20 mg/mL). At higher concentrations, the total number of scattering events is greatly increased. Additionally, measurements of dispersions take advantage of the continuous flow of NPs through the confocal excitation volume and therewith allow for efficient probing the NP coating.

## References

- (1) Vigderman, L.; Khanal, B. P.; Zubarev, E. R., Functional Gold Nanorods: Synthesis, Self-Assembly, and Sensing Applications. *Adv Mater* **2012**, *24*, 4811-4841.
- (2) Li, P.-C.; Wang, C.-R. C.; Shieh, D.-B.; Wei, C.-W.; Liao, C.-K.; Poe, C.; Jhan, S.; Ding, A.-A.; Wu, Y.-N., In vivo photoacoustic molecular imaging with simultaneous multiple selective targeting using antibody-conjugated gold nanorods. *Opt Express* **2008**, *16*, 18605-18615.
- (3) Kah, J. C. Y.; Olivo, M.; Chow, T. H.; Song, K. S.; Koh, K. Z. Y.; Mhaisalkar, S.; Sheppard, C. J. R., Control of optical contrast using gold nanoshells for optical coherence tomography imaging of mouse xenograft tumor model in vivo. *J Biomed Opt* **2009**, *14*, 054015-1-13.
- (4) Park, H.; Lee, S.; Chen, L.; Lee, E. K.; Shin, S. Y.; Lee, Y. H.; Son, S. W.; Oh, C. H.; Song, J. M.; Kang, S. H.; Choo, J., SERS imaging of HER2-overexpressed MCF7 cells using antibody-conjugated gold nanorods. *Phys Chem Chem Phys* **2009**, *11*, 7444-7449.
- (5) Huang, X.; El-Sayed, I. H.; Qian, W.; El-Sayed, M. A., Cancer Cell Imaging and Photothermal Therapy in the Near-Infrared Region by Using Gold Nanorods. *J Am Chem Soc* **2006**, *128*, 2115-2120.
- (6) Ray, P. C.; Yu, H.; Fu, P. P., Toxicity and Environmental Risks of Nanomaterials: Challenges and Future Needs. *J Environ Sci Health, Part C: Environ Carcinog Ecotoxicol Rev* **2009**, *27*, 1-35.
- (7) Iqbal, M.; Tae, G., Unstable Reshaping of Gold Nanorods Prepared by a Wet Chemical Method in the Presence of Silver Nitrate. *J Nanosci Nanotechnol* **2006**, *6*, 3355-3359.
- (8) Basiruddin, S. K.; Saha, A.; Pradhan, N.; Jana, N. R., Functionalized Gold Nanorod Solution via Reverse Micelle Based Polyacrylate Coating. *Langmuir* **2010**, *26*, 7475-7481.

- (9) Gole, A.; Murphy, C. J., Polyelectrolyte-Coated Gold Nanorods: Synthesis, Characterization and Immobilization. *Chem Mater* **2005**, *17*, 1325-1330.
- (10) Liao, H.; Hafner, J. H., Gold Nanorod Bioconjugates. *Chem Mater* **2005**, *17*, 4636-4641.
- (11) Sendroiu, I. E.; Warner, M. E.; Corn, R. M., Fabrication of Silica-Coated Gold Nanorods Functionalized with DNA for Enhanced Surface Plasmon Resonance Imaging Biosensing Applications. *Langmuir* **2009**, *25*, 11282-11284.
- (12) Wijaya, A.; Hamad-Schifferli, K., Ligand Customization and DNA Functionalization of Gold Nanorods via Round-Trip Phase Transfer Ligand Exchange. *Langmuir* **2008**, *24*, 9966-9969.
- (13) Orendorff, C. J.; Alam, T. M.; Sasaki, D. Y.; Bunker, B. C.; Voigt, J. A., Phospholipid–Gold Nanorod Composites. *ACS Nano* **2009**, *3*, 971-983.
- (14) Vigderman, L.; Manna, P.; Zubarev, E. R., Quantitative Replacement of Cetyl Trimethylammonium Bromide by Cationic Thiol Ligands on the Surface of Gold Nanorods and Their Extremely Large Uptake by Cancer Cells. *Angew Chem, Int Ed* **2012**, *51*, 636-641.
- (15) Leonov, A. P.; Zheng, J.; Clogston, J. D.; Stern, S. T.; Patri, A. K.; Wei, A., Detoxification of Gold Nanorods by Treatment with Polystyrenesulfonate. *ACS Nano* **2008**, *2*, 2481-2488.
- (16) Huang, H.-C.; Barua, S.; Kay, D. B.; Rege, K., Simultaneous Enhancement of Photothermal Stability and Gene Delivery Efficacy of Gold Nanorods Using Polyelectrolytes. *ACS Nano* **2009**, *3*, 2941-2952.
- (17) Prencipe, G.; Tabakman, S. M.; Welsher, K.; Liu, Z.; Goodwin, A. P.; Zhang, L.; Henry, J.; Dai, H., PEG Branched Polymer for Functionalization of Nanomaterials with Ultralong Blood Circulation. *J Am Chem Soc* **2009**, *131*, 4783-4787.

- (18) Chanda, N.; Shukla, R.; Katti, K. V.; Kannan, R., Gastrin Releasing Protein Receptor Specific Gold Nanorods: Breast and Prostate Tumor Avid Nanovectors for Molecular Imaging. *Nano Lett* **2009**, *9*, 1798-1805.
- (19) Alkilany, A. M.; Nagaria, P. K.; Wyatt, M. D.; Murphy, C. J., Cation Exchange on the Surface of Gold Nanorods with a Polymerizable Surfactant: Polymerization, Stability, and Toxicity Evaluation. *Langmuir* **2010**, *26*, 9328-9333.
- (20) Lee, S. W.; Kim, B.-S.; Chen, S.; Shao-Horn, Y.; Hammond, P. T., Layer-by-Layer Assembly of All Carbon Nanotube Ultrathin Films for Electrochemical Applications. *J Am Chem Soc* **2009**, *131*, 671-679.
- (21) Takahashi, H.; Niidome, Y.; Niidome, T.; Kaneko, K.; Kawasaki, H.; Yamada, S., Modification of Gold Nanorods Using Phosphatidylcholine to Reduce Cytotoxicity. *Langmuir* **2006**, *22*, 2-5.
- (22) Fernández-López, C.; Mateo-Mateo, C.; Álvarez-Puebla, R. A.; Pérez-Juste, J.; Pastoriza-Santos, I.; Liz-Marzán, L. M., Highly Controlled Silica Coating of PEG-Capped Metal Nanoparticles and Preparation of SERS-Encoded Particles. *Langmuir* **2009**, *25*, 13894-13899.
- (23) Kim, D. H.; Wei, A.; Won, Y.-Y., Preparation of Super-Stable Gold Nanorods via Encapsulation into Block Copolymer Micelles. *ACS Appl Mater Interfaces* **2012**, *4*, 1872-1877.
- (24) Xia, X.; Yang, M.; Wang, Y.; Zheng, Y.; Li, Q.; Chen, J.; Xia, Y., Quantifying the Coverage Density of Poly(ethylene glycol) Chains on the Surface of Gold Nanostructures. *ACS Nano* **2012**, *6*, 512-522.
- (25) Kinnear, C.; Dietsch, H.; Clift, M. J. D.; Endes, C.; Rothen-Rutishauser, B.; Petri-Fink, A., Gold Nanorods: Controlling Their Surface Chemistry and Complete Detoxification by a Two-Step Place Exchange. *Angew Chem, Int Ed* **2013**, *52*, 1934-1938.
- (26) Peng, G.; David, J. S. B.; Yu, C., Dye-doped polystyrene-coated gold nanorods: towards wavelength tuneable SPASER. *Methods Appl Fluoresc* **2014**, *2*, 024004-1-6.

- (27) Chen, Y.-S.; Frey, W.; Kim, S.; Kruizinga, P.; Homan, K.; Emelianov, S., Silica-Coated Gold Nanorods as Photoacoustic Signal Nanoamplifiers. *Nano Lett* **2011**, *11*, 348-354.
- (28) Chanana, M.; Correa-Duarte, M. A.; Liz-Marzán, L. M., Insulin-Coated Gold Nanoparticles: A Plasmonic Device for Studying Metal–Protein Interactions. *Small* **2011**, *7*, 2650-2660.
- (29) Strozyk, M. S.; Chanana, M.; Pastoriza-Santos, I.; Pérez-Juste, J.; Liz-Marzán, L. M., Protein/Polymer-Based Dual-Responsive Gold Nanoparticles with pH-Dependent Thermal Sensitivity. *Adv Funct Mater* **2012**, *22*, 1436-1444.
- (30) Chanana, M.; Rivera\_Gil, P.; Correa-Duarte, M. A.; Liz-Marzán, L. M.; Parak, W. J., Physicochemical Properties of Protein-Coated Gold Nanoparticles in Biological Fluids and Cells before and after Proteolytic Digestion. *Angew Chem, Int Ed* **2013**, *52*, 4179-4183.
- (31) Hanske, C.; Tebbe, M.; Kuttner, C.; Bieber, V.; Tsukruk, V. V.; Chanana, M.; König, T. A. F.; Fery, A., Strongly Coupled Plasmonic Modes on Macroscopic Areas via Template-Assisted Colloidal Self-Assembly. *Nano Lett* **2014**, *14*, 6863-6871.
- (32) Daniel, M.-C.; Astruc, D., Gold Nanoparticles: Assembly, Supramolecular Chemistry, Quantum-Size-Related Properties, and Applications toward Biology, Catalysis, and Nanotechnology. *Chem Rev* **2004**, *104*, 293-346.
- (33) Grzelczak, M.; Perez-Juste, J.; Mulvaney, P.; Liz-Marzan, L. M., Shape control in gold nanoparticle synthesis. *Chem Soc Rev* **2008**, *37*, 1783-1791.
- (34) Sardar, R.; Funston, A. M.; Mulvaney, P.; Murray, R. W., Gold Nanoparticles: Past, Present, and Future. *Langmuir* **2009**, *25*, 13840-13851.
- (35) Klinkova, A.; Choueiri, R. M.; Kumacheva, E., Self-assembled plasmonic nanostructures. *Chem Soc Rev* **2014**, *43*, 3976-3991.
- (36) Nie, Z.; Fava, D.; Kumacheva, E.; Zou, S.; Walker, G. C.; Rubinstein, M., Self-assembly of metal-polymer analogues of amphiphilic triblock copolymers. *Nat Mater* **2007**, *6*, 609-614.

- (37) Caswell, K. K.; Wilson, J. N.; Bunz, U. H. F.; Murphy, C. J., Preferential End-to-End Assembly of Gold Nanorods by Biotin–Streptavidin Connectors. *J Am Chem Soc* **2003**, *125*, 13914-13915.
- (38) Sethi, M.; Joung, G.; Knecht, M. R., Linear Assembly of Au Nanorods Using Biomimetic Ligands. *Langmuir* **2009**, *25*, 1572-1581.
- (39) Nikoobakht, B.; El-Sayed, M. A., Preparation and Growth Mechanism of Gold Nanorods (NRs) Using Seed-Mediated Growth Method. *Chem Mater* **2003**, *15*, 1957-1962.
- (40) Jana, N. R.; Gearheart, L.; Murphy, C. J., Wet Chemical Synthesis of High Aspect Ratio Cylindrical Gold Nanorods. *J Phys Chem B* **2001**, *105*, 4065-4067.
- (41) Vigdeman, L.; Zubarev, E. R., High-Yield Synthesis of Gold Nanorods with Longitudinal SPR Peak Greater than 1200 nm Using Hydroquinone as a Reducing Agent. *Chem Mater* **2013**, *25*, 1450-1457.
- (42) Ehlert, S.; Taheri, S. M.; Pirner, D.; Drechsler, M.; Schmidt, H.-W.; Förster, S., Polymer Ligand Exchange to Control Stabilization and Compatibilization of Nanocrystals. *ACS Nano* **2014**, *8*, 6114-6122.
- (43) Funston, A. M.; Novo, C.; Davis, T. J.; Mulvaney, P., Plasmon Coupling of Gold Nanorods at Short Distances and in Different Geometries. *Nano Lett* **2009**, *9*, 1651-1658.
- (44) Link, S.; Mohamed, M. B.; El-Sayed, M. A., Simulation of the Optical Absorption Spectra of Gold Nanorods as a Function of Their Aspect Ratio and the Effect of the Medium Dielectric Constant. *J Phys Chem B* **1999**, *103*, 3073-3077.
- (45) Link, S.; El-Sayed, M. A., ERRATUM: Simulation of the Optical Absorption Spectra of Gold Nanorods as a Function of Their Aspect Ratio and the Effect of the Medium Dielectric Constant. *J Phys Chem B* **2005**, *109*, 10531-10532.
- (46) Pérez-Juste, J.; Pastoriza-Santos, I.; Liz-Marzán, L. M.; Mulvaney, P., Gold nanorods: Synthesis, characterization and applications. *Coord Chem Rev* **2005**, *249*, 1870-1901.

- (47) Day, J. G.; Stacey, G. N., *Cryopreservation and Freeze-Drying Protocols*. 2nd ed ed.; Springer Science + Business Media: United States of America, New York, 2007.
- (48) Pazos-Perez, N.; Ni, W.; Schweikart, A.; Alvarez-Puebla, R. A.; Fery, A.; Liz-Marzan, L. M., Highly uniform SERS substrates formed by wrinkle-confined drying of gold colloids. *Chem Sci* **2010**, *1*, 174-178.
- (49) Pazos-Perez, N.; Wagner, C. S.; Romo-Herrera, J. M.; Liz-Marzán, L. M.; García de Abajo, F. J.; Wittemann, A.; Fery, A.; Alvarez-Puebla, R. A., Organized Plasmonic Clusters with High Coordination Number and Extraordinary Enhancement in Surface-Enhanced Raman Scattering (SERS). *Angew Chem, Int Ed* **2012**, *51*, 12688-12693.
- (50) Mueller, M.; Tebbe, M.; Andreeva, D. V.; Karg, M.; Alvarez Puebla, R. A.; Pazos Perez, N.; Fery, A., Large-Area Organization of pNIPAM-Coated Nanostars as SERS Platforms for Polycyclic Aromatic Hydrocarbons Sensing in Gas Phase. *Langmuir* **2012**, *28*, 9168-9173.
- (51) Alvarez-Puebla, R. A.; Liz-Marzán, L. M., SERS Detection of Small Inorganic Molecules and Ions. *Angew Chem, Int Ed* **2012**, *51*, 11214-11223.
- (52) Alba, M.; Pazos-Perez, N.; Vaz, B.; Formentin, P.; Tebbe, M.; Correa-Duarte, M. A.; Granero, P.; Ferré-Borrull, J.; Alvarez, R.; Pallares, J.; Fery, A.; de Lera, A. R.; Marsal, L. F.; Alvarez-Puebla, R. A., Macroscale Plasmonic Substrates for Highly Sensitive Surface-Enhanced Raman Scattering. *Angew Chem, Int Ed* **2013**, *52*, 6459-6463.
- (53) Lee, S.; Anderson, L. J. E.; Payne, C. M.; Hafner, J. H., Structural Transition in the Surfactant Layer that Surrounds Gold Nanorods as Observed by Analytical Surface-Enhanced Raman Spectroscopy. *Langmuir* **2011**, *27*, 14748-14756.
- (54) da Costa, A. M. A.; Geraldés, C. F. G. C.; Teixeira-Dias, J. J. C., Micellar aggregation of CTAB in water and chloroform solutions—a study by laser raman spectroscopy. *J Colloid Interface Sci* **1982**, *86*, 254-259.
- (55) Lin, V. J. C.; Koenig, J. L., Raman studies of bovine serum albumin. *Biopolymers* **1976**, *15*, 203-218.

- (56) Aliaga, A. E.; Osorio-Román, I.; Leyton, P.; Garrido, C.; Cárcamo, J.; Caniulef, C.; Célis, F.; Díaz F, G.; Clavijo, E.; Gómez-Jeria, J. S.; Campos-Vallette, M. M., Surface-enhanced Raman scattering study of L-tryptophan. *J Raman Spectrosc* **2009**, *40*, 164-169.
- (57) Snyder, R. G.; Schachtschneider, J. H., Vibrational analysis of the n-paraffins— I: Assignments of infrared bands in the spectra of C<sub>3</sub>H<sub>8</sub> through n-C<sub>19</sub>H<sub>40</sub>. *Spectrochim Acta* **1963**, *19*, 85-116.
- (58) Dendramis, A. L.; Schwinn, E. W.; Sperline, R. P., A surface-enhanced Raman scattering study of CTAB adsorption on copper. *Surf Sci* **1983**, *134*, 675-688.
- (59) Catalina, D.; Nicolas, G.; Hong, S.; Timothée, T.; Marc Lamy de la, C., SERS detection of biomolecules using lithographed nanoparticles towards a reproducible SERS biosensor. *Nanotechnology* **2010**, *21*, 475501-1-6.
- (60) Iosin, M.; Toderas, F.; Baldeck, P. L.; Astilean, S., Study of protein-gold nanoparticle conjugates by fluorescence and surface-enhanced Raman scattering. *J Mol Struct* **2009**, *924-926*, 196-200.



# *II*

## Controlled Alignment of Gold Nanorods



# 6

## Optically Anisotropic Substrates *via* Wrinkle-Assisted Convective Assembly of Gold Nanorods on Macroscopic Areas

Moritz Tebbe, Martin Mayer, Bernhard A. Glatz, Christoph Hanske, Patrick T. Probst, Mareen B. Müller, Matthias Karg, Munish Chanana, Tobias A. F. König, Christian Kuttner, Andreas Fery

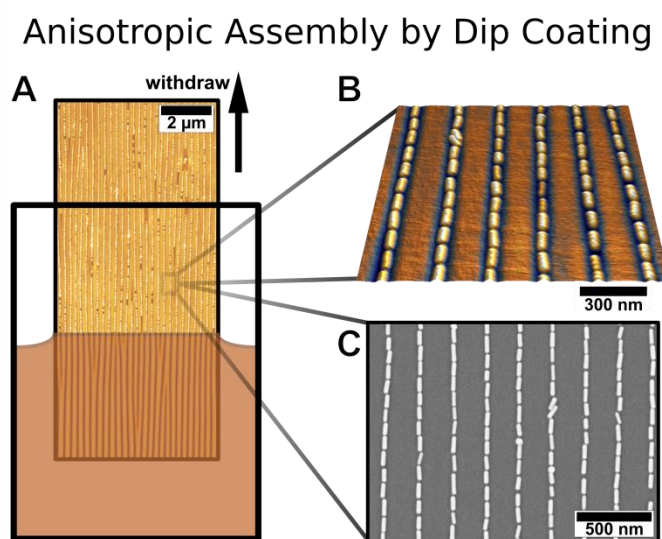


Figure 6.1 Table of Contents Figure (unpublished)

Published in **Faraday Discussions**.

Tebbe *et al.*, *Faraday Discuss* **2015**, *118*, 243-260. Reproduced by permission of The Royal Society of Chemistry.



## Abstract

We demonstrate the large-scale organisation of anisotropic nanoparticles into linear assemblies displaying optical anisotropy on macroscopic areas. Monodisperse gold nanorods with a hydrophilic protein shell are arranged by dip-coating on wrinkled surfaces and subsequently transferred to indium tin oxide (ITO) substrates by capillary transfer printing. We elucidate how tuning the wrinkle amplitude enables to precisely adjust the assembly morphology and fabricate single, double and triple nanorod lines. For the single lines, we quantify the order parameter of the assemblies as well as interparticle distances from scanning electron microscopy (SEM) images. We find an order parameter of 0.97 and a mean interparticle gap size of 7 nm. This combination of close to perfect uniaxial alignment and close-packing gives rise to pronounced macroscopic anisotropic optical properties due to strong plasmonic coupling. We characterise the optical response of the assemblies on ITO-coated glass *via* UV/vis/NIR spectroscopy and determine an optical order parameter of 0.91. The assemblies are thus plasmonic metamaterials, as their periodicity and building block sizes are well below the optical wavelength. The presented approach does not rely on lithographic patterning and provides access to functional materials, which could find application in subwavelength waveguiding, photovoltaics, and for large-area metamaterial fabrication.

## Introduction

Bottom-up assembly of noble metal nanoparticles into well-defined structures has been in the focus of scientific interest for the last decade and is expected to foster innovations in the fields of nanoelectronics,<sup>1-3</sup> non-linear optics,<sup>4-6</sup> photovoltaics,<sup>7,8</sup> and metamaterials.<sup>4,9-12</sup> Especially assemblies from gold and silver nanoparticles have received much attention. These nanoparticles display a localised surface plasmon resonance (LSPR) for which the resonance frequency depends on size, shape and dielectric environment of the particles. In assemblies, LSPRs of individual particles can couple resulting in characteristic shifts of the resonance frequencies, appearance of new resonances, and modification of near fields.<sup>13</sup> For these phenomena, the interparticle gap size along with the degree of

order are decisive.<sup>14</sup> Whereas the gap size strongly influences plasmonic coupling,<sup>15</sup> the overall alignment quality is crucial for homogeneity.<sup>14</sup>

Amongst various approaches for ordering nanoparticles, wrinkle-assisted assembly has shown potential for scalable organisation of nanoparticles. We have first shown the linear assembly of spherical polystyrene particles into well-defined linear chains using dip-coating on wrinkle-substrates.<sup>16</sup> Subsequently, the concept has been expanded to nanoparticles of varying chemical composition, size and aspect ratio.<sup>14,16-27</sup> Whereas these studies proved the capability of this method for nanofabrication on macroscopic areas, the introduction of noble metal nanoparticles represents a crucial step towards surfaces with tailored functionalities.<sup>14,17,20</sup> Only recently, we reported on the wrinkle-assisted assembly of protein-coated gold nanospheres into parallel chains covering centimetre-squared areas and characterised the effects of strong plasmonic coupling in these structures.<sup>14</sup> Such assemblies of spherical nanoparticles are promising candidates for various applications, *e.g.* surface enhanced Raman spectroscopy,<sup>20,28</sup> subwavelength waveguiding,<sup>29,30</sup> or plasmon enhanced solar cells.<sup>7,8</sup>

In contrast to spherical nanoparticles, nanorods already possess intrinsically anisotropic optical properties.<sup>13</sup> Noble metal nanorod plasmon coupling has thus drawn much attention and plenty of studies investigate interparticle coupling phenomena on a single particle level with respect to interparticle distance,<sup>15,31</sup> orientation,<sup>15,31</sup> aspect ratio,<sup>31,32</sup> shape,<sup>33</sup> template material,<sup>34</sup> and nanoparticle material.<sup>35</sup> The intrinsic optical anisotropy can be used in order to achieve more complex optical features like magnetic resonances for parallel rod structures<sup>9-12</sup> or three-dimensional plasmon rulers.<sup>36,37</sup> Thus, achieving regular assembly of plasmonic nanorods over large areas with high filling rates is the challenge in expanding our concept of wrinkle-assisted templating towards optical metamaterials.<sup>14</sup> Many groups have put effort in developing methods for nanorod organisation. Amongst those, several have taken advantage of topographically patterned substrates in combination with convective or capillary force assembly (CFA).<sup>1,38-42</sup> Recently, Rey and co-workers reported on the successful alignment of gold nanorods in poly(dimethylsiloxane) (PDMS) channels achieving filling rates of 25% in combination with a high quality of the assemblies.<sup>1</sup> However, many approaches utilise topographical patterns fabricated by top-down approaches, which are ultimately limited with respect to scalability. This bottleneck could be

eliminated by wrinkle-assisted assembly.

In this work, we show for the first time, that wrinkle-assisted assembly allows for the fabrication of close-packed gold nanorod assemblies covering macroscopic areas and the efficient capillary transfer print onto ITO substrates. We discuss the impact of particle surface chemistry, wrinkle periodicity, and amplitude on the assembly process. Based on statistical analysis, we quantitatively investigate the degree of order and filling factor in the nanoparticle patterns as well as the interparticle gap size distribution. Finally, we characterise the optical properties with a polarisation selective excitation. We discuss the strong polarisation dependency with respect to strong plasmonic interparticle coupling effects. These studies frame the principles for a linear assembly of plasmonic building blocks on macroscopic areas using a cost-efficient, lithography-free, and large-area self-assembly technique.

## Results and Discussion

### Gold Nanorod Synthesis and Characterisation

Monodisperse gold nanorods of high aspect ratio were synthesised using a method published by Vigderman and Zubarev in 2013.<sup>43</sup> This protocol employs seeded growth of single-crystalline gold seeds in the presence of cetyltrimethylammonium bromide (CTAB) as a directing agent and hydroquinone as a rather mild reducing agent.<sup>43</sup> Compared to other seeded growth protocols, which mostly employ ascorbic acid as reducing agent, the gold conversion is significantly increased, reaching almost 100%. Furthermore, the resulting nanoparticles show a low polydispersity along with a small fraction (< 1%) of particles exhibiting other shapes, such as spheres and cubes (**Figure 6.2A**).

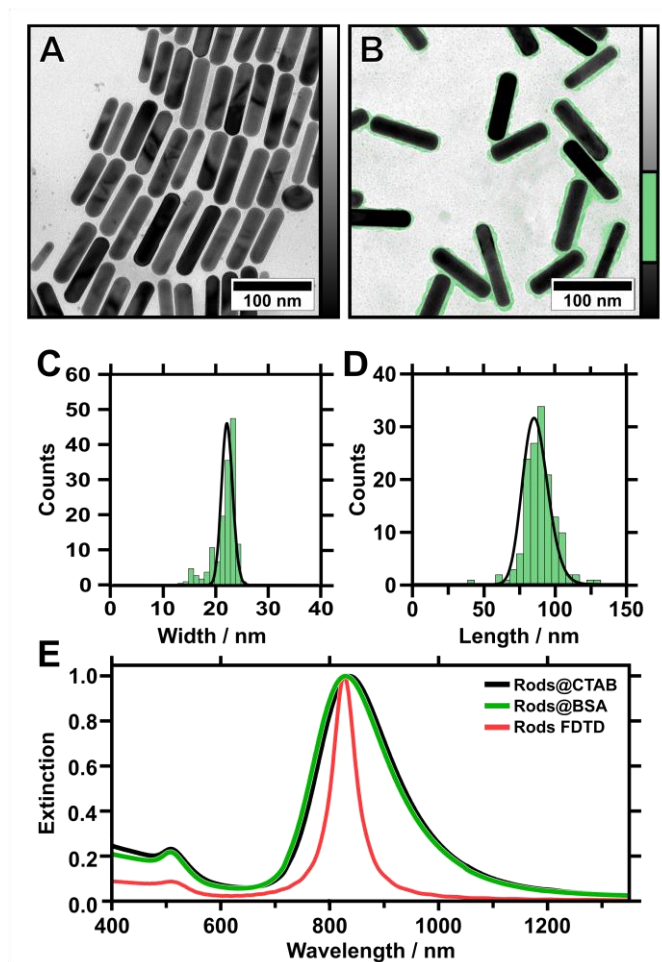


**Figure 6.2.** TEM images of gold nanorods stabilised with CTAB (as-prepared) (A) and stabilised with BSA after cleaning (B). The protein corona is highlighted in green colour (see adjacent colour table). Histogram plots showing the corresponding distribution of width (C) and length (D) of BSA-coated gold nanorods evaluated from TEM (investigation of 150 particles reveals:  $\langle \text{width} \rangle = 22.0 \pm 1.1$  nm,  $\langle \text{length} \rangle = 85.4 \pm 9.0$  nm). (E) UV/vis/NIR extinction spectra of gold nanorods in water stabilised with CTAB (black) and BSA (green) compared to the simulated extinction (red) of an 84 nm times 22 nm nanorod with 10 nm capping radius.

This purity and the remarkably narrow size distribution of the nanorods is a prerequisite for the assemblies presented in this study. The particle size was determined by TEM ( $N = 150$ ) yielding  $85.4 \pm 9.0$  nm in length and  $22.0 \pm 1.1$  nm in width (**Figure 6.2A-D**). This results in an aspect ratio (AR) of  $3.9 \pm 0.6$ . The optical properties of the nanoparticles in dilute solution were characterised with UV/vis/NIR spectroscopy. Two characteristic plasmon modes were observed (**Figure 6.2E**). The longitudinal mode is excited by light polarised parallel to the long axis of the particle (L-LSPR at 836 nm with a full width at half maximum

(FWHM) of 220 nm), whereas the transverse mode is excited by light polarised parallel to the short axis of the nanorod (T-LSPR at 508 nm). Using a simple empiric linear equation ( $AR = (L-LSPR - 420 \text{ nm}) / 95 \text{ nm}$ ) the AR was calculated to be  $4.4 \pm 1.0$ .<sup>43,44</sup> This result is in good agreement with the value determined from TEM ( $3.9 \pm 0.6$ ). Small deviations arise from variations of the nanorod shape (dimensions and cap rounding), which result in a blue shift of the L-LSPR and FWHM broadening.<sup>45</sup> The peak intensity ratio was determined to be 4.3 serving as an indicator for synthesis quality as spherical impurities will add up to the T-LSPR cross-section intensity. These results indicate the high quality of the synthesised gold nanorods and their narrow size distribution. Finally, we performed finite-difference time-domain (FDTD) method simulations for a single particle with the determined dimensions (TEM) to verify the quality. As shown in **Figure 6.2E**, we observed good agreement with the experimental spectroscopic results, which ensured the full consistency of morphological and spectroscopic features on single particle level.

### **Nanorod Functionalisation**

Previous work has shown that wrinkle-assisted assembly requires strongly hydrophilic (ideally, completely wetting) substrates.<sup>19</sup> Thus, as-received nanorods are not appropriate, as they are only colloiddally stable in the presence of an excess of CTAB. The amphiphilic character of CTAB however strongly influences the wetting behaviour of the nanoparticle solution on the substrate and results in a contact angle of  $32 \pm 0.8^\circ$  for hydrophilised PDMS.

First attempts showed, that the organisation of CTAB-stabilised nanorods on wrinkle-templates by dip-coating was not possible and prepared substrates showed a poor overall coverage. Thus, further surface functionalisation is necessary to adjust the wetting behaviour of the nanoparticle solution.<sup>14</sup> Consequently, CTAB was exchanged with bovine serum albumin (BSA) to adjust the nanoparticle surface chemistry and provide high colloidal stability following a recently published protocol.<sup>14,46,47</sup> BSA yields a negative surface charge in basic conditions ( $\text{pH} > \text{pI } 4.7$ ) as determined from zeta potential measurements and provides a defined protein corona with a thickness of 1.5 to 3 nm.<sup>14,46,48,49</sup> At the same time, the nanoparticle morphology is maintained after BSA functionalisation as we demonstrate by TEM micrographs in **Figure 6.2B**. The functionalised

nanoparticles exhibit a small shift of the L-LSPR towards blue (826 nm, FWHM 216 nm) (**Figure 6.2E**). This shift can be attributed to negligibly small morphological alterations due to the applied washing procedure.<sup>47</sup> The resulting nanorod solutions are free of excess surfactant and can be concentrated to high gold concentrations (20 mg/mL) because of the superior colloidal stability provided by the protein corona.<sup>47,48</sup> For the experiments presented here, the gold concentration was 1.2 mg/mL, if not stated differently. Thus, complete wetting of the nanoparticle solutions was achieved.

### **Wrinkle-Templates**

In order to achieve highly periodic particle arrays homogeneously distributed on large-areas, the templates have to comply with two requirements. First, the nanorods require nanoscale confinement on large-area. Second, the templates should provide macroscopic and homogeneous, ideally, complete wetting. The first condition is achieved with wrinkle-templates possessing periodicities close to 200 nm in combination with variable amplitudes in the range of the diameter of the nanorods. The second requirement demands avoiding cracks in the hydrophilic surface layer to prevent contact line pinning. Cracks occur parallel to the stretching directions due to the anisotropic mechanical stretching of the PDMS substrate (**Figure 2A**) in combination with the mechanical mismatch of the glassy top layer and substrate.<sup>50</sup> As inside the cracks hydrophobic PDMS is exposed, cracks cause local hydrophobisation as well as nonuniform wetting.

We found that the parameters listed in the experimental section in **Table 6.1** provide crack-free substrates with wrinkle periodicities of 200 to 300 nm and wrinkle amplitudes in the range of 20 to 30 nm.<sup>51</sup> To render the prepared substrates hydrophilic and to gain an even higher control over surface topology, defined plasma post-treatment was employed. A variation of the plasma dose at low pressure (0.2 mbar) facilitates a precise adjustment of the wrinkle amplitude, which is tuneable from the initial amplitude down to a completely flat surface, without affecting the wrinkle periodicity as shown in **Figure 6.3B-D**.

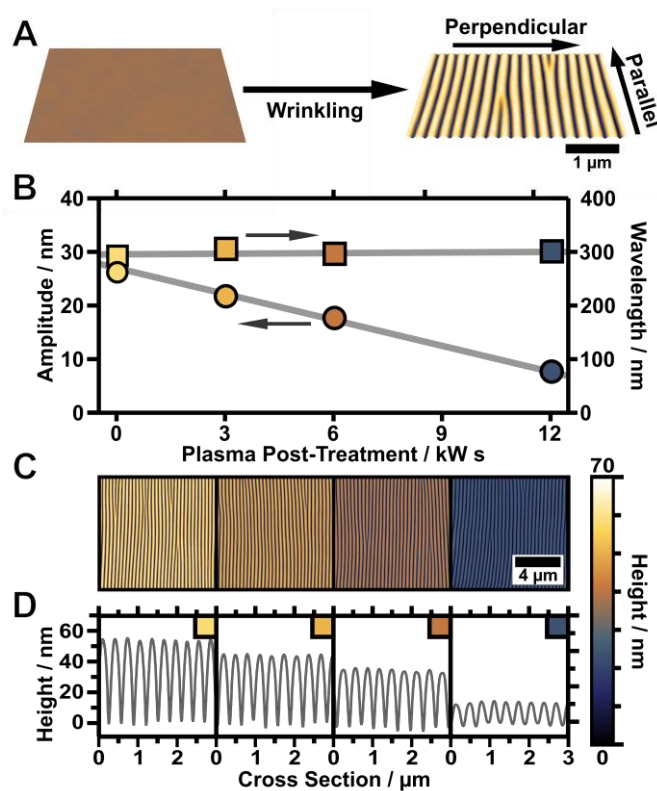


**Figure 6.3.** (A) Schematic depiction of wrinkle formation starting from a flat elastomeric PDMS substrate that is stretched and subsequently treated with oxygen plasma to form a thin silicon dioxide layer. Wrinkles form upon relaxation due to a mechanical mismatch between bulk elastomer and oxide top layer. (B) Amplitude (left axis and marked by circles) and periodicity (right axis and marked by rectangles) plotted vs plasma dose of the applied post-treatment procedure (plotted lines are guides to the eye). (C) Corresponding AFM image of the wrinkled substrate after post-treatment (please note, that for better comparison all images were scaled to the same height). (D) Corresponding cross-sections of the wrinkles after post-treatment revealing a linear decrease in amplitude while the periodicity remains constant.

**Table 6.1:** Parameters for wrinkle preparation.

Sample	Figure	Elongation (%)	Plasma time (s)	Periodicity* (nm)	Amplitude* (nm)
1	Fig. 6.4A	40	1200	276	25.2
2	Fig. 6.4B	60	1200	217	25.7
3	Fig. 6.4C & 6.5	40	1200	219	23.1
4	Fig. 6.7	40	1200	238	24.3

\*Initial periodicity and amplitude

This is a simple control parameter that enables a precise adjustment of the wrinkle aspect ratio to match the nanoparticle dimensions and directly regulates

nanoparticle arrangement inside the grooves of the wrinkle-templates (template requirements). For the representative sample shown in **Figure 6.3** the amplitude was tuned starting from 26 nm down to 5 nm keeping the periodicity constant at 300 nm. The presented process offers the possibility to tune the wrinkle aspect ratio (periodicity / amplitude) with a single experimental parameter, which is of great importance to match wrinkle dimensions with building block sizes.

### Nanorod Assemblies

We use dip-coating to organise the gold nanorods into well-defined structures. As drag forces caused by the moving contact line along with convective flow foster nanorod alignment,<sup>1</sup> the best results were obtained with the pulling direction oriented parallel to the wrinkles (**Figure 6.3A**). In comparison, samples produced with a perpendicular orientation displayed a higher degree of disorder and a tendency for rod alignment parallel to the withdrawing direction (data not shown). Despite the repulsive electrostatic interaction between the (equally charged) surfaces of the particles and the wrinkles, attractive capillary forces facilitate the nanorod deposition in close-packed assemblies. Due to the confining sinusoidally shaped channel walls, remarkable site-selectivity can be achieved.

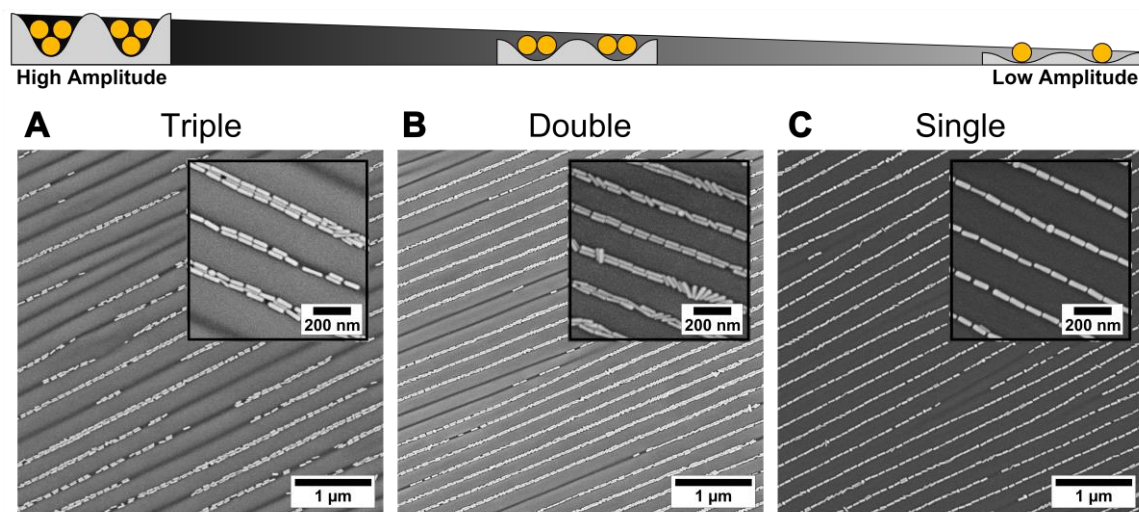


**Figure 6.4.** Amplitude dependency of linear assembly of BSA-functionalised gold nanorods into wrinkles using dip-coating. Organisation of gold nanorods into (A) triple lines, (B) double lines, and (C) single lines. From (A) to (C) the amplitude of the wrinkles decreases progressively. For all samples the withdrawal of the templates was performed with the wrinkles oriented perpendicular to the contact line with a withdrawing speed of 100, 10, and 10 µm/min, respectively, and a gold concentration of 1 mg/mL.

The wetting behaviour of the templates is determined by the hydrophilicity of the surface, the wetting properties of the solution and the contained nanoparticles. Purified solutions of BSA-functionalised gold nanorods completely spread on hydrophilised substrates and thus behave similar to neat water resulting in a contact angle close to zero.

The low contact angle of the BSA solution on the receding template leads to the formation of a meniscus and thus to confinement of the gold nanorods within the receding contact line resulting in high filling rates. For wrinkles with amplitudes slightly larger than the diameter of the anisotropic nanoparticles, the nanorods show a tendency to self-assemble into parallel triple lines as shown in **Figure 6.4A**. In this case, the wrinkles had a periodicity of 260 nm and an amplitude of 26.5 nm. If the wrinkle amplitude is reduced to values slightly below the nanorod diameter parallel double lines are formed preferentially as observed for a sample with a periodicity of 213 nm and an amplitude of 15.5 nm presented in **Figure 6.4B**. Further reduction of the amplitude, significantly below the diameter of the anisotropic building blocks, leads to a well-defined single line array of gold nanorods. This is shown in **Figure 6.4C** for a wrinkle with a periodicity of 228 nm and amplitude of 5.2 nm. The resulting structure showed an excellent degree of selectivity along with a good filling rate. Consequently, to promote a well-defined linear assembly of anisotropic nanoparticles in single lines on large areas, the dimensions of the wrinkle-template need to match nanoparticle dimensions within a small range.<sup>1</sup> Thus, utilising well-defined functionalised nanorods, wrinkle-templates with tuneable amplitudes, and dip-coating yield a plethora of interesting particle chain morphologies, namely, triple, double, and single lines. In the following, we will focus on the investigation of gold nanorods organised in single lines. This system showed the highest degree of order and homogeneity along with a good filling rate. We provide a thorough statistical analysis to quantitatively describe the degree of order and an assessment of the optical properties of single line arrays.

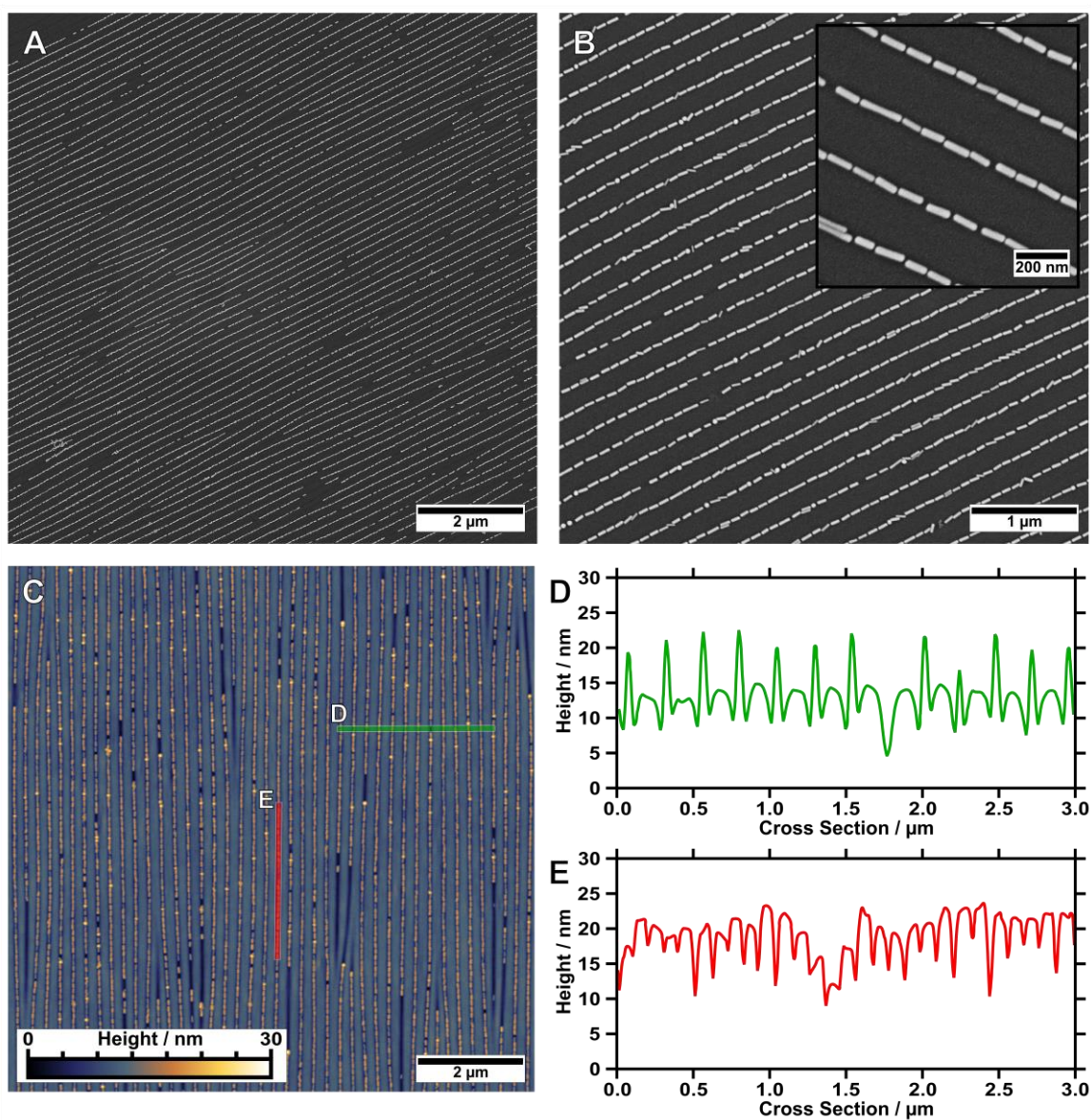


**Figure 6.5.** (A) Representative, low-magnification SEM image ( $10 \times 10 \mu\text{m}^2$ ) of gold nanorods organised in single lines on a wrinkle-substrate. (B) Gold nanorods organised in single lines show a remarkably low amount of morphological impurities. The magnified inset highlights the high degree of order as well as the small interparticle gap sizes. (C) Corresponding AFM image ( $10 \times 10 \mu\text{m}^2$ ) with cross-sections measured (D) perpendicular to the wrinkles (in green) and (E) along the channel direction (in red).

In order to, study the homogeneity of the assembled gold nanorod arrays and structural parameters such as periodicity and filling factor, we recorded a series of SEM images with different magnifications on different spots of the substrate. Representative SEM micrographs are shown in **Figure 6.5**. The SEM micrograph with lower magnification confirms the high degree of selectivity. On the investigated 10 times  $10 \mu\text{m}$  areas (**Figure 6.5A**), no rods were identified outside

the wrinkles. Furthermore, we found a high degree of filling along with well-defined orientation parallel to the wrinkles on the whole area. **Figure 6.5B** shows an SEM image measured with higher magnification highlighting the closepacking of the nanorods organised in single lines. The AFM measurements shown in **Figure 6.5C** and the cross-sections in **Figure 6.5D-E** confirm a wrinkle amplitude smaller than the particle diameter. In order to, quantitatively assess the quality of the arrays, we determined the overall order parameter  $S_{2D}$ , the interparticle gap size and the one-dimensional filling factor using a semi-automated IGOR Pro procedure (see experimental part).

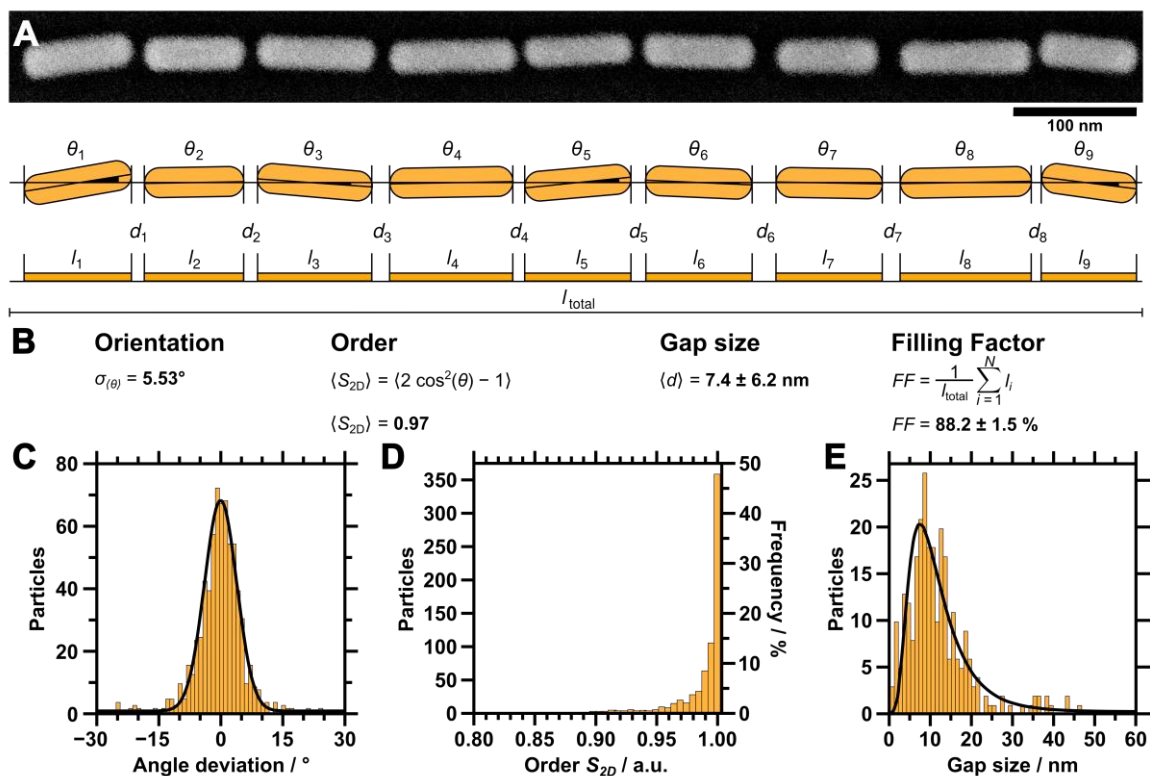


**Figure 6.6.** (A) High magnification SEM image of an exemplary single nanorod line (top) and a schematic depiction of the parameter evaluation (bottom). The angle deviations  $\theta$  of each single particle along with the interparticle gap distances  $d$  were determined with a semi-automated procedure (IGOR Pro, Wavemetrics). (B) Summary of the equations used for analysis. (C) Distribution of the deviation from the mean angle of individual particles (bin size  $1^\circ$ , Gaussian fit,  $\sigma_{(\theta)}$  of  $5.53^\circ$ ). (D) Distribution of the order of orientation as determined from the angle deviation (bin size 0.05,  $\langle S_{2D} \rangle = 0.97$ ). (E) Gap size distribution (bin size 1.117 nm, LogNormal fit,  $\langle d \rangle = 7.4 \pm 6.2 \text{ nm}$ ). The filling factor was determined to be  $88.2 \pm 1.5\%$ .

As shown in **Figure 6.6A** for a representative higher magnification SEM image, SEM images were in a first step converted to binary data that allowed for precisely

tracing the boundaries of the particles. The preferred orientation and deviations from it, as well as fill factor and interparticle distances could thus be evaluated as described in the experimental section in detail. **Figure 6.6B** summarises the results for these parameters. The determined angle deviations for individual nanorods are plotted as a histogram in **Figure 6.6C**. A Gaussian fit provides a standard deviation  $\sigma_{\langle\theta\rangle}$  of  $5.53^\circ$ . For quantifying the degree of the order of orientation we determine the averaged two-dimensional order parameter  $\langle S_{2D} \rangle$  from the angle deviation  $\theta$  of individual nanorods according to  $S_{2D} = 2 \cos(\theta)^2 - 1$ . For an ideal structure, one expects an order parameter of unity, whereas a completely disordered structure would result in an order parameter of zero. Our macroscopic assemblies allow us for the first time to evaluate  $\langle S_{2D} \rangle$  with high statistical significance.  $S_{2D}$  was determined for more than 700 particles on a sample area larger than  $15 \mu\text{m}^2$ . The resulting values are plotted in **Figure 6.6D**. Consequently, the averaged two-dimensional order parameter  $\langle S_{2D} \rangle$  was determined to be 0.97. This further validates the high degree of structural control with our process. Interparticle gaps were measured to determine the mean gap size and the overall filling factor. The results for the gap sizes are plotted as a histogram in **Figure 6.6E**. The applied LogNormal fit yields a mean gap size of only  $7.4 \pm 6.2 \text{ nm}$ . The filling factor was determined as  $88.2 \pm 1.5\%$  within the analysed area. The low average interparticle gap size will result in plasmonic coupling of adjacent nanoparticles as it is well below the dimensions of the individual constituents. At the same time, the high degree of filling should ensure that the effects are strong enough to be detectable in macroscopic UV/vis/NIR spectroscopy. Therefore, we proceeded with the transfer to flat substrates and spectroscopic characterisation.

### Capillary Printing Transfer and Spectroscopic Characterisation

To characterise the gold nanorod arrays optically, we transferred the single line assemblies onto transparent ITO-coated glass substrates. Besides its transparency, ITO provides electric conductivity, which allows for high magnification SEM characterisation without previous application of a conducting layer. Thus, the samples can be characterised with SEM prior to UV/vis/NIR measurements. Transfer onto flat ITO substrates that were cleaned by the RCA SC-1 method<sup>52</sup> and functionalised with a PEI layer for enhanced adhesion was conducted as described

before.<sup>14</sup> A 5  $\mu\text{L}$  droplet of water (pH 10) in between the organised films and the substrate promotes transfer from the hydrophobic wrinkle-substrate to the hydrophilic ITO surface driven by capillary forces. To ensure conformal contact between the wrinkles and the ITO target surface, the sample was pressed (140 kPa) onto the substrate using a metal block. This method is highly flexible and can be employed for transferring organised nanorods onto almost every target substrate as long as the substrate is flat and hydrophilic, *e.g.* gold and glass samples.<sup>14,19</sup> To verify the successful transfer, both the ITO substrate and the residual wrinkles were analysed by SEM and AFM. SEM images of the transferred structure show the transfer to the conductive substrate as displayed in **Figure 6.7A**.

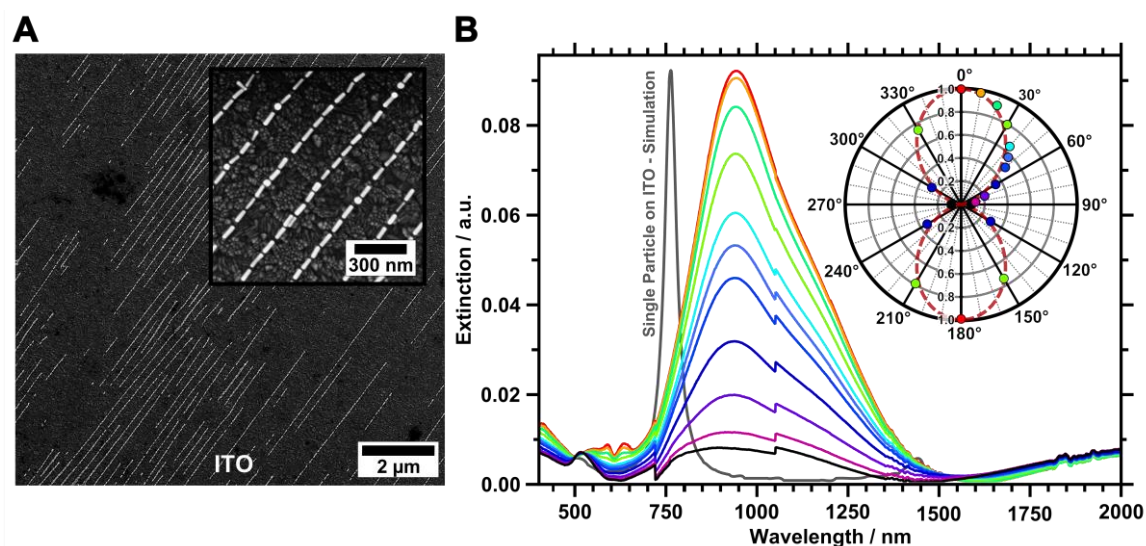


**Figure 6.7.** (A) SEM of gold nanoparticles transferred onto a flat ITO substrate surface functionalised with PEI. (B) Polarisation angle-dependent UV/vis/NIR extinction spectra were recorded from  $0^\circ$  (red) to  $90^\circ$  (black) in  $10^\circ$  steps including  $45^\circ$ . The normalised cross-section intensity of the L-LSPR is plotted as a polar plot (inset). The dashed red line represents a fitted cosine squared function.

Extinctions were measured with angles of polarisation between  $0^\circ$  (parallel to organised nanorod lines) and  $90^\circ$  (perpendicular to organised nanorod lines). The resulting extinction spectra are plotted in **Figure 6.7B**, and show strong polarisation dependency along with a complex plasmonic mode structure. The most prominent spectral feature is a pronounced longitudinal resonance in the range of 750 to 1500 nm. This resonance is characterised by a dominant peak at 941 nm along with a small shoulder around 1200 nm.

The extinction cross-section intensity of the longitudinal mode is strongly polarisation dependent. Thus, the highest extinction intensity is observed for excitation polarised parallel to the linear assembled nanorods. For light polarised perpendicular to the orientation of the gold nanorods a transversal mode is observed that is slightly shifted towards the red compared to particles in solution. The longitudinal mode is strongly reduced for this polarisation, resulting in an extinction cross-section of comparable intensity as observed for the transversal mode. The measured extinction spectra clearly reveal that the well-aligned gold nanorods render the sample optically anisotropic. This significant effect characterised by a strong decrease of the L-LSPR peak height is summarised in the polar plot in the inset in **Figure 6.7B** also including data measured for angles larger than 90°. The data shown in the polar plot were normalised to the peak maxima of the longitudinal mode at an angle of polarisation of zero degree. The changes in peak intensity are well described with a cosine square function. We used the equation  $S_{\text{optical}} = 1 - (A_{\perp} / A_{\parallel})$  to determine an optical order parameter  $S_{\text{optical}}$  of 0.91.<sup>53,54</sup> to the best of our knowledge, such a remarkably high optical order obtained from self-assembled anisotropic colloids has not been reported before.

FDTD modelling of a single nanorod located on an ITO substrate predicts the single particle L-LSPR at 761 nm as shown in **Figure 6.7B**. Thus, the experimentally found strongly red-shifted L-LSPR is clearly not a single particle feature, but due to strong coupling of multiple particles.<sup>14,15,45</sup> However, the detailed investigation of the observed fine structure of the plasmonic coupling modes will be subject of a future study.

## Conclusion

We presented an efficient method to prepare macroscopic arrays of well-aligned gold nanorods, which can be transferred to transparent substrates. The applied multistep procedure includes the synthesis of monodisperse gold nanorods as anisotropic building blocks, followed by a surface functionalisation which allows the elimination of the present surfactant while keeping the nanoparticles colloidally stable. Thus, the particles become compatible with wrinkle-assisted assembly on hydrophilic substrates. We demonstrated the preparation of triple,

double and single line structures *via* dip-coating. The key parameter for organising anisotropic nanoparticles into well-defined structures was found to be the amplitude of the wrinkle-templates, which can be tuned *via* variation of the plasma post-treatment duration. This parameter offers control over the structure type, finally enabling the strong confinement of nanorods in single lines with small average interparticle distances. Evaluation of SEM images for single lines revealed an extremely high averaged two-dimensional order parameter  $\langle S_{2D} \rangle$  with a value of 0.97. This finding correlates well with the resulting anisotropic optical behaviour yielding an optical order parameter  $S_{\text{optical}}$  of 0.91. For self-assembled nanorods such high order parameters on macroscopic areas have not been reported in literature yet. Furthermore, the nanorod double lines have a high potential for the preparation of bottom-up self-assembled optical metamaterials. Such assemblies could provide an effective negative refractive index as not only the permittivity but also the permeability should be below zero according to literature.<sup>12</sup> However, the presented multi-hierarchical structures already represent metamaterials as the effective optical properties are located in a spectral range 5 times larger than the periodicity and 10 times larger than the individual building blocks.<sup>55,56</sup> In consequence, the presented functional materials might find application in various emerging fields such as optical filters, waveguiding, non-linear optics, and metamaterials.

## Experimental

### Materials

Silver nitrate ( $\text{AgNO}_3$ , 99.9999%), sodium borohydride ( $\text{NaBH}_4$ , 99%), hydroquinone (HQ, > 99%), hydrogen tetrachloroaurate ( $\text{HAuCl}_4$ , > 99.9%), ammonia hydroxide solution (25%), hydrogen peroxide (30%), polyethylenimine (PEI, 25000 g/mol, highly branched), ITO substrates (roughness ( $R_a$ ) of 2.68 nm, resistance of 8 - 12  $\Omega/\text{sq}$ ) and bovine serum albumin (BSA, 98%) were purchased from Sigma Aldrich. Citrate (99%) and 1 M NaOH solutions were supplied by Grüssing. Cetyltrimethylammonium bromide (CTAB, 99%, 0.359 mg/kg iodine) was received from Merck KGaA. Sylgard 184 PDMS elastomer kits were purchased from Dow Corning. All chemicals and solvents were used as received. Pure-grade solvents and Milli-Q-grade water were used in all preparations.

### Gold Nanorods

The protocol for the preparation of single crystalline gold nanorods was adopted from Vigderman and Zubarev.<sup>43</sup> Briefly, single crystalline seeds were prepared by the addition of 5 mL of 0.2 M aqueous CTAB solution to 5 mL of an aqueous 0.5 mM HAuCl<sub>4</sub>·3H<sub>2</sub>O solution (47.3 μL of a 0.10569 M HAuCl<sub>4</sub>·3H<sub>2</sub>O stock solution). The reaction was initiated under rapid stirring at 1200 rpm by the injection of 600 μL of a 0.01 mM freshly prepared NaBH<sub>4</sub> solution. Stirring was continued for 2 min followed by aging of the seeds at 32 °C for 30 min without stirring. For the growth solution 1183 μL of an aqueous 0.10569 M solution of HAuCl<sub>4</sub>·3H<sub>2</sub>O (f.c.: 0.5 mM) were added to 250 mL of a 0.1 M aqueous CTAB solution. Followed by the addition of 500 μL of a 0.1 M AgNO<sub>3</sub> concentration (f.c.: 0.2 mM). After shaking, 12.5 mL of an aqueous solution containing 0.1 M hydroquinone (final concentration is 5 mM) were added. After the mixture became clear, 3 mL of the seeds were added under rapid stirring at 1000 rpm and the solution was stored at 32 °C overnight.

### BSA Functionalisation

BSA functionalisation was performed by concentrating 250 mL gold nanorods to 40 mL *via* centrifugation at 4000 RCF. Subsequently, 10 mL of this stock solution were used for further functionalisation. First, the CTAB concentration was set to 1 mM. Directly before functionalisation, the CTAB concentration was reduced to 0.1 mM followed by the addition of the 10 mL nanorod solution to 30 mL of a 10 mg/mL BSA solution containing 0.02 wt.% citrate. The solution was sonicated for 20 min and centrifuged at 3000 RCF. After removal of the supernatant, 20 mL of a 1 mg/mL BSA solution containing 0.02 wt.% citrate (adjusted to pH 10) was added. The nanoparticles were incubated overnight in a fridge at 8 °C. Functionalised nanorods were washed at least 4 times at 2500 RCF with Milli-Q water with a pH 10 adjusted with 1 M NaOH.

### Wrinkle-Templates

PDMS was prepared by casting 25 g of a well-dispersed (1:5 ratio) cross-linker / pre-polymer mixture into a balanced rectangular polystyrene dish. The plastic dish was covered to prevent the PDMS from impurities. Subsequently, the PDMS was cross-linked at RT for 24 h, followed by cross-linking at 80 °C for 5 h. Next, the cross-linked elastomer was cut into pieces of sizes of 1 x 4.5 cm<sup>2</sup> and stretched to the desired value in a home built stretching apparatus. By plasma treatment, with

an oxygen pressure in the range between 0.6 - 1.2 mbar, a thin stiff SiO<sub>2</sub> layer was applied.<sup>51</sup> Upon relaxation, wrinkles were formed on the surface of the PDMS. The applied plasma-treatment parameters are summarised in **Table 6.1**.

### Post-Treatment

Wrinkle-templates were cut into pieces of sizes of 7 x 10 mm<sup>2</sup>. To remove dust, the templates were sonicated in Milli-Q water at RT for 15 s and dried under a N<sub>2</sub> stream, followed by applying a low-pressure (0.2 mbar) oxygen plasma with controlled post-treatment parameters summarised in **Table 6.2**. Glass slides with sizes of 8 x 100 mm<sup>2</sup> were cut from commercially available glass slides and were sonicated with Milli-Q water at RT for 15 s. Next they were washed with EtOH and dried under a N<sub>2</sub> stream. The glass-slides were plasma activated together with the wrinkle-templates. Afterwards, the wrinkle-templates were placed onto the glass to fix them covalently. The wrinkles were always orientated parallel to the major axis of the glass slides.

**Table 6.2:** Parameters for post-treatment process.

Sample	Figure	Post-treatment time (s)	Periodicity* (nm)	Amplitude* (nm)
1	Fig. 6.4A	30	260	26.5
2	Fig. 6.4B	30	213	15.3
3	Fig. 6.4C & 6.5	60	228	5.2
4	Fig. 6	30	233 <sup>§</sup>	7.7 <sup>§</sup>

\*Final periodicity and amplitude

<sup>§</sup>Values were determined for transferred nanorods on ITO

### Dip-Coating

Dip-coating was performed on fixed wrinkle-templates. The as-prepared samples were clamped into the dip-coater with the wrinkle-templates at the bottom end. UV/vis/NIR glass cuvettes with a size of 10 x 10 mm<sup>2</sup> were used as containers for the gold-solutions. A volume of 500 µL with a gold concentration of 1.2 mg/mL (if not stated differently) was used for the dip-coating experiments. The samples were quickly immersed into the solution followed by slow removing with 10 µm/min (if not stated differently). All parameters used for dip-coating are summarised in **Table 6.3**.

**Table 6.3:** Parameters for dip-coating.

Sample	Figure	Particle concentration (mg/mL)	Orientation (°)	Withdrawing speed ( $\mu\text{m min}^{-1}$ )
1	Fig. 6.4A	1.2	0	100
2	Fig. 6.4B	1.2	0	10
3	Fig. 6.4C & 6.5	1	0	10
4	Fig. 6.7	0.8	0	10

### RCA Cleaning

RCA SC-1 cleaning was performed following a simplified protocol based on a procedure published by Kern and Puotinen.<sup>52</sup> Briefly, the ITO substrates were cut into pieces of  $10 \times 20 \text{ mm}^2$  and ultrasonically treated for 20 min in an isopropanol/water mixture with a ratio of 3:1 (v/v), rinsed with water, and placed in a bath containing an  $\text{NH}_3$  (25%) /  $\text{H}_2\text{O}_2$  (30%) / water mixture with a ratio of 1:1:5 (v/v/v) at 80 °C for 15 min. The cleaned substrates were rinsed with Milli-Q water and stored in a water bath until their usage.

### Transfer

The transfer of the organised gold nanorods in wrinkles onto ITO substrates was performed following a protocol published recently.<sup>14</sup> Briefly, the cleaned ITO substrates were coated with a PEI layer by placing them in an aqueous solution containing 10 g/L PEI. After 30 min the ITO substrates were rinsed with water and dried under a  $\text{N}_2$  stream. The functionalised substrates were directly used for transfer. A 5  $\mu\text{L}$  droplet of water (pH 10) was applied on the surface. Next, the wrinkle-templates were placed on the surface and for better adhesion pressed onto the ITO surface using a metal bar with an effective pressure of 140 kPa. After 4 h, the transfer was accomplished and the wrinkle-template was removed.

### Instrumentation and Data Evaluation

#### TEM Measurements

TEM measurements were performed on a Zeiss 922 OMEGA EFTEM at a voltage of 120 kV. Zero-loss filtered images were recorded using a bottom mounted Ultrascan 1000 (Gatan) CCD camera system. Gatan Digital Micrograph 3.9 for GMS 1.4 software was used for image acquisition. TEM samples were concentrated and

in the case of CTAB the surfactant concentration was set to 1 mM. Droplets of 2  $\mu$ L were dried on Quantifoil 300 mesh copper grid with carbon films. For size evaluation the software ImageJ (version 1.44p, U.S. National Institute of Health) was used. For the determination of the mean particle diameters 150 particles / sample were measured.

### **UV/vis/NIR Measurements**

UV/vis/NIR spectra were measured with a Cary 5000 spectrophotometer (Agilent, USA) with an attached Cary Universal Measurement Accessory (UMA). For film measurements, first, background spectra for all angles were recorded on the sample at a location without structure. All spectra were recorded with a slit width set to 1 nm for UV/vis and 4 nm for NIR with an integration time set to 0.2 s resulting in 300 nm/min recorded over a spectral range from 350 to 2500 nm. The measured spot size on the substrate was 4 x 4 mm<sup>2</sup>. All angles were measured in steps of 10° including 45°, beyond 90° the step size was set to 30°. The presented extinction spectra were calculated dividing the transmission spectra of the sample by the transmission spectra of the background followed by applying a negative logarithm to create extinction spectra. Due to slight inconsistency of the measured background and the background at the structure, the baseline corrected transmission spectra exhibited a value above 100% for parts of the spectral range (note this artefacts did not occur within the range of the peak position). This resulted in physically not meaningful negative extinction for small spectral ranges. To correct this artefact, all extinction spectra were shifted by a fixed value (0.014) not affecting the relative extinction values. Additionally, due to the low overall extinction, changeover artefacts are apparent. However, we decided not to correct the spectral data with respect to these artefacts and show them in a raw fashion. The authors are aware that, as a consequence, the calculated peak height is not fully consistent and the anisotropy might be slightly overestimated for angles above 45°.

### **AFM Measurements**

AFM images were obtained using two different commercial atomic force microscope instruments, a Nanoscope Dimension V and a Dimension Icon atomic force microscope (AFM) from Bruker, USA, operated in TappingMode™. Al-coated silicon cantilevers (OTESPA, Bruker) with a stiffness of typically 35 - 47.2 N/m and

typical resonance frequencies of 300 kHz were utilised. Image processing and analysis was conducted in Gwyddion by David Nečas and Petr Klapetek.<sup>57</sup>

### **SEM Measurements**

SEM micrographs were recorded on a LEO 1530 FE-SEM (Zeiss, Germany) with in-lens and SE2 detectors using an acceleration voltage of 3 kV. To enhance the conductivity on the wrinkle-templates they were covered with a 1.3 nm Pt layer using a HR208 sputter coater and a mtm20 thickness controller (Cressington Scientific Instruments).

### **Dip-Coating**

For dip-coating experiments a DC/D/LM system from KSV Instruments, Germany was used.

### **Plasma Treatment**

Oxygen plasma treatment was performed using a Flecto 10 from Plasma Technology, Germany.

### **Contact Angle Measurements**

Contact angle measurements were performed using a DataPhysica OCA instrument from DataPhysics, Germany. The measurements were done on a hydrophilised PDMS substrate (0.2 mbar, 30 s) using a 0.5 mM CTAB solution. The contact angles of the applied droplets were measured after 150 s to ensure for equilibrium conditions. The measurements were repeated 4 times.

### **Image Evaluation**

Image evaluation was performed by a semi-automatic procedure in IGOR Pro by Wavemetrics, USA. First, the 8 Bit SEM images were corrected for maximum contrast and converted to binary data based on a grey value threshold that allowed for precisely tracing the boundaries of the particles. Particles touching the edges of the image were excluded from the evaluation. Next, the positions of each particle were located at the centres of the individual particle boundaries. The particle orientation was determined based on the weighted boundary-to-centre distances in the 8 Bit image. The relative angle deviations were calculated in reference to the mean angle of the complete image. The equation  $S_{2D} = 2 \cos(\theta)^2 - 1$  was applied to calculate the two-dimensional order parameter  $S_{2D}$ . The distribution of gap sizes

was evaluated from the corrected 8 Bit images and the particle positions as overlay. The individual particle lines were identified and represented by a linear regression of the centres of contributing particles. Gaps were evaluated manually from the intensity profiles along each particle line based on a threshold grey value (half maximum). The filling factor describes the one-dimensional allocation of space of each particle based on its projection onto the aforementioned linear regression of the respective particle line. The sum of all projections was set in relation to the total length of the regression line.

### **FDTD Simulations**

Simulations of the extinction cross-section spectra were done using commercial software from Lumerical Solutions, Inc. (FDTD Solutions, Version 8.7.3). We modelled the gold nanorods in water (index of 1.333). In agreement with the experimental peak position, we chose a cap radius of 10 nm and nanorod dimensions according to TEM analysis. The simulation for nanorods on substrates were performed for a single nanorod covered with a 2 nm layer BSA (index of 1.48)<sup>14,58</sup> located on an ITO layer modified with a 2 nm roughness layer in air.<sup>59</sup> For a broadband source simulation (total-field scattered-field source, 300 - 1300 nm), the FDTD software approximates the refractive index of the materials by a polynomial function. For the optical constants of Au we applied a fitting of the experimental data by Johnson and Christy (JC) (6 coefficients, 1 imaginary weight: 0.211 RMS error).<sup>60</sup> A simulation mesh size of 1 nm was chosen and the zero-conformal-variant mesh refinement was used. For the best simulation stability, the mesh area was chosen to be 50 nm larger than the existing structure in all three principal directions. All simulations reached the auto shut off level of  $10^{-5}$  before reaching 150 fs simulation time. Anti-symmetric boundary conditions (BC) were used normal to the polarisation plane and symmetric BC are used parallel to the polarisation plane. In radiation direction we used in both directions the perfect match layer (PML) BCs.

### **Acknowledgements**

This study was funded by the European Research Council under grant ERC-2012-StG 306686 (METAMECH: Template-assisted assembly of METAmaterials using MECHanical instabilities) and by the German Research Foundation (DFG) within

the collaborative research centre SFB 840. M.T. was supported by the University of Bayreuth graduate school and by the Elite Network Bavaria in the framework of the Elite Study Program “Macromolecular Science” and funded *via* a grant for PhD candidates according to Bavarian elite promotion law (BayEFG).

## References

- (1) Rey, A.; Billardon, G.; Lortscher, E.; Moth-Poulsen, K.; Stuhr-Hansen, N.; Wolf, H.; Bjornholm, T.; Stemmer, A.; Riel, H., Deterministic assembly of linear gold nanorod chains as a platform for nanoscale applications. *Nanoscale* **2013**, *5*, 8680-8688.
- (2) Kim, Y.; Zhu, J.; Yeom, B.; Di Prima, M.; Su, X.; Kim, J.-G.; Yoo, S. J.; Uher, C.; Kotov, N. A., Stretchable nanoparticle conductors with self-organized conductive pathways. *Nature* **2013**, *500*, 59-63.
- (3) Kim, J.-Y.; Kotov, N. A., Charge Transport Dilemma of Solution-Processed Nanomaterials. *Chem Mater* **2013**, *26*, 134-152.
- (4) Ren, M.; Plum, E.; Xu, J.; Zheludev, N. I., Giant nonlinear optical activity in a plasmonic metamaterial. *Nat Commun* **2012**, *3*:833, 1-6.
- (5) Hentschel, M.; Utikal, T.; Giessen, H.; Lippitz, M., Quantitative Modeling of the Third Harmonic Emission Spectrum of Plasmonic Nanoantennas. *Nano Lett* **2012**, *12*, 3778-3782.
- (6) Hanke, T.; Cesar, J.; Knittel, V.; Trügler, A.; Hohenester, U.; Leitenstorfer, A.; Bratschitsch, R., Tailoring Spatiotemporal Light Confinement in Single Plasmonic Nanoantennas. *Nano Lett* **2012**, *12*, 992-996.
- (7) Atwater, H. A.; Polman, A., Plasmonics for improved photovoltaic devices. *Nat Mater* **2010**, *9*, 205-213.
- (8) Karg, M.; König, T. A. F.; Retsch, M.; Stelling, C.; Reichstein, P. M.; Honold, T.; Thelakkat, M.; Fery, A., Colloidal self-assembly concepts for light management in photovoltaics. *Mater Today* **2014**, *18*, 185-205.
- (9) Shalaev, V. M., Optical negative-index metamaterials. *Nat Photonics* **2007**, *1*, 41-48.

- (10) Drachev, V. P.; Cai, W.; Chettiar, U.; Yuan, H. K.; Sarychev, A. K.; Kildishev, A. V.; Klimeck, G.; Shalaev, V. M., Experimental verification of an optical negative-index material. *Laser Phys Lett* **2006**, *3*, 49-55.
- (11) Dolling, G.; Wegener, M.; Schädle, A.; Burger, S.; Linden, S., Observation of magnetization waves in negative-index photonic metamaterials. *Appl Phys Lett* **2006**, *89*, 231118-231121.
- (12) Dolling, G.; Enkrich, C.; Wegener, M.; Zhou, J. F.; Soukoulis, C. M.; Linden, S., Cut-wire pairs and plate pairs as magnetic atoms for optical metamaterials. *Opt Lett* **2005**, *30*, 3198-3200.
- (13) Vigderman, L.; Khanal, B. P.; Zubarev, E. R., Functional Gold Nanorods: Synthesis, Self-Assembly, and Sensing Applications. *Adv Mater* **2012**, *24*, 4811-4841.
- (14) Hanske, C.; Tebbe, M.; Kuttner, C.; Bieber, V.; Tsukruk, V. V.; Chanana, M.; König, T. A. F.; Fery, A., Strongly Coupled Plasmonic Modes on Macroscopic Areas via Template-Assisted Colloidal Self-Assembly. *Nano Lett* **2014**, *14*, 6863–6871.
- (15) Funston, A. M.; Novo, C.; Davis, T. J.; Mulvaney, P., Plasmon Coupling of Gold Nanorods at Short Distances and in Different Geometries. *Nano Lett* **2009**, *9*, 1651-1658.
- (16) Lu, C.; Moehwald, H.; Fery, A., A lithography-free method for directed colloidal crystal assembly based on wrinkling. *Soft Matter* **2007**, *3*, 1530-1536.
- (17) Mueller, M.; Tebbe, M.; Andreeva, D. V.; Karg, M.; Alvarez-Puebla, R. A.; Pazos-Perez, N.; Fery, A., Large-Area Organization of pNIPAM-Coated Nanostars as SERS Platforms for Polycyclic Aromatic Hydrocarbons Sensing in Gas Phase. *Langmuir* **2012**, *28*, 9168-9173.
- (18) Mueller, M.; Karg, M.; Fortini, A.; Hellweg, T.; Fery, A., Wrinkle-assisted linear assembly of hard-core/soft-shell particles: impact of the soft shell on the local structure. *Nanoscale* **2012**, *4*, 2491-2499.

- (19) Hanske, C.; Mueller, M. B.; Bieber, V.; Tebbe, M.; Jessl, S.; Wittemann, A.; Fery, A., The Role of Substrate Wettability in Nanoparticle Transfer from Wrinkled Elastomers: Fundamentals and Application toward Hierarchical Patterning. *Langmuir* **2012**, *28*, 16745-16750.
- (20) Schweikart, A.; Pazos-Perez, N.; Alvarez-Puebla, R. A.; Fery, A., Controlling inter-nanoparticle coupling by wrinkle-assisted assembly. *Soft Matter* **2011**, *7*, 4093-4100.
- (21) Schweikart, A.; Fortini, A.; Wittemann, A.; Schmidt, M.; Fery, A., Nanoparticle assembly by confinement in wrinkles: experiment and simulations. *Soft Matter* **2010**, *6*, 5860-5863.
- (22) Horn, A.; Hiltl, S.; Fery, A.; Boeker, A., Ordering and Printing Virus Arrays: A Straightforward Way to Functionalize Surfaces. *Small* **2010**, *6*, 2122-2125.
- (23) Horn, A.; Schoberth, H. G.; Hiltl, S.; Chiche, A.; Wang, Q.; Schweikart, A.; Fery, A.; Boeker, A., Nanostructured wrinkled surfaces for templating bionanoparticles-controlling and quantifying the degree of order. *Faraday Discuss* **2009**, *143*, 143-150.
- (24) Lee, J.; Seo, J.; Kim, D.; Shin, S.; Lee, S.; Mahata, C.; Lee, H.-S.; Min, B.-W.; Lee, T., Capillary Force-Induced Glue-Free Printing of Ag Nanoparticle Arrays for Highly Sensitive SERS Substrates. *ACS Appl Mater Interfaces* **2014**, *6*, 9053-9060.
- (25) Lee, S. G.; Kim, H.; Choi, H. H.; Bong, H.; Park, Y. D.; Lee, W. H.; Cho, K., Evaporation-Induced Self-Alignment and Transfer of Semiconductor Nanowires by Wrinkled Elastomeric Templates. *Adv Mater* **2013**, *25*, 2162-2166.
- (26) Endo, H.; Mochizuki, Y.; Tamura, M.; Kawai, T., Bio-inspired, topologically connected colloidal arrays via wrinkle and plasma processing. *Colloids Surf A* **2014**, *443*, 576-582.

- (27) Brück, R.; Hiltl, S.; Schröder, V.; von Essen, C.; Böker, A., Designing Zwitterionic SiO<sub>2</sub>NH<sub>2</sub>-Au Particles with Tunable Patchiness using Wrinkles. *Part Part Syst Charact* **2014**, *31*, 871-878.
- (28) Pazos-Perez, N.; Ni, W.; Schweikart, A.; Alvarez-Puebla, R. A.; Fery, A.; Liz-Marzan, L. M., Highly uniform SERS substrates formed by wrinkle-confined drying of gold colloids. *Chem Sci* **2010**, *1*, 174-178.
- (29) Solis, D.; Willingham, B.; Nauert, S. L.; Slaughter, L. S.; Olson, J.; Swanglap, P.; Paul, A.; Chang, W.-S.; Link, S., Electromagnetic Energy Transport in Nanoparticle Chains via Dark Plasmon Modes. *Nano Lett* **2012**, *12*, 1349-1353.
- (30) Lal, S.; Link, S.; Halas, N. J., Nano-optics from sensing to waveguiding. *Nat Photonics* **2007**, *1*, 641-648.
- (31) Slaughter, L. S.; Wu, Y.; Willingham, B. A.; Nordlander, P.; Link, S., Effects of Symmetry Breaking and Conductive Contact on the Plasmon Coupling in Gold Nanorod Dimers. *ACS Nano* **2010**, *4*, 4657-4666.
- (32) Funston, A. M.; Gómez, D. E.; Karg, M.; Vernon, K. C.; Davis, T. J.; Mulvaney, P., Aligned Linear Arrays of Crystalline Nanoparticles. *J Phys Chem Lett* **2013**, *4*, 1994-2001.
- (33) Gupta, M. K.; König, T.; Near, R.; Nepal, D.; Drummy, L. F.; Biswas, S.; Naik, S.; Vaia, R. A.; El-Sayed, M. A.; Tsukruk, V. V., Surface Assembly and Plasmonic Properties in Strongly Coupled Segmented Gold Nanorods. *Small* **2013**, *9*, 2979-2990.
- (34) Vernon, K. C.; Funston, A. M.; Novo, C.; Gómez, D. E.; Mulvaney, P.; Davis, T. J., Influence of Particle–Substrate Interaction on Localized Plasmon Resonances. *Nano Lett* **2010**, *10*, 2080-2086.
- (35) Becker, J.; Zins, I.; Jakab, A.; Khalavka, Y.; Schubert, O.; Sönnichsen, C., Plasmonic Focusing Reduces Ensemble Linewidth of Silver-Coated Gold Nanorods. *Nano Lett* **2008**, *8*, 1719-1723.

- (36) Liu, N.; Giessen, H., Kopplungseffekte in optischen Metamaterialien. *Angew Chem* **2010**, *122*, 10034-10049.
- (37) Liu, N.; Hentschel, M.; Weiss, T.; Alivisatos, A. P.; Giessen, H., Three-Dimensional Plasmon Rulers. *Science* **2011**, *332*, 1407-1410.
- (38) Wang, J.; Li, M.; Tang, B.; Xie, P.; Ma, L.; Hu, Z.; Zhao, Y.; Wei, Z., Assembling single gold nanorods into large-scale highly aligned nanoarrays via vacuum-enhanced capillarity. *Nanoscale Res Lett* **2014**, *9*, 556-556.
- (39) Liu, Z.; Huang, H.; He, T., Large-Area 2D Gold Nanorod Arrays Assembled on Block Copolymer Templates. *Small* **2013**, *9*, 505-510.
- (40) Kuemin, C.; Nowack, L.; Bozano, L.; Spencer, N. D.; Wolf, H., Oriented Assembly of Gold Nanorods on the Single-Particle Level. *Adv Funct Mater* **2012**, *22*, 702-708.
- (41) Kuemin, C.; Stutz, R.; Spencer, N. D.; Wolf, H., Precise Placement of Gold Nanorods by Capillary Assembly. *Langmuir* **2011**, *27*, 6305-6310.
- (42) Holzner, F.; Kuemin, C.; Paul, P.; Hedrick, J. L.; Wolf, H.; Spencer, N. D.; Duerig, U.; Knoll, A. W., Directed Placement of Gold Nanorods Using a Removable Template for Guided Assembly. *Nano Lett* **2011**, *11*, 3957-3962.
- (43) Vigderman, L.; Zubarev, E. R., High-Yield Synthesis of Gold Nanorods with Longitudinal SPR Peak Greater than 1200 nm Using Hydroquinone as a Reducing Agent. *Chem Mater* **2013**, *25*, 1450-1457.
- (44) Huang, X.; Neretina, S.; El-Sayed, M. A., Gold Nanorods: From Synthesis and Properties to Biological and Biomedical Applications. *Adv Mater* **2009**, *21*, 4880-4910.
- (45) Solís, D. M.; Taboada, J. M.; Obelleiro, F.; Liz-Marzán, L. M.; García de Abajo, F. J., Toward Ultimate Nanoplasmonics Modeling. *ACS Nano* **2014**, *8*, 7559-7570.

- (46) Strozyk, M. S.; Chanana, M.; Pastoriza-Santos, I.; Pérez-Juste, J.; Liz-Marzán, L. M., Protein/Polymer-Based Dual-Responsive Gold Nanoparticles with pH-Dependent Thermal Sensitivity. *Adv Funct Mater* **2012**, *22*, 1436-1444.
- (47) Tebbe, M.; Kuttner, C.; Männel, M.; Fery, A.; Chanana, M., Colloidally Stable and Surfactant-Free Protein-Coated Gold Nanorods in Biological Media. *ACS Appl Mater Interfaces* **2015**, *7*, 5984-5991.
- (48) Chanana, M.; Rivera\_Gil, P.; Correa-Duarte, M. A.; Liz-Marzán, L. M.; Parak, W. J., Physicochemical Properties of Protein-Coated Gold Nanoparticles in Biological Fluids and Cells before and after Proteolytic Digestion. *Angew Chem, Int Ed* **2013**, *52*, 4179-4183.
- (49) Chanana, M.; Correa-Duarte, M. A.; Liz-Marzán, L. M., Insulin-Coated Gold Nanoparticles: A Plasmonic Device for Studying Metal-Protein Interactions. *Small* **2011**, *7*, 2650-2660.
- (50) Efimenko, K.; Rackaitis, M.; Manias, E.; Vaziri, A.; Mahadevan, L.; Genzer, J., Nested self-similar wrinkling patterns in skins. *Nat Mater* **2005**, *4*, 293-297.
- (51) Glatz, B. A.; coworkers, (*in preparation*).
- (52) Kern, W.; Puotinen, D. A., Cleaning Solutions Based on Hydrogen Peroxide for Use in Silicon Semiconductor Technology. *RCA Rev* **1970**, *31*, 187-206.
- (53) Liu, Q.; Cui, Y.; Gardner, D.; Li, X.; He, S.; Smalyukh, I. I., Self-Alignment of Plasmonic Gold Nanorods in Reconfigurable Anisotropic Fluids for Tunable Bulk Metamaterial Applications. *Nano Lett* **2010**, *10*, 1347-1353.
- (54) Pérez-Juste, J.; Rodríguez-González, B.; Mulvaney, P.; Liz-Marzán, L. M., Optical Control and Patterning of Gold-Nanorod-Poly(vinyl alcohol) Nanocomposite Films. *Adv Funct Mater* **2005**, *15*, 1065-1071.
- (55) Smith, D. R.; Pendry, J. B.; Wiltshire, M. C. K., Metamaterials and Negative Refractive Index. *Science* **2004**, *305*, 788-792.

- (56) Linden, S.; Enkrich, C.; Wegener, M.; Zhou, J.; Koschny, T.; Soukoulis, C. M., Magnetic Response of Metamaterials at 100 Terahertz. *Science* **2004**, *306*, 1351-1353.
- (57) Necas, D.; Klapetek, P., Gwyddion: an Open-Source Software for SPM Data Analysis. *Cent Eur J Phys* **2012**, *10*, 181-188.
- (58) Mueller, M. B.; Kuttner, C.; Koenig, T. A. F.; Tsukruk, V. V.; Foerster, S.; Karg, M.; Fery, A., Plasmonic Library Based on Substrate-Supported Gradiential Plasmonic Arrays. *ACS Nano* **2014**, *8*, 9410-9421.
- (59) König, T. A. F.; Ledin, P. A.; Kerszulis, J.; Mahmoud, M. A.; El-Sayed, M. A.; Reynolds, J. R.; Tsukruk, V. V., Electrically Tunable Plasmonic Behavior of Nanocube–Polymer Nanomaterials Induced by a Redox-Active Electrochromic Polymer. *ACS Nano* **2014**, *8*, 6182-6192.
- (60) Johnson, P. B.; Christy, R. W., Optical Constants of the Noble Metals. *Phys Rev B: Condens Matter Mater Phys* **1972**, *6*, 4370-4379.



# 7

## Reversible Gold Nanorod Alignment in Mechano-Responsive Elastomers

*Holger Pletsch, Moritz Tebbe, Martin Dulle, Beate Förster, Andreas Fery, Stephan Förster, Andreas Greiner, and Seema Agarwal*

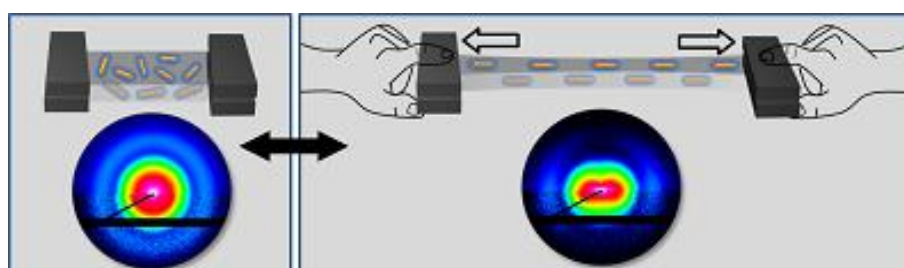


**Figure 7.1.** Table of Contents Figure.

Published in **Polymer**.

Reprinted from Publication title, *Polymer*, 66, 2015, H. Pletsch *et al.*, Reversible gold nanorod alignment in mechano-responsive elastomers, 167-172, ©2015, with permission from Elsevier.



## Abstract

Inspired by an increasing demand for stimuli-controlled assembly of nanostructures, mechano-responsive nanocomposites are designed with tremendous scope in material applications. Providing switchable properties by means of mechanical stimulation, elastomer-incorporated gold nanorods (AuNR) are presented herein. Stepless and reversible control over the orientational AuNR alignment - and therefore over macroscopic anisotropy - is exerted by uniaxial film elongation. In context of optical applications, substantial impact on the plasmonic properties within adjustable spectral ranges is demonstrated. Mechano-responsive nanocomposites with high thermal colloidal stability are prepared *via* a facile hetero-phase ligand exchange procedure where complete coverage of the AuNR surface with hydrophobic ligands is achieved.

## Introduction

Nanocomposites are amongst the most versatile materials gaining their unique properties from synergistic effects. Fabrication of continuous matrices with incorporated, homogeneously dispersed nano-sized functional particles is essential for bridging the gap between singular material properties and complex devices.<sup>1-4</sup> Noble metal nanoparticles are in the center of research interest especially due to their inherent size and shape-dependent physical and chemical properties. Most prominently, localized surface plasmon resonance (LSPR) modes are exploited in various emerging fields such as sensing,<sup>5-7</sup> optical filters,<sup>8,9</sup> wave guiding,<sup>10,11</sup> and metamaterials.<sup>12,13</sup> Most of these applications rely on precise spatial control and orientation of multi-dimensional, hierarchical nanoparticle assemblies. In this context, alignment of nanorods with polarization-dependent resonance modes is one of the recent paramount research objectives for the purpose of designing matter with high optical anisotropy efficiency.<sup>14-16</sup> In contrast to self-assembly efforts in solution,<sup>17</sup> real material applications require solid state alignment, which has amongst others been accomplished for noble metal nanorods by embedment in electrospun polymeric nanofibers,<sup>10,18,19</sup> by selective incorporation in block copolymer microphase domains,<sup>20,21</sup> by co-alignment within liquid crystal phases<sup>22</sup> or by thermoplastic deformation of nanocomposite films.<sup>2,14-16,23-27</sup> However, those systems

were ultimately fixed to one nanorod alignment constitution in which the alignment degree could not be altered by external stimuli. Yet the capability to change nanoparticle distances or orientation in a reversible and controllable fashion raises functionality to another level.<sup>7,28</sup> Therefore, we incorporate gold nanorods (AuNR) into an elastic matrix, assuming that the orientational distribution of dispersed AuNR reversibly scales with mechanical stimulation during uniaxial elongation and relaxation (**Scheme 7.2**). As a consequence from nematic-like AuNR ordering, reversible macroscopic anisotropy for the use in strain sensor and mechano-responsive filter applications is expected. In context of optical applications, substantial impact on the plasmonic properties within adjustable spectral ranges is demonstrated.

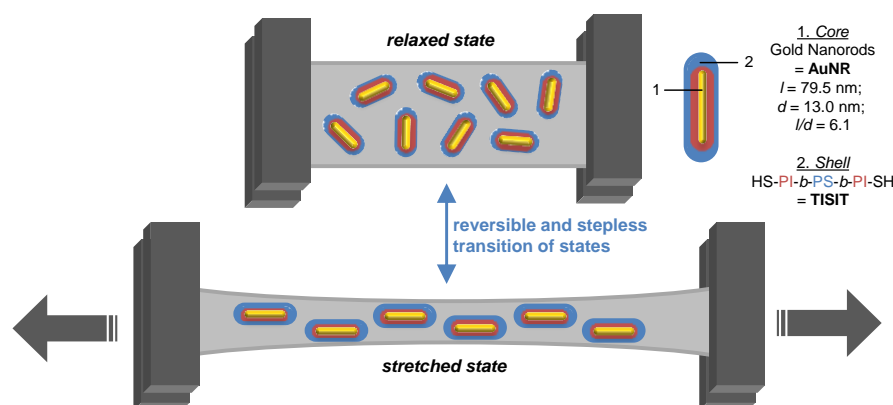


**Figure 7.2.** Concept illustration of mechano-responsive nanocomposites. AuNRs are homogeneously dispersed into an elastic film where uniaxial mechanical elongation induces stepless and reversible alignment of AuNRs within the direction of elongation. Scheme is not true to scale.

## Results and discussion

Cetyltrimethylammonium bromide (CTAB)-stabilized gold nanorods (AuNR) (in the following designated as AuNR@CTAB) in aqueous dispersion were prepared following a protocol by Vigderman *et al.*,<sup>29</sup> yielding rods with an aspect ratio (AR) of 6.1 (lengths  $l = 79.5 \pm 9.3$  nm; diameters  $d = 13.0 \pm 0.9$  nm; see also **Figure 7.S1**). UV-Vis-NIR characterization of as-prepared AuNRs reveals a longitudinal localized surface plasmon resonance (L-LSPR) within the NIR spectral range (peak maximum at 1039 nm) in good agreement with their determined AR. Previous attempts to incorporate AuNR@CTAB into hydrophobic, elastic matrices with homogeneous particle distribution were limited to elaborate physicochemical routes where noxious

CTAB was not removed from the particle surface but covered either with two layers of polyelectrolyte, followed by incorporation in PDMS matrix<sup>30</sup> or with a silica shell and subsequent doping of ureasil,<sup>31</sup> yielding materials with low AuNR filling fractions. Herein, a non-microphase-separated  $\alpha,\omega$ -dithiol functionalized ABA triblock copolymer ( $M_n = 4800$  g/mol, PDI = 1.25) consisting of isoprene (A) and styrene (B) with a total molar styrene content of 36% (in the following designated as TISIT standing for the sequence thiol-isoprene-styrene-isoprene-thiol; characterization details provided in **Text 7.S2** and **Figure 7.S2**) was used as the exchanging ligand for the preparation of thermally processable and CTAB-free AuNR nanocomposites *via* hetero-phase ligand exchange. TISIT is a promising liquid precursor for the preparation of thermally processable elastomers with high mechanical strength as shown recently.<sup>32</sup> Quantitative CTAB-to-TISIT replacement (proved by the nonexistence of nitrogen in elementary analysis) in hetero-phase water- toluene system yielded a soft material, charged with 1.9 wt.% AuNR which is designated as AuNR@TISIT in the following. Key factors for complete ligand exchange were vigorous reduction of CTAB concentration below the critical micelle concentration of 1 mM followed by the generation of a particle and surfactant stabilized emulsion with droplet sizes of  $3.5 \pm 1.4$   $\mu\text{m}$  through stirring (**Figure 7.3a-b**). Neither further emulsifiers and phase transfer agents were added nor ultrasound applied to induce phase transfer. According to similar hetero-phase ligand exchange studies, the reaction is promoted through orientation of thiol groups towards the liquid-liquid interface (**Figure 7.3c**).<sup>33</sup> After complete phase transfer, KI is added to trigger phase separation (**Figure 7.3d**), allowing separation of the AuNR-loaded toluene phase. TEM micrographs of AuNR@TISIT dispersions prove that the particle sizes and shapes were not changed during ligand exchange and that isolated core-shell structures are obtained (**Figure 7.3e**). Comparison of UV-Vis-NIR extinction spectra of AuNR@TISIT dispersions with AuNR@CTAB reveal a red shift of about +48 nm for the L-LSPR band typical for changes in environmental refractive index and a slight peak broadening usually attributed to agglomeration (**Figure 7.3f**). However, SEM micrographs of the isolated and purified materials in the solid state, obtained by precipitation (**Figure 7.3g**), reveal efficient sterical protection against particle aggregation during phase transfer as 95% of AuNR are found to be well-dispersed (**Figure 7.3h**). Only 4% of AuNRs are aggregated in dimers and 1% in clusters of three or more particles (sample size  $n = 655$ ), noteworthy in the context of very high filling

fraction. TISIT not only serves as ligand but also as dispersing medium as it can be detected in the supernatant of centrifuged AuNR@TISIT dispersions (see also **Figure 7.S3**). The conversion of liquid TISIT into a mechanically stable material holding an E-modulus of  $7.07 \pm 1.32$  MPa, tensile strength of  $0.60 \pm 0.01$  MPa and ultimate elongation of  $320 \pm 11\%$  (please refer to **Figure 7.S4**) upon charging with AuNR is attributed to attractive oligomer-particle interaction forces such as demonstrated in simulation experiments.<sup>34</sup>

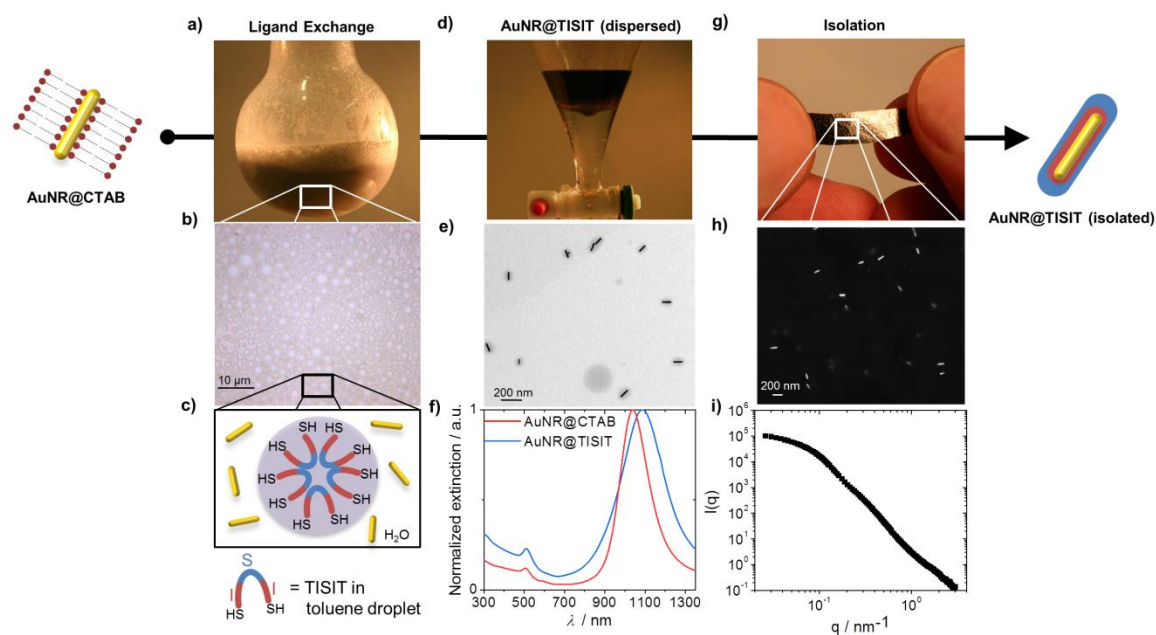


**Figure 7.3.** Preparation procedure of AuNR@TISIT. a) One-step CTAB-to-TISIT replacement is done *via* hetero-phase ligand exchange in emulsion. b) Optical micrograph of Pickering emulsion with droplet sizes of  $3.5 \pm 1.4$   $\mu\text{m}$  c) Scheme of preferred thiol orientation towards the liquid-liquid interface within emulsion droplet. d) Complete AuNR transfer is indicated by discoloration of the aqueous phase. e) TEM micrograph of AuNR@TISIT from toluene dispersion shows isolated arrangements of AuNR cores and TISIT shells with preserved particle dimensions compared to AuNR@CTAB. f) Extinction spectra of AuNR@CTAB in aqueous dispersion and of AuNR@TISIT in THF dispersion. g) If isolated, AuNR@TISIT is a thermally processable soft material which is redispersible in apolar solvents. h) SEM micrograph of AuNR@TISIT in the solid state shows well-dispersed AuNR within the TISIT matrix (the micrograph shown here is modified in graphical appearance for enhanced contrast). i) 1D SAXS profile of AuNR@TISIT showing no aggregation of the particles.

Possible methods to introduce elasticity are (1) chemical crosslinking of the isoprene block for example in solution using  $\text{S}_2\text{Cl}_2$  as cross-linking reagent to yield a thermoset elastomer, (2) physical cross-linking to yield a thermally reversible elastomer or (3)

embedding into a thermoplastic elastomer matrix. Aiming at designing processable materials, (2) and (3) were performed. Physical cross-linking was done by *in situ* incorporation of silver nanoparticles (AgNPs) along the lines of a previous report on TISIT@AgNP materials,<sup>32</sup> yielding a hybrid nanocomposite network from coexisting AuNRs (1.9 wt%) and small AgNPs (9.3 wt%). Reversible mechano-responsive alignment of AuNR is confirmed in SAXS experiments, however, the alignment performance is rather poor (please find details in the Supporting Information **Text 7.S3** and **Figure 7.S5**). Therefore, and for the purpose of decreasing the optical density, AuNR@TISIT was embedded into a thermoplastic elastic matrix. Coprecipitation with a five-fold weight amount of highly resilient and optically transparent Kraton FG1901x yielded a material with high stretchability of more than 1000%, tensile strength of  $20.7 \pm 3.0$  MPa, E-Modulus of  $20.3 \pm 2.4$  MPa and reduced optical density. AuNR@TISIT are not selectively sequestered in one of the microphase-separated blocks within the matrix (see also **Figure 7.S6** in the Supporting Information). We therefore assume compatibility of AuNR@TISIT with both the rubber and the plastic phase of the matrix. Characterization of these nanocomposites was done using thin films made by hot pressing at 110 °C and 300 bar. No variations in shape, size or aggregation behavior were observed upon processing.

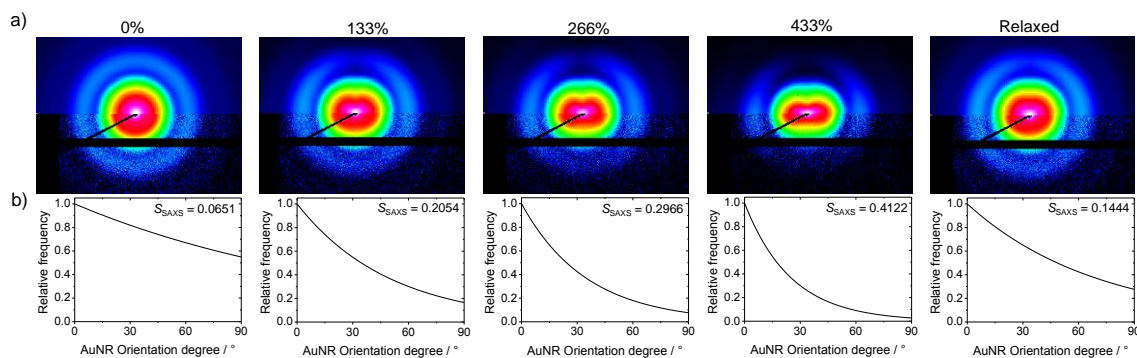


**Figure 7.4.** Elongation-dependent SAXS measurements. a) 2D SAXS scattering patterns (upper half: calculated pattern; lower half: recorded pattern) at 0%, 133%, 266% and 433% elongation as well as for the relaxed sample after this elongation sequence. b) Corresponding ODs with the orientational order parameter  $S_{SAXS}$ .

Elongation-dependent SAXS measurements (the scattering response of neat Kraton FG1901x is insignificant compared to AuNR; see also **Figure 7.S7**) were performed in the sequence of 0%, 133%, 266%, 433% and 0% elongation and strongly substantiate

the hypothesis that nematic-like AuNR alignment can be controlled as a function of mechanical stimulation in a stepless and reversible fashion since the corresponding orientational order parameter  $S_{SAXS}$  (calculated from the respective orientational distribution (OD) functions with 0 standing for random orientational distribution and 1 for perfect alignment) scales with increasing elongation and decreases upon film relaxation (Figure 7.4). It is noteworthy that minor pre-alignment was observed at 0% elongation for the freshly melt-processed sample which is attributed to the strong shear forces during hot pressing. In detail,  $S_{SAXS}$  was increased from 0.0651 at 0% elongation up to 0.4122 at 433% elongation.

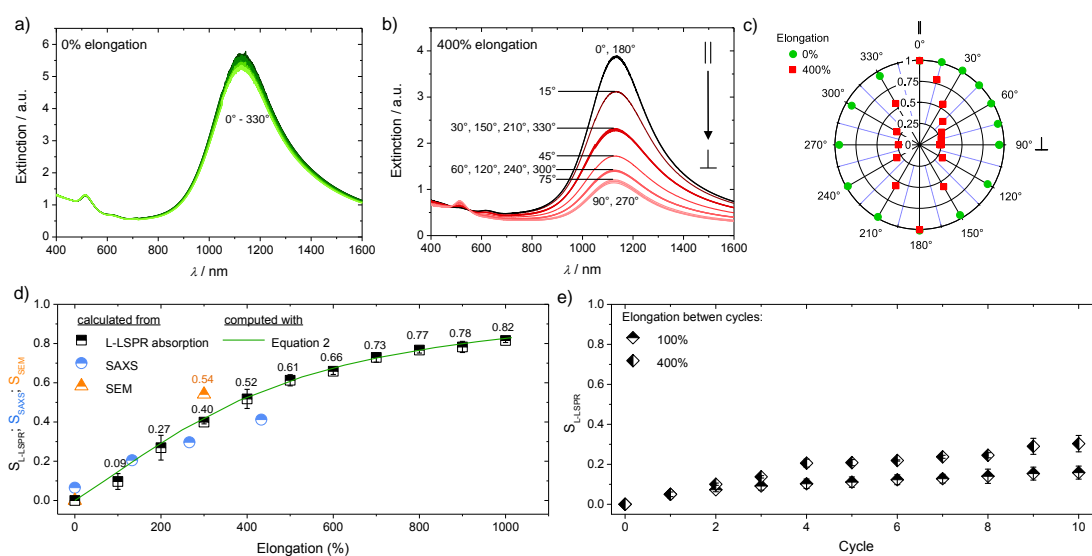


**Figure 7.5.** Mechano-responsive optical properties of AuNR@TISIT, embedded in Kraton FG1901x. The film stretching direction is defined as 0°. a) Light absorption is independent of the polarization angle of incident light at 0% elongation. b) When stretched to 400%, the polarization angle of incident light has tremendous impact on the absorption behavior of the film. c) This behavior is summarized in a dipole plot of the absorbance against the angle of the incident polarized light. The absorbance under the influence of 0° polarized light is defined as 1 in order to compensate changing film thicknesses during elongation. d) SL-LSPR (average values from 3 measurements) scales as a function of elongation, reaching a maximum of 0.82 shortly before failure and matches well with the computed  $S$  from Equation (2) (green line).  $S_{SAXS}$  and  $S_{SEM}$  are also shown for comparison. Please find the elongation-dependent extinction plots in the supplementary information **Figure 7.S12**). e)  $S_{L-LSPR}$  (average values from 3 measurements) according to Equation (1) in the relaxed state between stretching cycles. (For interpretation of the references to color in this figure caption, the reader is referred to the web version of this article.)

Upon relaxation,  $S_{SAXS}$  decreases to 0.1444, indicating a slight memory effect, *i.e.* the initial orientational distribution is not entirely restored which can be attributed to partial plastic deformation of the film and Mullin's effect which is very common in filled and unfilled elastomers leading to a residual strain.<sup>35</sup> Finding exact reason is beyond the scope of this work.

In the non-stretched state, the extinction spectra from UV-Vis-NIR measurements are independent of the angle of polarization of the incident light, indicating a random distribution of well-dispersed AuNRs in the polymer matrix (**Figure 7.5a**). In contrast to that, substantial uniaxial AuNR orientation is observed in the stretched state under constant strain. Similar to previously reported non-reversible AuNR alignment through thermoplastic deformation in PVA nanocomposites,<sup>2,14,15</sup> our reversible system is characterized by a significant dependency of the AuNR longitudinal plasmon resonance mode on incident polarization in the stretched state: Light polarized parallel to the stretching direction ( $0^\circ$ ) is more intensely absorbed whereas the absorption of the longitudinal mode is strongly reduced if subject to incident light polarized perpendicular to the stretching direction ( $90^\circ$ ) (**Figure 7.5b**). The polarization dependent behavior is summarized in **Figure 7.5c** by plotting the normalized absorbance of the longitudinal plasmon resonance band against the angle of polarization of the incident light. In the following we describe the reversible elongation dependent optical properties of our nematic-like system. Along the lines of previous data evaluation,<sup>15</sup> a relative orientational order parameter  $S_{L-LSPR}$  is calculated according to Equation (1) where  $Abs(\perp)_\varepsilon$  is the absorbance of the longitudinal plasmon resonance band subject to light polarized perpendicular to the stretching direction at a corresponding elongation  $\varepsilon$  and  $B(\perp)_\varepsilon$  is the absorbance of the corresponding baseline.

$$S_{L-LSPR} = 1 - \frac{Abs(\perp)_\varepsilon - B(\perp)_\varepsilon}{Abs(\perp)_{\varepsilon=0} - B(\perp)_{\varepsilon=0}} \quad (1)$$

$S_{L-LSPR}$  clearly scales with elongation in a range between 0 and 1000% elongation, ending in a flatter course while approaching ultimate elongation with a maximum of  $S_{L-LSPR} = 0.82$  at 1000% elongation shortly before failure (**Figure 7.5d**). The observed trend is in approximate agreement with  $S_{SAXS}$  and also with the orientational order parameter  $S_{SEM}$  which is calculated by compiling the SEM micrographical orientational order of a set of AuNRs into an OD function both at 0% and 300% elongation (see also **Figure 7.S8** and **7.S9**). In comparison, AuNR alignment within nematic liquid crystal

phases provides a maximum of  $S = 0.474$  as reported recently.<sup>22</sup> The herein observed relationship between  $S$  and elongation can be compared to theoretical predictions for stretched nematic elastomers, assuming that the nematic mesogenic units correspond to AuNRs.<sup>36</sup> The theory is based on the minimization of the nematic energy contribution due to the interaction of mesogenic units and on an elastic energy contribution arising from the stretching of the cross-linked polymer chains. It derives a relation between the elastic deformation  $\lambda$  and the nematic orientational order parameter  $S$  given by

$$\lambda^3 = \frac{\mu_1 + \mu_2(1-S)^{-1}}{\mu_1 + \mu_2(1+2S)^{-1}} \quad (2)$$

where  $\mu_1$  and  $\mu_2$  are dimensionless elastic moduli of the nematic system along and perpendicular to the director. The experimentally measured elongation  $\varepsilon$  can be related to the deformation  $\lambda$  obtained from Equation (2) *via*  $\varepsilon = \alpha(\lambda - 1) * 100\%$ , where  $\alpha$  is a coupling constant. It takes into account that in theory the nematic mesogens are strongly coupled to the polymer network *via* covalent bonds ( $\alpha = 1$ ), whereas in our case the AuNRs are only weakly coupled to the network *via* steric or excluded volume interactions ( $\alpha < 1$ ). The measured order parameters can be well described by  $\mu_1 = \mu_2 = 1$  with a coupling constant  $\alpha = 0.07$  as shown by the solid line in **Figure 7.5d**. Thus, the observed behavior can be well understood based on this model. The reversibility of AuNR orientation based on intrinsic mechanical relaxation of the elastomer film was also probed *via* UV-Vis-NIR spectroscopy by irradiating a freshly hot pressed film with  $90^\circ$  polarized light as reference (cycle 0), followed by ten stretching cycles to either 100% or 400% elongation, each for a duration of 10 s. Between the stretching cycles, extinction spectra were measured at  $\varepsilon = 0$ , followed by calculation of  $S_{L-LSPR}$  according to Equation (1). Perfect AuNR alignment reversibility is assumed if  $S_{L-LSPR}$  match with the reference cycle 0. Our films exhibit considerable reversibility of AuNR alignment. However, similar to what can be seen in SAXS measurements, a slight memory effect is observed, scaling with increasing number of cycles and with increasing elongation between the cycles (**Figure 7.5e**). The memory effect can be reset by bringing the material into the melt; *e.g.* using the hot press.

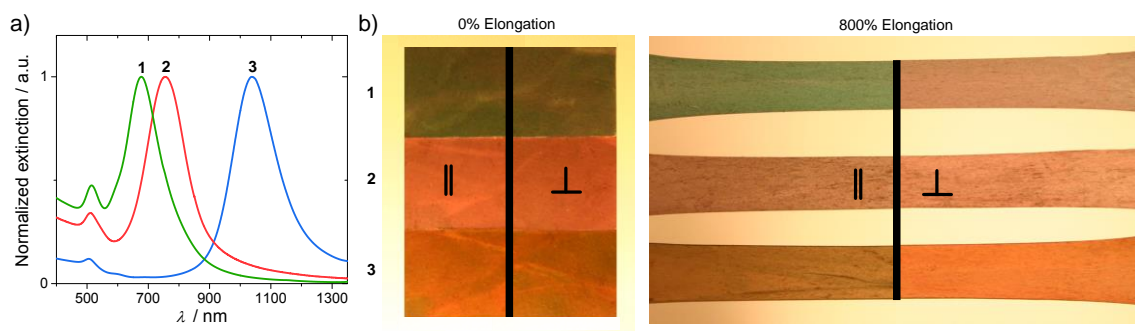


**Figure 7.6.** Adjustment of spectral ranges as a function of AuNR aspect ratio. a) Extinction spectra of AuNR@CTAB with longitudinal plasmon resonances at 677 nm, 756 nm and 1039 nm corresponding to aspect ratios of 2.1, 3.0 and 6.1 for traces 1, 2 and 3, respectively. b) Polarized photo images of illuminated films made *via* CTAB-to-TISIT ligand exchange and embedment procedure. The films 1-3 consist of AuNR with different aspect ratios as indicated in the extinction spectra, having total Au contents of 0.08, 0.33 and 0.32 wt%, respectively. The polarizer was either set parallel or perpendicular to the stretching direction.

Materials with longitudinal plasmon resonance modes in other spectral ranges are obtained if AuNR@CTAB with different aspect ratios are provided to the herein discussed preparation procedure (see **Figures 7.S10** and **7.S11**). The considerable impact of light polarization on the visible color is summarized in **Figure 7.6** for AuNR aspect ratios of 2.1 and 3.0 in comparison with the above discussed 6.1, having longitudinal plasmon resonances at 677 nm, 756 nm and 1039 nm, respectively.

## Conclusion

In conclusion, reversible and stepless stimuli-controlled assembly of nanostructures is facilitated *via* mechano-responsive nanocomposites made from elastomer-incorporated AuNRs. Key steps for the design of such a material are the compatibility between ligand and matrix through hydrophobization using TISIT and the employment of a highly resilient and thermally processable matrix. Nematic-like AuNR arrangements up to  $S = 0.82$  are achieved at high uniaxial film elongation whereas film relaxation reestablishes random AuNR orientation. In comparison with previous attempts to align anisotropic nanoparticles into ordered superstructures with respect to their orientation, the herein presented mechanical driving force as well as distinct reversibility opens unique perspectives especially in context of strain sensor or reversible optical filter applications.

## Experimental section

### 4.1. Instrumentation

Ag and Au mass fractions were determined by TGA ash yield analysis with a Netzsch Libra TG209 F1 device.

TEM measurements were done with a Zeiss 922 OMEGA EFTEM at a voltage of 200 kV. Zero-loss filtered images were recorded using a bottom mounted Ultrascan 1000 (Gatan) CCD camera system. Samples were prepared from solution by drop-casting on a Quantifoil 300 mesh copper grid with carbon coating.

Stress-strain measurements were done using a Zwick Roell Z0.5 device with a Zwick Roell KAF-TC 1000 N load sensor at a strain rate of 200 mm·min<sup>-1</sup> at 23 °C on dumbbell-shaped specimen with diameters of 2 mm and thicknesses of 0.5 mm. A slack which was observed upon loading was subtracted manually subsequent to the measurement. Values represent the average of three measurements and refer to the engineering curves.

Films were obtained by hot-pressing using a Carver 2518 setup at 300 bar and 110 °C for 3 min.

Polarization angle-dependent extinction spectra of films (thickness: 400 nm) at 0% and 400% elongation were measured on an Agilent Cary 5000 spectrophotometer with an attached Cary Universal Measurement Accessory (UMA) with polarization angles ranging from 0 to 330°.

Elongation-dependent extinction spectra and extinction measurements between elongation cycles were performed using 90° incident light on a Jasco V-670 spectrophotometer equipped with a GPH-506 polarizer between the light source and the sample.

SAXS was measured using a “Double Ganesha AIR” (SAXSLAB) equipped with a rotating anode X-ray source (copper, MicoMax 007HF, Rigaku Corporation) providing a micro-focused beam at  $\lambda = 0.154$  nm and a position-sensitive detector (PILATUS 300 K, Dectris). Liquid samples were measured in 1 mm glass capillaries (Hilgenberg, code 4007610) at different detector positions to cover a range of scattering vectors between 0.026 and 2 nm<sup>-1</sup>. The scattering contribution of the solvent and the capillary were subtracted. Films (thickness: 500 nm; length: 2.5 cm; width: 5 mm) were measured in a tensile stage (TST 350 Linkam; maximum elongation: 433%) at a sample detector distance of 1.11 m covering a q-range between 0.045 and 2 nm<sup>-1</sup>. The

AuNR form factor was determined by fitting the data of the AuNR@CTAB dispersion with a model of a homogeneous cylinder SASfit.<sup>37</sup> The 2D data were fitted to an exponential function using Scatter.<sup>38</sup> By changing the width of the OD the orientational order parameter  $S_{SAXS}$  was calculated from the best fitting OD according to  $S_{SAXS} = \langle \frac{3\cos^2\theta - 1}{2} \rangle$ .

SEM imaging of films was done on a Zeiss Ultra plus FE-SEM equipped with a Schottky field emission cathode and in lens, SE2, EsB and AsB detectors using an acceleration voltage of 7-10 kV. The samples were covered with a layer of platinum (1.3 nm thickness) prior to imaging using a Cressington HR208 sputter coater and a Cressington mtm20 thickness controller. A manually operated tensile stage was used to measure films (thickness: 500 nm) in the stretched state. The stretched samples were covered with a second 1.3 nm layer of platinum. The OD has the form of an exponential function and was fitted according to  $S_{SEM} = \langle \frac{3\cos^2\theta - 1}{2} \rangle$ .

*Preparation of AuNR@TISIT:* Concentration of the aqueous AuNR@CTAB suspension was done from 240 mL to 1 mL by centrifugation at 4000 rcf. The CTAB concentration was adjusted to 1 mM by consecutive washing cycles and a final washing step with 1 mM CTAB solution. 784 mg TISIT (163 mmol) were dissolved in 12 mL toluene and mixed with 12 mL of a freshly prepared aqueous AuNR suspension (1 mL of concentrated AuNR solution dissolved in 11 mL of a 1 mM CTAB solution). After stirring for 18 h, KI was added until the phase mixture demulgated, followed by phase separation and concentration of the toluene phase. After precipitation in MeOH, the supernatant was decanted and the residue was dried. 716 mg of a dark brown soft material were obtained. Au content: 1.9 wt.% (determined by TGA ash yield analysis). N content: 0% (determined by elemental analysis). The preparation of AuNR@TISIT with AuNR of shorter aspect ratios was carried out accordingly by using the respective AuNR@CTAB suspension.

*Embedding of AuNR@TISIT in Kraton FG1901x:* 203.0 mg AuNR@TISIT and 1.01 g Kraton FG1901x were dissolved in 10 mL THF, followed by precipitation in MeOH, decantation of the supernatant and drying of the residue. Please find more details on materials, preparation and analysis of TISIT and AuNR@CTAB in the Supporting Information **Text 7.S1**.

## Acknowledgments

This work was funded by German Research Foundation (DFG: AG 24/18-1, SFB 840) and the European Research Council (ERC-2012-StG 306686 METAMECH). M.T. was supported by the Elite Network Bavaria in the frame of the Elite Study Program “Macromolecular Science” and funded *via* a grant for Ph.D. candidates according to Bavarian elite promotion law (BayEFG). We gratefully acknowledge M. Heider, M. Krekhova and T. Löbling for technical assistance and N. Pazos-Pérez for fruitful discussion.

## Supporting Information

### Text 7.S1: Experimental Section

*Instrumentation:* The number-average molecular weights ( $M_n$ ) and the weight-average molecular weights ( $M_w$ ) of TISIT was determined by gel permeation chromatography (GPC) in THF at 26 °C using a Agilent 1200 series system equipped with a PSS-SDV (10  $\mu$ m) 50  $\times$  8 mm<sup>2</sup> pre-column and three linear PSS-SDV (10  $\mu$ m) 300  $\times$  8 mm<sup>2</sup> columns at a flow rate of 0.8 mL/min (sample concentration 2 mg/mL). A Wyatt Dawn Heleos multi angle laser light scattering (MALLS) detector was used to calculate the absolute molecular weight.  $dn/dc$  was determined with a PSS DnDc-2010  $\lambda$ 620 device.

<sup>1</sup>H-NMR (300.13 MHz) spectra were recorded on a Bruker Avance 300 A spectrometer using CDCl<sub>3</sub> as solvent with a concentration of 100 g/L. The solvent signal was used for calibration.

A Mettler thermal analyzer 821 DSC was utilized for DSC scans. Temperature and enthalpy calibration was carried out with indium and zinc standards and tested with *n*-octane as a reference. 5  $\pm$  2 mg of the samples were analyzed under nitrogen atmosphere (flow rate 80 mL/min) at a heating rate of 10 °C/min. The glass transition temperature ( $T_g$ ) was taken as the inflection point of the observed shift in the baseline of the second heating cycle.

For optical microscopy, a Keyence VH-Z500 digital microscope was used with a VHX-100 recording unit.

Elemental analysis was carried out using a CHN(S) analyser by Elementar.

*Materials:* Tetrahydrofuran (THF) and cyclohexane have been purified by consecutive drying over CaH<sub>2</sub> and potassium with subsequent distillation under nitrogen atmosphere. MeOH has been purified by distillation. Et<sub>3</sub>N (Aldrich, >99%), 1,3-diisopropenylbenzene (97%, Aldrich), *N,N,N',N',N''*-pentamethyldiethylenetriamine (99%, Aldrich) and ethylene sulfide (98%, Aldrich) have been dried over CaH<sub>2</sub>, distilled, degassed by freeze-pump-thaw (three cycles) and stored at 5 °C under argon. Isoprene (98%, Acros) has been consecutively dried over CaH<sub>2</sub> and di-*n*-butylmagnesium (1 M in heptane, Aldrich), distilled, degassed (by freeze-pump-thaw, three cycles) and used immediately. Styrene has been dried over CaH<sub>2</sub>, distilled, degassed (by freeze-pump-thaw, three cycles) and used immediately. *Tert*-butyllithium (Sigma-Aldrich, 1.6 M in pentane), sodium borohydride (NaBH<sub>4</sub>, ≥99.99%, Sigma-Aldrich), gold(III) chloride trihydrate (HAuCl<sub>4</sub>·3H<sub>2</sub>O, ≥99.9%, Sigma-Aldrich), silver(I) nitrate (AgNO<sub>3</sub>, ≥99.9%, Sigma-Aldrich), ascorbic acid (99 %, Sigma Aldrich) and hexadecyltrimethylammonium bromide (CTAB, 99%, Merck) were used as received.

*Preparation procedure of TISIT:* 20.0 mL (32.0 mmol) *tert*-butyllithium solution were cooled to -20 °C and charged with 4.44 mL (32.0 mmol) Et<sub>3</sub>N after which 2.72 mL (16.0 mmol) 1,3-diisopropenylbenzene was added dropwise at -20 °C with subsequent stirring for 5 h. This initiator solution was used without further purification. 500 mL cyclohexane were degassed and titrated with the initiator solution at 0 °C until a slight color stayed constant. After addition of 15.0 mL (9.00 mmol) of the initiator solution, 10.3 mL (90.0 mmol) styrene were injected quickly. The solution was heated to 45 °C and stirred for 90 min. 18.0 mL (180 mmol) isoprene were added quickly, followed by stirring for 18 h at 45 °C. 30.0 mL (144 mmol) *N,N,N',N',N''*-pentamethyldiethylenetriamine were added at room temperature, stirred for 1 h, after which 1.13 mL (18.9 mmol) ethylene sulfide were added. The solution was stirred for 2 h, concentrated and precipitated in degassed MeOH. The supernatant was decanted under Ar atmosphere and TISIT was dried *in vacuo*.  $M_n = 4800$ ,  $M_w = 6000$ , PDI = 1.25 (calculated from GPC-MALLS). Block length ratio styrene:isoprene = 21:37, equals 36% molar styrene content (calculated from <sup>1</sup>H-NMR).  $T_g = -42$  °C (calculated from DSC).

*Preparation of AuNR@CTAB:* According to a protocol recently published by Vigderman *et al.*<sup>26</sup> seeds were prepared by mixing 10 mL of a 0.2 M aqueous CTAB solution with 10 mL of a 0.5 mM aqueous H<sub>2</sub>AuCl<sub>4</sub> x H<sub>2</sub>O solution, prepared by the addition of 50 μL of a 0.1 M H<sub>2</sub>AuCl<sub>4</sub> x H<sub>2</sub>O solution to 10 mL water. Subsequently, 120 μL of a freshly prepared 0.2 M NaBH<sub>4</sub> solution was quickly added under vigorous stirring at 1200 rpm. After 2 min of stirring the solution was allowed to age undisturbed for 30 min. GNR growth was performed in 1 L of a 0.1 M CTAB solution containing 0.5 mM H<sub>2</sub>AuCl<sub>4</sub> at 32 °C. The gold concentration was adjusted by adding 5 mL of a 0.1 M aqueous H<sub>2</sub>AuCl<sub>4</sub> stock solution. AgNO<sub>3</sub> concentration was adjusted to a final concentration of 0.4 mM by adding 4 mL of a 0.1 M aqueous AgNO<sub>3</sub> solution followed by the addition of 50 ml of an aqueous 0.1 M hydroquinone solution. The solution was stirred until colorless (3 min). GNR growth was induced by the addition of 15 mL of the as prepared seed solution. Growth was performed at 32 °C over night. Please find experimental details for the preparation of AuNR with shorter aspect ratios in the Supporting Information.

*Preparation procedure of hybrid nanocomposite AuNR@TISIT + AgNP:* 1.21 mg (244 μmol) AuNR@TISIT were dissolved in 30 mL THF and charged with 269 mg (1.22 μmol) AgCO<sub>2</sub>CF<sub>3</sub> (98%, Acros, recrystallized from Et<sub>2</sub>O), followed by slow addition of 4.88 mL (4.88 mmol) lithium triethylborohydride (Sigma-Aldrich, 1 mol L<sup>-1</sup> in THF). After stirring for 30 min the solution was precipitated in MeOH, after which the supernatant was decanted and the residue dried to constant weight. 1.09 g of a dark brown elastomer was obtained. Au content: 1.9 wt.%; Ag content: 9.3 wt.% (determined by TGA ash yield analysis).

*Preparation procedure of CTAB@AuNR with AR of 2.1 and 3.0:* Following a modified procedure published by Nikoobakht *et al.*<sup>39</sup>, seeds were prepared by adding 25 μL of an aqueous 0.1 M H<sub>2</sub>AuCl<sub>4</sub> stock solution to 10 mL of an aqueous 0.1 M CTAB solution. The mixture was stirred at 1200 rpm and reduction was performed by quick addition of 600 μL of a freshly prepared 0.01 M NaBH<sub>4</sub> solution at RT. After 2 min stirring was stopped and seeds were aged undisturbed for 30 min. For nanorod growth 1 L (AR 3.0) or 500 mL (AR 2.1) of a 0.1 M CTAB solution in water were prepared at 32 °C to ensure CTAB solubility. Subsequently, 2.5 mL (AR 3.0) or 1.25 μL (AR 2.1) of aqueous 0.1 M H<sub>2</sub>AuCl<sub>4</sub> solution were added to yield a 0.25 mM H<sub>2</sub>AuCl<sub>4</sub> solution followed by the addition of 8 mL or 4 mL of an aqueous 5 mM AgNO<sub>3</sub> solution resulting in a final

concentration of 0.04 mM AgNO<sub>3</sub>. The pH was adjusted to 3-4 by adding 3.25 mL of a 0.1 M aqueous HBr solution. Finally, 3.75 mL of a 0.1 M aqueous ascorbic acid solution was added going along with a change in color from yellow to colorless. With the addition of 7 mL (AR 3.0) or 0.6 mL (AR 2.1) seeds the growths of nanorods was initiated. The solution was kept at 32 °C undisturbed overnight.

### Characterization of AuNR@CTAB

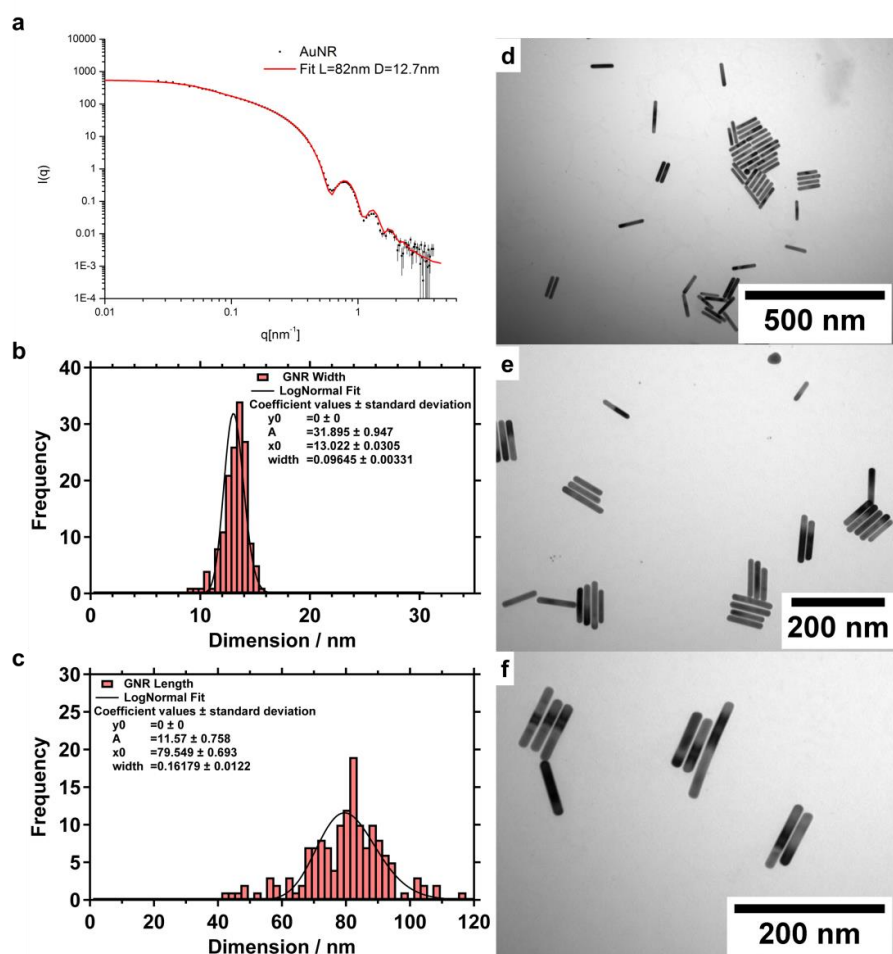


**Figure 7.S1.** Characterization of AuNR@CTAB in aqueous dispersion. a) SAXS measurements exhibit scattering responses characteristic for non-aggregated, well-stabilized AuNR. b) Frequency distribution of AuNR widths, derived from TEM images. c) Frequency distribution of AuNR lengths, derived from TEM images. d)-f) Representative TEM images of AuNR@CTAB.

### Text 7.S2: Characterization of TISIT

TISIT with a molecular weight of 4800 g·mol<sup>-1</sup> (determined by GPC-MALLS), a molar styrene content of 36% (determined by <sup>1</sup>H-NMR by comparing characteristic oligostyrene signals at  $\delta = 6.51$ -7.14 ppm with oligoisoprene signals at  $\delta = 4.72$ -5.17 ppm) and a 1,4-:3,4-oligoisoprene ratio of 84:16 (determined by <sup>1</sup>H-NMR by

comparing the respective signals at  $\delta = 5.17$  ppm and  $\delta = 4.72$ - $4.79$  ppm) is prepared *via* sequential anionic polymerization of styrene and isoprene, starting with an difunctional lithium initiator. Thiol end groups are obtained by subsequent ring-opening of ethylene sulfide by the living ABA block co-oligomer. **Figure S2** includes a summary of the preparation route as well as the  $^1\text{H-NMR}$  spectrum and the GPC elugram.

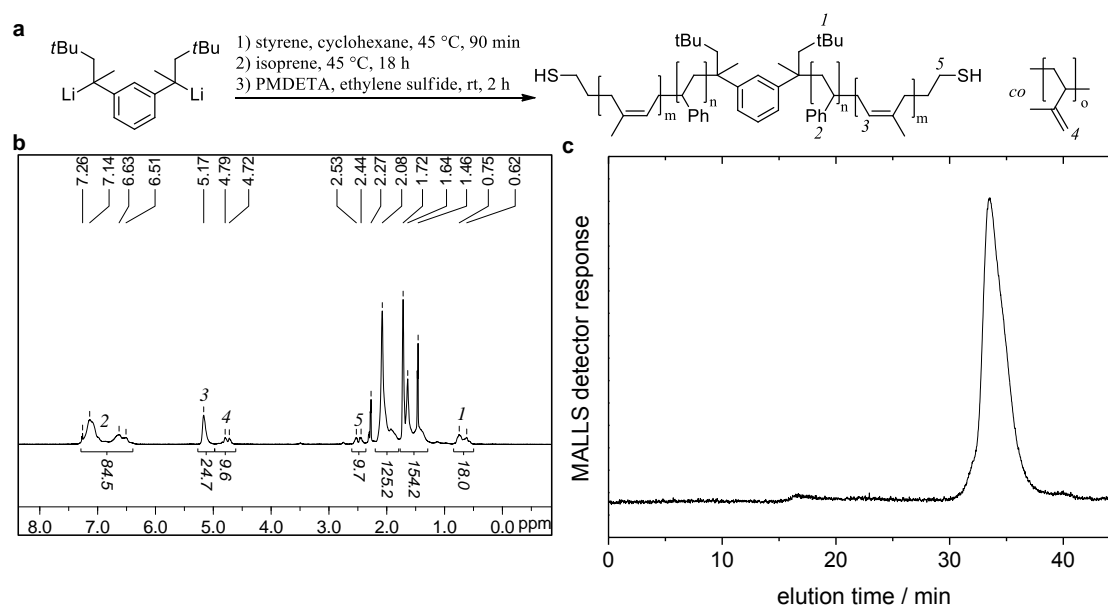


**Figure 7.S2.** Preparation and Characterization of TISIT. a) TISIT is prepared by anionic polymerization of styrene and isoprene with subsequent end-capping using ethylene sulfide. b)  $^1\text{H-NMR}$  spectrum of TISIT. The molar styrene content of 36% was calculated from comparing the signals the characteristic signals for oligostyrene at  $\delta = 6.51$ - $7.14$  ppm with oligoisoprene signals at  $\delta = 4.72$ - $5.17$  ppm. The 1,4-:3,4-oligoisoprene ratio of 84:16 was calculated from comparing the respective signals at  $\delta = 5.17$  ppm and  $\delta = 4.72$ - $4.79$  ppm. c) GPC-MALLS elugram of TISIT showing monomodal molecular weight distribution. A molecular weight of  $M_n = 4800 \text{ g}\cdot\text{mol}^{-1}$  was calculated (PDI = 1.25).

### Characterization of AuNR@TISIT

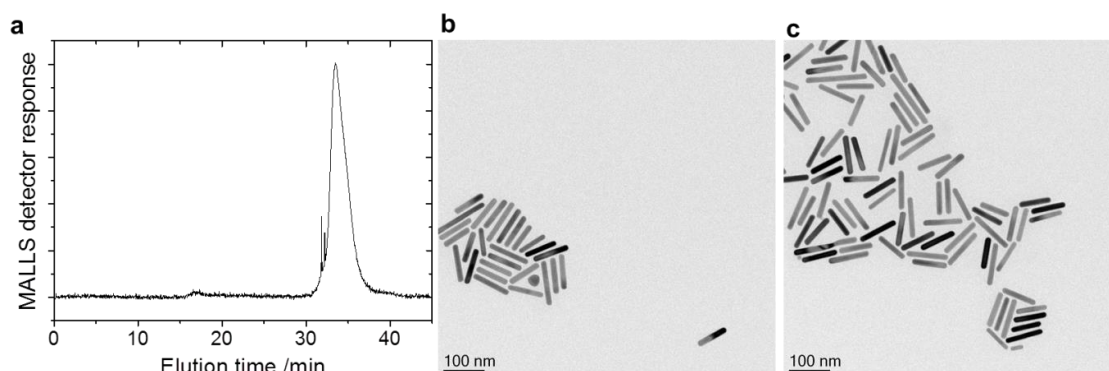


**Figure 7.S3.** Separation of grafted and unbound TISIT in AuNR@TISIT dispersion. A diluted dispersion was centrifuged at 14,000 rpm for 60 min after which the supernatant was characterized by GPC and the residue by TEM. a) GPC-MALLS trace of the supernatant shows a signal for TISIT which proves the presence of unbound TISIT chains in AuNR@TISIT materials. b) As a consequence from centrifugation, AuNR agglomerate to clusters, but remain sterically protected against flocculation.

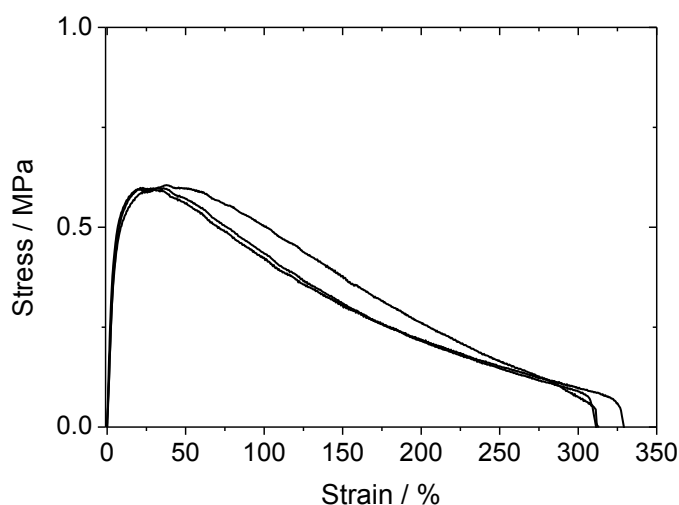
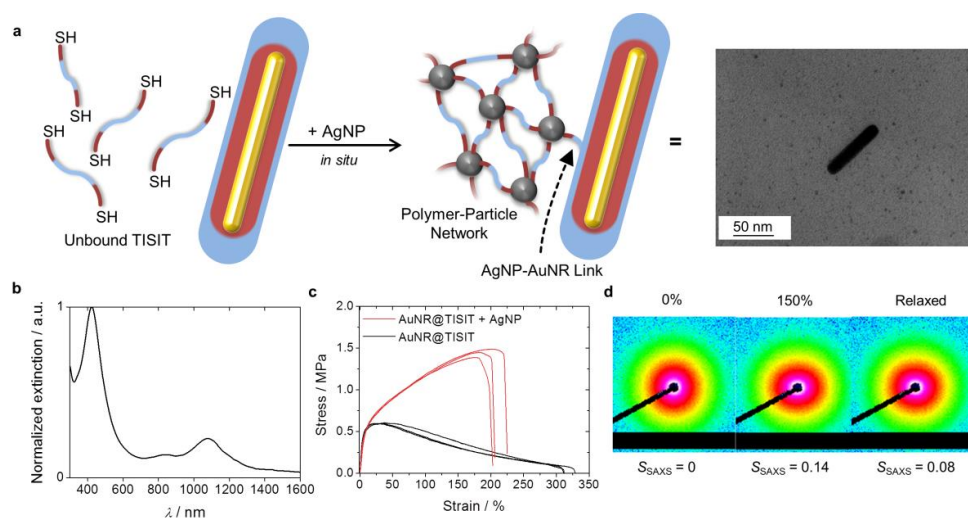


**Figure 7.S4.** Stress-Strain curves of AuNR@TISIT. E-Modulus =  $7.1 \pm 1.3$  MPa. Tensile strength =  $0.60 \pm 0.01$  MPa.

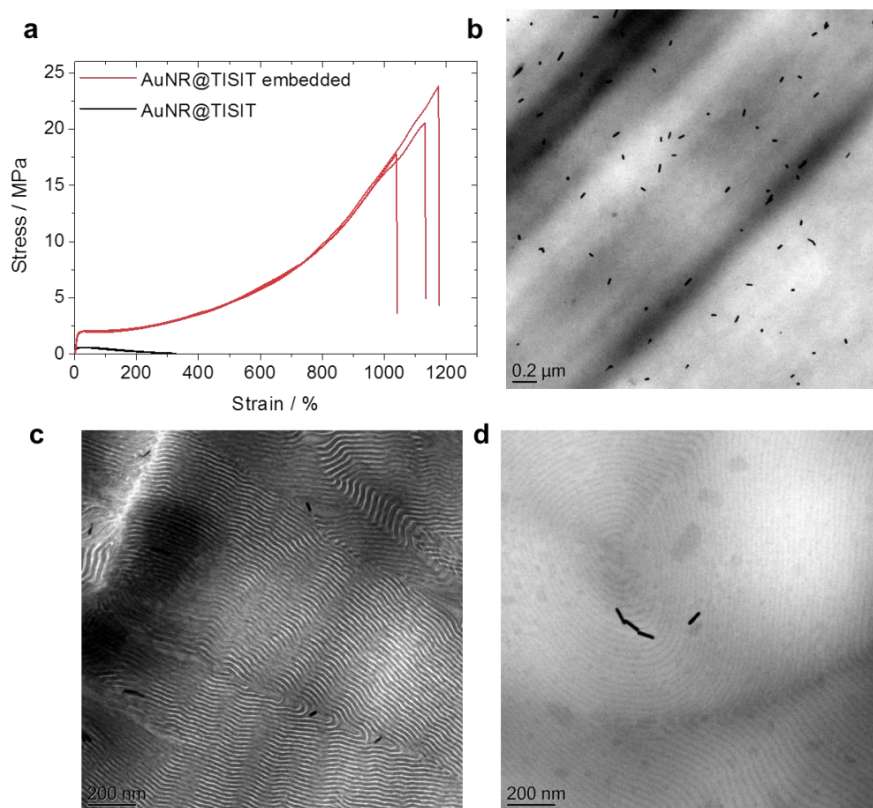
#### **Text 7.S3: Physically cross-linked hybrid nanocomposite network**

Cross-linking of AuNR@TISIT with small, spherical silver nanoparticles yielded a hybrid nanocomposite network from coexisting AuNRs (1.9 wt%) and small AgNPs (9.3 wt%) with diameters of  $d_{\text{AgNP}} = 2.6 \pm 0.4$  nm (**Figure S5a**). Mechanistically, AgNP occupy the unbound thiol end groups of the TISIT matrix. Possible dangling chain ends emerging from the AuNR surface may supply a link between the two particle types. As

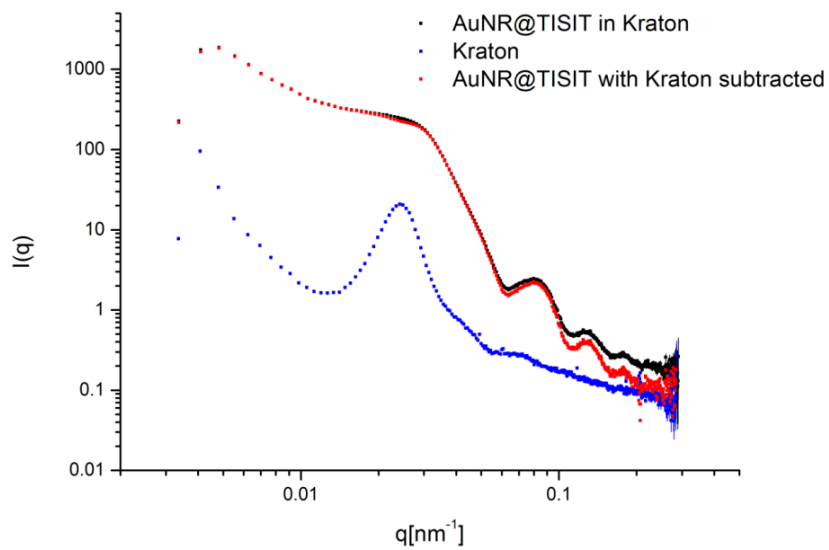
a result, a soft material of low solubility is obtained, having characteristic plasmon resonance modes of both spherical AgNP at 438 nm and AuNR (**Figure S5b**) at 1149 nm as well as considerably improved tensile properties (**Figure S5c**). SAXS measurements show characteristic signals corresponding to both AgNP and to AuNR with the latter being randomly distributed with respect to their orientation (**Figure S5d**). Through stretching the film to 150% elongation, the SAXS scattering patterns reveal that AuNR tend to align into the direction of stretching with the orientational order parameter  $S_{\text{SAXS}}$  (calculated from the corresponding orientational distribution (OD) functions with 0 standing for random orientational distribution and 1 for perfect alignment) being increased from 0 to 0.14. The orientation is partially reversible as  $S_{\text{SAXS}}$  reduces down to 0.08 upon relaxation of the elastic film.



**Figure 7.S5.** a) Unbound TISIT telecheles within AuNR@TISIT nanocomposite are cross-linked using small AgNP with diameters of  $d_{\text{AgNP}} = 2.6 \pm 0.4$  nm as cross-linking sites. AgNP are prepared *in situ* by reduction of  $\text{AgCO}_2\text{CF}_3$  with lithium triethylborohydride in homogeneous THF solution. Scheme is not true to scale. TEM images of this hybrid nanocomposite prove the coexistence of AgNP and AuNR. b) Extinction spectrum of AgNP-charged AuNR@TISIT, redispersed in THF for a duration of 2 d, shows plasmon resonance modes of both AgNP at  $\lambda = 423$  nm and AuNR at  $\lambda = 1077$  nm. c) Engineering stress-strain curves reveal a considerable improvement of mechanical properties as a consequence from cross-linking with E-Moduli increasing from  $7.1 \pm 1.3$  MPa to  $8.0 \pm 1.2$  MPa and tensile strengths increasing from  $0.60 \pm 0.01$  MPa to  $1.45 \pm 0.06$  MPa. d) SAXS measurements of a film at 0% and 150% elongation as well as in the relaxed state after elongation. In the stretched state, AuNR tend to align along the axis of elongation. Relaxation of the same film causes the AuNR to return to a less ordered orientation.

**Characterization of AuNR@TISIT, embedded in Kraton FG1901x**

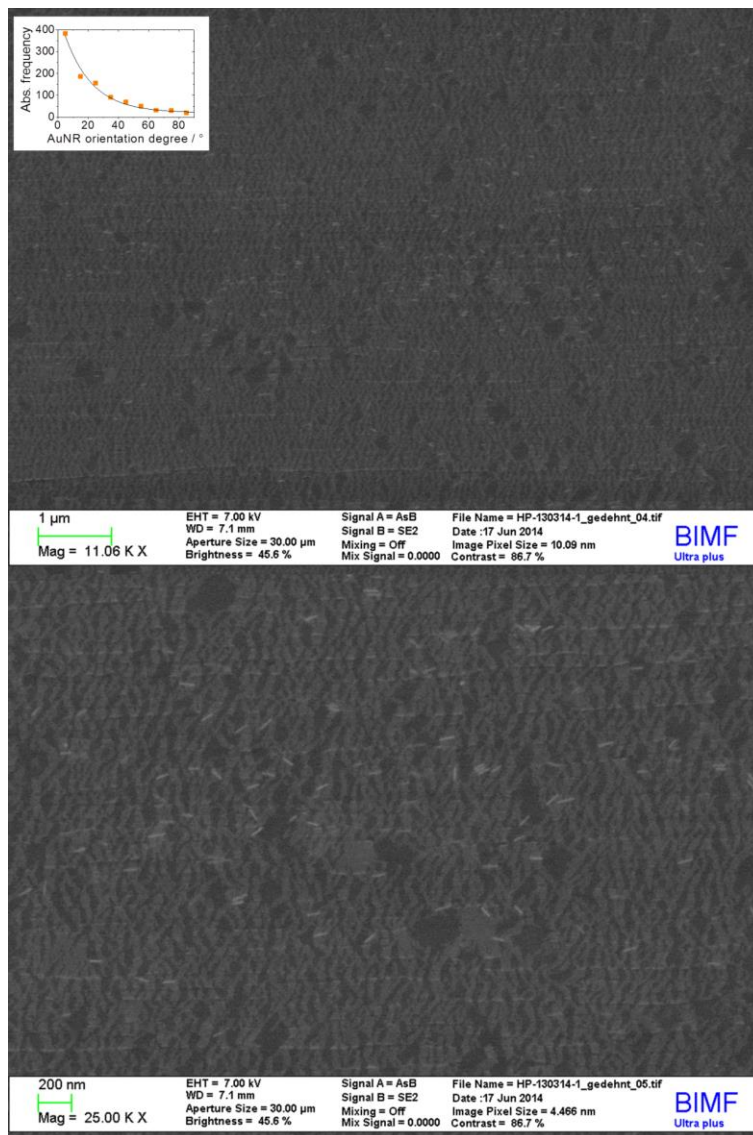
**Figure 7.S6.** Embedding of AuNR@TISIT in Kraton FG1901x by co-precipitation from THF. a) Stress-strain curve of neat and embedded AuNR@TISIT. E-Modulus increases from  $7.1 \pm 1.3$  MPa to  $20.3 \pm 2.4$  MPa. Tensile strengths increase from  $0.60 \pm 0.01$  MPa to  $20.7 \pm 3.0$  MPa. b) TEM micrographs of cryo-cut, freshly hot pressed films of Kraton FG1901x-embedded AuNR@TISIT, showing homogeneous distribution of isolated particles. c-d) TEM micrographs of cryo-cut, RuO<sub>4</sub>-stained Kraton FG1901x-embedded AuNR@TISIT film made by solvent evaporation from THF reveal that AuNR are not selectively dispersed in one of the matrix microphases.



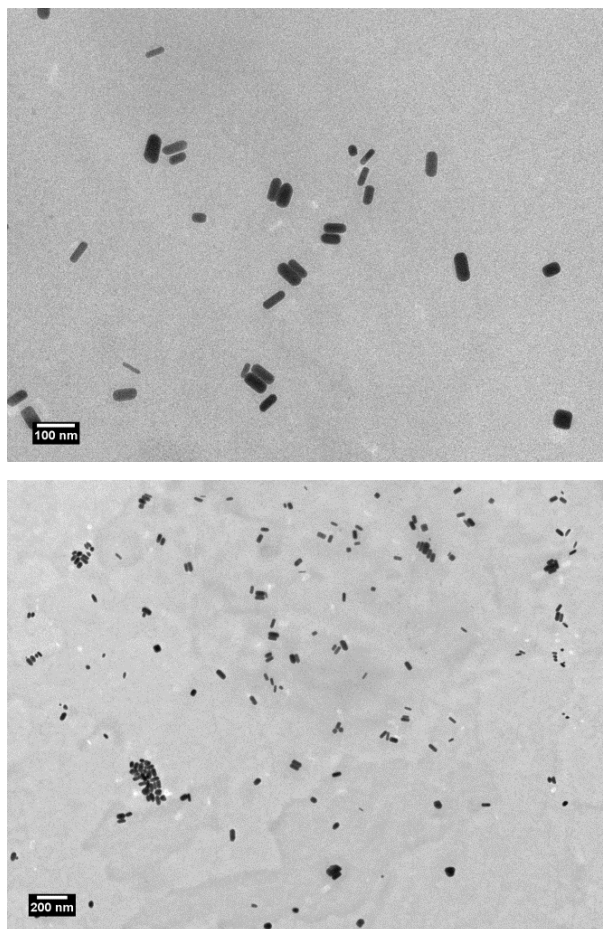
**Figure 7.S7.** SAXS response is dominated by AuNR. Kraton FG1901x only adds very little signal to the scattering curve and is therefore not included in fitting and calculation of the orientational distribution functions.



**Figure 7.S8.** SEM micrographs of AuNR@TISIT embedded in Kraton FG1901x at 0% elongation, including the corresponding OD function.



**Figure 7.S9.** SEM micrographs of AuNR@TISIT embedded in Kraton FG1901x during elongation to 300%, including the corresponding OD function.

**TEM characterization of AuNR@CTAB with AR = 2.1 and 3.0.**

**Figure 7.S10.** TEM micrographs of AuNR@CTAB with AR = 2.1 ( $l = 54.7 \pm 10.0$  nm;  $d = 25.9 \pm 6.6$  nm).

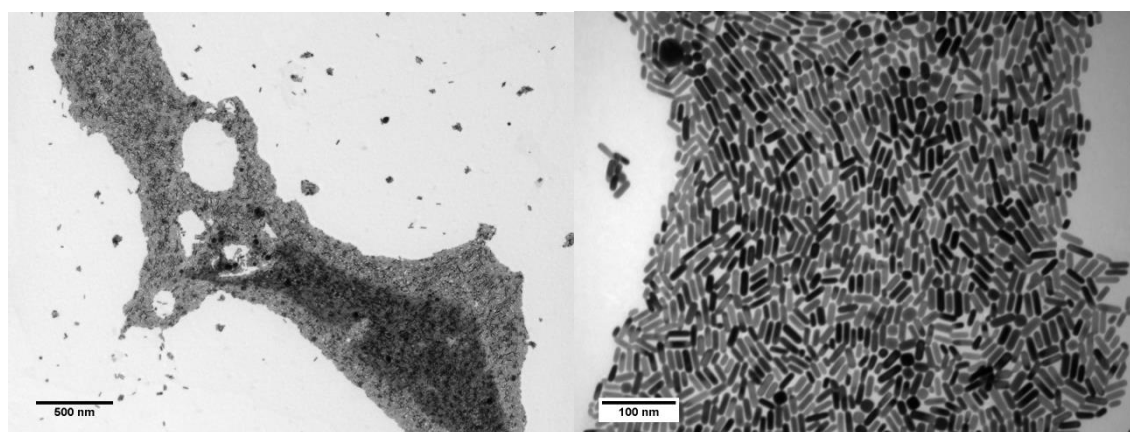


**Figure 7.S11.** TEM micrographs of AuNR@CTAB with AR = 3.0 ( $l = 31.3 \pm 4.4$  nm;  $d = 10.3 \pm 1.1$  nm).

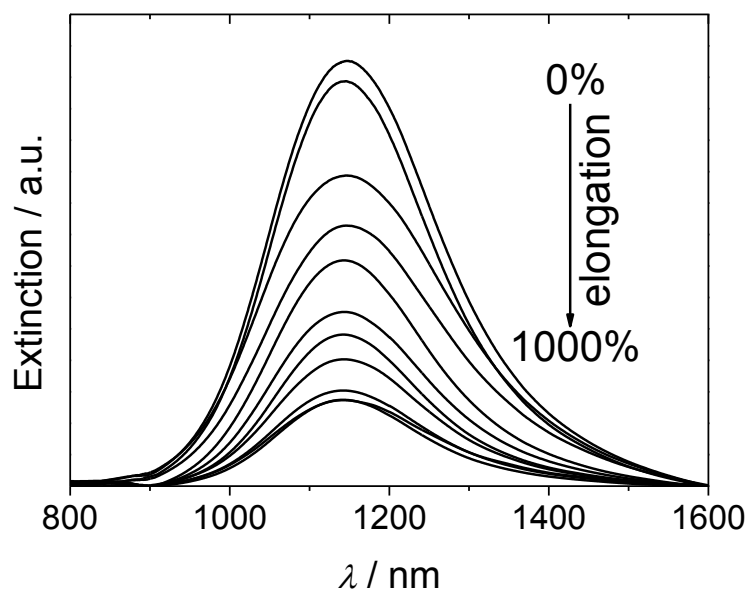


**Figure 7.S12.** Extinction plots of AuNR@CTAB, embedded in Kraton FG1901x as a function of elongation. This experiment was performed three times (here shown exemplarily: one out of three experiments) and the averaged data was used to calculate  $S_{L-LSPR}$  (cf. **Figure 7.5d**) according to Equation 1.

## References

- (1) Zijlstra, P.; Chon, J. W. M.; Gu, M., Five-dimensional optical recording mediated by surface plasmons in gold nanorods. *Nature* **2009**, *459*, 410-413.
- (2) Liu, S.; Li, J.; Li, Z.-Y., Macroscopic Polarized Emission from Aligned Hybrid Gold Nanorods Embedded in a Polyvinyl Alcohol Film. *Adv Opt Mater* **2013**, *1*, 227-231.
- (3) Vigdeman, L.; Khanal, B. P.; Zubarev, E. R., Functional Gold Nanorods: Synthesis, Self-Assembly, and Sensing Applications. *Adv Mater* **2012**, *24*, 4811-4841.
- (4) Lee, J.; Kim, S.; Lee, J.; Yang, D.; Park, B. C.; Ryu, S.; Park, I., A stretchable strain sensor based on a metal nanoparticle thin film for human motion detection. *Nanoscale* **2014**, *6*, 11932-11939.
- (5) Tebbe, M.; Cherepanov, P.; Skorb, E. V.; Poznyak, S. K.; de Abajo, J. G.; Fery, A.; Andreeva, D. V.; Puebla, R. A. A.; Pazos-Perez, N., SERS Platforms of Plasmonic Hydrophobic Surfaces for Analyte Concentration: Hierarchically Assembled Gold Nanorods on Anodized Aluminum. *Part Part Syst Charact* **2014**, *31*, 1134-1140.
- (6) Alba, M.; Pazos-Perez, N.; Vaz, B.; Formentin, P.; Tebbe, M.; Correa-Duarte, M. A.; Granero, P.; Ferré-Borrull, J.; Alvarez, R.; Pallares, J.; Fery, A.; de Lera, A. R.; Marsal, L. F.; Alvarez-Puebla, R. A., Macroscale Plasmonic Substrates for Highly Sensitive Surface-Enhanced Raman Scattering. *Angew Chem, Int Ed* **2013**, *52*, 6459-6463.
- (7) Segev-Bar, M.; Haick, H., Flexible Sensors Based on Nanoparticles. *ACS Nano* **2013**, *7*, 8366-8378.
- (8) Xu, T.; Wu, Y.-K.; Luo, X.; Guo, L. J., Plasmonic nanoresonators for high-resolution colour filtering and spectral imaging. *Nat Commun* **2010**, *1*:59, 1-5.

- (9) Millyard, M. G.; Min Huang, F.; White, R.; Spigone, E.; Kivioja, J.; Baumberg, J. J., Stretch-induced plasmonic anisotropy of self-assembled gold nanoparticle mats. *Appl Phys Lett* **2012**, *100*, 073101-1-3.
- (10) Wang, P.; Zhang, L.; Xia, Y.; Tong, L.; Xu, X.; Ying, Y., Polymer Nanofibers Embedded with Aligned Gold Nanorods: A New Platform for Plasmonic Studies and Optical Sensing. *Nano Lett* **2012**, *12*, 3145-3150.
- (11) Lal, S.; Link, S.; Halas, N. J., Nano-optics from sensing to waveguiding. *Nat Photonics* **2007**, *1*, 641-648.
- (12) Liu, Q.; Cui, Y.; Gardner, D.; Li, X.; He, S.; Smalyukh, I. I., Self-Alignment of Plasmonic Gold Nanorods in Reconfigurable Anisotropic Fluids for Tunable Bulk Metamaterial Applications. *Nano Lett* **2010**, *10*, 1347-1353.
- (13) Guerrero-Martínez, A.; Auguie, B.; Alonso-Gómez, J. L.; Džolić, Z.; Gómez-Graña, S.; Žinić, M.; Cid, M. M.; Liz-Marzán, L. M., Intense Optical Activity from Three-Dimensional Chiral Ordering of Plasmonic Nanoantennas. *Angew Chem, Int Ed* **2011**, *50*, 5499-5503.
- (14) Li, J.; Liu, S.; Liu, Y.; Zhou, F.; Li, Z.-Y., Anisotropic and enhanced absorptive nonlinearities in a macroscopic film induced by aligned gold nanorods. *Appl Phys Lett* **2010**, *96*, 263103.
- (15) Pérez-Juste, J.; Rodríguez-González, B.; Mulvaney, P.; Liz-Marzán, L. M., Optical Control and Patterning of Gold-Nanorod-Poly(vinyl alcohol) Nanocomposite Films. *Adv Funct Mater* **2005**, *15*, 1065-1071.
- (16) Murphy, C. J.; Orendorff, C. J., Alignment of Gold Nanorods in Polymer Composites and on Polymer Surfaces. *Adv Mater* **2005**, *17*, 2173-2177.
- (17) Nie, Z.; Fava, D.; Kumacheva, E.; Zou, S.; Walker, G. C.; Rubinstein, M., Self-assembly of metal-polymer analogues of amphiphilic triblock copolymers. *Nat Mater* **2007**, *6*, 609-614.
- (18) Zhang, C.-L.; Lv, K.-P.; Cong, H.-P.; Yu, S.-H., Controlled Assemblies of Gold Nanorods in PVA Nanofiber Matrix as Flexible Free-Standing SERS Substrates by Electrospinning. *Small* **2012**, *8*, 648-653.

- (19) Roskov, K. E.; Kozek, K. A.; Wu, W.-C.; Chhetri, R. K.; Oldenburg, A. L.; Spontak, R. J.; Tracy, J. B., Long-Range Alignment of Gold Nanorods in Electrospun Polymer Nano/Microfibers. *Langmuir* **2011**, *27*, 13965-13969.
- (20) Thorkelsson, K.; Nelson, J. H.; Alivisatos, A. P.; Xu, T., End-to-End Alignment of Nanorods in Thin Films. *Nano Lett* **2013**, *13*, 4908-4913.
- (21) Deshmukh, R. D.; Liu, Y.; Composto, R. J., Two-Dimensional Confinement of Nanorods in Block Copolymer Domains. *Nano Lett* **2007**, *7*, 3662-3668.
- (22) Liu, Q.; Campbell, M. G.; Evans, J. S.; Smalyukh, I. I., Orientationally Ordered Colloidal Co-Dispersions of Gold Nanorods and Cellulose Nanocrystals. *Adv Mater* **2014**, *26*, 7178-7184.
- (23) van der Zande, B. M. I.; Pagès, L.; Hikmet, R. A. M.; van Blaaderen, A., Optical Properties of Aligned Rod-Shaped Gold Particles Dispersed in Poly(vinyl alcohol) Films. *J Phys Chem B* **1999**, *103*, 5761-5767.
- (24) Stoenescu, S.; Truong, V.-V.; Packirisamy, M., Non-destructive quantification of alignment of nanorods embedded in uniaxially stretched polymer films. *J Appl Phys* **2014**, *115*, 114301.
- (25) Wilson, O.; Wilson, G. J.; Mulvaney, P., Laser Writing in Polarized Silver Nanorod Films. *Adv Mater* **2002**, *14*, 1000-1004.
- (26) Zhang, H.; Zhang, J.; Tong, X.; Ma, D.; Zhao, Y., Light Polarization-Controlled Shape-Memory Polymer/Gold Nanorod Composite. *Macromol Rapid Commun* **2013**, *34*, 1575-1579.
- (27) Tao, J.; Lu, Y.; Chen, J.; Lu, D.; Chen, C.; Wang, P.; Ming, H., Polarization-Dependent Surface-Enhanced Raman Scattering via Aligned Gold Nanorods in Poly(Vinyl Alcohol) Film. *Plasmonics* **2011**, *6*, 785-789.
- (28) Kim, Y.; Zhu, J.; Yeom, B.; Di Prima, M.; Su, X.; Kim, J.-G.; Yoo, S. J.; Uher, C.; Kotov, N. A., Stretchable nanoparticle conductors with self-organized conductive pathways. *Nature* **2013**, *500*, 59-63.

- (29) Vigderman, L.; Zubarev, E. R., High-Yield Synthesis of Gold Nanorods with Longitudinal SPR Peak Greater than 1200 nm Using Hydroquinone as a Reducing Agent. *Chem Mater* **2013**, *25*, 1450-1457.
- (30) Alkilany, A. M.; Thompson, L. B.; Murphy, C. J., Polyelectrolyte Coating Provides a Facile Route to Suspend Gold Nanorods in Polar Organic Solvents and Hydrophobic Polymers. *ACS Appl Mater Interfaces* **2010**, *2*, 3417-3421.
- (31) Boev, V. I.; Pérez-Juste, J.; Pastoriza-Santos, I.; Silva, C. J. R.; Gomes, M. d. J. M.; Liz-Marzán, L. M., Flexible Ureasil Hybrids with Tailored Optical Properties through Doping with Metal Nanoparticles. *Langmuir* **2004**, *20*, 10268-10272.
- (32) Pletsch, H.; Schnepf, M. J.; Agarwal, S., Design of Soft Materials from Liquid Triblock Co-Oligomers and Metal Nanoparticles. *Chem Mater* **2014**, *26*, 4805-4811.
- (33) Pletsch, H.; Peng, L.; Mitschang, F.; Schaper, A.; Hellwig, M.; Nette, D.; Seubert, A.; Greiner, A.; Agarwal, S., Ultrasound-Mediated Synthesis of High-Molecular Weight Polystyrene-Grafted Silver Nanoparticles by Facile Ligand Exchange Reactions in Suspension. *Small* **2014**, *10*, 201-208.
- (34) Desai, T.; Koblinski, P.; Kumar, S. K., Molecular dynamics simulations of polymer transport in nanocomposites. *J Chem Phys* **2005**, *122*, 134910.
- (35) Dorfmann, A.; Ogden, R. W., A constitutive model for the Mullins effect with permanent set in particle-reinforced rubber. *Int J Solids Struct* **2004**, *41*, 1855-1878.
- (36) Fried, E.; Sellers, S., Orientational order and finite strain in nematic elastomers. *J Chem Phys* **2005**, *123*, 044901-1-9.
- (37) Porod, G., Die Abhängigkeit der Röntgen-Kleinwinkelstreuung von Form und Größe der kolloiden Teilchen in verdünnten Systemen, IV. *Acta Phys Austriaca* **1948**, *2*, 255-292.
- (38) Förster, S.; Apostol, L.; Bras, W., Scatter: software for the analysis of nano- and mesoscale small-angle scattering. *J Appl Crystallogr* **2010**, *43*, 639-646.

- (39) Nikoobakht, B.; El-Sayed, M. A., Preparation and Growth Mechanism of Gold Nanorods (NRs) Using Seed-Mediated Growth Method. *Chem Mater* **2003**, *15*, 1957-1962.



# *III*

## Close-Packed Nanoparticle Assemblies as SERS Platforms



# 8

## Organized Solid Thin Films of Gold Nanorods with Different Sizes for Surface-Enhanced Raman Scattering Applications

*Moritz Tebbe, Max Maennel, Andreas Fery, Nicolas Pazos-Perez, and Ramon A. Alvarez-Puebla*

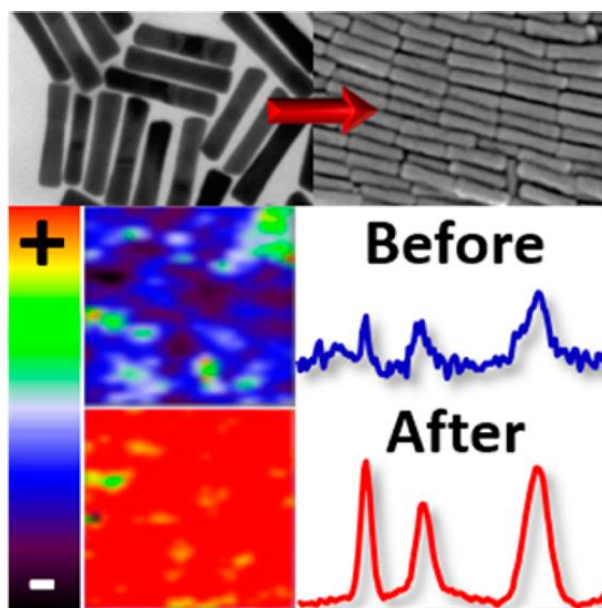


**Figure 8.1.** Table of Content Figure.

Published in **The Journal of Physical Chemistry C**.

Reprinted with permission from Tebbe *et al.*, *J Phys Chem C* **2014**, 118, 28095 - 28100.

©2014 American Chemical Society.



## Abstract

Gold nanorods are among the most efficient structures for optical applications, especially in surface-enhanced Raman scattering applications. Notably, their use directly in colloidal solutions decreases their optical enhancing properties because of the impossibility of generating hot spots and the passivation of their surfaces by the surfactants used during their preparation, hindering the interaction of the analyte with the plasmonic surface. We present an easy and fast method for preparing organized lying-down nanorod films with particles of different aspect ratios, yielding efficient and clean plasmonic films populated with a large number of homogeneous hot spots.

## Introduction

Gold nanorods (AuNRs) are among the most efficient structures for nanooptical applications.<sup>1</sup> As anisotropic particles, their plasmonic response consist of two different bands corresponding to the transversal and longitudinal modes.<sup>1</sup> Notably, these elongated structures are also capable of concentrating the electromagnetic field at the nanoparticle tip when the incoming light is in resonance with the longitudinal plasmon mode.<sup>2</sup> Additionally, the coupling of two close-packed anisotropic nanoparticles in tip-to-tip geometry further amplifies this field focalization because of “hot-spot” formation and constraint fields.<sup>3</sup> These characteristics make AuNRs very suitable structures for applications based on surface-enhanced spectroscopies in general, and specially in surface-enhanced Raman scattering (SERS) spectroscopy.<sup>4-6</sup> Thus, in recent years, a number of applications using AuNRs have been developed including their use in ultrasensitive biology,<sup>7,8</sup> diagnostics,<sup>9-11</sup> and environmental monitoring.<sup>12,13</sup>

Although the synthesis of AuNRs with controlled dimensions (aspect ratio, AR) and crystallinity is well-established,<sup>14</sup> it requires the use of surfactants and directing agents (*i.e.*, cetyltrimethylammonium bromide, CTAB) that adhere strongly to the plasmonic surfaces and are potentially cytotoxic.<sup>15</sup> This strong adhesion to the gold surface hinders the interaction of the particle with the target analyte.<sup>6,16</sup> Thus, for the maximization of the SERS signal, particle surfaces need to be cleaned before their use as an optical platform. Protocols for cleaning usually establish the centrifugation of

samples several times for the removal of the excess of CTAB.<sup>17</sup> However, this process leads to the loss of colloidal stability (if samples are centrifuged in excess)<sup>18</sup> and may not allow for the complete elimination of the CTAB. Several alternative routes proposed solve this problem by immobilizing the particles in micro-sized substrates, which allow for further centrifugation without aggregation because the particles are already immobilized on the support material.<sup>18,19</sup> This approach works well for SERS analysis in solution but does not allow for a fine control of the aggregation and the subsequent formation of hot-spots between anisotropic particles (*i.e.*, spatial regions where the electromagnetic field is maximized because of the plasmon intercoupling of two or more particles). Alternatively, several studies have shown that particles with CTAB as surfactant undergo a spontaneous self-assembly process into ordered colloidal supercrystals when deposited on a surface under controlled conditions (*i.e.*, wetting properties, ambient humidity, and temperature to control the drying rate and colloidal concentration of the solution).<sup>11,20-22</sup> These supercrystal films can be easily processed by applying an etching plasma, giving rise to clean and optimal surfaces for SERS analysis.<sup>11,22</sup> In addition, it has been demonstrated that the organization of rods into crystals yields an extremely high SERS signal due to the transport and accumulation of the plasmonic electromagnetic field to the last layer of the material,<sup>11,17,22-24</sup> the only available surface to react with the analyte. Although extremely efficient for SERS, these colloidal superstructures are not easy to obtain and require very high concentrations of nanoparticles in solution, which hinders its mass production. Other methods for the controlled immobilization of rods on a surface may imply the use of templates to drive nanorod lines, where the plasmon of the particles interact tip-to-tip, generating a very active hot spot.<sup>3,25</sup> Still, these methods require an adequate template not accessible to a broad scientific community.

We present the easy and fast preparation of organized lying down nanorod films with Au particles of different aspect ratios, studying the influence of the AR and the effect of plasma etching as cleaning method to obtain efficient plasmonic films populated with a large number of homogeneous hot-spots.

## Experimental Section

**Materials.** Silver nitrate ( $\text{AgNO}_3$ , 99.9999%, 169.87 g/mol), sodium borohydride ( $\text{NaBH}_4$ , 99%, 37.83 g/mol), hydroquinone (>99%, 110.11 g/mol), benzenethiol (BT),

and hydrogen tetrachloroaurate ( $\text{HAuCl}_4$ , >99.9%, 393.83 g/mol) were purchased from Sigma-Aldrich. CTAB (364.45 g/mol, 0.359 mg/kg Iodine) was received from Merck KGaA.

**Gold Seeds.** A 5 mL sample of an aqueous 0.5 mM  $\text{HAuCl}_4 \cdot 3\text{H}_2\text{O}$  solution was added to 5 mL of a 0.1 M CTAB solution in water. The mixture was gently mixed by hand. Subsequently, 0.6 mL of an aqueous 0.01 M  $\text{NaBH}_4$  solution was added quickly under vigorous stirring at 1200 rpm. The solution was stirred for another 2 min. The color changed from dark yellow to brown. The solution was aged at room temperature without stirring for 30 min.

**Synthesis of AuNRs.** For the synthesis of different AR AuNRs with longitudinal localized surface plasmon resonance (LLSPR) over 900 nm, a modification of the procedure published by Vigderman and Zubarev was followed.<sup>26</sup> Briefly, 500 mL of a 0.1 M CTAB solution was prepared by dissolving 18.22 g of CTAB in water *via* sonication in a tempered water bath at 35 °C. Then, 2430  $\mu\text{L}$  of an aqueous 0.103 M  $\text{HAuCl}_4 \cdot 3\text{H}_2\text{O}$  solution was added. This solution was divided into five bottles, and the final volume of each sample was 100 mL. Next, 500  $\mu\text{L}$  of 0.1 M  $\text{AgNO}_3$  solution was added to each bottle. Followed by the addition of 5 mL of an aqueous solution of 0.1 M hydroquinone (final concentration was 5 mM). The resulting mixture was hand-shaken until it became clear. Finally, various amounts of seed solution were added to each mixture (1.5, 2.3, 3.1, 3.9, and 4.8 mL to obtain AR of 4.7, 5.2, 5.8, 6.2, and 6.4, respectively) and the samples were stored at 32 °C overnight.

**Film Fabrication and Plasma Cleaning.** Because of their narrow size distribution, the AuNRs self-organize when a concentrated drop of their aqueous suspension is cast on a flat substrate and allowed to dry very slowly (24 h) in a saturated moist atmosphere. In order to do that, the as-synthesized gold nanoparticle solutions ( $5 \times 10^{-4}$  M, 10 mL) were centrifuged at 6000 rpm for 20 min two times to remove the excess of surfactant and concentrate the solution. The supernatant was discarded, and the precipitate after the second centrifugation was redispersed in 1 mL of  $\text{H}_2\text{O}$ . The final concentration of the gold dispersions before the assembly was  $5 \times 10^{-3}$  M and of CTAB 1 mM. To produce the films, 10  $\mu\text{L}$  of each concentrated gold suspension was deposited on a glass slide and allowed to dry for 24 h in a saturated moist atmosphere. Dried samples on glass were cleaned with plasma before scanning electron

microscopy (SEM) characterization and SERS analysis (SEM characterization was also performed before plasma cleaning). Plasma was generated in oxygen atmosphere at 0.2 mbar using a plasma etcher operating at 0.1 kW (flecto10, Plasma Technology) and an exposition time of 2 min.

**Characterization.** Ultraviolet–visible–near-infrared (UV–vis–NIR) spectra were recorded using an Agilent 8453 diode array spectrophotometer. SEM images were obtained with a JEOL JSM 6700F field-emission microscope. Transmission electron microscopy (TEM) was conducted with a LEO 922 microscope operating at an acceleration voltage of 200 kV.

**Surface-Enhanced Raman Scattering Spectroscopy.** SERS experiments were performed with a micro-Renishaw InVia Reflex system. The spectrograph uses a high-resolution grating (1800 or 1200 grooves  $\text{cm}^{-1}$  for the visible or NIR, respectively) with additional band-pass filter optics, a confocal microscope, a 2D-CCD camera, and an automatized stage of 100 nm of spatial resolution. Excitation was carried out using laser lines at 633 or 785 nm. Average SERS analysis of colloidal dispersions was carried out in 1 mL of the particle solution with a fixed gold concentration of  $5 \times 10^{-4}$  M and an analyte (benzenethiol) concentration of  $10^{-5}$  M. Measurements were made by using a macrosampler accessory with integration times of 10 s and a power at the sample of 10 mW. To characterize the gold films, 10  $\mu\text{L}$  of  $10^{-5}$  M benzenethiol solution in ethanol was cast onto the film surfaces. Surfaces were then mapped using the Renishaw StreamLine accessory, with a step size of 0.6 nm. Acquisition times were set to 2 s with power at the sample of 0.2 mW. The same protocol was followed to set detection limits by diluting the molecular probe solution.

## Results and Discussion

One of the key factors for the spontaneous organization of particles is their homogeneity in size and shape.<sup>11,27,28</sup> **Figure 8.2** shows representative TEM images of different AuNRs and their size distributions plotted as histograms. AuNRs were synthesized by varying the amount of seeds during their growth, keeping all other parameters constant.<sup>26</sup> The TEM images clearly reveal the high quality of the anisotropic nanoparticles obtained without further purification. Localized surface plasmon resonance (LSPR) maxima are observed around 510 nm for the transversal

LSPR and between 940 and 1040 nm for the longitudinal LSPR as a linear function of their aspect ratio (**Figure 8.3A**).

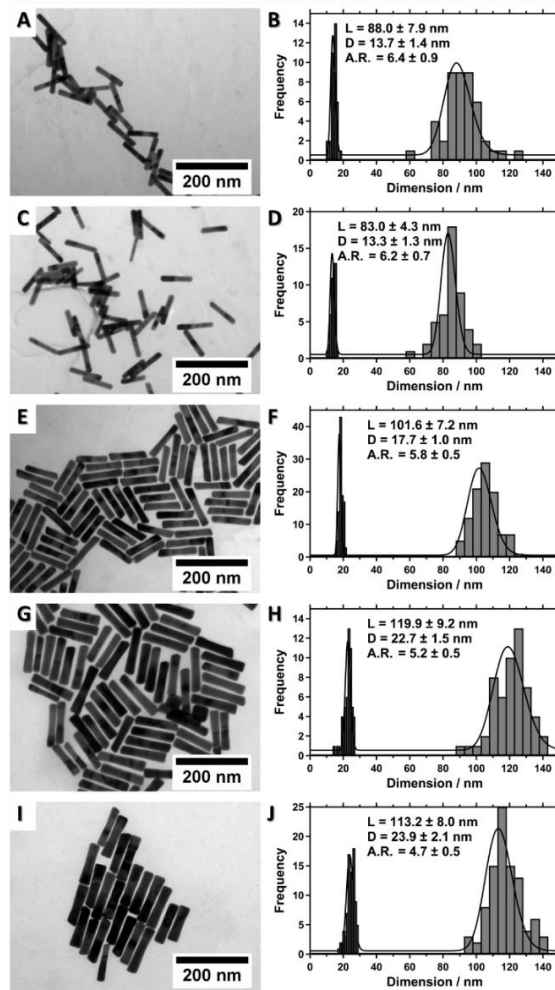


**Figure 8.2.** (A–J) TEM images of different AuNRs types with decreasing AR and their corresponding size distribution plotted as histograms.

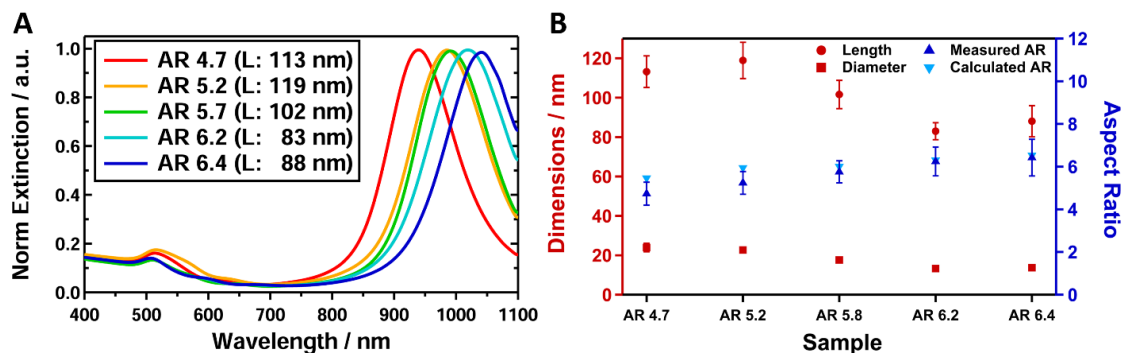


**Figure 8.3.** (A) UV–vis spectra of AuNRs in solution normalized at the longitudinal LSPR maxima. (B) Dimensions (red) and aspect ratios (blue) of the different samples obtained by TEM evaluation. Circles and rectangles in red indicate the length and diameter, respectively. The measured and calculated aspect ratios are plotted as triangles in dark blue and light blue, respectively.

The narrow distribution of the band and the large longitudinal-to-transversal LSPR peak ratio indicate high monodispersity and purity of all samples in good agreement with the aspect ratio of the different samples obtained through TEM and theoretically calculated by applying the equation  $AR_{\text{calculated}} = (\lambda_{\text{LLSPR}} - 420)/95$  (Figure 8.3B).<sup>26,29</sup> SERS response of these colloidal solutions was evaluated by adding a minute amount of benzenethiol to reach a final concentration of  $10^{-5}$  M (Figure 8.4).

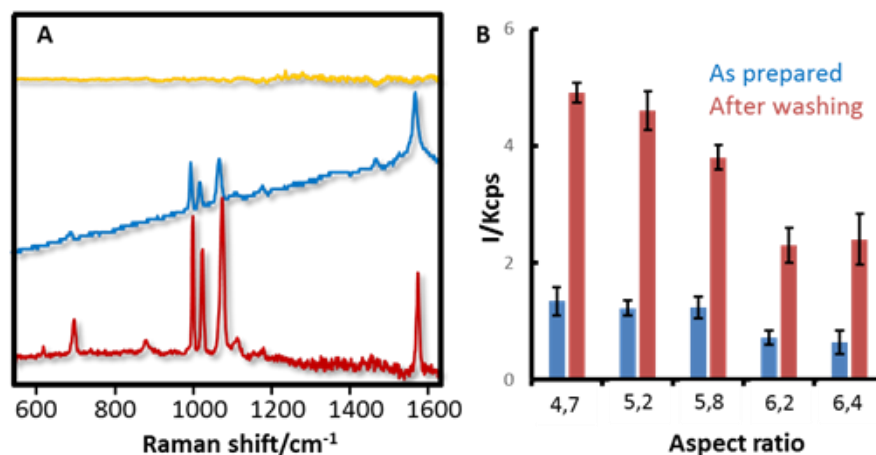
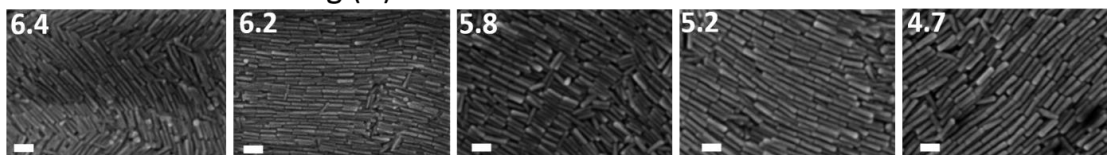


**Figure 8.4.** (A) SERS spectra of BT ( $10^{-5}$  M) on AuNR (AR 4.7) upon excitation with a 633 nm (yellow spectrum) and a NIR laser before (blue spectrum) and after (red spectrum) removing the excess of CTAB by centrifugation (3 times). (B) SERS intensities obtained by monitoring the ring breathing of BT ( $1073\text{ cm}^{-1}$ ,  $10^{-5}$  M) on AuNR samples with varied AR before (blue bars) and after (red bars) removing the excess of CTAB.

Samples were studied as prepared (0.1 M CTAB) and after repeated washing (three times) by centrifugation and redispersion (1 mM CTAB). Notably, excitation with the 633 nm laser did not yield any discernible SERS signals, probably because of the complete lack of resonance between the longitudinal plasmon resonance and the laser. However, upon excitation with the NIR laser source (785 nm), all the samples give rise to the characteristic spectral profile of BT (ring stretching mode at  $1573\text{ cm}^{-1}$ , C–H bending at  $1022\text{ cm}^{-1}$ , and ring breathing at  $1073$  and  $999\text{ cm}^{-1}$ ).<sup>30</sup> Remarkably, the SERS intensity decays as the AR increases probably because of the loss of resonance with the optical enhancer as the LSPR shifts to the red, as observed in the case of the red excitation. Although as-prepared samples show clear SERS signals for the NIR excitation laser,<sup>31</sup> the intensity is modest and consistently increases after reducing the CTAB concentration in solution by washing, which improves the analyte accessibility to the AuNR surface. However, the determined final SERS intensity is not exceptional for the relatively high concentrations used for the experiment.

Furthermore, the detection limit, after sequential dilution of BT into AuNRs (AR 4.7), was set to  $\sim 3 \times 10^{-7}$  M. These observations can be explained by the limited adsorption of the analyte onto the nanorod surfaces hindered by the presence of a dense CTAB double-layer, in good agreement with our previous results<sup>18</sup> and those obtained by Murphy's group.<sup>6</sup>

Before Plasma Cleaning (A)



After Plasma Cleaning (B)

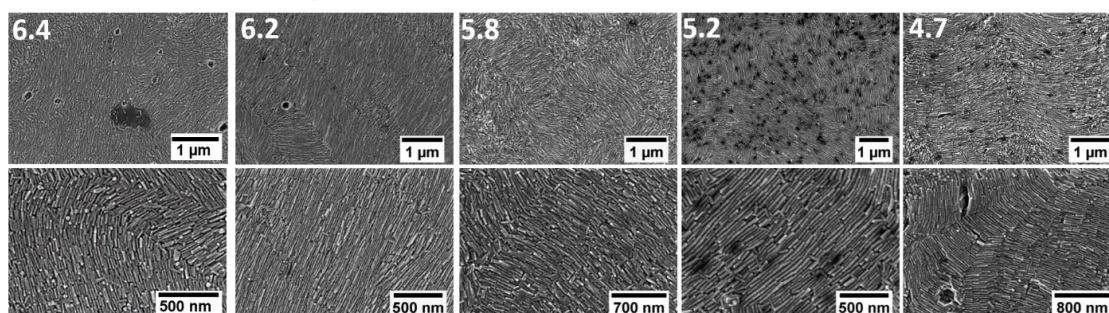


**Figure 8.5.** (A) SEM images of the AuNR films before the cleaning step (scale bar is 100 nm). (B) SEM images at two different magnifications of the cleaned AuNR films. From left to right: the corresponding AR of the AuNRs used to form the films are 6.4, 6.2, 5.8, 5.2, and 4.7.

Organization of plasmonic particles into densely packed films is known to generate active optical hot-spots responsible for the enhancement of the measured SERS signal of several orders of magnitude.<sup>32,33</sup> The classical transversal hot-spot generation found for individual nanorods was described by Brus<sup>34,35</sup> some time ago. Currently, we know that in addition a hot-spot due to the tip-to-tip interaction between AuNRs can be generated by appropriate organization of the rods. Notably, when CTAB coated nanoparticles are dispersed in a good solvent, they experience a repulsive interaction force due to positive surface charges and short-range steric repulsion essential for keeping them colloidally stable. On the other hand, if the nanoparticles are highly concentrated and confined in small volumes, a drying process will increase the concentration of nanoparticles at the three-phase borderline because of convective flow. When the particle concentration in solution exceeds a critical value, they finally undergo a spontaneous self-assembly process to minimize the free energy in the system and assemble into well-defined superlattices. In our case, films were produced by controlled air-drying of a pre-concentrated solution of nanorods on cleaned glass

slides. Because of the low particle concentrations used here, as compared to that necessary to form supercrystals,<sup>11,22</sup> rods tend to organize lying down on the substrate rather than standing up (**Figure 8.5**). This configuration allows for the generation of both side-to-side and tip-to-tip hotspots, as can be seen from SEM images shown in **Figure 8.5**. Thus, superlattices of organized gold nanorods will show several plasmon couplings leading to complex absorption and scattering behavior as reported in the literature.<sup>11</sup>

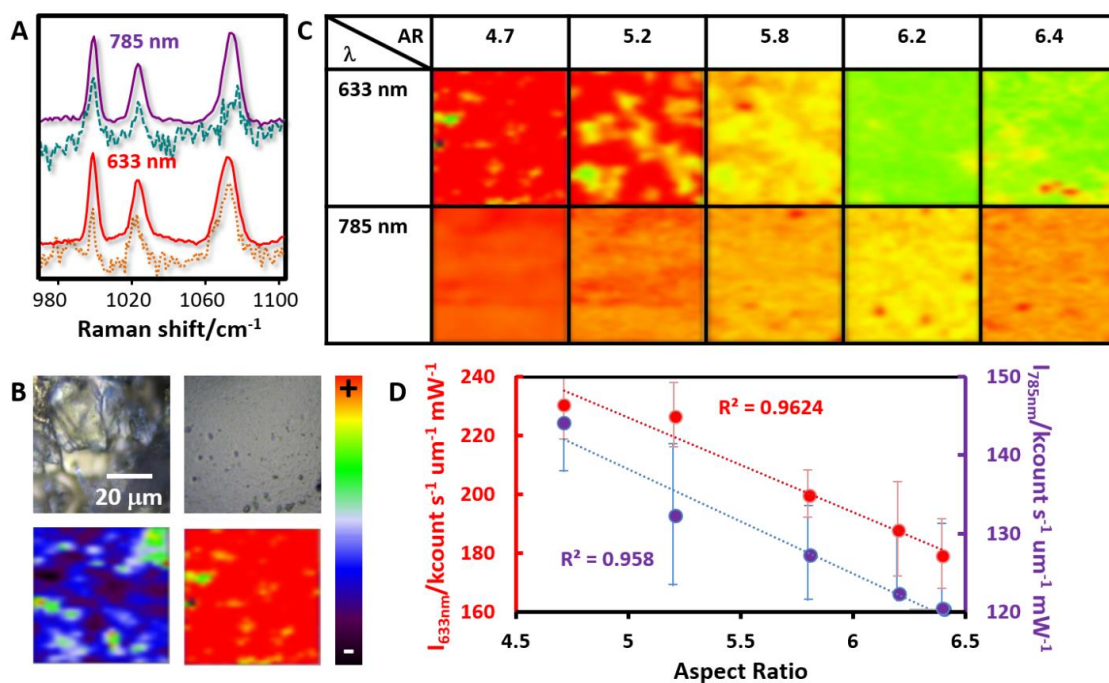


**Figure 8.6.** (A) SERS spectra of BT on a AuNRs film (AR 4.7) before (dotted lines) and after (solid lines) the plasma cleaning. (B) Optical and SERS images (mapped at the ring breathing, 1073 cm<sup>-1</sup>) before (left-hand panels) and after (right-hand panels) the plasma treatment. Comparison of the SERS (C) homogeneity and (D) intensity for the different films studied with the excitation lines at 633 and 785 nm.

To test the optical enhancing properties and efficiency of the films, the as-prepared samples were cleaned with oxygen plasma to remove all the organic material retained on their surface (*i.e.*, CTAB). SERS properties were studied before and after the cleaning process by drop-casting and air-drying an ethanolic solution of BT which interacts strongly with the Au surface through the thiol.<sup>36</sup> **Figure 8.6A,B** shows the resulting SERS spectra, the optical images, and SERS mapping of the sample with the lowest aspect ratio (4.7) before and after plasma cleaning. Before the plasma treatment, the interaction between Au surface and BT is hindered because of the

presence of a compact thin film of CTAB.<sup>18</sup> Thus, the SERS intensity provided by the film is weak and inconsistent. On the contrary, after the cleaning process, the analyte can easily reach the Au surface. Thus, a subsequent increase in both the SERS intensity and the point-to-point reproducibility is observed. Note that after plasma treatment no structural changes on the films or in the morphology of the AuNRs forming them is observed (**Figure 8.5**).

**Figure 8.6C** shows the SERS maps obtained for the two excitation laser lines for the different cleaned AuNR films. Contrary to the results in solution, SERS signals obtained for the organized films arise strongly from all samples with detection limits for an aspect ratio of 4.7 of  $2 \times 10^{-9}$  M and  $4 \times 10^{-9}$  M for 633 and 785 nm, respectively. Furthermore, all the films show good point-to-point intensity reproducibility. Additionally, a linear tendency to increase SERS intensities with decreasing aspect ratio is observed for both laser lines (**Figure 8.6D**). In Au NRs, the linear relationship between the position of the longitudinal plasmon and their aspect ratio is well-known.<sup>26,29</sup> Because of the close packing of the organized AuNRs on the films, the consequent plasmon coupling very likely displays the same trend. Our results show that the intensity obtained for excitation with the red laser line at 633 nm is higher than that for the NIR laser at 785 nm. Although there is not a remarkable difference between them, a more pronounced increase is observed for the red laser line. This may be due to the close-packing of the organized AuNRs and the consequent plasmon coupling. The strong coupling of the plasmon resonances of both transversal and longitudinal modes leads to a red-shift and broadening.<sup>36</sup> Consequently, the longitudinal LSPR loses resonance even with the NIR laser. This indicates that obtained SERS signals are provided mainly from the hot-spot formed by the side-to-side nanorod interactions rather than tip-to-tip, which also explains why the increase in intensity is more pronounced for the 633 nm laser.

Furthermore, in our experiments, the nanoparticles with lower AR have larger dimensions resulting in lower hot-spot density on the surface. This effect is readily overcompensated for lower AR AuNRs by the red-shift of the plasmon resonances due to the strong coupling in the film and consequently better overlap of the excitation laser.

## Conclusion

We have shown a fast and easy method of fabricating efficient optical films based on the organization of nanorods for SERS applications. Notably, the SERS efficiency of the prepared films strongly depends on the surface cleaning procedure and on the nanoparticle aspect ratio. Because of the close-packing of the AuNRs, the plasmon resonances of both transversal and longitudinal modes strongly couple and are strongly redshifted; thus, the longitudinal LSPR loses resonance even with the NIR laser, whereas for the 633 nm laser, intensity is more pronounced, indicating that obtained SERS signals are provided mainly by the side-to-side nanorod interactions.

## Acknowledgements

This work was funded by the Spanish Ministerio de Economía y Competitividad (CTQ2011-23167), the European Research Council (CrossSERS, FP7MC-IEF329131, PRIOSERS FP7MC-IEF-623527, and ERC-2012-StG 306686 METAMECH), NatoCBRN collaborative project CLG 984267, the German Research Foundation (DFG) within the collaborative research center SFB 840, and Medcom Advance SA. M.T. was supported by the Elite Network Bavaria in the frame of the Elite Study Program “Macromolecular Science” and funded *via* a grant for Ph.D. candidates according to Bavarian elite promotion law (BayEFG).

## References

- (1) Myroshnychenko, V.; Rodriguez-Fernandez, J.; Pastoriza-Santos, I.; Funston, A. M.; Novo, C.; Mulvaney, P.; Liz-Marzan, L. M.; Garcia de Abajo, F. J., Modelling the optical response of gold nanoparticles. *Chem Soc Rev* **2008**, *37*, 1792-1805.
- (2) Bryant, G. W.; García De Abajo, F. J.; Aizpurua, J., Mapping the plasmon resonances of metallic nanoantennas. *Nano Lett* **2008**, *8*, 631-636.
- (3) Tebbe, M.; Cherepanov, P.; Skorb, E. V.; Poznyak, S. K.; de Abajo, J. G.; Fery, A.; Andreeva, D. V.; Puebla, R. A. A.; Pazos-Perez, N., SERS Platforms of Plasmonic Hydrophobic Surfaces for Analyte Concentration: Hierarchically Assembled Gold Nanorods on Anodized Aluminum. *Part Part Syst Charact* **2014**, *31*, 1134–1140.
- (4) Gou, L.; Murphy, C. J., Fine-Tuning the Shape of Gold Nanorods. *Chem Mater* **2005**, *17*, 3668-3672.
- (5) Orendorff, C. J.; Gearheart, L.; Jana, N. R.; Murphy, C. J., Aspect ratio dependence on surface enhanced Raman scattering using silver and gold nanorod substrates. *Phys Chem Chem Phys* **2006**, *8*, 165-170.
- (6) Sivapalan, S. T.; Devetter, B. M.; Yang, T. K.; Van Dijk, T.; Schulmerich, M. V.; Carney, P. S.; Bhargava, R.; Murphy, C. J., Off-resonance surface-enhanced raman spectroscopy from gold nanorod suspensions as a function of aspect ratio: Not what we thought. *ACS Nano* **2013**, *7*, 2099-2105.
- (7) Huang, X.; El-Sayed, I. H.; Qian, W.; El-Sayed, M. A., Cancer Cells Assemble and Align Gold Nanorods Conjugated to Antibodies to Produce Highly Enhanced, Sharp, and Polarized Surface Raman Spectra: A Potential Cancer Diagnostic Marker. *Nano Lett* **2007**, *7*, 1591-1597.
- (8) Zong, S.; Wang, Z.; Yang, J.; Cui, Y., Intracellular pH sensing using p-aminothiophenol functionalized gold nanorods with low cytotoxicity. *Anal Chem* **2011**, *83*, 4178-4183.

- (9) Jokerst, J. V.; Cole, A. J.; Van De Sompel, D.; Gambhir, S. S., Gold nanorods for ovarian cancer detection with photoacoustic imaging and resection guidance via Raman imaging in living mice. *ACS Nano* **2012**, *6*, 10366-10377.
- (10) Song, J.; Pu, L.; Zhou, J.; Duan, B.; Duan, H., Biodegradable theranostic plasmonic vesicles of amphiphilic gold nanorods. *ACS Nano* **2013**, *7*, 9947-9960.
- (11) Alvarez-Puebla, R. A.; Agarwal, A.; Manna, P.; Khanal, B. P.; Aldeanueva-Potel, P.; Carbó-Argibay, E.; Pazos-Pérez, N.; Vigderman, L.; Zubarev, E. R.; Kotov, N. A.; Liz-Marzán, L. M., Gold nanorods 3D-supercrystals as surface enhanced Raman scattering spectroscopy substrates for the rapid detection of scrambled prions. *Proc Natl Acad Sci U S A* **2011**, *108*, 8157-8161.
- (12) Peng, B.; Li, G.; Li, D.; Dodson, S.; Zhang, Q.; Zhang, J.; Lee, Y. H.; Demir, H. V.; Yi Ling, X.; Xiong, Q., Vertically aligned gold nanorod monolayer on arbitrary substrates: Self-assembly and femtomolar detection of food contaminants. *ACS Nano* **2013**, *7*, 5993-6000.
- (13) Saute, B.; Premasiri, R.; Ziegler, L.; Narayanan, R., Gold nanorods as surface enhanced Raman spectroscopy substrates for sensitive and selective detection of ultra-low levels of dithiocarbamate pesticides. *Analyst* **2012**, *137*, 5082-5087.
- (14) Grzelczak, M.; Perez-Juste, J.; Mulvaney, P.; Liz-Marzan, L. M., Shape control in gold nanoparticle synthesis. *Chem Soc Rev* **2008**, *37*, 1783-1791.
- (15) Alkilany, A. M.; Nagaria, P. K.; Hexel, C. R.; Shaw, T. J.; Murphy, C. J.; Wyatt, M. D., Cellular Uptake and Cytotoxicity of Gold Nanorods: Molecular Origin of Cytotoxicity and Surface Effects. *Small* **2009**, *5*, 701-708.
- (16) Guerrini, L.; Jurasekova, Z.; del Puerto, E.; Hartsuiker, L.; Domingo, C.; Garcia-Ramos, J. V.; Otto, C.; Sanchez-Cortes, S., Effect of Metal–Liquid Interface Composition on the Adsorption of a Cyanine Dye onto Gold Nanoparticles. *Langmuir* **2013**, *29*, 1139-1147.

- (17) Pazos-Perez, N.; Garcia De Abajo, F. J.; Fery, A.; Alvarez-Puebla, R. A., From nano to micro: Synthesis and optical properties of homogeneous spheroidal gold particles and their superlattices. *Langmuir* **2012**, *28*, 8909-8914.
- (18) Spuch-Calvar, M.; Rodríguez-Lorenzo, L.; Morales, M. P.; Álvarez-Puebla, R. A.; Liz-Marzán, L. M., Bifunctional nanocomposites with long-term stability as SERS optical accumulators for ultrasensitive analysis. *J Phys Chem C* **2009**, *113*, 3373-3377.
- (19) Sanles-Sobrido, M.; Correa-Duarte, M. A.; Carregal-Romero, S.; Rodríguez-González, B.; Álvarez-Puebla, R. A.; Hervés, P.; Liz-Marzán, L. M., Highly Catalytic Single-Crystal Dendritic Pt Nanostructures Supported on Carbon Nanotubes. *Chem Mater* **2009**, *21*, 1531-1535.
- (20) Kang, Y.; Ye, X.; Chen, J.; Qi, L.; Diaz, R. E.; Doan-Nguyen, V.; Xing, G.; Kagan, C. R.; Li, J.; Gorte, R. J.; Stach, E. A.; Murray, C. B., Engineering Catalytic Contacts and Thermal Stability: Gold/Iron Oxide Binary Nanocrystal Superlattices for CO Oxidation. *J Am Chem Soc* **2013**, *135*, 1499-1505.
- (21) Ye, X.; Chen, J.; Diroll, B. T.; Murray, C. B., Tunable Plasmonic Coupling in Self-Assembled Binary Nanocrystal Superlattices Studied by Correlated Optical Microspectrophotometry and Electron Microscopy. *Nano Lett* **2013**, *13*, 1291-1297.
- (22) Alba, M.; Pazos-Perez, N.; Vaz, B.; Formentin, P.; Tebbe, M.; Correa-Duarte, M. A.; Granero, P.; Ferré-Borrull, J.; Alvarez, R.; Pallares, J.; Fery, A.; De Lera, A. R.; Marsal, L. F.; Alvarez-Puebla, R. A., Macroscale plasmonic substrates for highly sensitive surface-enhanced raman scattering. *Angew Chem, Int Ed* **2013**, *52*, 6459-6463.
- (23) Ben, X.; Park, H. S., Strain engineering enhancement of surface plasmon polariton propagation lengths for gold nanowires. *Appl Phys Lett* **2013**, *102*, 041909-1-4.
- (24) Solis, D.; Chang, W.-S.; Khanal, B. P.; Bao, K.; Nordlander, P.; Zubarev, E. R.; Link, S., Bleach-Imaged Plasmon Propagation (BIIPP) in Single Gold Nanowires. *Nano Lett* **2010**, *10*, 3482-3485.

- (25) Kraus, T.; Brodoceanu, D.; Pazos-Perez, N.; Fery, A., Colloidal surface assemblies: Nanotechnology meets bioinspiration. *Adv Funct Mater* **2013**, *23*, 4529-4541.
- (26) Vigdeman, L.; Zubarev, E. R., High-Yield Synthesis of Gold Nanorods with Longitudinal SPR Peak Greater than 1200 nm Using Hydroquinone as a Reducing Agent. *Chem Mater* **2013**, *25*, 1450-1457.
- (27) Mueller, M.; Tebbe, M.; Andreeva, D. V.; Karg, M.; Alvarez Puebla, R. A.; Pazos Perez, N.; Fery, A., Large-area organization of pNIPAM-coated nanostars as SERS platforms for polycyclic aromatic hydrocarbons sensing in gas phase. *Langmuir* **2012**, *28*, 9168-9173.
- (28) Schweikart, A.; Pazos-Pérez, N.; Alvarez-Puebla, R. A.; Fery, A., Controlling inter-nanoparticle coupling by wrinkle-assisted assembly. *Soft Matter* **2011**, *7*, 4093-4100.
- (29) Huang, X.; Neretina, S.; El-Sayed, M. A., Gold Nanorods: From Synthesis and Properties to Biological and Biomedical Applications. *Adv Mater* **2009**, *21*, 4880-4910.
- (30) Jung, H. Y.; Park, Y.-K.; Park, S.; Kim, S. K., Surface enhanced Raman scattering from layered assemblies of close-packed gold nanoparticles. *Anal Chim Acta* **2007**, *602*, 236-243.
- (31) Moskovits, M., Surface-enhanced spectroscopy. *Rev Mod Phys* **1985**, *57*, 783-826.
- (32) Braun, G.; Pavel, I.; Morrill, A. R.; Seferos, D. S.; Bazan, G. C.; Reich, N. O.; Moskovits, M., Chemically Patterned Microspheres for Controlled Nanoparticle Assembly in the Construction of SERS Hot Spots. *J Am Chem Soc* **2007**, *129*, 7760-7761.
- (33) Qin, L.; Zou, S.; Xue, C.; Atkinson, A.; Schatz, G. C.; Mirkin, C. A., Designing, fabricating, and imaging Raman hot spots. *Proc Natl Acad Sci U S A* **2006**, *103*, 13300-13303.

- (34) Bosnick, K. A.; Jiang; Brus, L. E., Fluctuations and Local Symmetry in Single-Molecule Rhodamine 6G Raman Scattering on Silver Nanocrystal Aggregates. *J Phys Chem B* **2002**, *106*, 8096-8099.
- (35) Jiang; Bosnick, K.; Maillard, M.; Brus, L., Single Molecule Raman Spectroscopy at the Junctions of Large Ag Nanocrystals. *J Phys Chem B* **2003**, *107*, 9964-9972.
- (36) Tritschler, U.; Zlotnikov, I.; Keckeis, P.; Schlaad, H.; Cölfen, H., Optical Properties of Self-Organized Gold Nanorod-Polymer Hybrid Films. *Langmuir* **2014**, *30*, 13781–13790.



# 9

## Macroscale Plasmonic Substrates for Highly Sensitive Surface-Enhanced Raman Scattering

*Maria Alba, Nicolas Pazos-Perez, Belen Vaz, Pilar Formentin, Moritz Tebbe, Miguel A. Correa-Duarte, Pedro Granero, Josep Ferre-Borrull, Rosana Alvarez, Josep Pallares, Andreas Fery, Angel R. de Lera, Lluís F. Marsal, and Ramon A. Alvarez-Puebla*



**Figure 9.1.** Inside Back Cover.

Published in **Angewandte Chemie International Edition**.

Reprinted with permission from Macroscale Plasmonic Substrates for Highly Sensitive Surface-Enhanced Raman Scattering, Alba *et al.*, *Angew Chem, Int Ed* **2013**, 52, 6459 - 6463. ©2013 The authors.



The fabrication of macroscale optical materials from plasmonic nanoscale building blocks is the focus of much current multidisciplinary research. In these macromaterials, the nanoscale properties are preserved, and new (metamaterial) properties are generated as a direct result of the interaction of their ordered constituents.<sup>1</sup> These macroscale plasmonic assemblies have found application in a myriad of fields, including nanophotonics, nonlinear optics, and optical sensing.<sup>2,3</sup> Owing to their specific requirements in terms of size and shape, their fabrication is not trivial and was until recently restricted to the use of lithographic techniques, especially those based on electron- or ion-beam patterning.<sup>4,5</sup> However, these techniques are not only expensive, time-consuming, and demanding but are also restricted to small simple and solid geometries, which are good for proof of concepts but less suitable for real-life applications. Approaches based on colloidal chemistry are gaining relevance as an alternative. During the past few years, several examples of the fabrication of organized particles have been reported, including the preparation of complex colloidal particles<sup>6,7</sup> and the use of preformed colloids to create large crystalline organized entities known as supercrystals.<sup>8-10</sup> The latter approach provides optical platforms with unprecedented plasmonic properties that can be exploited for the design of cheap ultrasensitive and ultrafast sensors with surface-enhanced Raman scattering (SERS)<sup>11</sup> spectroscopy as the transducer.

We report a new template-assisted method based on the stamping of colloidal particles for the large-area fabrication of organized pyramidal supercrystal periodical arrays. The extraordinary optical activity of these pyramidal supercrystals is demonstrated both theoretically and experimentally. The plasmonic platform is then exploited for the development of a handheld reversible SERS sensor for the live monitoring of carbon monoxide in the atmosphere. CO is a ubiquitous colorless, odorless, and tasteless gas produced during incomplete combustion (during tobacco smoking or in car engines and furnaces) which poses a potentially fatal threat to human health.

The method used for the preparation of the nanostructured pyramidal arrays is illustrated in the **Figure 9.2**. First, inverted pyramidal templates were prepared by direct laser writing lithography on oxidized p-type silicon wafers, followed by a chemical etching process (see the Supporting Information for details). This method yields periodically patterned surfaces with homogeneous inverted pyramids with dimensions that can be tuned from 1 to 10  $\mu\text{m}$  as a function of the etching time (see

Figure S3 in the Supporting Information). In this study we chose a period of  $8\ \mu\text{m}$  to generate pyramids with sides of  $4.5\ \mu\text{m}$  and a height of  $3.3\ \mu\text{m}$  (**Figure 9.2B**). This size enables the preparation of a truly macroscale nanostructured material that can be observed with a conventional optical microscope and permits detailed characterization of the optical-enhancing properties of the nanostructures. Prior to the deposition of the nanoparticles (NPs), the surfaces were cleaned with an oxygen plasma. A concentrated solution of gold NPs was then cast on the template, allowed to dry, and then transferred to the surface to yield a periodic array of square pyramids (**Figure 9.2C**; see the Supporting Information for details) derived from the compact packing of plasmonic particles (**Figure 9.2D**; see also **Figures 9.S4-S6**). Although the film was transferred to many surfaces, including glass, silicon wafers, and double-sided tape, we describe herein the studies carried out on versatile and flexible poly-(dimethylsiloxane) films (1 mm thick). AFM characterization of the film (see **Figure 9.S7**) showed nanoparticle pyramids with high homogeneity in all directions, with side lengths of  $4.4\ \mu\text{m}$  and a height of  $3.0\ \mu\text{m}$ .

Close observation of single pyramids (**Figure 9.2D**; see also **Figure 9.S4**) offers some insight into their structure, which in combination with the results of other studies allows us to propose a mechanism of formation. A monodisperse collection of spherical, organic-ligand-coated (in this case, with cetyltrimethylammonium bromide, CTAB) nanocrystals is expected to form a face-centered cubic lattice in a confined volume.<sup>8-10,12</sup> When dispersed in a solvent, the nanocrystals experience short-range steric repulsions.<sup>13</sup> However, when the nanoparticles are compressed together and their total density exceeds a critical value, the nanocrystals spontaneously assemble into a supercrystal. This ordering transition is driven by entropy. With negligible energetic interactions between nanocrystals, only the excluded volume of each particle matters, and the structure with the highest entropy is favored. The nanocrystals in a “dry” superlattice are held together by strong cohesive interactions between neighboring ligands and nanocrystals. Also, the repulsions between the hydrophobic supercrystal and the hydrophilic walls of the template favor the impression of the nanostructured features when the template is stamped against a surface.<sup>14,15</sup> Prior to its optical characterization, the film was cleaned with an oxygen plasma to remove CTAB and favor the contacts between the gold surfaces and the analytes used for SERS. This cleaning process does not affect

the geometry of the pyramids (see **Figure 9.S8**), as previously demonstrated with other supercrystals.<sup>8,10</sup>

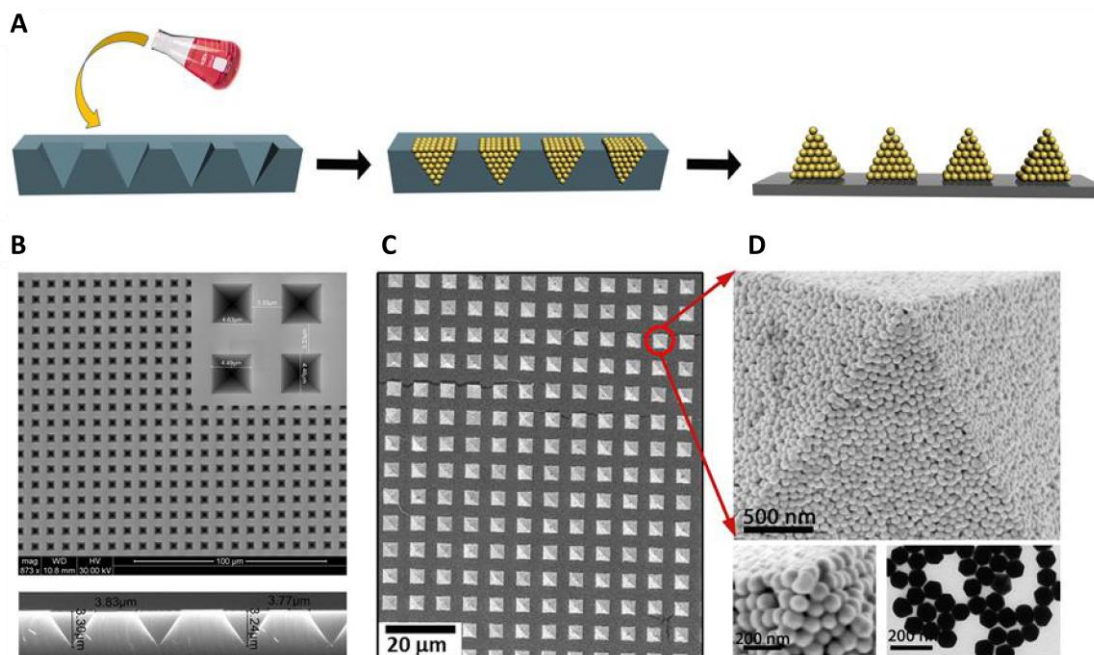


**Figure 9.2.** A) Schematic representation of the fabrication of the macroscale nanostructured film. B) Empty inverse pyramidal lithographic surfaces used as templates. C) SEM image of the macroscale plasmonic film after stamping. D) High-resolution SEM images of the pyramids and TEM image of the gold nanoparticle building blocks.

The formation of pyramidal supercrystals leads to strong plasmon coupling between the AuNPs. **Figure 9.3A** shows the experimental localized surface plasmon resonances (LSPRs) of the AuNPs in solution and after assembly into macroscale pyramids. Noninteracting nanoparticles exhibited a maximum at 540 nm characteristic of their dipolar plasmon mode. After assembly, the dipolar mode was red-shifted to 590 nm, which indicates a significant interparticle coupling. The supercrystals also showed a stronger LSPR contribution in the near-infrared (NIR) region, between 700 and 950 nm. To clarify the nature of this broad feature, we performed finite element method (FEM) calculations with the COMSOL Multiphysics package (see the Supporting Information for details). Tight binding analysis of the plasmon resonances in the supercrystal indicated the accumulation of an electric near field at the surface and the apex of the pyramid (inset in **Figure 9.3A**; see also **Figure 9.S9**). This effect is of central importance for the next generation of rapid and portable optical sensors. As a proof of concept, a diluted solution of 1-naphthalenethiol (1NAT; 10 mL,  $10^{-8}$  M) was spin coated on 1 cm<sup>2</sup> of the pyramid film,

and the surfaces were studied with an NIR laser line (785 nm). Although extremely strong SERS signals were acquired for 1NAT (**Figure 9.3B**) at all points, SERS mapping (**Figure 9.3C**) with a very low laser power at the sample (10 mW, with an acquisition time of 10 ms) clearly indicated a significant signal concentration at the apex of the pyramids. This effect was confirmed by high-resolution confocal SERS measurements on a single pyramid with spatial-resolution steps of 500 nm (**Figure 9.3D**).

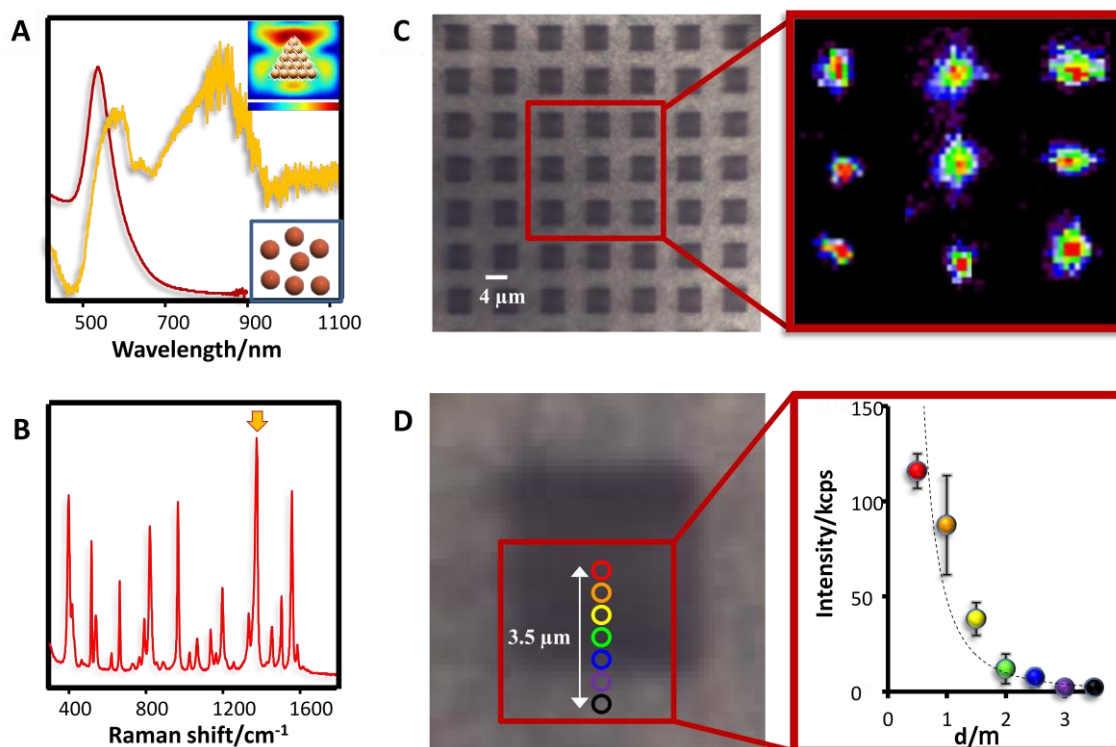


**Figure 9.3.** A) Normalized UV/Vis/NIR spectra of the gold nanoparticles in solution (red) and after their impression into plasmonic films (yellow). Top inset: distribution of the near electric field in a pyramid composed of particles. B) Representative SERS spectrum of 1-naphthalenethiol on the pyramid film. The spectrum is characterized by ring stretching (1553, 1503, and 1368  $\text{cm}^{-1}$ ), CH bending (1197  $\text{cm}^{-1}$ ), ring breathing (968 and 822  $\text{cm}^{-1}$ ), ring deformation (792, 664, 539, and 517  $\text{cm}^{-1}$ ), and C-S stretching (389  $\text{cm}^{-1}$ ). C) Optical image and SERS imaging of the band highlighted in B with an arrow. The SERS image shows enhancement mapping with higher signals concentrated around the center of the pyramids. D) Optical image of one pyramidal structure and comparison of the intensities provided by different areas of the plasmonic film. All spectra were acquired with a benchtop high-resolution confocal Raman microscope (acquisition conditions:  $\lambda_{\text{ex}} = 785 \text{ nm}$ , 10 ms, power at the sample: 10 mW, spatial resolution: 500 nm).

Although the remarkable optical activity of these macroscale plasmonic platforms makes them exceptional candidates for academic applications, such as single-molecule detection<sup>16</sup> (see **Figure 9.S10**), in this study we designed an ultrafast and reversible optical sensor for the monitoring of carbon monoxide (CO) with an inexpensive handheld Raman spectrometer (see **Figure 9.S11**). Optical nanoantennas have already been reported for the detection of analytes in solution<sup>17</sup> and of inorganic gases.<sup>18</sup> In the case of inorganic gases, these approaches rely on the fabrication of segregated alloys containing silver or gold as the optically active material and another metal (usually platinum or palladium) as the capture material. However, the deposition of the trapping metal not only hinders the adsorption of the gas onto the optical material and leads to the corresponding decrease in sensitivity, but it is also not reversible. Once the gas is adsorbed on the metal, it does not desorb; thus, the sensor can only be used once. This strategy may be suitable for the detection of exotic gases, such as chemical warfare agents, but not for the effective monitoring of a toxic but ubiquitous gas, such as CO. In this case, the sensor should not only be quantitative, sensitive, and fast, but also operate reversibly so that it can inform the user when the concentration of the toxic species is above or below the toxic range. An alternative approach that fulfills these requirements is the monitoring of the vibrational changes induced on a SERS highly active secondary probe directly bound to the sensor, before and after interaction with the target.<sup>19,20</sup> The good affinity and reversible binding of myoglobin and hemoglobin to oxygen and carbon monoxide are known and in fact form the basis of the toxicity of carbon monoxide. Unfortunately, the use of proteins in SERS is not the best solution, as these biopolymers are usually characterized by poor SERS cross-sections. Alternatively, it is possible to functionalize the plasmonic surfaces with an iron porphyrin, the genuine factor responsible for selective and reversible gas capture in blood with binding affinities even higher than those of the proteins.<sup>21</sup> However, to force a perpendicular orientation of these molecules on the pyramids, as required for the efficient capture of atmospheric gases, the introduction of a single thiol group at just one location of the porphyrin periphery was necessary. Thus, 5-[(triisopropylsilyl)thio]-10,20-diphenylporphyrin (TDPP) was synthesized, complexed with Fe<sup>II</sup>, and self-assembled onto the gold pyramids (see the Supporting Information for details).

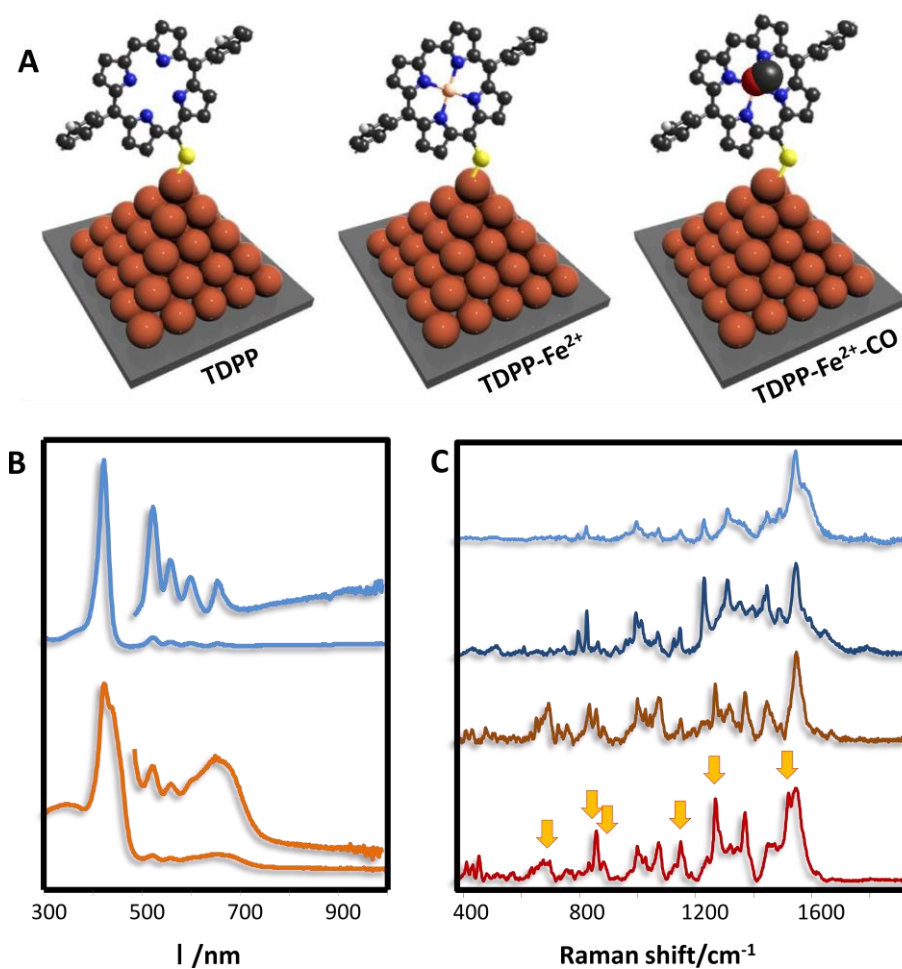


**Figure 9.4.** A) Schematic representation of the CO sensor composed of a macroscale plasmonic film and an iron porphyrin (TDPP). B) UV/Vis/NIR spectra of the porphyrin before and after complexation with Fe<sup>II</sup>. C) SERS spectra of the free porphyrin, the porphyrin coordinated to iron, and the iron porphyrin complexed with CO. The spectra are characterized by ring stretching (1549, 1490, 1444, 1370, and 1320 cm<sup>-1</sup>), CCN bending (1268 and 1240 cm<sup>-1</sup>), CCH bending (1146 and 1070 cm<sup>-1</sup>), ring breathing (1026 and 999 cm<sup>-1</sup>), ring deformation (880 and 857 cm<sup>-1</sup>), and N-Fe stretching (591, 569, 506, and 420 cm<sup>-1</sup>). Arrows in the red spectrum highlight the spectral changes after CO complexation. All spectra were acquired with a handheld Raman macrosystem (acquisition conditions:  $\lambda_{\text{ex}} = 785$  nm, 1 s, power at the sample: 1 mW, spatial resolution: 1  $\mu\text{m}$ ). Double-headed arrows indicate the intensity.

**Figure 9.4B** shows the optical response of TDPP before and after iron coordination. Although both spectra showed the characteristic Soret and Q bands, the Soret band was redshifted from 420 to 442 nm upon formation of the iron porphyrin as a result of the distinct electronic environment brought about by the metal coordinated to the porphyrin center, and the four Q bands in the visible region collapsed into essentially two bands owing to the higher D<sub>4h</sub> symmetry of the TDPP-Fe complex. These two

features clearly indicate the successful coordination of the metal. Comparison of the Raman and SERS spectra of TDPP (see **Figure 9.S13**) showed an intensification of the modes corresponding to ring stretching and in-plane deformations and indicated that the molecular plane of TDPP is perpendicular to the plasmonic surface, in full agreement with the surface selection rules.<sup>22</sup> This result is also consistent with the preparation method, in which a dilute solution of the molecular probe was cast on the plasma-cleaned surfaces of the pyramids. SERS spectra for free and metal-coordinated TDPP (**Figure 9.4C**) were also consistent with the electronic spectra. Although bands directly related to the iron atom can be clearly seen below  $700\text{ cm}^{-1}$ ,<sup>23</sup> the most remarkable differences are found for the chromophore (*i.e.*, band joining and shifting) as a consequence of the constraints induced by the coordination of  $\text{Fe}^{\text{II}}$ .<sup>23</sup> Notably, after the complexation of TDPP–Fe with CO, several characteristic changes were observed (highlighted with arrows in **Figure 9.4C**). In fact, by following these spectral changes for TDPP–Fe before and after CO complexation it is possible to obtain quantitative information on the amount of CO present in the environment at a given moment.

The detection limits and ranges of these indirect sensors depend strictly on the amount of sensing molecules on the plasmonic surfaces. The amount of molecules required for a good SERS signal depends also on the SERS cross-section of the probe molecule. TDPP–Fe, as any porphyrin, is characterized by its high SERS cross-section, which enables single-molecule detection to be reached.<sup>24</sup> Thus, in principle, the use of this biointerlayer mimic would enable the detection of CO in the single-molecule regime. In practice, this sensitivity is unnecessary. Exposure to 500 ppm of CO for 1 h can be fatal, whereas CO at a concentration of 100 ppm causes headaches and drowsiness, and 50 ppm of CO induces deterioration of motor skills; however, at CO concentrations below 40 ppm, no symptoms have been reported.<sup>25</sup> Thus, to set a detection-limit range between 1 and 100 ppm, we explored the effects of different amounts of TDPP–Fe molecules on the pyramid film. Optimal results were obtained by the spin coating of 10 mL of a  $3 \times 10^{-6}$  M solution of TDPP–Fe per square centimeter of surface. Under a confocal Raman microscope, this concentration yielded a very high SERS signal with very low power at the sample ( $1\ \mu\text{W}$ ) and an acquisition time of 10 ms owing to the extraordinary optical activity of the pyramids.

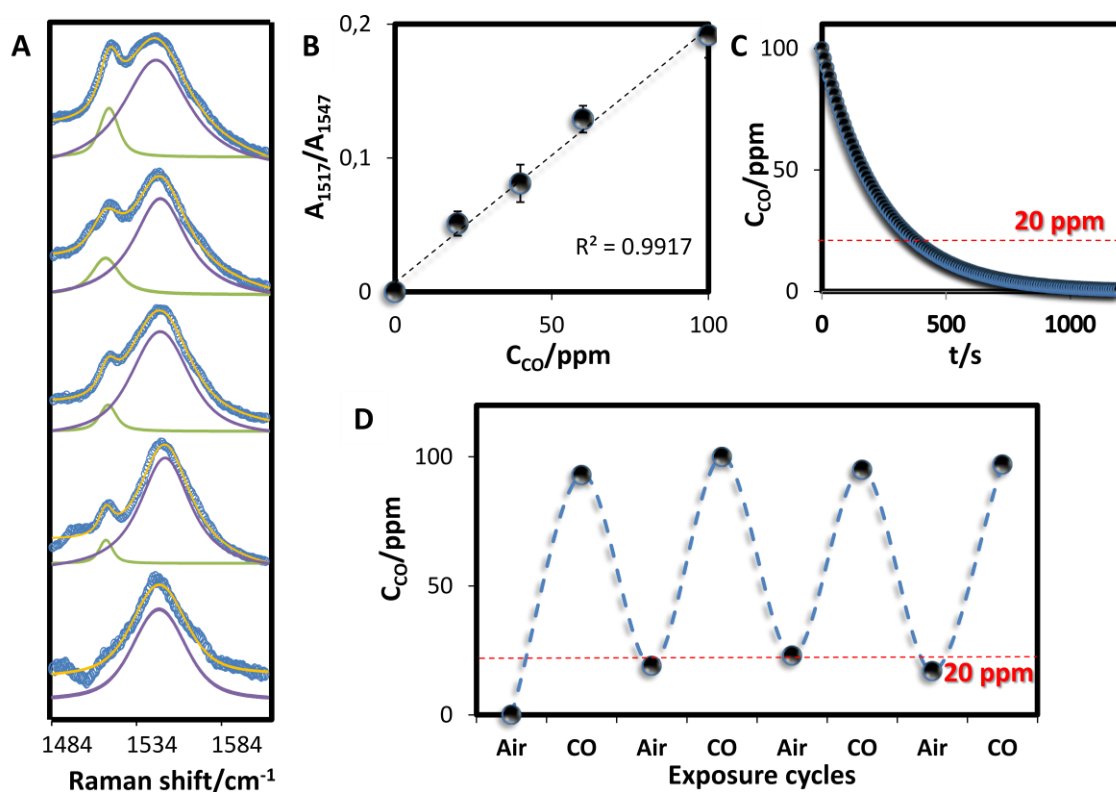


**Figure 9.5.** A) Normalized deconvolution of bands 1547 and 1517 cm<sup>-1</sup> (both of which are due to pyrrole-ring stretching) on the basis of an assumed Lorentzian shape, whereby the band position and the full width at half-maximum are fixed. Blue: experimental spectrum; yellow: spectrum resulting from the addition of peak 1 (green) to peak 2 (purple). B) Linear plot of the area ratio of the peaks at 1517 and 1547 cm<sup>-1</sup> as a function of CO concentration. Error bars represent the standard deviation for five replicated experiments. C) Signal decay due to the displacement of CO by O<sub>2</sub> as a function of time. D) Sensor reversibility during several cycles of exposure to CO and air.

These parameters enable the use of the portable handheld Raman system for macroscopic measurements. Deconvolution of the bands at 1516 and 1552 cm<sup>-1</sup> (**Figure 9.5A**)<sup>26</sup> and plotting of the band-area ratio against the CO concentration gave a linear correlation, with an impressive  $R^2$  value of 0.9917 (**Figure 9.5B**). This result demonstrates the quantitative nature of this method of analysis. Furthermore, under normal atmospheric conditions, the signal decreases over time (**Figure 9.5C**) owing to the competition between CO and O<sub>2</sub>. After about 20 min, the signal could not be observed; however, after only 5 min, the signal decreased below 20 ppm CO: a tolerable level for humans. With this information in mind, we designed several experiments on the same substrate for the evaluation of the reversibility of the sensor. The active sensor was always recovered in less than 5 min after exposure to air (**Figure 9.5D**); it could therefore be used for continuous monitoring of this gas in the

environment. In summary, we have demonstrated the feasibility of patterning homogeneous macroscale nanoparticle architectures over large areas. Owing to the interaction of the nanoparticles, the pyramids show a considerable plasmon accumulation on their surfaces and, in particular, at the tips. These plasmonic macrosubstrates were exploited for the fabrication of a reversible and portable optical sensor for CO.

## Keywords

macroscale arrays, nanoparticles, optical sensors, plasmonic films, surface-enhanced Raman scattering

## Supporting Information

### Materials and Methods:

**Inverted pyramid template fabrication:** p-type silicon wafers were oxidized in dry O<sub>2</sub> at 1000 °C for 15 min, in order to grow a thin silicon dioxide film (SiO<sub>2</sub>). The oxide film only serves as a mask and as a protective layer in the subsequent anisotropic etch of the silicon in tetramethyl ammonium hydroxide (TMAH, Aldrich) solution. The oxidation step cannot be avoided as the normal resists used in the lithography are easily dissolved by TMAH. Direct laser writing lithography, was used to define the arrangement and period of the resulting pore lattice. A positive photoresist AZ 1505 with a developer AZ 726 metal ion free (Micro Chemicals) were used in the lithography. Following, the lithographic pattern was then transferred into the oxide layer by etching the silicon oxide in buffered hydrofluoric acid (BHF, Aldrich). The used BHF etching mixture (Ammonium fluoride etching mixture HF (6%) and NH<sub>4</sub>F (35%), Honeywell Specialty Chemicals Seelze GmbH) has an etching rate of about 680 Å/min. Therefore, a few seconds are needed to etch the oxide which can result in an over-etching if very thin oxide layers are used. Next, the photoresist was removed and the silicon wafers were immersed in 8% TMAH solutions at 80 °C temperature for 7-9 min, in order to prepare the defect sites on the wafer surface. The TMAH etch is an anisotropic process; the resulting structure is a lattice of inverted pyramids. After the TMAH etch, the oxide layer is no longer needed so was removed with a HF 5% solution.

**Synthesis of gold nanoparticles:** Highly monodisperse spherical gold nanoparticles (~70 nm) were prepared using a previously reported seed mediated approach<sup>10</sup> similar to that used for the production of gold nanorods.<sup>27,28</sup> Briefly, a seed solution was prepared by mixing an aqueous solution (20 mL) containing H<sub>AuCl</sub><sub>4</sub> ( $2.5 \cdot 10^{-4}$  M, Aldrich) and trisodium citrate ( $2.5 \cdot 10^{-4}$  M, Aldrich). The mixture was vigorously stirring meanwhile NaBH<sub>4</sub> (0.1 M, 600  $\mu$ L, Aldrich) was added. A fast color change into red was observed after the NaBH<sub>4</sub> addition indicating the formation of the gold particles. The seeds were left under stirring for 1 h to allow the NaBH<sub>4</sub> decomposition and with the open bottle to avoid over pressure. Next, a grow solution was prepared by dissolving cetyltrimethylammonium bromide (CTAB, Merck) in milli-Q water (0.1 M, 250 mL) and 0.3 mg per kg of CTAB of potassium iodide (Aldrich). Followed by the addition of H<sub>AuCl</sub><sub>4</sub> (0.103 M, 1271  $\mu$ L) and ascorbic acid (0.1 M, 2088  $\mu$ L, Aldrich). After each addition the bottle was energetically agitated. After that, 500  $\mu$ L of the seeds solution were added to the growth solution and was vigorously stirred. The bottle was left undisturbed at 28 °C for 48 h. Afterwards a small amount of sediment is observed in the bottom of the flask. Carefully, the supernatant is collected and the precipitate discarded. The gold particles (200 mL) were concentrated by centrifugation (4 x 7000 rpm, 15 min) to a total volume of 2 mL. Then, the CTAB concentration was decreased from 0.1 M to a final concentration of 0.006 M by diluting 100  $\mu$ L of the concentrated Au solution with water (1.7 mL). Finally a centrifugation (6000 rpm, 10 min) step was done to achieve a final gold concentration of 3.5 mg/mL.

**Nanoparticle Assembly:** The preparation of the macroscaled nanostructured pyramidal arrays was achieved as follows. First, the inverted pyramid templates were treated with an oxygen plasma (O<sub>2</sub> 0.2 mbar, at 0.1 kW and 2 min in a Flecto10, from Plasma Technology) in order to clean and make the surfaces hydrophilic. Then 0.05 mL of the clean and concentrated gold particle solution was cast on the top of the template. The system was placed in a chamber with controlled humidity (99%) until the particle sedimentation (24 h). After that, the system was removed from the humidity chamber and allowed to dry. This procedure allows for the direct stamping of pyramidal arrays on whatever surface including silicon wafers, glass, Tesafilm or cured PDMS.

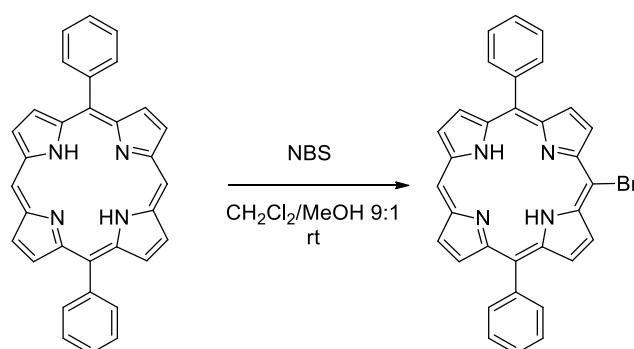
**Characterization.** UV-VIS spectroscopy was recorded with a PerkinElmer, Lambda 19. Size, shape and topographical characterization of the nanoparticles and their assemblies were characterized with transmission and scanning electron microscopy (TEM, LEO 922 EFTEM operating at 200 kV and LEO 1530 FE-SEM, Zeiss) and atomic force microscopy (NanoScope Dimension III and NanoScope V, Veeco Metrology Group). For the mass spectra, a Micromass® Quattro micro™ API was used and ions were generated using electrospray ionization (ESI) source, with a voltage of 5000 V (to optimize ionization efficiency) applied to the needle, and a cone voltage of 55 V.  $^1\text{H}$  NMR spectra were recorded in  $\text{CDCl}_3$  and  $\text{CD}_2\text{Cl}_2$  at ambient temperature on a Bruker AMX-400 spectrometer at 400 MHz with residual protic solvent as the internal reference [ $\text{CDCl}_3$ ,  $\delta_{\text{H}} = 7.26$  ppm;  $\text{CD}_2\text{Cl}_2$ ,  $\delta_{\text{H}} = 5.32$  ppm].  $^{13}\text{C}$  NMR spectra were recorded in  $\text{CDCl}_3$  and  $\text{CD}_2\text{Cl}_2$  at ambient temperature on the same spectrometer at 100 MHz, with the central peak of  $\text{CDCl}_3$ ,  $\delta_{\text{C}} = 77.16$  ppm;  $\text{CD}_2\text{Cl}_2$ ,  $\delta_{\text{C}} = 54.0$  ppm) as the internal reference. FTIR-ATR spectra were obtained on a JASCO IR 4200 spectrophotometer, with an ATR accessory (PIKE instruments) having a diamond ATR crystal. Raman and SERS were carried out with either a Renishaw Invia system or a handheld portable DeltaNu Raman Inspector instrument, exciting the sample with a 785 (diode) nm.

**Theoretical calculations.** Finite element method (FEM) electromagnetic simulations were performed with the COMSOL Multiphysics package using the RF module to completely solve the Maxwell equations. Gold spheres of 70 nm in diameter were considered, with the metal described through its measured dielectric function<sup>29</sup> and including a 0.5 nm coating of refractive index 1.3 to effectively represent the linking layer. The gold-to-gold gap distance was set to 1 nm in all cases. Excitation was carried out considering a monochromatic light (785 nm) parallel to the z axis.

**SERS characterization of the supercrystals:** In order to characterize the optical enhancing properties of the pyramidal supercrystals, a minute amount (10  $\mu\text{L}$ ) of a diluted solution ( $10^{-8}$  M) of 1-naphthalenethiol (1NAT, Aldrich) was spin-coated on 1  $\text{cm}^2$  of the pyramid film. Surfaces were then mapped using the Renishaw's StreamLine accessory, taking mapping areas of  $26 \times 36 \mu\text{m}^2$ , with a step size of 500 nm (x100 objective) upon excitation with an NIR (785 nm) laser line. Acquisition times were set to 10 ms with power at the sample of 10  $\mu\text{W}$ . The SERS response with the same analyte on other common substrates including evaporated gold and silver

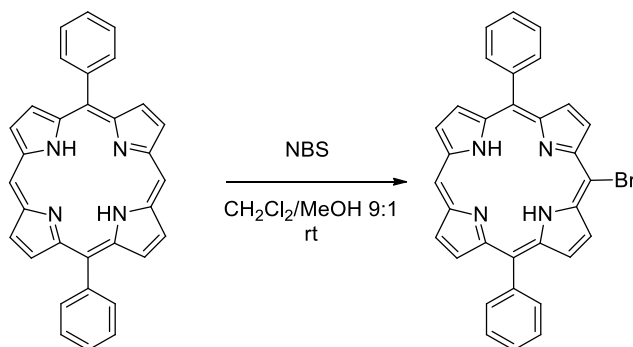
island films and aggregated gold and silver colloids can be found in ref. <sup>30</sup>. Intensity dependence with the morphology of the pyramid was studied point by point by with and step size of 500 nm and setting the autofocus track in a high confocality mode for each measurement. To probe single molecule detection, the same procedure was carried out using ethanolic solutions of crystal violet ( $10 \mu\text{L}$ ,  $10^{-12} \text{ M}$  per  $\text{cm}^2$ ) giving rise to an average concentration of less than 1 molecule/ $\mu\text{m}$  ( $0.06 \text{ molecules}/\mu\text{m}^2$ ).<sup>24</sup> The film was mapped using the Renishaw's StreamLine accessory with a 100x objective (spatial resolution of 500 nm), acquisition times of 2 s and a power at the sample of  $1 \mu\text{W}$ . Comparison between the Raman microscope and the handheld Raman system were carried out on the samples prepared with 1 NAT by using, in the case of the Raman microscope, a macrosampling objective with a spatial resolution of 1 mm, equivalent to that of the portable system.

**Phorphyrin synthesis:** Solvents were dried according to published methods and distilled before use. All other reagents were commercial compounds of the highest purity available. Unless otherwise indicated all reactions were carried out under argon atmosphere in oven-dried glassware. Analytical thin layer chromatography (TLC) was performed on aluminum plates with Merck Kieselgel 60F254 and visualized by UV irradiation (254 nm) or by staining with an ethanolic solution of phosphomolibdic acid. Flash column chromatography was carried out using Merck Kieselgel 60 (230-400 mesh) under pressure.



5-Bromo-10,20-diphenylporphyrin (BDPP):<sup>31</sup> 5,15-Diphenylporphyrin (9.6 mg, 0.021 mmol) was dissolved in  $\text{CH}_2\text{Cl}_2/\text{MeOH}$  (9:1, 4.9 mL) and NBS (4.1 mg, 0.023 mmol) was added. The reaction mixture was stirred under air at room temperature for 15 min and quenched with acetone (1.0 mL). The solvent was evaporated. The residue obtained was purified by flash chromatography (silicagel, hexane/ $\text{CH}_2\text{Cl}_2$ , gradient from 20% to 40%) to provide 8.5 mg (75%) of 5-bromo-

10,20-diphenylporphyrin (BDPP).  $^1\text{H}$  NMR (400 MHz,  $\text{CD}_2\text{Cl}_2$ ):  $\delta$  = 10.19 (s, 1H), 9.75 (d,  $J$  = 4.8 Hz, 2H), 9.31 (d,  $J$  = 4.6 Hz, 2H), 8.97 (d,  $J$  = 4.7 Hz, 4H), 8.22 (dd,  $J$  = 1.5, 7.5 Hz, 4H), 7.88 - 7.76 (m, 6H), - 3.08 (s, 2H) ppm.  $^{13}\text{C}$  NMR (100 MHz,  $\text{CD}_2\text{Cl}_2$ ):  $\delta$  = 141.8 (2x), 135.2 (4x), 132.9 (4x), 132.6 (4x), 132.3 (8x), 128.5 (2x), 127.5 (4x), 120.9 (2x), 106.1 (1x), 103.9 (1x) ppm. FTIR-ATR:  $\nu$  = 2920 (s), 2851 (s), 1461 (m), 1260 (m)  $\text{cm}^{-1}$ . MS (ESI $^+$ )  $m/z$ : 541.4 (90,  $[\text{M}+\text{H}]^+$ ,  $^{79}\text{Br}$ ), 543.4 (100,  $[\text{M}+\text{H}]^+$ ,  $^{81}\text{Br}$ ).



5-[(Triisopropylsilyl)thio]-10,20-diphenylporphyrin (TDPP):<sup>32</sup> A sealable tube was charged with  $\text{Pd}(\text{OAc})_2$  (1.9 mg, 0.003 mmol),  $\text{PPh}_3$  (3.1 mg, 0.012 mmol)  $\text{Cs}_2\text{CO}_3$  (36.2 mg, 0.111 mmol), 5-bromo-10,20-diphenylporphyrin (30 mg, 0.055 mmol) and dry toluene (0.6 mL). The mixture was carefully degassed by freeze/thaw cycles (3x). Triisopropylsilanethiol (15.5  $\mu\text{L}$ , 0.072 mmol) were added subsequently *via* syringe and the tube was sealed afterwards. The solution was warmed to 100  $^\circ\text{C}$  for 2 h. After cooling to room temperature, a saturated aqueous solution of  $\text{NH}_4\text{Cl}$  was added and the mixture was extracted with  $\text{CH}_2\text{Cl}_2$  (3x). The collected organic layers were dried ( $\text{Na}_2\text{SO}_4$ ) and filtered, and the solvent was evaporated. The crude was purified by flash chromatography (silicagel, gradient from 60:40 to 40:60 hexane/ $\text{CH}_2\text{Cl}_2$ ) to obtain 13.1 mg (36%) of 5-[(triisopropylsilyl)thio]-10,20-diphenylporphyrin.  $^1\text{H}$  NMR (400 MHz,  $\text{CDCl}_3$ ):  $\delta$  = 10.12 (s, 1H), 10.10 (d,  $J$  = 4.8 Hz, 2H), 9.27 (d,  $J$  = 4.6 Hz, 2H), 8.96 (d,  $J$  = 4.6 Hz, 2H), 8.93 (d,  $J$  = 11.2, 4.8 Hz, 2H), 8.31 - 8.20 (m, 4H), 7.86 - 7.74 (m, 6H), 1.38 (h,  $J$  = 7.5 Hz, 3H), 0.89 (d,  $J$  = 7.5 Hz, 18H), -2.87 (s, 2H) ppm.  $^{13}\text{C}$  NMR (100 MHz,  $\text{CDCl}_3$ ):  $\delta$  = 141.9 (2x), 134.8 (4x), 131.6 (4x), 131.3 (4x), 131.1 (8x), 127.9 (2x), 126.9 (4x), 119.9 (2x), 110.2 (1x), 105.3 (1x), 18.5 (6x), 13.9 (3x) ppm. FTIR-ATR:  $\nu$  = 2924 (s), 2854 (s), 1465 (m), 1252 (m)  $\text{cm}^{-1}$ . MS (ESI $^+$ )  $m/z$ : 987.8.4 (20, [thiol-dimer +H] $^+$ ), 493.5 (93, [thiol-dimer +2H] $^{2+}$ ).<sup>33</sup>

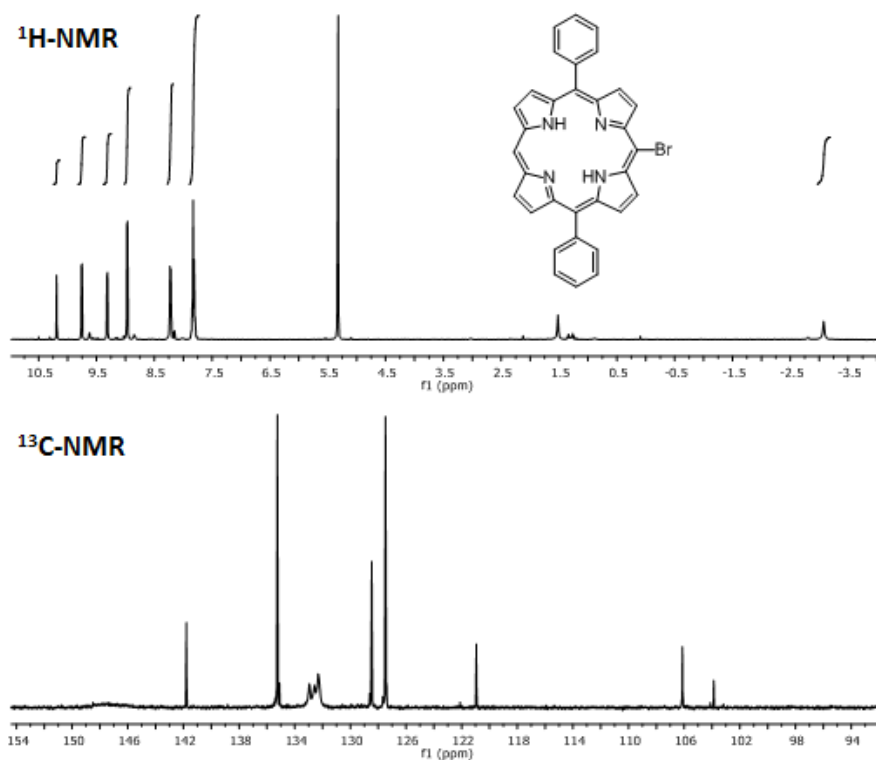


**Figure 9.S1:** <sup>1</sup>H and <sup>13</sup>C-NMR spectra for 5-Bromo-10,20-diphenylporphyrin (BDPP).

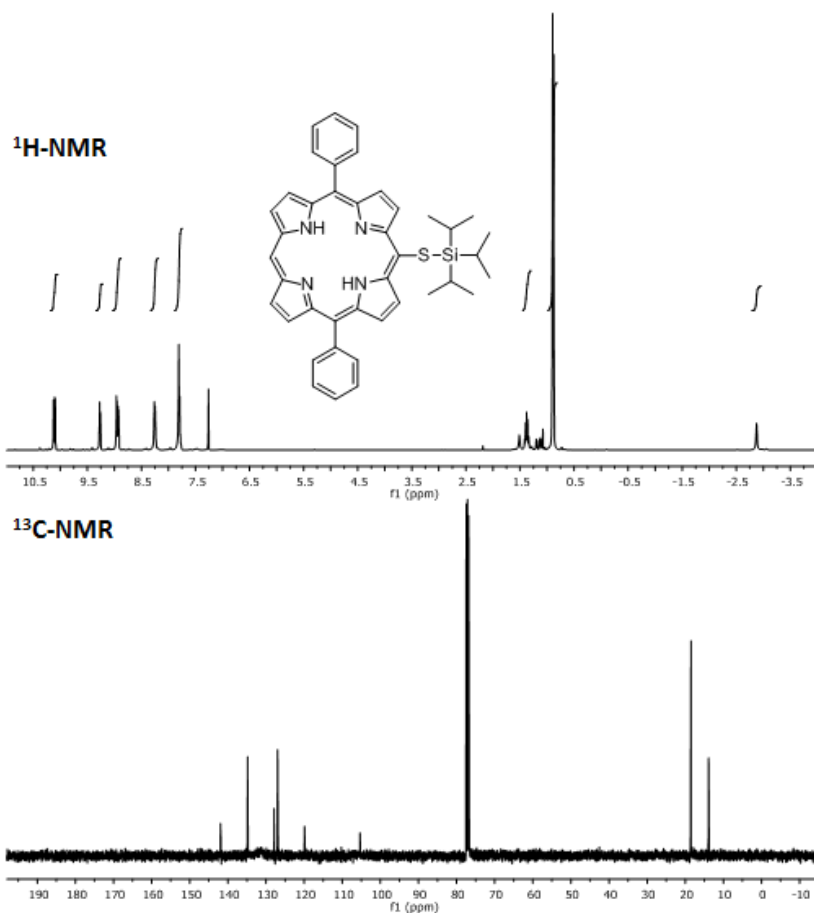


**Figure 9.S2:** <sup>1</sup>H and <sup>13</sup>C-NMR spectra for 5-[(Triisopropylsilyl)thio]-10,20-diphenylporphyrin (TDPP).

**Supercrystal functionalization and sensing:** The porphyrin was metallized by adding equimolecular concentrations of porphyrin and iron (II) acetate dihydrate to a solution of 5:1 dichloromethane/methanol. The solution was heated for 30 min and then allowed to stir overnight under a nitrogen atmosphere. Then, 10  $\mu\text{L}$  of diluted solutions of TDPP-Fe ( $3 \times 10^{-5}$ ,  $3 \times 10^{-6}$ ,  $3 \times 10^{-7}$ ,  $3 \times 10^{-8}$ ,  $3 \times 10^{-9}$ ,  $3 \times 10^{-10}$ , or  $3 \times 10^{-11}$  M) were cast on the pyramidal arrays ( $1 \text{ cm}^2$ ) and air dried. The biosensor mimic was evaluated against pure atmospheres of CO (Air Liquide) with the hand held Raman system to set the amount of TDPP-Fe necessary to quantitative detect the gas with detection ranges in between 1 to 400 ppm. The sensor was then evaluated in a close chamber containing normal atmosphere and controlling the amount of CO from a commercial mixture of CO (100 ppm) in  $\text{N}_2$  (Airliquid) with the help of a manoreductor and a gas flow-meter. Reversibility studies were carried out on the same sample by exposure the sensor several times to the atmospheres containing 100 ppm of CO and clean air.

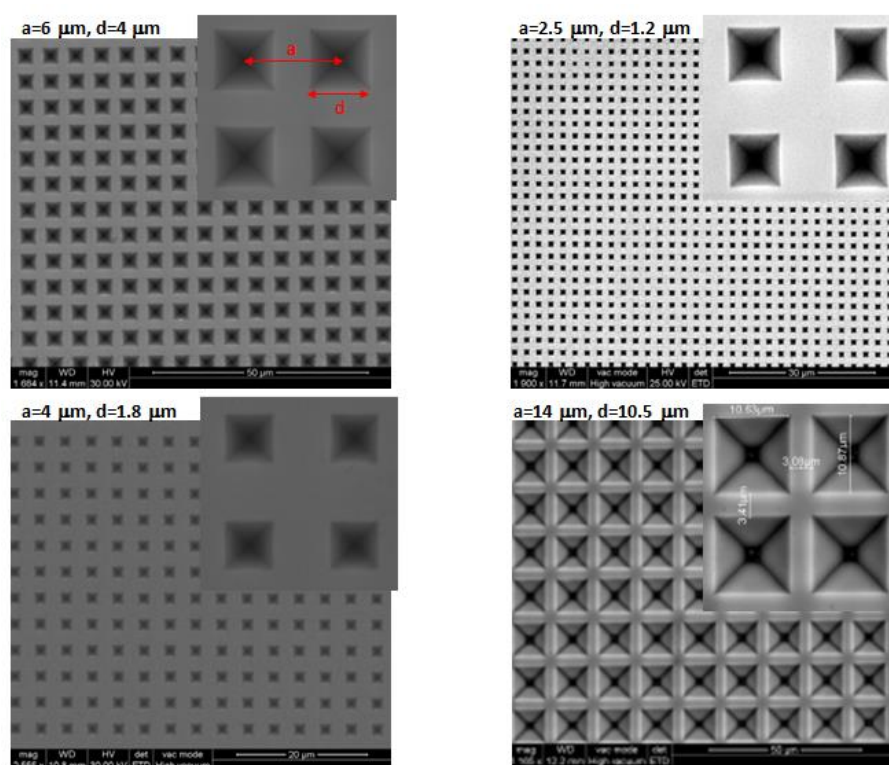


**Figure 9.S3:** Examples of other inverted pyramid templates obtained with direct laser writing lithography. Interestingly the resolution of the period and size can be controlled at the 100 nm.

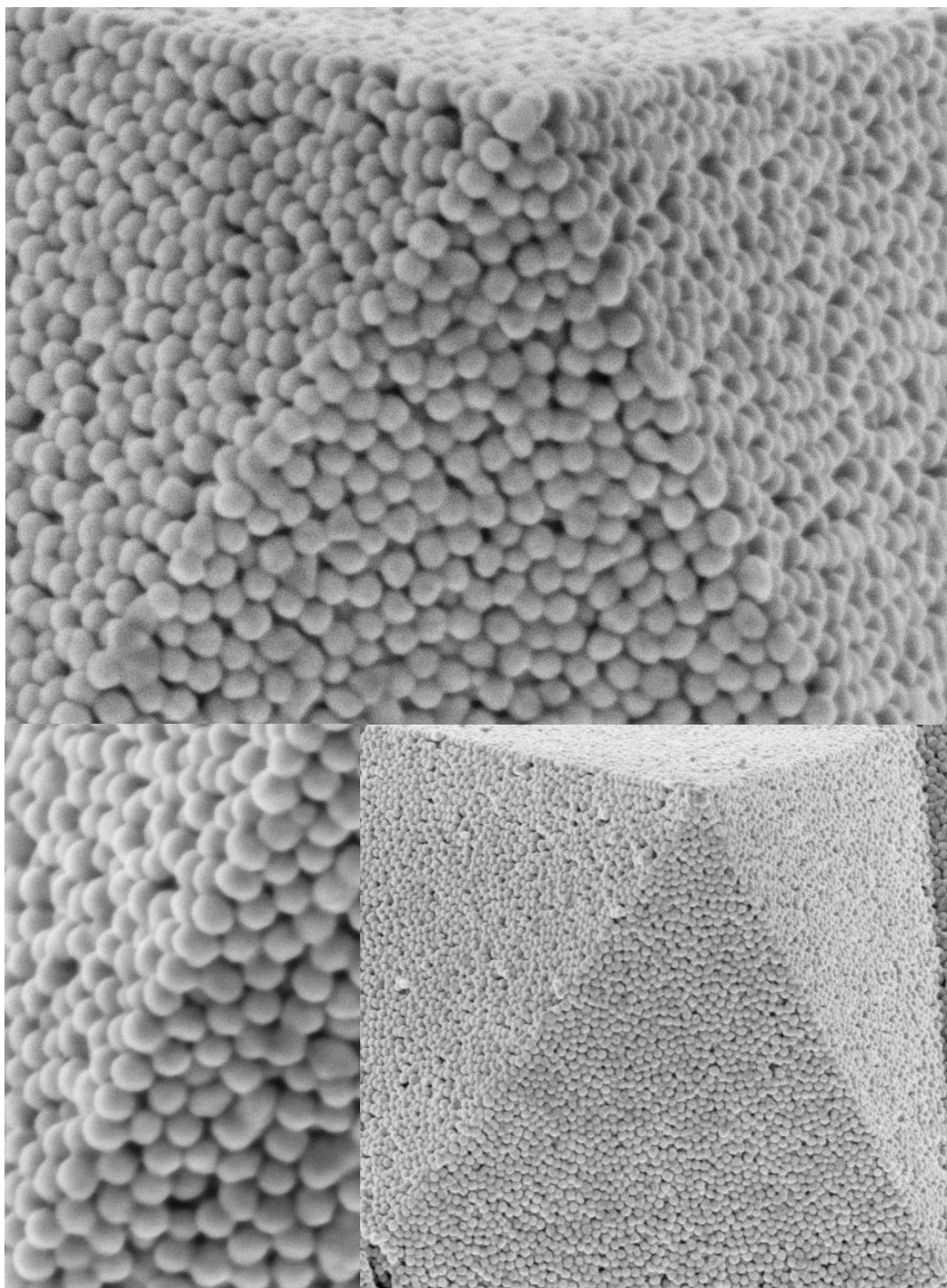


**Figure 9.S4:** High magnification SEM image of the tip (A), edge (B) and whole (C) of pyramidal structures (after (A) and before (B, C) plasma treatment) showing its nanostructure formed by individual gold nanoparticles.

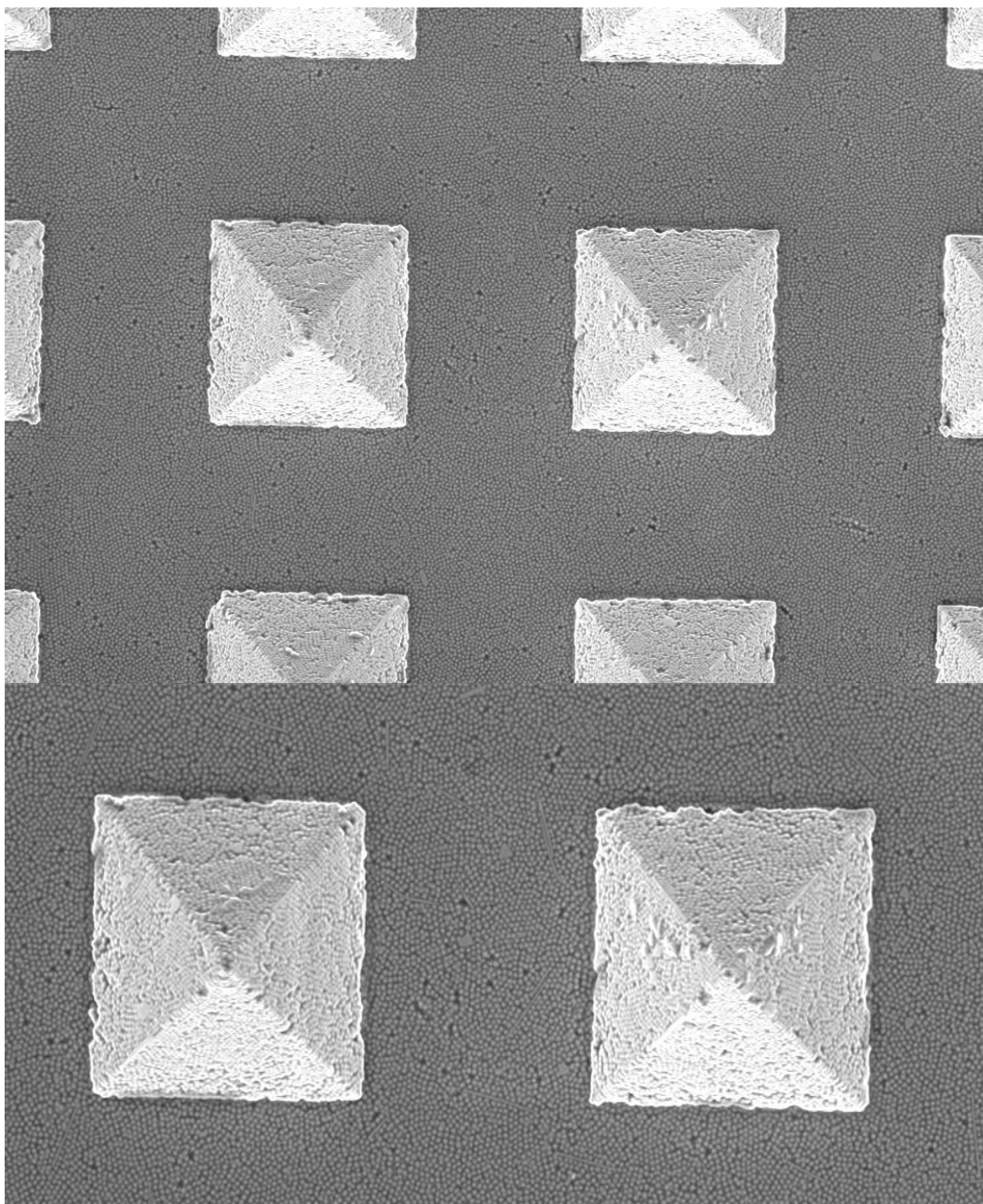


**Figure 9.S5:** Lower magnification SEM images (A, B) of various pyramidal structures still showing its nanostructure formed by individual gold nanoparticles and revealing the homogeneity of the assemblies.

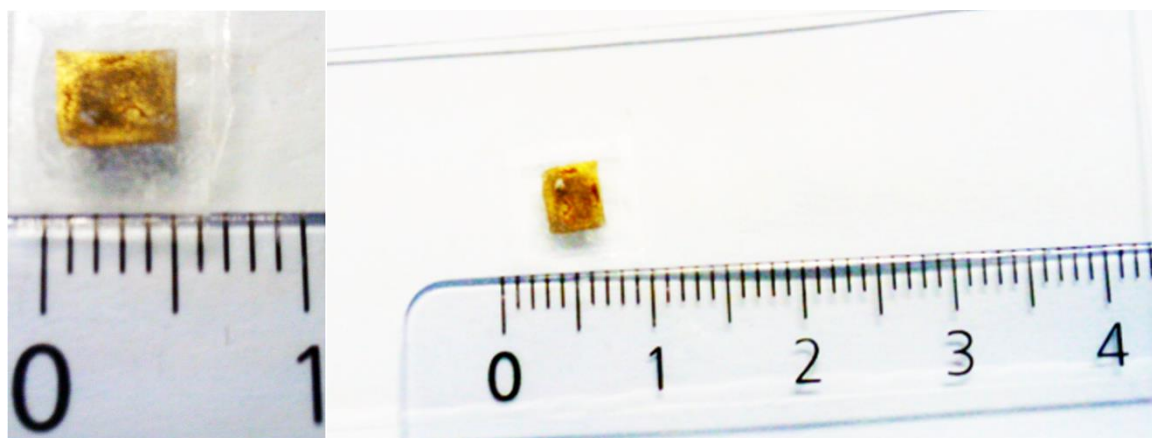


**Figure 9.S6:** Digital photograph images of macro-scale (0.5 X 0.4 cm) stamped substrates consisting of ordered micro-pyramidal structures of 4.4  $\mu\text{m}$  side and 3.0  $\mu\text{m}$  height formed with nanoparticles of 70 nm as building blocks.

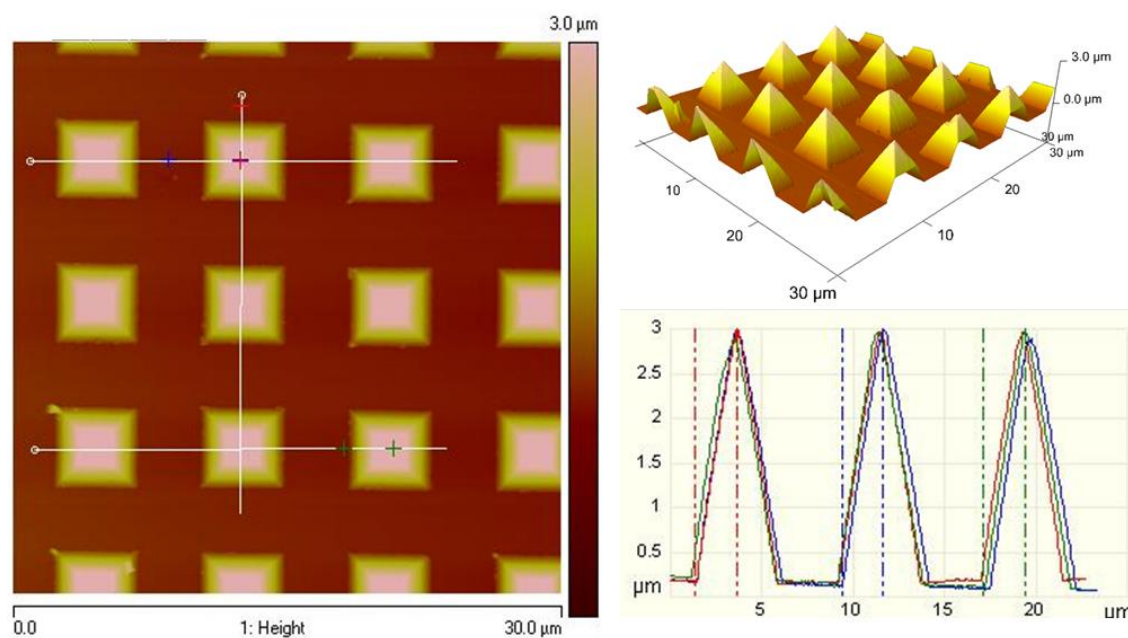


**Figure 9.S7:** Atomic force microscopy of the macroscaled nanostructured Au NP pyramid array film.

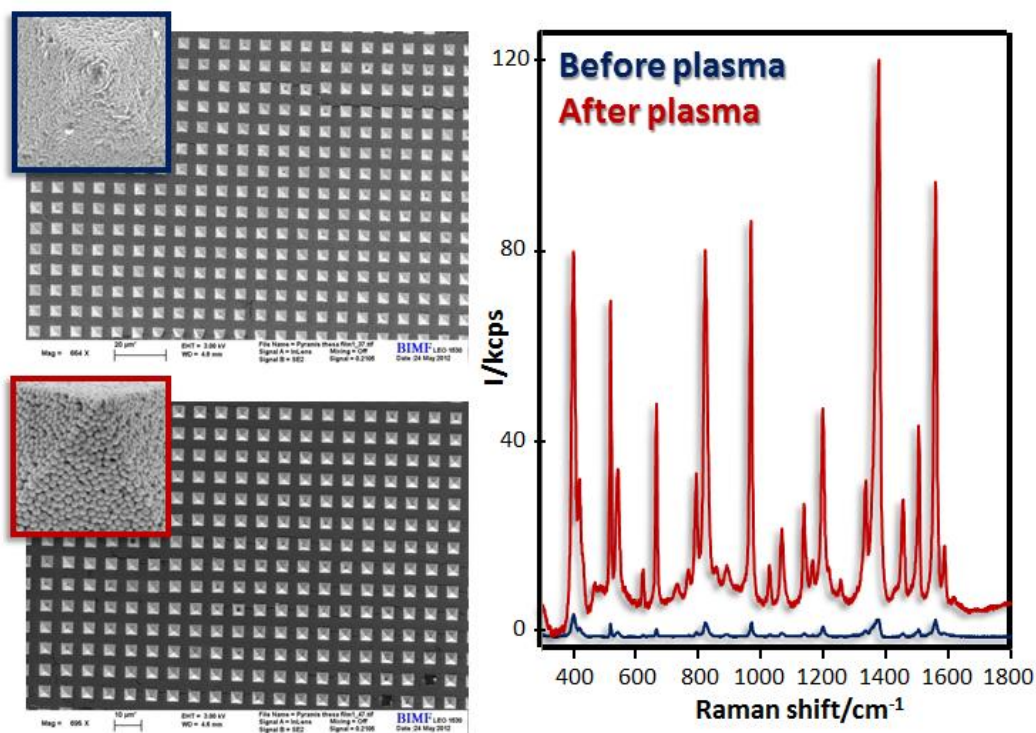


**Figure 9.S8:** SEM images and SERS spectra of macroscaled nanostructured Au NP pyramid array film before and after the plasma cleaning.

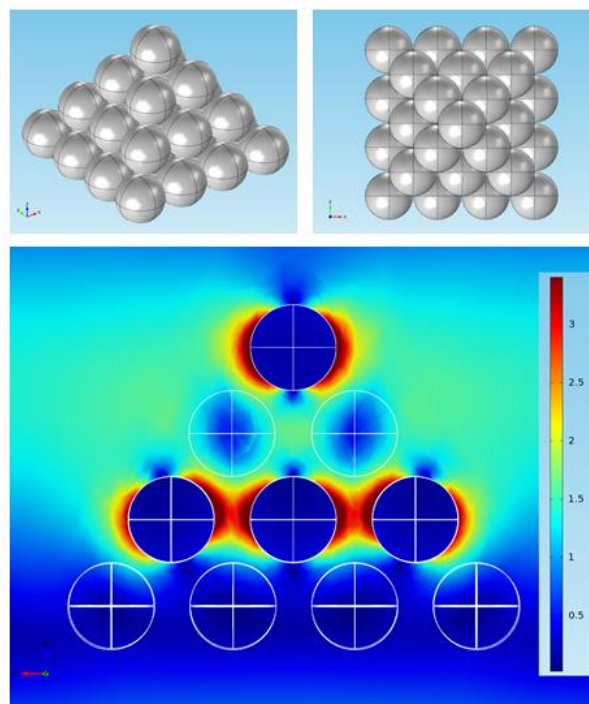


**Figure 9.S9:** Geometrical models used for the simulation and near-field electric distribution (V/m) upon excitation with 785 nm light.

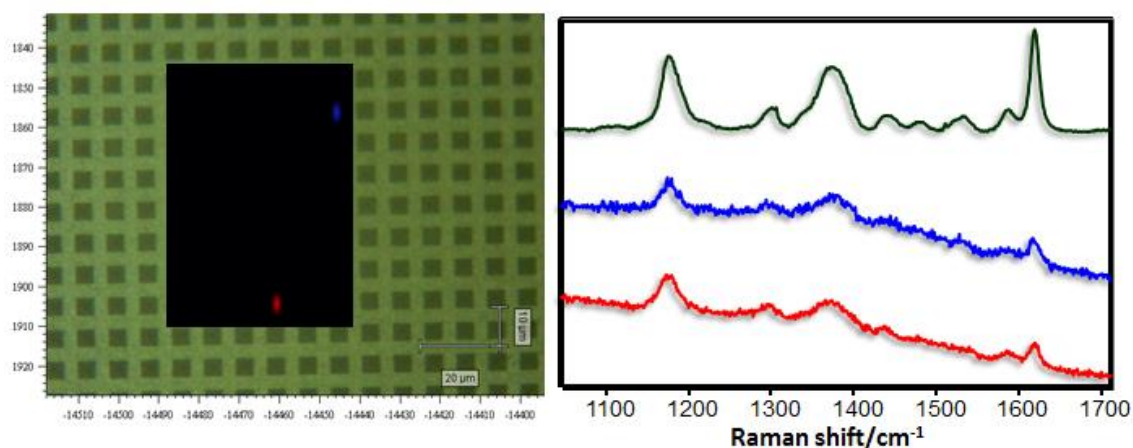


**Figure 9.S10:** Single molecule detection of crystal violet (CV) on the macroscaled nanostructured Au NP pyramid array film. Green spectrum represents the resembled SERS signal of CV; blue and red spectra correspond to the signal recorded at the blue and red spots in the Raman map. The CV film was prepared by spin-coating a minute volume (10  $\mu\text{L}$ ) of CV  $10^{-12}$  M giving rise to an average concentration of less than 1 molecule/ $\mu\text{m}$  (0.06 molecules/ $\mu\text{m}^2$ ). The film was mapped using the Renishaw's StreamLine accessory with a 100x objective (spatial resolution of 500 nm), acquisition times of 2 s and a power at the sample of 1  $\mu\text{W}$ .

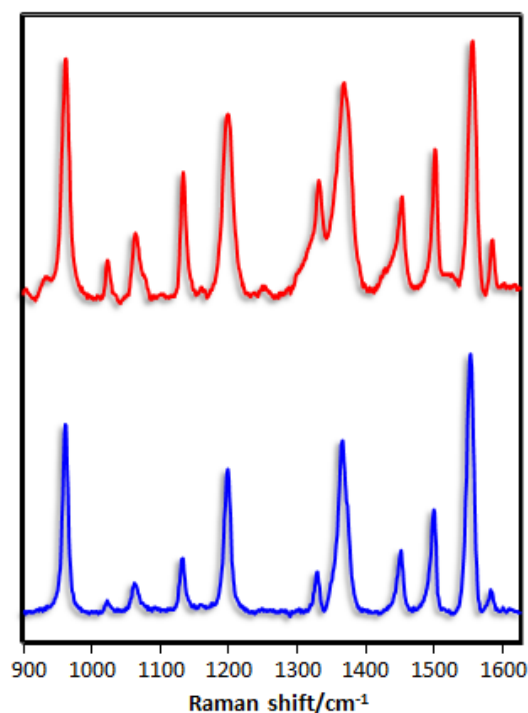


**Figure 9.S11:** Comparison of the SERS spectra of 1NAT as acquired with a portable handheld Raman system (red) or a bench microRaman instrument (using a macrosampling objective, W.D. 15 mm). Note that although both spectra fit band to band, for the one obtained with the portable the FWH is slightly larger as a consequence of the smaller focal length grating-detector.

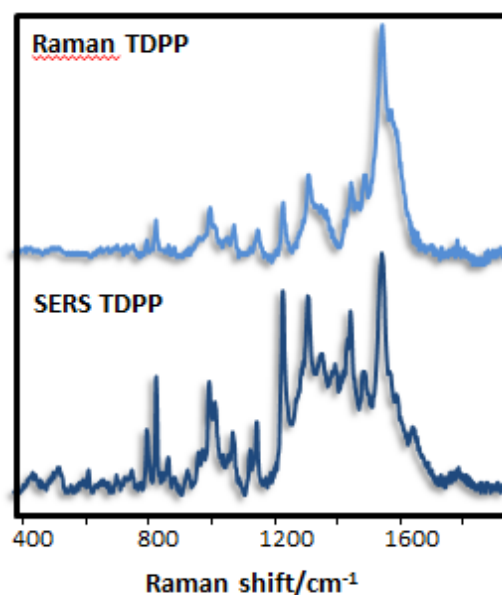


**Figure 9.S12:** Raman and SERS spectra of the TDPP. Both spectra fit band to band but with some differences in the relative intensity of some bands. Changes in relative intensity are due to the surface selection rules<sup>22</sup> and can be used to discern the orientation of the molecule at the metallic surface.<sup>34</sup> First, with the use of the 785 nm laser line excitation at the red of the bulk plasma resonance, the main component of the field at the surface is the normal to the surface. Considering the high affinity of the thiol and amino groups for gold, the adsorbed molecule could be either flat on the metal surface, interacting by porphyrin ring or with the molecular plane almost perpendicular to the metal surface if interacting through the terminal thiol group. The observed SERS bands can be safely assigned to ring deformations in the plane of the molecule. In fact, the SERS spectra contain all of the in-plane vibrational frequencies (ring stretching and C-H bending in the 1000-1650  $\text{cm}^{-1}$  region) with remarkably strong relative intensity, as compared to those corresponding to out-of-plane modes. These latter observations discard the flat-on orientation and indicate that the ligand is bonded through the thiol group with its aromatic chromophore perpendicular to the gold surface, consistent with the higher reactivity toward gold of the thiols as compared with ternary amines.

## References

- (1) Hess, O.; Pendry, J. B.; Maier, S. A.; Oulton, R. F.; Hamm, J. M.; Tsakmakidis, K. L., Active nanoplasmonic metamaterials. *Nat Mater* **2012**, *11*, 573-584.
- (2) Brongersma, M. L.; Shalaev, V. M., Applied Physics. The Case for Plasmonics. *Science* **2010**, *328*, 440-441.
- (3) Lal, S.; Link, S.; Halas, N. J., Nano-optics from sensing to waveguiding. *Nat Photonics* **2007**, *1*, 641-648.
- (4) Benson, O., Assembly of hybrid photonic architectures from nanophotonic constituents. *Nature* **2011**, *480*, 193-199.
- (5) Soukoulis, C. M.; Wegener, M., Past achievements and future challenges in the development of three-dimensional photonic metamaterials. *Nat Photonics* **2011**, *5*, 523-530.
- (6) Fan, J. A.; Wu, C.; Bao, K.; Bao, J.; Bardhan, R.; Halas, N. J.; Manoharan, V. N.; Nordlander, P.; Shvets, G.; Capasso, F., Self-Assembled Plasmonic Nanoparticle Clusters. *Science* **2010**, *328*, 1135-1138.
- (7) Pazos-Perez, N.; Wagner, C. S.; Romo-Herrera, J. M.; Liz-Marzán, L. M.; García de Abajo, F. J.; Wittemann, A.; Fery, A.; Alvarez-Puebla, R. A., Organized Plasmonic Clusters with High Coordination Number and Extraordinary Enhancement in Surface-Enhanced Raman Scattering (SERS). *Angew Chem, Int Ed* **2012**, *51*, 12688-12693.
- (8) Alvarez-Puebla, R. A.; Agarwal, A.; Manna, P.; Khanal, B. P.; Aldeanueva-Potel, P.; Carbo-Argibay, E.; Pazos-Perez, N.; Vigdeman, L.; Zubarev, E. R.; Kotov, N. A.; Liz-Marzan, L. M., Gold nanorods 3D-supercrystals as surface enhanced Raman scattering spectroscopy substrates for the rapid detection of scrambled prions. *Proc Natl Acad Sci U S A* **2011**, *108*, 8157-8161.
- (9) Henzie, J.; Gruenwald, M.; Widmer-Cooper, A.; Geissler, P. L.; Yang, P., Self-assembly of uniform polyhedral silver nanocrystals into densest packings and exotic superlattices. *Nat Mater* **2012**, *11*, 131-137.

- (10) Pazos-Perez, N.; Garcia de Abajo, F. J.; Fery, A.; Alvarez-Puebla, R. A., From Nano to Micro: Synthesis and Optical Properties of Homogeneous Spheroidal Gold Particles and Their Superlattices. *Langmuir* **2012**, *28*, 8909-8914.
- (11) Stiles, P. L.; Dieringer, J. A.; Shah, N. C.; Van Duyne, R. R., Surface-Enhanced Raman Spectroscopy. In *Annu Rev Anal Chem*, 2008; Vol. 1, pp 601-626.
- (12) Bodnarchuk, M. I.; Li, L.; Fok, A.; Nachtergaele, S.; Ismagilov, R. F.; Talapin, D. V., Three-Dimensional Nanocrystal Superlattices Grown in Nanoliter Microfluidic Plugs. *J Am Chem Soc* **2011**, *133*, 8956-8960.
- (13) Majetich, S. A.; Wen, T.; Booth, R. A., Functional Magnetic Nanoparticle Assemblies: Formation, Collective Behavior, and Future Directions. *ACS Nano* **2011**, *5*, 6081-6084.
- (14) Mueller, M.; Tebbe, M.; Andreeva, D. V.; Karg, M.; Alvarez-Puebla, R. A.; Pazos-Perez, N.; Fery, A., Large-Area Organization of pNIPAM-Coated Nanostars as SERS Platforms for Polycyclic Aromatic Hydrocarbons Sensing in Gas Phase. *Langmuir* **2012**, *28*, 9168-9173.
- (15) Pazos-Perez, N.; Ni, W.; Schweikart, A.; Alvarez-Puebla, R. A.; Fery, A.; Liz-Marzan, L. M., Highly uniform SERS substrates formed by wrinkle-confined drying of gold colloids. *Chem Sci* **2010**, *1*, 174-178.
- (16) Le Ru, E. C.; Etchegoin, P. G., Single-Molecule Surface-Enhanced Raman Spectroscopy. *Annu Rev Phys Chem* **2012**, *63*, 65-87.
- (17) De Angelis, F.; Gentile, F.; Mearini, F.; Das, G.; Moretti, M.; Candeloro, P.; Coluccio, M. L.; Cojoc, G.; Accardo, A.; Liberale, C.; Zaccaria, R. P.; Perozziello, G.; Tirinato, L.; Toma, A.; Cuda, G.; Cingolani, R.; Di Fabrizio, E., Breaking the diffusion limit with super-hydrophobic delivery of molecules to plasmonic nanofocusing SERS structures. *Nat Photonics* **2011**, *5*, 683-688.
- (18) Liu, N.; Tang, M. L.; Hentschel, M.; Giessen, H.; Alivisatos, A. P., Nanoantenna-enhanced gas sensing in a single tailored nanofocus. *Nat Mater* **2011**, *10*, 631-636.

- (19) Alvarez-Puebla, R. A.; Liz-Marzan, L. M., Traps and cages for universal SERS detection. *Chem Soc Rev* **2012**, *41*, 43-51.
- (20) Alvarez-Puebla, R. A.; Liz-Marzán, L. M., SERS Detection of Small Inorganic Molecules and Ions. *Angew Chem, Int Ed* **2012**, *51*, 11214-11223.
- (21) Collman, J. P.; Brauman, J. I.; Doxsee, K. M., Carbon-monoxide binding to iron porphyrins. *Proc Natl Acad Sci U S A* **1979**, *76*, 6035-6039.
- (22) Moskovits, M.; Suh, J. S., Surface Selection-Rules for Surface-Enhanced Raman-Spectroscopy - Calculations and Application to the Surface-Enhanced Raman-Spectrum of Phthalazine on Silver. *J Phys Chem* **1984**, *88*, 5526-5530.
- (23) Li, X. Y.; Czernuszewicz, R. S.; Kincaid, J. R.; Su, Y. O.; Spiro, T. G., Consistent Porphyrin Force-Field .1. Normal-Mode Analysis for Nickel Porphine and Nickel Tetraphenylporphine from Resonance Raman and Infrared-Spectra and Isotope Shifts. *J Phys Chem* **1990**, *94*, 31-47.
- (24) Pieczonka, N. P. W.; Aroca, R. F., Single molecule analysis by surfaced-enhanced Raman scattering. *Chem Soc Rev* **2008**, *37*, 946-954.
- (25) Hall, J. E., *Guyton and Hall Textbook of Medical Physiology*. 12th ed.; Elsevier Saunders: United States of America, Philadelphia, 2010; p 1091.
- (26) Thomas, G. J.; Agard, D. A., Raman Spectral Studies of Nucleic-Acids .27. Quantitative-Analysis of Nucleic-Acids, Proteins, and Viruses by Raman Band Deconvolution. *Biophys J* **1984**, *46*, 763-768.
- (27) Burda, C.; Chen, X.; Narayanan, R.; El-Sayed, M. A., Chemistry and Properties of Nanocrystals of Different Shapes. *Chem Rev* **2005**, *105*, 1025-1102.
- (28) Orendorff, C. J.; Sau, T. K.; Murphy, C. J., Shape-Dependent Plasmon-Resonant Gold Nanoparticles. *Small* **2006**, *2*, 636-639.
- (29) Johnson, P. B.; Christy, R. W., Optical Constants of the Noble Metals. *Phys Rev B: Condens Matter Mater Phys* **1972**, *6*, 4370-4379.

- (30) Alvarez-Puebla, R. A.; Dos Santos Jr, D. S.; Aroca, R. F., Surface-enhanced Raman scattering for ultrasensitive chemical analysis of 1 and 2-naphthalenethiols. *Analyst* **2004**, *129*, 1251-1256.
- (31) Liu, C.; Shen, D.-M.; Chen, Q.-Y., Unexpected bromination ring-opening of tetraarylporphyrins. *Chem Commun* **2006**, 770-772.
- (32) Kreis, M.; Bräse, S., A General and Efficient Method for the Synthesis of Silyl-Protected Arenethiols from Aryl Halides or Triflates. *Adv Synth Catal* **2005**, *347*, 313-319.
- (33) *Due to the instability of the protected thiol under the conditions of ESI-MS, only the product of deprotection and subsequent dimerization of the original thiol was observed by mass spectrometry.*
- (34) *The orientation of molecules at metal surfaces can be inferred through the propensity toward enhancement of vibrational modes perpendicular to the surface. This propensity arises from the boundary condition which requires the electrostatic displacement,  $D$ , normal to the surface to be continuous across the interface:  $D_{\perp,in} = \epsilon_{Au} E_{r=a}$ ;  $D_{\perp,out} = \epsilon_{surroundings} E_{r=a}$ . While the parallel component is simply:  $E_{\parallel,in,r=a} = E_{\parallel,out,r=a}$ . This leads to a preferential enhancement of the perpendicular electric field by a factor of  $\epsilon$ .*



# 10

## **SERS Platforms of Plasmonic Hydrophobic Surfaces for Analyte Concentration: Hierarchically Assembled Gold Nanorods on Anodized Aluminum**

*Moritz Tebbe , Pavel Cherepanov , Ekaterina V. Skorb , Sergey K. Poznyak , Javier Garcia de Abajo , Andreas Fery , Daria V. Andreeva , Ramon A. Alvarez Puebla , and Nicolas Pazos-Perez*

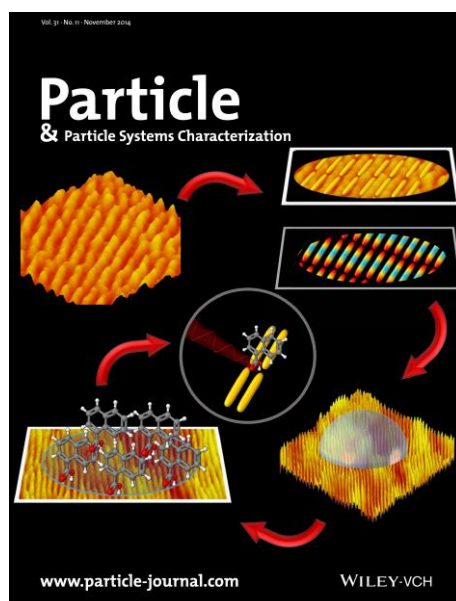


**Figure 10.1.** Inside Back Cover.

Published in **Particle & Particle Systems Characterization**.

Reprinted with permission from SERS Platforms of Plasmonic Hydrophobic Surfaces for Analyte Concentration: Hierarchically Assembled Gold Nanorods on Anodized Aluminum, Tebbe *et al.*, *Part Part Syst Charact* **2014**, *31*, 1134–1140. ©2014 WILEY-VCH Verlag GmbH & Co. KGaA, Weinheim.



## Abstract

Efficient and homogeneous surface-enhanced Raman scattering (SERS) substrates are usually prepared using lithographic approaches, physical evaporation, or *in situ* chemical reduction. However, these approaches are time-consuming, expensive, and very difficult to upscale. Alternatively, template-assisted approaches using colloidal suspensions of preformed nanoparticles have become more popular because of their low cost, fast production, and ability to be scaled up easily. One of the limitations of these methods is the dimensions of the structured surfaces. In this context, a new method for designing low-cost, up-scalable surface patterns that match building block dimensionality based on anodization of aluminum, enabling a hierarchical organization of anisotropic nanoparticles, is presented. The proposed new technology starts with anodized aluminum oxide with regular parallel linear periodicities. To produce a highly efficient plasmonic surface, gold nanorods are assembled into parallel lines where the long axes of the Au rods are also oriented along the substrate lines, thus inducing reproducible tip-to-tip plasmonic coupling with the corresponding generation of highly active hotspots. Additionally, this advanced material presents an inherent hydrophobicity that can be exploited as a method for concentration of analytes on the surface. SERS detection is demonstrated with benzenethiol and 2-naphtoic acid.

## Introduction

Surface-enhanced Raman scattering (SERS) is an ultrasensitive analytical technique with potential detection limits down to the single molecule, the possibility of multiplex analysis, and small sample preparation requirements.<sup>1,2</sup> SERS relies in the excitation of the vibrational fingerprint of the analytical target through the localized surface plasmon resonance (LSPR) generated by a plasmonic material, in close proximity to the analyte, upon illumination with a plasmon-frequency-tuned laser line.<sup>3</sup> Beside factors arising from the molecular structure of the probe under study or its interaction with the plasmonic material (chemical effects),<sup>4</sup> the intensity in SERS is extremely sensitive to the optical efficiency of the plasmonic enhancer, which is capable of amplifying the signal of extremely diluted targets against the inelastic optical background.

SERS can be achieved directly in solution or in thin films. Although SERS in solution (*i.e.*, in colloidal dispersions of nanoparticles) represents a convenient way of analyzing certain samples,<sup>5</sup> thin films add versatility and can be prepared on fully portable optimal substrates that are used in a similar fashion as a reactive strip in field analysis.<sup>6</sup> A way of producing plasmonic thin films is by using physical methods such as physical evaporation on flat or patterned substrates.<sup>7</sup> Although this is an efficient method, it usually leads to rather inhomogeneous films in which plasmonic coupling takes place randomly at so-called hotspots, therefore resulting in a loss of linearity of the signal with analyte concentration.<sup>8</sup>

In an effort to produce geometrically homogeneous substrates, well-established lithographic approaches such as e-beam, focused-ion beam or dip-pen patterning have been proposed.<sup>9,10</sup> These approaches are however time-consuming, expensive, and very difficult to upscale. Alternatively, evaporation can be also carried out on complex surfaces such as monolayers of self-assembled polymer beads with a subsequent treatment to remove the polymer (*i.e.*, nanosphere lithography).<sup>11</sup> In this case, the resulting material presents homogeneous patterned features with controlled dimensions and localized surface plasmon resonances (LSPRs). However, this method leads to large nanostructured features (over hundreds of nanometers) and is rather constrained to the few obtainable shapes and dispositions.<sup>12</sup> Alternatively, optical thin films can be also produced by *in-situ* chemical reduction of metallic salts on polymers or even using colloidal suspensions of preformed nanoparticles with their posterior retention on the desired surface by self-assembly,<sup>13</sup> Langmuir-Blodgett<sup>14</sup> or layer-by-layer methodologies.<sup>15</sup> Both methods present a low degree of control on the position of the nanoparticles, which yields materials with similar drawbacks to those obtained by physical evaporation.

During the last years, the development of routes to organize particles down to the nanometer scale has significantly improved. Recently, our groups developed new methodologies for the fabrication of homogeneous and efficient plasmonic surfaces for SERS, including supercrystals and organized lines of particles.<sup>16,17</sup> Specifically, nanoparticle line imprinting using wrinkles as templates has some advantages over other approaches. It is easily up scalable, inexpensive, and highly efficient. The main limitation for nanoparticle assembly using template-assisted methods is the texture size of the structured surface that is employed. As for bottom-up assembly approaches, the dimensions of the structures and the building blocks have to match.

This implies that the features of the template require dimensions within the nanometer scale.

Anodized aluminum<sup>18,19</sup> surfaces emerge as good alternatives to the above-mentioned methodologies. In general, these materials consist of a packed array of hexagonal columnar cells with central, cylindrical, uniformly sized holes ranging from 4 to 200 nm in diameter with inter-hole distances between 50 and 500 nm.<sup>20</sup> The geometrical characteristics make of these self-ordered structures a very exciting alternative material for organization of nanoparticles. Additionally, anodized aluminum presents a natural hydrophobicity that may favor the spontaneous concentration of the target analyte onto the plasmonic surface. In this work, we suggest a new pathway to design low-cost, up-scalable surface patterns based on anodization of aluminum (Al), which match template and building block dimensionality, enabling a hierarchical organization of anisotropic nanoparticles. Moreover, the proposed new technological approach shows the unprecedented formation of a periodic linear parallel array nanostructure on the surface of anodized aluminum oxide (AAO). This structure enables the organization of Au NRs and due to its hydrophobic nature, creates a SERS substrate capable of concentrating an analyte deposited from solution increasing its sensitivity.

## Results and Discussion

A schematic representation of the electrochemical cell for AAO formation with platinum and aluminum electrodes immersed in the electrolyte is shown in **Figure 10.2a**. The mechanism of pore formation in AAO is based on two processes: dissolution and growth of aluminum oxide. The diameter, length, and arrangement of the pores depend on the electrolyte used, the applied voltage, the current density, the reaction time, and the temperature.<sup>21</sup> Consequently, the morphology of the final AAO can be tuned by adjusting the preparation conditions. In the present work, porous AAO templates were prepared *via* electrochemical oxidation of aluminum in phosphoric acid solutions under galvanostatic regime. As aluminum anodization is a time-dependent process, a study of the temporal evolution of the obtained structure was carried out. **Figure 10.2b** shows SEM images of AAO revealing different structures after anodization times of 10, 30, 90, and 180 s. After 10 s, we observed formation of the hillock-like surface morphology,<sup>22,23</sup> followed by formation of the

porous surface after 30 s. The grooved morphology reveals after 90 s of modification, finally converting into the cell-like surface morphology of the used template.

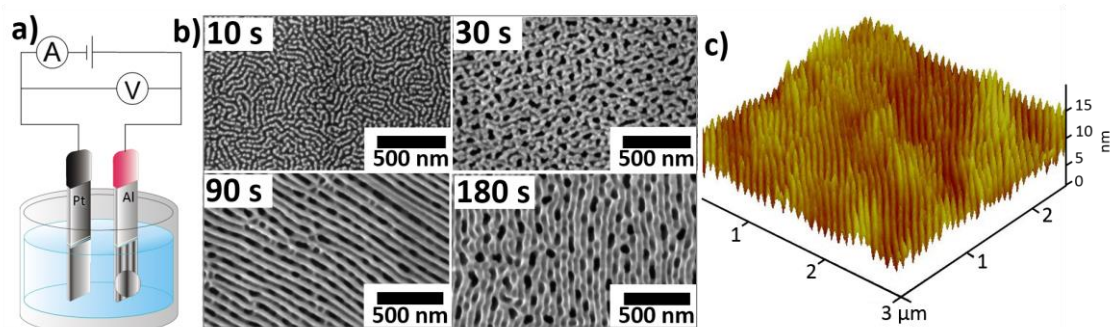


**Figure 10.2.** a) Schematic representation of the ionized aluminum oxide (AAO) substrate preparation through galvanostatic anodization. b) Time dependent evolution of surface morphology of aluminum substrate. c) AFM image of aluminum plate anodized for 90 s.

The mechanism formation of this peculiar hillock-like surface morphology can be explained in a similar way to that already described for porous AAO.<sup>24</sup> Briefly, upon the initiation of the anodization process, a constant current was applied and a nonconductive layer of aluminum oxide start to grow, and associated with it the anodizing voltage increases. Thus, the phosphate ions present in the working electrolyte incorporate into the AAO crystal structure. This incorporation takes place by replacing oxygen atoms on the surface of aluminum causing the formation of hillocks (**Figure 10.2 b** (10 s)).<sup>23</sup> With longer (>30 s) anodization times, a further transformation into porous AAO occurs (**Figure 10.2b**). For our purpose, the periodically grooved AAO structure (see **Figure 10.2b**, 90 s) is the most interesting one. Accordingly, the current density and anodization time were tuned in order to up scale the process for the formation of a grooved template after relatively short times. For this purpose, we adjusted the applied current density to a value of  $16 \text{ mA}\cdot\text{cm}^{-2}$ , allowing the preparation of a grooved template in 90 s. The resulting periodically grooved template exhibited a mean groove width of 36 nm (**Figure 10.2c**). Although parallel aligned pores with controllable size has been previously described,<sup>24</sup> the formation of periodically grooved AAO surfaces with periodicities in the nanometer regime has not been reported to the best of our knowledge. The generation of such structures could be explained by a voltage change during the anodization process. The application of a constant current implies that as the nonconductive layer of aluminum oxide grows, the resistance changes and produces a reduction in the voltage. The merging of newly formed hillocks occurs in lateral directions, forming well-

pronounced corrugated morphologies of the AAO layer. Further continuation of anodization induces the formed grooves to merge with each other to reestablish a porous morphology (**Figure 10.2b**, 180 s). Consequently, the competing processes of oxide layer creation and metal dissolution<sup>25</sup> lead to the formation of variety of different AAO morphologies.

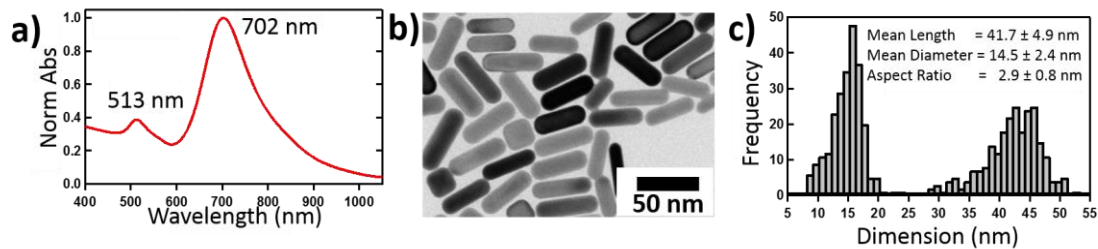


**Figure 10.3.** a) UV-vis-NIR spectrum, b) TEM image, and c) size distribution histograms of the prepared gold nanorods (GNRs).

The linear features formed on AAO are ideal substrates on which to arrange gold nanorods (GNRs) and have those interacting in close tip-to-tip proximity. Among the plasmonic properties and applications of these particles,<sup>26</sup> GNRs are known to generate extremely efficient plasmon coupling when interacting tip-to-tip.<sup>27-29</sup> Therefore, we chose these particles as the plasmonic material to generate a densely populated surface of highly active hotspots. GNRs were prepared to match the size of the structures (36 nm mean groove width) by using the Murphy method,<sup>30</sup> with cetyltrimethylammonium bromide (CTAB) as stabilizer and Ag(I) to induce rod-like growth along the single crystalline facets of the seed particle. **Figure 10.3** shows GNRs of  $\approx 42$  nm in length with a thickness of  $\approx 15$  nm (aspect ratio of  $\approx 3$ ) exhibiting LSPRs at 513 and 702 nm, corresponding to their transversal and longitudinal modes, respectively. In order to organize the particles onto the template, a concentrated solution of GNRs was first centrifuged to decrease the amount of free CTAB and avoid the crystallization of the surfactant in the pores, and then spin-coated onto the template (**Figure 10.4a**) using a suitable spin speed and concentrations of CTAB and particles. The matching of particle size and nanoscale surface topography is critical to generate macroscopic hierarchical structures of anisotropic particles by bottom-up template-assisted self-assembly. Besides, the compatible wettability of the nanostructure surface with the particle solution is responsible for successful particle organization using spin coating. The latter is a well-established method of material deposition based on centrifugal forces and evaporation of the residual solvent.<sup>31,32</sup>

Upon evaporation of the solvent on the nanostructured surfaces, capillary forces drag the nanoparticles into the cavities, assembling them in a close packed arrangement because of the Rayleigh instabilities and the preceding solvent front along the alumina grooves and inside the pores.<sup>33,34</sup>

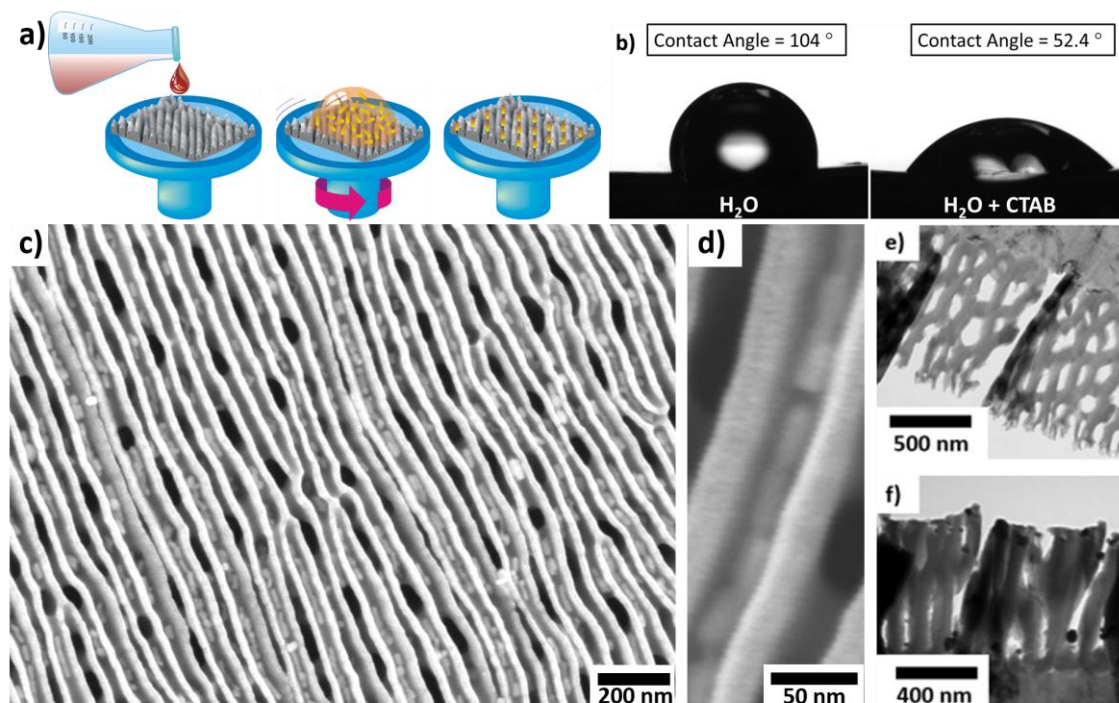


**Figure 10.4.** a) Scheme illustrating the organization of GNRs on the AAO template. b) Wettability of AAO for pure water and water solution of CTAB. c,d) SEM images of the GNRs organized onto the AAO template at different magnifications. e,f) TEM images of the microtomed template (e) before and (f) after GNRs organization.

The contact angle of a drop of water on the unmodified alumina is  $79^\circ$ . For porous surfaces, their wettability increases as a function of pore size. The contact angle for the used substrate was measured to be  $104^\circ$  (**Figure 10.4b**) for a mean pore size of 36 nm (estimated by PSD analysis of the AFM images).<sup>35,36</sup> The nanostructured surface thus becomes more hydrophobic after modification, in good agreement with the modified Laplace model or the capillarity and line-tension model for AAO.<sup>37</sup> For spin coating, we need to provide the surfaces with adequate wettability. The aqueous suspensions of GNRs stabilized by CTAB have a surface tension of  $35 \text{ mN}\cdot\text{m}^{-1}$  (above critical micelle concentration of CTAB).<sup>38</sup> At the same time, the contact angle between the used solution containing CTAB and the AAO was  $52.4^\circ$ . Consequently, CTAB provided the enhanced wettability of the nanostructured alumina substrate. **Figure 10.4c,d** shows that GNRs are linearly aligned inside the grooves. We stress

again that the observed preferential organization along the long axes of the rods (**Figure 10.4c,d**) is achieved because of the chosen sizes of the rods ( $42 \times 15$  nm) and the width of the grooves (36 nm).

Furthermore, we observe the presence of darker spots within these grooves, corresponding to pores of the anodized surface. The TEM images of the ultramicrotomed surfaces before (**Figure 10.4e**) and after (**Figure 10.4f**) particle deposition reveals the presence of GNRs inside both grooves and pores.

Optical reflectance spectroscopy of the Au nanorod arrays supported in AAO matrix reveals an interference pattern with several features in the UV-Vis-NIR region (see **Figure 10.5**). The interferometric signals are shifted toward longer wavelengths when Au rods are present, this effect arise from a modulation of the local dielectric causing a shift in signals<sup>39</sup> and, can be related to a change of the effective optical thickness (product of thickness and refractive index),<sup>40</sup> which is attributed to a change in the refractive index of the layer medium when Au rods are present.<sup>39,41</sup>

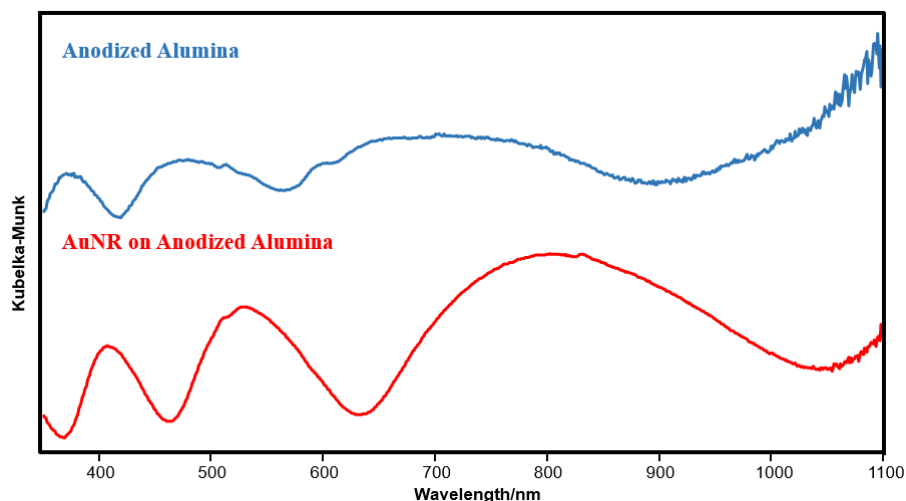


**Figure 10.5.** UV-vis-NIR reflectance spectra of the AAO template before and after the GNR organization. Both measurements were made at  $60^\circ$ .

Although there is a high density of AuNRs on AAO substrates that are aligned along the surface indentations, their plasmonic resonances are sensitive to variations in their geometrical dimensions, as well as to the gap distances between contiguous rods (see **Figure 10.6**). Additionally, these plasmons are generally expected to lie below 700 nm light wavelength (**Figure 10.3 a,b**), and therefore, they cannot be directly excited neither by the 785 nm laser light nor by the emitted inelastic signal at even larger wavelengths. However, the gap geometry leads to large field enhancements near the surface even at lower photon energies due to non-resonant plasmon

polarization, thus contributing to a substantial SERS enhancement, as shown in **Figure 10.6c**. The actual value of the enhancement depends on the specific gap separations. In our samples, we expect to have a distribution of separations of the order of a few nanometers down to touching. The effect of the substrate is not contemplated in the calculations shown in **Figure 10.6**, but as already mentioned the substrate will have a strong influence on the dielectric environment and will lead to a substantial redshift of the spectra similar to the simulations shown in **Figure 10.6a,c** for rods in water compared with air. Furthermore, the tip-to-tip dimer configuration may also lead to a further red shift as depicted in **Figure 10.6a,b**. Thus, both effects will lead to a larger SERS enhancement because of a greater degree of overlap with the wavelengths of excitation of the light.

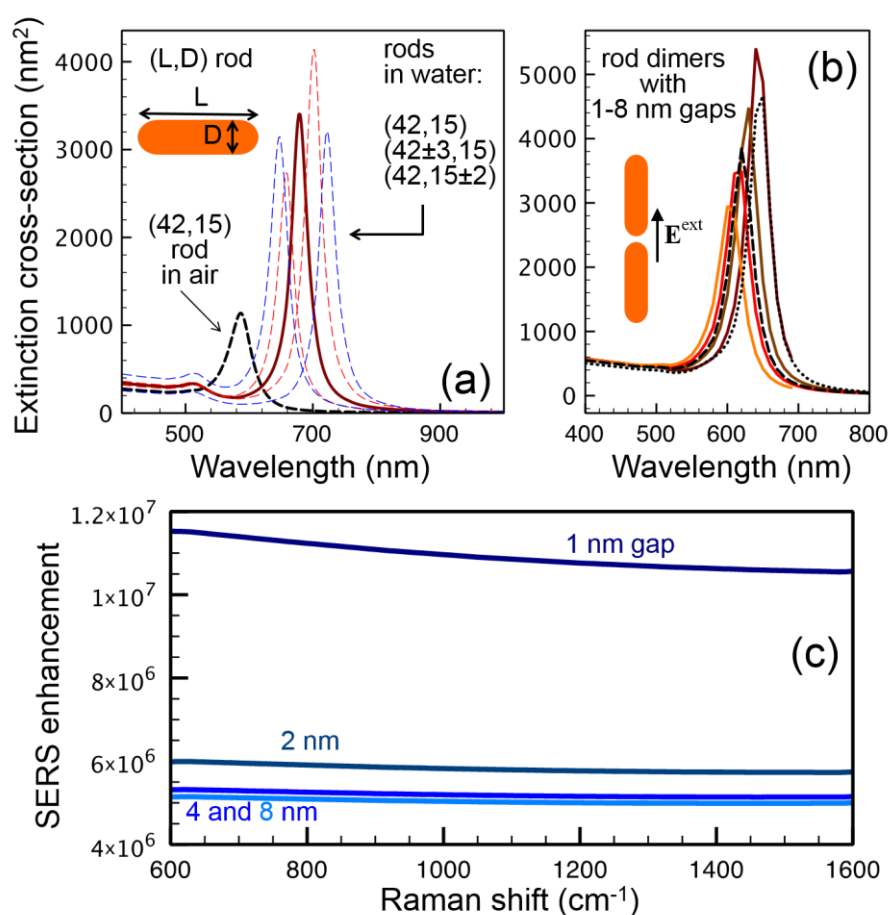


**Figure 10.6.** Optical response and SERS activity of individual and paired GNRs. a) Extinction cross-section of individual AuNRs of dimensions similar to those shown in Figure 2. The longitudinal resonance of rods in water (right curves) is considerably red-shifted with respect to airborne rods (left curves), and it is also shifted due to variations in rod dimensions, giving rise to an observed broad peak (Figure 2a). b) Optical resonance of pairs of AuNRs

longitudinally aligned as observed on an AAO sample (Figure 10.4). A plasmon redshift accompanied by an increase in cross section is observed as the gap is narrowed down from 8 to 1 nm (solid curves). The plasmon is also sensitive to the dimensions of the rods (see dotted curve, corresponding to a (39,15)–(42,15) dimer, and dashed curve, for (42,13)–(42,15), both of them with a 2-nm gap). c) Surface-averaged SERS enhancement factors for molecules distributed 0.5 nm away from the surface of two neighboring nanorods aligned as shown in the inset of (b). The rods are assumed to be either in air (broken curves) or in water (solid curves) and illuminated with 785 nm light (a water environment might be more appropriate to describe residual humidity surrounding the rods during the SERS measurements). The enhancement is referred to the Raman signal from the same molecules away from the rods, averaged over polarizations and molecule orientations for both illumination and light collection along directions normal to the rod axes. The inset in (c) shows the near-field intensity of the gap mode in the 4-nm-gap dimer in water (linear scale saturated to 5000 times the incident field).

In order to test the optical efficiency of our materials for SERS, we designed an experiment involving two well-known analytes, benzenethiol (BT) and 2-naphtioic acid (NA). Furthermore, the same experiment was carried out on a commercial optical surface (Klarite) (see **Figure 10.7**) in order to compare the results with those obtained from a common SERS substrate. Before the analyte deposition, the plasmonic substrates were treated with oxygen plasma to eliminate residual CTAB from the plasmonic surfaces.<sup>42</sup> Both substrates were subsequently exposed to benzenethiol in gas phase. It is important to note that with this experimental setup the gaseous BT is adsorbed onto the entire plasmonic surfaces. Although both plasmonic substrates show clearly the vibrational pattern of BT (C–H bending at  $1022\text{ cm}^{-1}$ , ring breathings at  $1073$  and  $999\text{ cm}^{-1}$ , and ring stretching at  $1570\text{ cm}^{-1}$ ),<sup>43</sup> the average intensity of the obtained spectra is remarkably different, as shown in **Figure 10.7**.

It is thus instructive to point out some differences between both types of samples (AAO-GNRs and Klarite®). First, AAO-GNRs films provide a homogeneous signal through the entire film, which is covered with a rather homogeneous density of hotspots (mainly rod ends and tip-to-tip gaps), while Klarite® substrates present a high activity only in a sparse set of randomly occurring spots on the surface. The homogeneous distribution of hotspots (tip-to-tip plasmonic coupling between the rods trapped in the grooves) in our films is in clear contrast with the commercial

substrate, which exhibits a characteristic random distribution of such optically high-efficient regions for evaporated films. Furthermore and importantly, our substrates provide a five-fold higher signal than provided by the best spots in the Klarite® substrate.

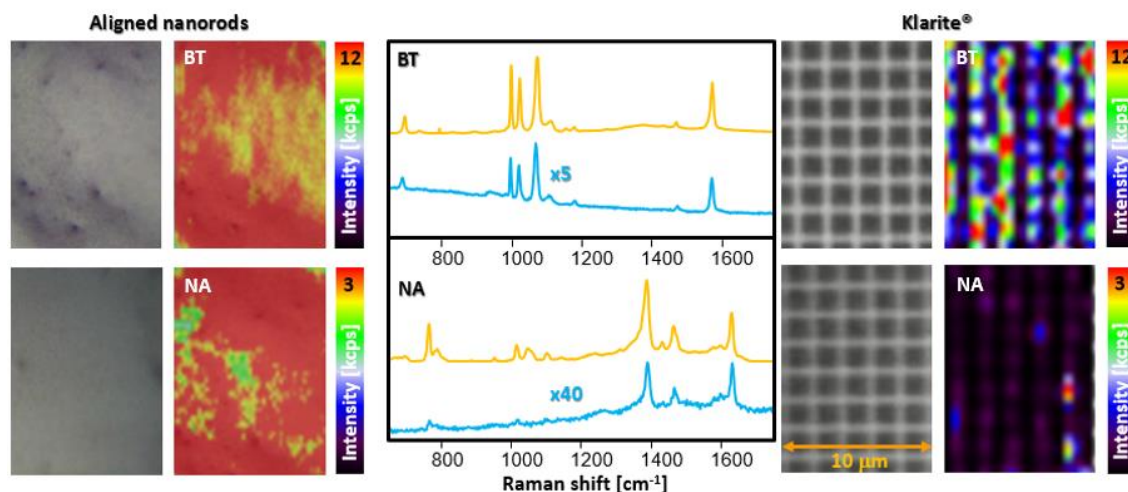


**Figure 10.7.** Optical and SERS images (left) and SERS spectra (yellow) of BT and NA in AAO-GNRs compared with the same analytes on a commercial surface Klarite® (right and blue spectra).

The effect of hydrophobicity provided by the AAO-GNRs substrate after plasma cleaning of CTAB on aqueous solutions deserves further consideration. We studied it, a diluted solution of NA in water ( $10\ \mu\text{L}$ ,  $10^{-5}\ \text{M}$ ) was cast over both substrates and air dried. The intrinsic hydrophobicity of the alumina seems to determine the contact angle of occurring droplets in the AAOGNRs substrates, which is similar to the one reported above ( $105^\circ$ ), with the final result of a concentration of the analyte on a small spatial region that is fully covered with plasmonic particles. In contrast, the drop contact angle in the commercial substrate was much smaller ( $68^\circ$ ), thus resulting in more diluted analyte distributions on the surface. As a consequence, although both surfaces show SERS activity of NA (ring stretching at  $1632$  and at  $1388\ \text{cm}^{-1}$ , CH bending at  $1468\ \text{cm}^{-1}$ , ring breathing at  $1018\ \text{cm}^{-1}$ , and C-H deformation at  $770\ \text{cm}^{-1}$ ),<sup>44</sup> AAO-GNRs substrates exhibit a similar surface homogeneity to that commented above, but with an additional intensification of the SERS signal that is quantified by a 40-fold observed increase in intensity with respect to the commercial substrate.

## Conclusion

In summary, we demonstrate a new method for the large-scale production of efficient plasmonic surfaces based on controlled organization of gold nanorods retained on AAO surfaces. We take advantage of colloid synthesis methods to prepare particles with appropriate dimensions and we use surface chemistry to retain and align them on grooved AAO substrates. This results in an abundant distribution of hotspots originating in tip-to-tip interaction between the rods, where SERS amplification is taking place. We further exploit the physical and chemical properties of the AAO surface to design an optical sensor with the ability of concentrating trace amounts of analytes in an aqueous solution, yielding further intensification of the SERS signals. This method of preparing plasmonic substrates paves the road for the fabrication of reactive-strip optical sensors that are especially suitable for field analysis in environmental monitoring or the design of diagnostic devices for medical applications.

## Experimental Section

*Materials:* Silver nitrate (99.9999%,  $\text{AgNO}_3$ ), sodium borohydride (99.99%,  $\text{NaBH}_4$ ), gold(III) chloride trihydrate (99.9%,  $\text{HAuCl}_4 \cdot 3\text{H}_2\text{O}$ ), nitric acid (32.5%,  $\text{HNO}_3$ ), benzenethiol, 2-naphthoic acid, and ascorbic acid (99%) were purchased from Sigma–Aldrich (Germany). Cetyltrimethylammonium bromide (99%, CTAB) was obtained from Merck. All reactants were used without further purification. Mili-Q water ( $18 \text{ M}\Omega \cdot \text{cm}^{-1}$ ) was used in all aqueous solutions, and all the glassware was cleaned with aqua regia before the experiments. High-purity Al foil of 1-mm thickness (99.997%) supplied by Sigma–Aldrich was used as a substrate for fabrication of AAO. Phosphoric acid, perchloric acid, and ethanol were also supplied by Sigma–Aldrich (Germany) and used as received.

*Preparation of AAO Substrates:* Al foils were cut in rectangles (7 mm  $\times$  40 mm), cleaned with acetone, and distilled water in order to remove any residuals and then dried under dry air. After cleaning, the Al foils were electrochemically polished in a 1:4 mixture solution of 65 wt%  $\text{HClO}_4$  and 96 vol% ethanol. Temperature during the polishing procedure was kept under 5 °C. Mirror-finished Al foils with exposed-to-anodization area of 3 cm<sup>2</sup> were used as an anode in a home-made two-electrode

electrochemical cell with Pt-wire electrode serving as a cathode (distance between electrodes was set to 1 cm). The anodization process was performed in galvanostatic mode under a constant current of  $16 \text{ mA cm}^{-2}$  for time periods of 10, 30, 90, and 180 s at ambient temperature.  $1.0 \text{ M H}_3\text{PO}_4$  was used as a working electrolyte.

*Preparation of Gold Nanorods:* Particles of  $\approx 42 \text{ nm}$  length and  $15 \text{ nm}$  width were produced by adapting an established procedure reported.<sup>30,45</sup> Briefly, seed particles were prepared by adding  $300 \mu\text{L}$  of a  $0.01 \text{ M NaBH}_4$  solution in a  $5 \text{ mL}$  mixture of  $0.1 \text{ M CTAB}$  and  $0.25 \times 10^{-3} \text{ M HAuCl}_4$  under vigorous stirring. The solution was stirred rapidly for 2 min followed by continued slow stirring. A  $200 \text{ mL}$  of a  $0.1 \text{ M CTAB}$  solution containing  $0.25 \times 10^{-3} \text{ M HAuCl}_4$ ,  $0.04 \times 10^{-3} \text{ M AgNO}_3$ ,  $1.3 \text{ mL}$  of a  $0.1 \text{ M HNO}_3$  solution to adjust the pH, and  $0.35 \times 10^{-3} \text{ M}$  ascorbic acid as reducing agent were prepared.  $2 \text{ mL}$  of the prepared seeds was added to this solution after 30 min of stirring. The entire solution was mixed extensively and reaction took place at  $32 \text{ }^\circ\text{C}$  for 24 h. The particles were cleaned and concentrated *via* multiple centrifugation steps at  $16000 \text{ rcf}$  for 30 min to a final gold concentration of  $5 \text{ mg mL}^{-1}$  and  $7.5 \times 10^{-3} \text{ M CTAB}$ .

*Nanorod Organization:* In order to organize the particles, a solution containing Au NRs was spin-coated on the aluminum substrates, which were pasted on a glass slide as support. The most critical experimental parameters to achieve a good particle organization are the CTAB and particle concentration together with the spin speed and time. These parameters were adjusted in order to achieve the best results as follow:  $20 \mu\text{L}$  of the particle solution ( $5 \text{ mg}\cdot\text{mL}^{-1} \text{ Au}$  and  $7.5 \times 10^{-1} \text{ M CTAB}$ ) were spin-coated at  $2000 \text{ rpm}$  for  $120 \text{ s}$ . The substrates with the deposited nanoparticles show a red color.

*Characterization:* UV–vis spectroscopy (PerkinElmer, Lambda 19), UV–vis reflectance spectroscopy (Analytik Jena AG, SPECORD PLUS), transmission and scanning electron microscopy (TEM, LEO 922 EFTEM operating at  $200 \text{ kV}$  and LEO 1530 FE-SEM, Zeiss, respectively) were applied to characterize the optical response, structure, and size of the nanoparticles and their arrays. AFM images were obtained using a commercial atomic force microscope (Dimension<sup>TM</sup> 3100M equipped with a Nanoscope IIIa controller, Veeco Instruments Inc., USA) operating in tapping mode. Silicon

cantilevers with a force constant of typically 35–47.2 N·m<sup>-1</sup> (OMCL-AC160TS, Olympus, Japan, typical frequency of 303 kHz) were utilized.

*SERS Characterization:* Benzenethiol was adsorbed in gas phase on the whole surface of the metallic samples by casting a drop of BT (0.1 M in ethanol) in a Petri dish where the substrate was also contained. A diluted solution of naphthoic acid (10 μL, 10<sup>-5</sup> M) was cast on the plasmonic surfaces and air dried. SERS spectra were collected in backscattering geometry with a Renishaw Invia Reflex system equipped with a 2D-CCD detector and a Leica confocal microscope. The spectrograph used a high-resolution grating (1200 g·cm<sup>-1</sup>) with additional band pass filter optics. Excitation of the sample was carried out with a 785 nm diode laser line, with acquisition times of 200 ms and power at the sample of about 1 mW, using the Renishaw's StreamLine accessory. The laser was focused onto the sample with a 50× objective providing a spatial resolution of ca. 1 μm.

## Acknowledgements

M.T. and P.C. contributed equally to this work. This work was funded by the Spanish Ministerio de Economía y Competitividad (CTQ2011-23167), the European Research Council (CrossSERS, FP7MC-IEF329131, PRIOSERS FP7MC-IEF-623527, and ERC-2012-StG 306686 METAMECH), NatoCBRN collaborative project CLG 984267, the German Research Foundation (DFG) within the collaborative research center SFB 840. M.T. was supported by the Elite Network Bavaria in the frame of the Elite Study Program “Macromolecular Science” and funded *via* a grant for Ph.D. candidates according to Bavarian elite promotion law (BayEFG).

## References

- (1) Halas, N. J.; Moskovits, M., Surface-enhanced Raman spectroscopy: Substrates and materials for research and applications. *MRS Bull* **2013**, *38*, 607-614.
- (2) Sharma, B.; Cardinal, M. F.; Kleinman, S. L.; Greeneltch, N. G.; Frontiera, R. R.; Blaber, M. G.; Schatz, G. C.; Van Duyne, R. P., High-performance SERS substrates: Advances and challenges. *MRS Bull* **2013**, *38*, 615-624.
- (3) Alvarez-Puebla, R. A., Effects of the Excitation Wavelength on the SERS Spectrum. *J Phys Chem Lett* **2012**, *3*, 857-866.
- (4) Otto, A., The 'chemical' (electronic) contribution to surface-enhanced Raman scattering. *J Raman Spectrosc* **2005**, *36*, 497-509.
- (5) Andreou, C.; Hoonejani, M. R.; Barmi, M. R.; Moskovits, M.; Meinhart, C. D., Rapid Detection of Drugs of Abuse in Saliva Using Surface Enhanced Raman Spectroscopy and Microfluidics. *ACS Nano* **2013**, *7*, 7157-7164.
- (6) Zhang, R.; Xu, B.-B.; Liu, X.-Q.; Zhang, Y.-L.; Xu, Y.; Chen, Q.-D.; Sun, H.-B., Highly efficient SERS test strips. *Chem Commun* **2012**, *48*, 5913-5915.
- (7) Lacy, W. B.; Williams, J. M.; Wenzler, L. A.; Beebe, T. P.; Harris, J. M., Characterization of SiO<sub>2</sub>-overcoated silver-island films as substrates for surface-enhanced Raman scattering. *Anal Chem* **1996**, *68*, 1003-1011.
- (8) Otto, A., On the significance of Shalaev's "hot spots" in ensemble and single-molecule SERS by adsorbates on metallic films at the percolation threshold. *J Raman Spectrosc* **2006**, *37*, 937-947.
- (9) Abu Hatab, N. A.; Oran, J. M.; Sepaniak, M. J., Surface-enhanced Raman spectroscopy substrates created via electron beam lithography and nanotransfer printing. *ACS Nano* **2008**, *2*, 377-385.
- (10) Rosi, N. L.; Mirkin, C. A., Nanostructures in biodiagnostics. *Chem Rev* **2005**, *105*, 1547-1562.
- (11) Sharma, B.; Frontiera, R. R.; Henry, A.-I.; Ringe, E.; Van Duyne, R. P., SERS: Materials, applications, and the future. *Mater Today* **2012**, *15*, 16-25.

- 
- (12) Matczyszyn, K.; Olesiak-Banska, J., DNA as scaffolding for nanophotonic structures. *J Nanophotonics* **2012**, *6*, 1-15.
- (13) Guerrini, L.; Pazos, E.; Penas, C.; Vázquez, M. E.; Mascareñas, J. L.; Alvarez-Puebla, R. A., Highly Sensitive SERS Quantification of the Oncogenic Protein c-Jun in Cellular Extracts. *J Am Chem Soc* **2013**, *135*, 10314-10317.
- (14) Tao, A.; Kim, F.; Hess, C.; Goldberger, J.; He, R. R.; Sun, Y. G.; Xia, Y. N.; Yang, P. D., Langmuir-Blodgett silver nanowire monolayers for molecular sensing using surface-enhanced Raman spectroscopy. *Nano Lett* **2003**, *3*, 1229-1233.
- (15) Pieczonka, N. P. W.; Goulet, P. J. G.; Aroca, R. F., Chemically selective sensing through layer-by-layer incorporation of biorecognition into thin film substrates for surface-enhanced resonance Raman scattering. *J Am Chem Soc* **2006**, *128*, 12626-12627.
- (16) Alba, M.; Pazos-Perez, N.; Vaz, B.; Formentin, P.; Tebbe, M.; Correa-Duarte, M. A.; Granero, P.; Ferre-Borrull, J.; Alvarez, R.; Pallares, J.; Fery, A.; de Lera, A. R.; Marsal, L. F.; Alvarez-Puebla, R. A., Macroscale Plasmonic Substrates for Highly Sensitive Surface-Enhanced Raman Scattering. *Angew Chem, Int Ed* **2013**, *52*, 6459-6463.
- (17) Pazos-Perez, N.; Ni, W.; Schweikart, A.; Alvarez-Puebla, R. A.; Fery, A.; Liz-Marzan, L. M., Highly uniform SERS substrates formed by wrinkle-confined drying of gold colloids. *Chem Sci* **2010**, *1*, 174-178.
- (18) Masuda, H.; Fukuda, K., Ordered Metal Nanohole Arrays Made by a 2-Step Replication of Honeycomb Structures of Anodic Alumina. *Science* **1995**, *268*, 1466-1468.
- (19) Skorb, E. V.; Andreeva, D. V., Surface Nanoarchitecture for Bio-Applications: Self-Regulating Intelligent Interfaces. *Adv Funct Mater* **2013**, *23*, 4483-4506.
- (20) Nielsch, K.; Choi, J.; Schwirn, K.; Wehrspohn, R. B.; Gosele, U., Self-ordering regimes of porous alumina: The 10% porosity rule. *Nano Lett* **2002**, *2*, 677-680.

- (21) Li, F. Y.; Zhang, L.; Metzger, R. M., On the growth of highly ordered pores in anodized aluminum oxide. *Chem Mater* **1998**, *10*, 2470-2480.
- (22) Chaudhar.P, Hillock Growth in Thin-Films. *J Appl Phys* **1974**, *45*, 4339-4346.
- (23) Michalska-Domanska, M.; Norek, M.; Stepniowski, W. J.; Budner, B., Fabrication of high quality anodic aluminum oxide (AAO) on low purity aluminum-A comparative study with the AAO produced on high purity aluminum. *Electrochim Acta* **2013**, *105*, 424-432.
- (24) Kant, K.; Low, S. P.; Marshal, A.; Shapter, J. G.; Losic, D., Nanopore Gradients on Porous Aluminum Oxide Generated by Nonuniform Anodization of Aluminum. *ACS Appl Mater Interfaces* **2010**, *2*, 3447-3454.
- (25) Rana, K.; Kucukayan-Dogu, G.; Bengu, E., Growth of vertically aligned carbon nanotubes over self-ordered nano-porous alumina films and their surface properties. *Appl Surf Sci* **2012**, *258*, 7112-7117.
- (26) Chen, H.; Shao, L.; Li, Q.; Wang, J., Gold nanorods and their plasmonic properties. *Chem Soc Rev* **2013**, *42*, 2679-2724.
- (27) Aizpurua, J.; Bryant, G. W.; Richter, L. J.; de Abajo, F. J. G.; Kelley, B. K.; Mallouk, T., Optical properties of coupled metallic nanorods for field-enhanced spectroscopy. *Phys Rev B: Condens Matter Mater Phys* **2005**, *71*, 235420-1-13.
- (28) Lee, A.; Ahmed, A.; dos Santos, D. P.; Coombs, N.; Park, J. I.; Gordon, R.; Brolo, A. G.; Kumacheva, E., Side-by-Side Assembly of Gold Nanorods Reduces Ensemble-Averaged SERS Intensity. *J Phys Chem C* **2012**, *116*, 5538-5545.
- (29) Wang, L.; Zhu, Y.; Xu, L.; Chen, W.; Kuang, H.; Liu, L.; Agarwal, A.; Xu, C.; Kotov, N. A., Side-by-Side and End-to-End Gold Nanorod Assemblies for Environmental Toxin Sensing. *Angew Chem, Int Ed* **2010**, *49*, 5472-5475.
- (30) Jana, N. R.; Gearheart, L.; Murphy, C. J., Wet chemical synthesis of high aspect ratio cylindrical gold nanorods. *J Phys Chem B* **2001**, *105*, 4065-4067.
- (31) Bornside, D. E.; Macosko, C. W.; Scriven, L. E., Spin Coating - One-Dimensional Model. *J Appl Phys* **1989**, *66*, 5185-5193.

- (32) Colson, P.; Cloots, R.; Henrist, C., Experimental Design Applied to Spin Coating of 2D Colloidal Crystal Masks: A Relevant Method? *Langmuir* **2011**, *27*, 12800-12806.
- (33) Seemann, R.; Brinkmann, M.; Herminghaus, S.; Khare, K.; Law, B. M.; McBride, S.; Kostourou, K.; Gurevich, E.; Bommer, S.; Herrmann, C.; Michler, D., Wetting morphologies and their transitions in grooved substrates. *J Phys: Condens Matter* **2011**, *23*, 184108-1-16.
- (34) Seemann, R.; Brinkmann, M.; Kramer, E. J.; Lange, F. F.; Lipowsky, R., Wetting morphologies at microstructured surfaces. *Proc Natl Acad Sci USA* **2005**, *102*, 1848-1852.
- (35) Karan, S.; Mallik, B., Power spectral density analysis and photoconducting behavior in copper(II) phthalocyanine nanostructured thin films. *Phys Chem Chem Phys* **2008**, *10*, 6751-6761.
- (36) Xu, C.; Tian, H.; Reece, C. E.; Kelley, M. J., Topographic power spectral density study of the effect of surface treatment processes on niobium for superconducting radio frequency accelerator cavities. *Phys Rev Spec Top--Accel Beams* **2012**, *15*, 043502-1-18.
- (37) Raspal, V.; Awitor, K. O.; Massard, C.; Feschet-Chassot, E.; Bokalawela, R. S. P.; Johnson, M. B., Nanoporous Surface Wetting Behavior: The Line Tension Influence. *Langmuir* **2012**, *28*, 11064-11071.
- (38) Yacilla, M. T.; Herrington, K. L.; Brasher, L. L.; Kaler, E. W.; Chiruvolu, S.; Zasadzinski, J. A., Phase behavior of aqueous mixtures of cetyltrimethylammonium bromide (CTAB) and sodium octyl sulfate (SOS). *J Phys Chem* **1996**, *100*, 5874-5879.
- (39) Lyvers, D. P.; Moon, J.-M.; Kildishev, A. V.; Shalaev, V. M.; Wei, A., Gold Nanorod Arrays as Plasmonic Cavity Resonators. *ACS Nano* **2008**, *2*, 2569-2576.
- (40) Lin, V. S. Y.; Motesharei, K.; Dancil, K. P. S.; Sailor, M. J.; Ghadiri, M. R., A porous silicon-based optical interferometric biosensor. *Science* **1997**, *278*, 840-843.

- (41) Kim, D.-K.; Kerman, K.; Saito, M.; Sathuluri, R. R.; Endo, T.; Yamamura, S.; Kwon, Y.-S.; Tamiya, E., Label-free DNA biosensor based on localized surface plasmon resonance coupled with interferometry. *Anal Chem* **2007**, *79*, 1855-1864.
- (42) Alvarez-Puebla, R. A.; Agarwal, A.; Manna, P.; Khanal, B. P.; Aldeanueva-Potel, P.; Carbo-Argibay, E.; Pazos-Perez, N.; Vigderman, L.; Zubarev, E. R.; Kotov, N. A.; Liz-Marzan, L. M., Gold nanorods 3D-supercrystals as surface enhanced Raman scattering spectroscopy substrates for the rapid detection of scrambled prions. *Proc Natl Acad Sci U S A* **2011**, *108*, 8157-8161.
- (43) Pazos-Perez, N.; Wagner, C. S.; Romo-Herrera, J. M.; Liz-Marzan, L. M.; Javier Garcia de Abajo, F.; Wittemann, A.; Fery, A.; Alvarez-Puebla, R. A., Organized Plasmonic Clusters with High Coordination Number and Extraordinary Enhancement in Surface-Enhanced Raman Scattering (SERS). *Angew Chem, Int Ed* **2012**, *51*, 12688-12693.
- (44) Alvarez-Puebla, R. A.; Aroca, R. F., Synthesis of Silver Nanoparticles with Controllable Surface Charge and Their Application to Surface-Enhanced Raman Scattering. *Anal Chem* **2009**, *81*, 2280-2285.
- (45) Nikoobakht, B.; El-Sayed, M. A., Preparation and growth mechanism of gold nanorods (NRs) using seed-mediated growth method. *Chem Mater* **2003**, *15*, 1957-1962.

# *11*

## Perspectives



## 11.1 Investigation of Metal Nanocrystal Synthesis utilizing slow Reaction Kinetics

As outlined in **Section 3.4**, the central synthesis parameters for the controlled seed-mediated wet-chemical nanocrystal growth are the seed crystallinity, the reduction agent, the growth directing agents and their counterions.<sup>1,2</sup> Adjustment of these synthesis parameters allows the preparation of a plethora of different metal nanocrystal morphologies. However, there is still a lack of detailed knowledge about the underlying growth mechanisms facilitating defined nanocrystal growth and especially the reaction kinetics are not fully understood, yet. Recently, several research groups reported on the positive effects of aromatic additives and hydroquinone as reducing agent on the size-distribution, the amount of byproducts, and the size-tunability of single-crystalline gold nanorods.<sup>3-5</sup> These approaches are characterized by slow reaction kinetics compared to the standard protocols. In **Chapter 4**, we show that changing the surfactant from cetyltrimethylammonium chloride (CTAC) to benzyldimethylhexadecylammonium chloride (BDAC) strongly reduces the overgrowth kinetics of gold nanorods with silver. At the same time, the crystalline structure and the quality of the obtained Au@Ag cuboids remains unaffected and, thus, this approach represents a simple means to effectively control growth kinetics.

The above discussed examples clearly reveal that aromatic compounds have a great impact on the underlying growth mechanism and strongly alter the reaction kinetics without affecting the crystallinity of the obtained nanoparticles. Investigating the specific role of aromatic compounds within the growth process is the logical next step to further elucidate and enhance the tailored synthesis of metal nanocrystals.

In this context, especially *in-situ* small-angle X-ray scattering (SAXS) is a powerful tool, since this technique provides absolute scattering intensities and information about transient changes in nanoparticle morphology at the same time.<sup>6</sup> However, fast reaction kinetics require high X-ray intensities (synchrotron) and elaborate experimental set-ups. In contrast, slow reaction kinetics obtained for aromatic additives, surfactants, and reducing agents can be resolved in lab-scale SAXS equipment and allow *in-situ* investigation of the nanocrystal growth process.

This opens up new opportunities and investigation of the slow and highly specific anisotropic silver overgrowth process performed with BDAC *via in-situ* SAXS combined with *in-situ* UV-vis-NIR measurements might deliver important new insights into this process. In combination with isothermal calorimetry measurements to determine the binding energies of metal complexes (CTAC vs. BDAC) and colloidal probe AFM measurements to determine the surfactant bilayer stiffness the rate limiting step of the silver overgrowth reaction kinetics might be identified.

In general, similar approaches, to reduce the reaction kinetics of nanocrystal growth and enable in-depth SAXS studies, could be applied to a broad variety of different surfactant-based synthesis protocols, *e.g.* synthesis of gold nanospheres with BDAC or gold nanorods with benzyltrimethylhexadecylammonium bromide (BDAB). These studies might provide a more quantitative picture of the impact of additives (*e.g.* salicylic acid), reducing agents (*e.g.* hydroquinone) and surfactants (CTAB vs. BDAB) and might pave the road towards a better understanding of the underlying growth mechanisms.

## 11.2 Towards a Rational Design Approach for Self-Assembled Metamaterials

As outlined in **Section 3.3** negative index metamaterials require an effective negative permittivity and negative permeability at the same resonance frequency.<sup>7</sup> For metamaterials operating in the visible frequency range, the antisymmetric bonding mode of side-by-side aligned metal nanorods can result in a circular current flow providing negative permeability.<sup>8</sup> However, this dark mode cannot be directly excited and breaking of the symmetry is a pre-requisite to overcome this problem turning the dark into a grey mode, that can be excited. This is a prerequisite for obtaining a magnetic response along this line.

In **Chapter 6** we present the wrinkle-assisted convective self-assembly of gold nanorods into uniaxially oriented single, dimer and trimer chains. The obtained structure type could be tuned *via* precise adjustment of the wrinkle amplitude. This work is a proof of concept and opens up a wide-range of potential follow-up research projects.

The highest degree in assembly quality was achieved for single gold nanorod chains. The longitudinal coupling in tip-to-tip assembled single nanorod chains resulted in a

red-shift of the dominant super-radiant mode. However, the obtained hybridized modes for this assembly configuration do not exhibit any magnetic response. Transfer of uniaxially aligned gold nanorod single chains onto smooth gold substrates will give rise to mirror charges for transversal excitation and, consequently, might provide a significant magnetic response.

Furthermore, gold nanorods assembled into side-by-side configuration are of great interest, as these structures can exhibit an antisymmetric bonding mode for transversal excitation. Because of the polydispersity of the pair-wise assembled gold nanorods and small offsets in relative orientation, this antisymmetric mode might be efficiently excited, providing a magnetic response.

In some cases, side-by-side staggered particle chains were obtained. The formation of these structures was triggered by structural defects, such as small spherical particles. Such assemblies potentially give rise to unusual optical effects such as Fano resonances. To gain control over the formation process of these interesting structures small amounts of spheres might be added to the gold nanorod solution (co-assembly). Furthermore, such structures are preferentially formed for a wrinkle-template withdrawal direction perpendicular to the moving contact line.

Further variation of parameters will render this method routinely applicable for the large-area assembly of gold nanorods into desired structures in close future. Especially, controlling the environmental conditions, *e.g.* temperature and humidity, will be of central importance as they strongly affect the convective self-assembly process.

Furthermore, to fully unravel the complex structure-property relationship of the obtained gold nanorod assemblies, computational modelling in combination with more elaborate characterization techniques, *e.g.* all-angle transmission and reflection UV-vis-NIR measurements, and spectroscopic ellipsometry, need to be applied. This might eventually enable a rational gold nanorod surface-assembly design, which simultaneously provides negative permeability and permittivity within the same frequency range.

In **Chapter 4** we present the lateral epitaxial silver overgrowth of single-crystalline gold nanorods yielding Au@Ag cuboids with precisely tunable silver shell-thickness. The obtained plasmonic building blocks display mirror charges at the metal-metal interface, if excited in the overlap region of the intraband transition of the silver shell and the interband region of the gold core. Wrinkle-assisted self-assembly of these

building blocks (see **Chapter 6**) might result in periodic surface-assemblies exhibiting a magnetic resonance within the visible frequency range. Printing of assembled Au@Ag cuboids onto flat gold surfaces or side selective silver etching of assembled structures will result in symmetry breaking and might enhance the excitation efficiency of the magnetic modes.

Silver shells are chemically instable and can either be etched utilizing nitric acid or serve as precursor layer to form a dielectric silver sulfide shell *via* chemical reaction with sodium sulfide. This renders silver shells as interesting sacrificial spacer layers that can be tuned with nanometer precision *via* controlled epitaxial overgrowth. Consequently, silver shells might be used as means to precisely tune the interparticle distance and coupling efficiency within non-close packed surface-assemblies of gold nanorods (etching, dielectric spacer) or between gold nanorods and the supporting substrate (dielectric spacer).

## References

- (1) Lohse, S. E.; Murphy, C. J., The Quest for Shape Control: A History of Gold Nanorod Synthesis. *Chem Mater* **2013**, *25*, 1250-1261.
- (2) Vigderman, L.; Khanal, B. P.; Zubarev, E. R., Functional Gold Nanorods: Synthesis, Self-Assembly, and Sensing Applications. *Adv Mater* **2012**, *24*, 4811-4841.
- (3) Scarabelli, L.; Grzelczak, M.; Liz-Marzán, L. M., Tuning Gold Nanorod Synthesis through Prereduction with Salicylic Acid. *Chem Mater* **2013**, *25*, 4232-4238.
- (4) Ye, X.; Jin, L.; Caglayan, H.; Chen, J.; Xing, G.; Zheng, C.; Doan-Nguyen, V.; Kang, Y.; Engheta, N.; Kagan, C. R.; Murray, C. B., Improved Size-Tunable Synthesis of Monodisperse Gold Nanorods through the Use of Aromatic Additives. *ACS Nano* **2012**, *6*, 2804-2817.
- (5) Vigderman, L.; Manna, P.; Zubarev, E. R., Quantitative Replacement of Cetyl Trimethylammonium Bromide by Cationic Thiol Ligands on the Surface of Gold Nanorods and Their Extremely Large Uptake by Cancer Cells. *Angew Chem, Int Ed* **2012**, *51*, 636-641.
- (6) Henkel, A.; Schubert, O.; Plech, A.; Sönnichsen, C., Growth Kinetic of a Rod-Shaped Metal Nanocrystal. *J Phys Chem C* **2009**, *113*, 10390-10394.
- (7) Shalaev, V. M.; Cai, W.; Chettiar, U. K.; Yuan, H.-K.; Sarychev, A. K.; Drachev, V. P.; Kildishev, A. V., Negative index of refraction in optical metamaterials. *Opt Lett* **2005**, *30*, 3356-3358.
- (8) Dolling, G.; Enkrich, C.; Wegener, M.; Zhou, J. F.; Soukoulis, C. M.; Linden, S., Cut-wire pairs and plate pairs as magnetic atoms for optical metamaterials. *Opt Lett* **2005**, *30*, 3198-3200.



# *12*

Summary/Zusammenfassung



## Summary

Recent advances in the field of plasmonics are intimately linked to developments in design and fabrication of plasmonic nanostructures. Within this context, my thesis aimed on the large-scale, template-assisted self-assembly of well-defined, anisotropic metal nanoparticles to generate tailored plasmonic surface-assemblies with strong near-field coupling and novel optical properties. This approach requires the preparation of macroscopic structures with control on the nanometer scale (*e.g.* highly selective orientation and small gap sizes, see **Chapters 6-10**) and periodicities below the visible wavelength range of light (*e.g.* 200-400 nm line period, see **Chapter 6**). The collective optical properties of these materials are defined by the optical properties of the individual constituent and coupling effects of close-packed assembled plasmonic building blocks. They hold great potential for different applications, *e.g.* surface-enhanced Raman scattering (SERS), and optical metamaterials. Furthermore, the bottom-up approaches developed within this work are scalable and allow assembly of nanoparticles with different geometries and composition (*e.g.* spherical, rod-like and core-shell particles).

In my thesis I mainly focused on self-assembly of anisotropic plasmonic particles, in particular gold nanorods exhibiting well-defined crystallinity and tunable optical properties depending on their size and aspect ratio. Precise organization into hierarchical surface-assemblies *via* bottom-up self-assembly techniques requires large amounts of high-quality metal nanoparticles along with compatible surface functionalization. My contributions to this research field are summarized in **Part I (Chapter 4-5)** of my thesis entitled: “**Synthesis of Plasmonic Building Blocks**”.

In **Chapter 4**, I presented anisotropic silver-shell gold-core nanoparticles (Au@Ag cuboids) with an optical response precisely tunable within the visible frequency range. These Au@Ag cuboids were grown from well-defined single-crystalline gold nanorods *via* surfactant controlled seed-mediated anisotropic silver overgrowth giving rise to nanometer precision in shell thickness. Variation of the surfactant lead to a reduction of the reaction kinetics by a factor of 10, intimately linked to an increase in growth control. These complex plasmonic core-shell nanoparticles exhibited mirror charges at the metal-metal interface rendering them potential candidates as meta-atoms with intrinsic magneto-optical properties for bottom-up fabrication of metamaterials.

Cationic surfactants that are vital for the controlled synthesis of anisotropic noble metal nanorods come along with several drawbacks, such as cytotoxicity and often unfavorable effects on wetting properties. Thus, I developed a method to completely exchange the surfactant cetyltrimethylammonium bromide (CTAB), used for gold nanorod synthesis, with bovine serum albumin (BSA) presented in **Chapter 5**. The protein functionalized gold nanorods were highly colloidally stable in various biological media and at high nanoparticle concentrations ([Au] of >20 mg/mL). Furthermore, they could even be lyophilized and completely redispersed afterwards. The complete absence of any CTAB on the nanorod surface was proven *via* SERS, which is a central requirement for bio-applications. Additionally, BSA functionalized gold nanorods were successfully implemented into template-assisted self-assembly processes, due to their compliant wetting properties.

Starting from well-defined anisotropic plasmonic building blocks, I prepared large-scale hierarchical surface-assemblies *via* template-assisted self-assembly on wrinkle-substrates and mechano-responsive nanocomposites with highly anisotropic optical properties. My contributions to this research topic are summarized in **Part II (Chapter 6-7)** of my thesis entitled: “**Controlled Alignment of Gold Nanorods**”.

One-dimensional periodic surface-assemblies of gold nanorods were realized on large substrate areas *via* wrinkle-assisted convective self-assembly presented in **Chapter 6**. Precise tuning of wrinkle periodicities and amplitudes down to values of 200 and 5 nm, respectively, in combination with an adjustment of the assembly process enabled, for the first time, the preparation of single, double and triple lines of tip-to-tip aligned gold nanorods on macroscopic sample areas. The resulting plasmonic surface-assemblies exhibited periodicities below the wavelength of the visible light. Furthermore, they displayed an exceptionally high alignment quality with an orientational order parameter determined to be as high as 0.97. Far-field measurements of effective optical properties of transferred macroscopic single-line assemblies revealed their strong dichroism giving rise to an optical order parameter of 0.91. Near-field coupling of tip-to-tip assembled particles with interparticle gap sizes of 7.5 nm resulted in a red-shift of the dominant hybridized super-radiant mode. Breaking of the symmetry, *e.g.* by printing these structures on gold films, or by assembling dimers of parallel rods separated by a dielectric spacer, will give rise to antisymmetric bonding modes with circular current flow patterns. These modes can

provide negative magnetic permeability being a core requirement for bottom-up self-assembly of optical metamaterials.

Plasmonic nanocomposites are another class of materials with optical properties on the macroscale that can be tuned *via* external stimulation. In **Chapter 7**, I presented a strategy to incorporate gold nanorods into an elastomer *via* a phase transfer reaction. The prepared nanocomposites changed their optical properties in a reversible manner upon applying a macroscopic strain. Thorough characterization *via* small-angle x-ray scattering and UV-vis-NIR spectroscopy revealed that the alignment of individual gold nanorods, responsible for the macroscopic optical dichroism, directly scales with the applied strain. Thus, for an elongation of 1000% an optical order parameter as high as 0.82 could be obtained. The prepared stimulus-responsive nanocomposites represent strain sensors and can be used as tunable polarizers. Increasing the filling fraction might result in near-field coupling of dispersed plasmonic particles. Such materials might display highly sensitive optical responses upon local stimulation and might even give rise to strain-dependent anisotropic conductivity for very high filling fractions.

Surface-enhanced Raman spectroscopy (SERS) allows highly efficient characterization and detection of molecules. This is achieved for SERS platforms exhibiting strong electromagnetic field enhancement within nanoscale gaps in between strongly coupled plasmonic nanoparticles. In this context, template-assisted self-assembly holds great potential for the controlled fabrication of close-packed metal nanocrystal surface-assemblies providing homogeneous and high field enhancement. My research results within this field are presented in **Part III (Chapter 8-10)** of my thesis entitled: “**Close-Packed Nanoparticle Assemblies as Surface-Enhanced Raman Spectroscopy Platforms**”.

Since SERS relies on close proximity of the analyte to the metal surface, I investigated the impact of cleaning procedures on the SERS efficiency for gold nanorods in solution and assembled into close-packed films, presented in **Chapter 8**. Particles in solution exhibited a 4 times higher SERS intensity after removing excess CTAB. Plasma-cleaning of gold nanorod films lead to an enhancement in homogeneity and intensity of SERS signals. Furthermore, I investigated the impact of the aspect ratio of assembled gold nanorods on the SERS intensity. Increasing the aspect ratio resulted in a decrease of the SERS enhancement, due to a decrease in coupling efficiency of the exciting laser light with the resonant modes of the coupled assemblies.

Another access route to SERS platforms is the fabrication of macroscopic pyramidal assemblies of close-packed spherical gold nanoparticles. These substrates were prepared *via* template-assisted self-assembly and exhibited 100 times higher SERS intensities, at the nanoparticulate apex of the pyramids, compared to close-packed gold nanoparticle crystals, as presented in **Chapter 9**. Thus, these substrates enabled single-molecule detection, probed for crystal-violet at a surface concentrations of less than 0.06 molecules/ $\mu\text{m}^2$ . Subsequent surface functionalization with a thiolated iron porphyrin that reversibly traps carbon monoxide gave rise to an efficient reversible optical sensor platform. The carbon monoxide concentration within the environmental atmosphere was monitored online in a cyclic fashion for a concentration range of 20 to 100 ppm. Such optical sensor platforms can be implemented into handheld spectrometers and allow sensitive and reversible detection of trace amounts of toxic compounds.

Gold nanorods, inherently focussing the electromagnetic field at their tips, provide additional strong field enhancement, if assembled in tip-to-tip configuration, due to near-field coupling. In **Chapter 10**, I introduced a strategy for the controlled assembly of gold nanorods akin to the wrinkle-based approach discussed in **Chapter 6**. Anodized aluminum oxide substrates with periodic nanoscale grooves were used as templates to self-assemble close-packed uniaxially aligned single chains of gold nanorods. The obtained SERS substrates displayed homogeneous SERS intensities 40 times higher compared to a commercially available standard substrate.

In conclusion, my thesis aimed on developing comprehensive strategies to prepare macroscopic plasmonic surface-assemblies *via* bottom-up self-assembly approaches and with tailored optical properties. Template-assisted self-assembly of anisotropic plasmonic building blocks allowed precise control over spatial placement and orientation within the prepared plasmonic arrays. The fabricated surface-assemblies displayed unique optical properties without precedent in nature, *e.g.* strong electromagnetic field enhancement, and macroscopic anisotropic optical response.

Still there is a long way to go, to implement current research results within the field of plasmonics into useful applications, such as optical computing, display technology, optical sensing, energy harvesting or optical metamaterials. Nevertheless, there is a great potential for nanostructured plasmonic materials to significantly enhance our future daily lives.

## Zusammenfassung

Aktuelle Fortschritte im Forschungsfeld der Plasmonik sind eng verknüpft mit der Entwicklung im Bereich des Designs und der Herstellung von plasmonischen Nanostrukturen. In diesem Kontext zielte meine Dissertation auf die großflächige, oberflächenkontrollierte Selbstanordnung von wohldefinierten, anisotropen, metallischen Nanopartikeln ab, um maßgeschneiderte plasmonischen Anordnungen auf Oberflächen mit ausgeprägter Nahfeldkopplung und neuen optischen Eigenschaften zu erzeugen. Dieser Ansatz setzt die Herstellung von makroskopischen Strukturen mit Präzision auf der Nanometerskala (z.B. hohe selektive Ausrichtung der Bausteine und kleine Partikelabstände, siehe **Kapitel 6-10**) und einer Periodizität unterhalb der Wellenlänge des Lichtes (z.B. 200-400 nm Linienperiodizität, siehe **Kapitel 6**) voraus. Die kollektiven optischen Eigenschaften, der hergestellten Strukturen, sind definiert durch die optischen Eigenschaften der einzelnen plasmonischen Bausteine und durch Kopplungseffekte innerhalb dichtgepackter Anordnungen. Die erzeugten plasmonischen Oberflächenstrukturen haben ein großes Potential für verschiedene Anwendungen, wie z.B. im Bereich der oberflächenverstärkten Raman-Spektroskopie und für optische Metamaterialien. Die in dieser Arbeit entwickelten „Bottom-up“-Ansätze sind darüber hinaus skalierbar und ermöglichen die Anordnung von Nanopartikeln verschiedener Geometrie und Zusammensetzung (z.B. sphärische, stäbchen-förmige oder Kern-Schale Partikel).

In meiner Dissertation habe ich mich im Wesentlichen auf die Selbstanordnung von anisotropen Goldnanopartikeln mit wohldefinierter Kristallinität konzentriert, deren optische Eigenschaften über ihre Größe und ihr Aspektverhältnis steuerbar sind. Die präzise Anordnung der partikulären Bausteine in hierarchische Überstrukturen mittels Bottom-up Selbstanordnungsmethoden benötigt große Mengen einheitlicher und hochqualitativer Metallnanopartikel mit geeigneter Oberflächenfunktionalisierung. Mein Beitrag zu diesem Forschungsfeld ist in **Teil I (Kapitel 4-5)** meiner Dissertation mit dem Titel „**Synthese von plasmonischen Bausteinen**“ zusammengefasst.

In **Kapitel 4** präsentiere ich anisotrope Silber-Schale Gold-Kern Nanopartikel (Au@Ag Quader) mit präzise einstellbaren optischen Eigenschaften im Bereich des sichtbaren Lichts. Die Herstellung der Au@Ag Quader erfolgte über eine Tensidkontrollierte, Keim-vermittelte anisotrope Silberüberwachung wohldefinierter,

einkristalliner Goldnanostäbchen. Dieser Ansatz ermöglichte die Einstellung der Schalendicke mit Nanometerpräzision. Eine Variation des eingesetzten Tensids resultierte in einer zehnfachen Absenkung der Reaktionskinetik, welche direkt mit einer Erhöhung der Wachstumskontrolle einhergeht. Die hergestellten, komplexen Kern-Schale Partikel kennzeichnen sich durch Spiegelladungen an der Metall-Metall-Grenzfläche. Spiegelladungen lassen auf magneto-optische Eigenschaften schließen, die diese Partikel zu interessanten Kandidaten für die „Bottom-up“-Anordnung von Metamaterialien machen.

Kationische Tenside sind essentiell für die Synthese hochqualitativer, anisotroper, plasmonischer Edelmetallnanopartikel. Allerdings haben sie Eigenschaften die für einige Anwendungsfelder von Nachteil sind, wie zum Beispiel ihre Zelltoxizität oder ihr negativer Einfluss auf das Benetzungsverhalten. Daher habe ich in **Kapitel 5** eine Methode entwickelt, um das Tensid Cetyltrimethylammoniumbromid (CTAB), welches für die Synthese von Goldnanostäbchen genutzt wird, vollständig mit Rinderserumalbumin (BSA) auszutauschen. Die hergestellten protein-funktionalisierten Goldnanostäbchen waren in verschiedenen biologischen Medien und in hohen Konzentrationen ([Au] von >20 mg/mL) kolloidal stabil. Außerdem konnten sie ohne negative Beeinträchtigungen lyophilisiert und anschließend vollständig redispergiert werden. Mittels oberflächenverstärkter Raman-Spektroskopie konnte nachgewiesen werden, dass das Tensid CTAB nicht mehr auf der Oberfläche der Partikel vorhanden war. Dies stellt eine wichtige Voraussetzung für potentielle biologische Anwendungen dar. Darüber hinaus konnten BSA funktionalisierte Goldnanostäbchen, aufgrund ihrer kompatiblen Benetzungseigenschaften erfolgreich in oberflächenkontrollierte Selbstanordnungsmethoden implementiert werden.

Ausgehend von wohldefinierten, anisotropen, plasmonischen Bausteinen habe ich einerseits großflächige und hierarchisch angeordnete Strukturen auf Oberflächen mittels Selbstanordnung auf faltenstrukturierten Substraten erzeugt und andererseits mechanisch einstellbare Nanokomposite hergestellt. Diese Materialien kennzeichnen sich durch ihre makroskopischen anisotropen optischen Eigenschaften. Mein Beitrag zu diesem Forschungsfeld ist in **Teil II (Kapitel 6-7)** dieser Arbeit zusammengefasst und trägt den Titel „**Kontrollierte Anordnung von Goldnanostäbchen**“.

In **Kapitel 6** präsentiere ich die Herstellung großflächiger, eindimensionaler, periodischer Oberflächenanordnungen von Goldnanostäbchen mittels oberflächenkontrollierter, konvektiver Selbstanordnung auf faltenstrukturierten Substraten. Eine präzise Anpassung der Periodizität und der Amplitude der faltenstrukturierten Substrate auf unter 250 nm, beziehungsweise unter 5 nm in Kombination mit der Anpassung des Anordnungsprozesses, ermöglichte zum ersten Mal die erfolgreiche Herstellung von Einzel-, Doppel-, und Dreifachketten von Goldnanostäbchen in Spitze-zu-Spitze Konfiguration auf makroskopischen Substratflächen. Die erzeugten plasmonischen Nanostrukturen hatten eine Periodizität unterhalb der Wellenlänge des sichtbaren Lichts. Außerdem, waren sie durch eine außerordentliche Anordnungsqualität, mit einem Anordnungsparameter von 0.97, gekennzeichnet. Fernfeld-Messungen der effektiven optischen Eigenschaften von übertragenen Einzellinien bewiesen den starken Dichroismus der makroskopischen Anordnungen und der optische Anordnungsparameter wurde auf 0.91 bestimmt. Die Nahfeld-Kopplung, der in Spitze-zu-Spitze angeordneten Partikel mit einem Abstand von 7.5 nm, resultierte in einer Rotverschiebung der dominanten, hybridisierten, strahlenden Mode. In Kombination mit der Möglichkeit die Symmetrie zu brechen, zum Beispiel durch eine Übertragung der Strukturen auf Goldfilme, oder mittels Anordnung von parallel angeordneten Nanostäbchendimeren, getrennt durch ein Dielektrikum, kann eine optische Anregung dieser Strukturen in antisymmetrische, bindende Kopplungsmoden resultieren. Diese Moden können zu einer negativen magnetischen Permeabilität führen, welches eine zentrale Grundvoraussetzung für die Herstellung von Metamaterialien mittels Selbstanordnung darstellt.

Plasmonische Nanokomposite sind eine weitere Klasse von Materialien, deren optische Eigenschaften über externe Stimuli eingestellt werden können. In **Kapitel 7** präsentiere ich eine Strategie zur Einbettung von Goldnanostäbchen in eine Elastomermatrix über eine Phasentransferreaktion. Die erzeugten Nanokomposite haben reversible optische Eigenschaften, die durch das Anlegen einer makroskopischen Zugkraft gesteuert werden können. Eine sorgfältige Charakterisierung mittels Röntgenkleinwinkelstreuung und UV-vis-NIR Spektroskopie zeigte, dass die Ausrichtung der Nanostäbchen, die für die optische Anisotropie verantwortlich ist, direkt mit der angelegten Zugspannung skaliert. Für eine Dehnung von 1000% wurde ein optischer Anordnungsparameter von 0.82

bestimmt. Die hergestellten Nanokomposite mit mechanisch einstellbaren optischen Eigenschaften stellen Zugsensoren dar und können als durchstimmbare optische Polarisatoren genutzt werden. Eine Erhöhung des Füllgrades könnte zu einer Nahfeld-Kopplung der Partikel führen. Dies könnte Materialien ergeben, welche bei lokaler Stimulation mit einer sensitiven optischen Antwort reagieren und eine weitere Erhöhung des Füllgrades könnte sogar zu einer anisotropen und einstellbaren Leitfähigkeit führen.

Oberflächenverstärkte Raman-Spektroskopie (SERS) ist eine Technik, welche die Charakterisierung und Detektion von Molekülen bis hin zur Einzelmolekülspektroskopie ermöglicht. Dies kann mit Substraten, die extreme Feldverstärkung zeigen, erreicht werden, z.B. aufgrund starker Nahfeld-Kopplung in dichtgepackten plasmonischen Oberflächenanordnungen. In diesem Kontext haben oberflächenkontrollierte Selbstanordnungsmethoden ein großes Potential für die Herstellung dichtgepackter Metallnanopartikelstrukturen mit starker und homogener Feldverstärkung. Meine Forschungsergebnisse zu diesem Themengebiet sind in **Teil III (Kapitel 8-10)** meiner Dissertation, mit dem Titel **„Dichtgepackte Nanopartikelanordnungen als Plattform für Oberflächenverstärkte Raman-Spektroskopie“** zusammengefasst.

Da SERS ein Oberflächeneffekt ist, muss sich der Analyt in einem geringen Abstand zur Metalloberfläche befinden. In **Kapitel 8** habe ich daher den Einfluss von Reinigungsprozeduren auf die SERS Effizienz von Goldnanostäbchen in Lösung und in dichtgepackten Anordnungen untersucht. Nanopartikel die von überschüssigem CTAB gereinigt wurden, zeigten eine vierfach erhöhte SERS Intensität. Eine Plasmareinigung von dichtgepackten angeordneter Goldnanostäbchen führte zu einer Erhöhung der Homogenität und der Intensität der erhaltenen SERS Signale. Außerdem habe ich den Einfluss des Aspektverhältnisses der angeordneten Goldnanostäbchen untersucht. Eine Erhöhung des Aspektverhältnisses führte zu einer Absenkung der SERS Intensität, ausgelöst durch eine verringerte Kopplungseffizienz des anregenden Laserlichts mit den resonanten Moden der koppelnden Anordnungen.

Dichtgepackte sphärische Goldnanopartikel, angeordnet in makroskopische pyramidale Überstrukturen stellen eine weitere Möglichkeit dar, effiziente SERS Plattformen herzustellen. Diese Strukturen werden in **Kapitel 9** präsentiert. Die pyramidalen Anordnungen wurden über oberflächenkontrollierte Selbstanordnung

auf strukturierten Substraten hergestellt und wiesen eine hundertfach erhöhte SERS Intensität an ihrer nanometergroßen Pyramidenspitze, verglichen mit dichtgepackten flachen Goldnanopartikelkristallen, auf. Die extreme Feldverstärkung ermöglichte eine Detektion von Molekülen auf dem Einzelmoleküllevel. Dies wurde für Kristallviolett mit einer Oberflächenkonzentration von 0.06 Molekülen/ $\mu\text{m}^2$  nachgewiesen. Durch eine anschließende Oberflächenfunktionalisierung der Pyramiden mit einem Thiol-funktionalisierten Eisenporphyrin, welches eine reversible Bindung mit Kohlenstoffmonoxid eingehen kann, konnte ein hocheffizienter, reversibler optischer Sensor hergestellt werden. Dieser Ansatz erlaubte zyklische Echtzeitmessungen von Kohlenstoffmonoxid in der Atmosphäre in einem Konzentrationsbereich von 20 bis 100 ppm. In Zukunft könnten solche optischen Sensorplattformen in tragbare Spektrometer eingebaut werden und eine sensitive und reversible Messung von Kleinstmengen toxischer Verbindungen in der Atmosphäre ermöglichen.

Goldnanostäbchen, die das elektromagnetische Feld an ihren Spitzen verstärken, erzeugen zusätzlich eine starke Feldverstärkung durch Nahfeld-Kopplung, wenn sie in Spitze-zu-Spitze Geometrie angeordnet werden. In **Kapitel 10** präsentiere ich eine Strategie für die kontrollierte Anordnung von Goldnanostäbchen, ähnlich zu dem oberflächenkontrollierten Ansatz aus **Kapitel 6**. Im Gegensatz zu den faltenstrukturierten Substraten wurden hier anodisierte Aluminiumoxid Substrate mit linearen, nanometergroßen Furchen verwendet, um die Goldnanostäbchen in uniaxial ausgerichtete Ketten anzuordnen. Die erhaltenen Substrate zeigten hydrophobe Oberflächeneigenschaften, die eine lokale Konzentration des in wässriger Lösung gelösten Analyten ermöglichten. Die hergestellten SERS Substrate weisen deutlich homogenere und vierzigfach höhere SERS Intensitäten auf, als ein parallel getestetes, kommerziell erhältliches Standardsubstrat.

Das zentrale Ziel meiner Dissertation war es, umfassende Strategien zur Herstellung großflächiger, plasmonischer Oberflächenstrukturen mit maßgeschneiderten optischen Eigenschaften mittels „Bottom-up“ Selbstanordnungsprozessen zu entwickeln. Die oberflächenkontrollierte Selbstanordnung von anisotropen, plasmonischen Bausteinen auf strukturierten Substraten ermöglichte eine präzise Kontrolle der Position und Ausrichtung innerhalb hergestellter nanostrukturierter Anordnungen. Die über diesen Ansatz erzeugten Oberflächenanordnungen zeigten

spezielle optische Eigenschaften ohne vergleichbare Beispiele in der Natur, wie z.B. ausgeprägte Verstärkung des elektromagnetischen Feldes oder makroskopisch anisotropes optisches Verhalten.

Es ist noch ein langer Weg bis aktuelle Forschungsergebnisse im Bereich der Plasmonik ihren Weg in reale Anwendungen finden werden, wie zum Beispiel optische Computer, Bildschirmtechnologie, optische Detektoren, Energiegewinnung, oder optische Metamaterialien. Dessen ungeachtet, haben die aktuellen Forschungsbemühungen ein großes Potential unser zukünftiges tägliches Leben signifikant zu verbessern.

## Acknowledgements/Danksagungen

An dieser Stelle möchte ich mich bei den zahlreichen Personen die zum Gelingen dieser Arbeit beigetragen haben bedanken.

Ganz besonders möchte ich mich bei meinem Doktorvater Prof. Dr. **Andreas Fery** bedanken. Andreas hat mir dieses interessante und zukunftsweisende Thema überlassen und mich die gesamte Zeit, die ich in seiner Gruppe verbringen durfte, unterstützt, gefördert und motiviert. In den intensiven fachlichen und auch manchmal privaten Diskussionen in den letzten Jahren, habe ich vieles gelernt, das zum Erfolg dieser Arbeit beigetragen hat und mir für die Zukunft in Erinnerung bleiben wird. Ich wünsche Andreas alles Gute für seine zukünftige Herausforderung in Dresden.

Dr. **Nicolas Pazos Perez** hat mich in die Welt der Nanopartikelsynthese eingeführt und auf meinen ersten Schritten im Bereich der Plasmonik unterstützt. Viele Ideen, die in dieser Arbeit enthalten sind, haben wir gemeinsam entwickelt. Er steht mir nicht nur in fachlichen Fragen als Kollege, sondern auch privat als guter Freund, immer mit Rat und Tat zur Seite, dafür möchte ich mich bedanken.

Bei Dr. **Munish Chanana** möchte ich mich für seine hilfreiche fachliche Unterstützung und die vielen guten Ideen, aber ganz besonders auch für seine positive, ehrliche und diskussionsfreudige Art bedanken. Ich wünsche Munish viel Glück, Ausdauer und Geduld für seine zukünftige, ganz private Herausforderung.

Nicht nur bei kleineren Verständnisproblemen, sondern auch in anspruchsvollen wissenschaftlichen Detailfragen konnte ich mich immer an Dr. **Christian Kuttner** und Dr. **Tobias König** wenden. Oft haben die Diskussionen nicht nur die gestellte Frage beantwortet, sondern neue interessante Fragestellungen aufgeworfen und auf diesem Wege zum Gelingen dieser Arbeit beigetragen.

Des Weiteren möchte ich mich ganz besonders bei meinen Kollegen Dr. **Christoph Hanske**, **Mareen Müller** und **Pavel Cherepanov** bedanken. Zusammen haben wir die Zeit der Doktorarbeit durchgestanden und uns nicht nur gegenseitig bei der Arbeit unterstützt und gemeinsam Projekte bearbeitet, sondern uns auch von Zeit zu Zeit gemeinsam vom täglichen Stress abgelenkt. Ohne euch wäre diese Arbeit unmöglich gewesen. Außerdem möchte ich mich bei meinen ehemaligen und aktuellen Kollegen

Dr. **Alexandra Schweikart**, Dr. **Johann Erath**, **Bernhard Glatz**, **Benedikt Neugirg** und **Maximilian Seuß** für die Unterstützung bedanken.

In der Zeit meiner Doktorarbeit hatte ich Gelegenheit einige herausragende Studenten zu betreuen. Besonders bedanken möchte ich mich an dieser Stelle bei **Martin Mayer**. Zusammen haben wir zahlreiche Projekte bearbeitet, nicht immer erfolgreich, aber immer mit viel Enthusiasmus, Spaß und Kreativität. Ebenfalls einen besonderen Dank an **Patrick Probst**, **Max Männel**, **Sarah Lentz** und **Sarah Jessl** für die angenehme und erfolgreiche Zusammenarbeit.

Ohne die Helfer im Hintergrund kann ein Lehrstuhl nicht funktionieren und erfolgreiche Wissenschaft wäre unmöglich. Daher gebührt ein großer Dank **Sybille Zimmerman**, unserer „Lehrstuhl-Mama“. Wann immer ein Problem anfällt, es wird schnell gelöst und wenn man Trost, Motivation oder einfach nur Hilfe braucht, findet sie die richtigen Worte. Darüber hinaus möchte ich mich bei Dr. **Wolfgang Häfner**, **Carmen Kunert**, **Markus Hund** und **Petra Zippelius** für die fachliche und technische Unterstützung während meiner Zeit in der PC II bedanken.

Dem gesamten Lehrstuhl der **PC II** und allen anderen **Kollegen**, **Bekanntem** und **Freunden** aus Bayreuth möchte ich an dieser Stelle noch einmal meine Dankbarkeit für die zurückliegende gute Zeit aussprechen, sie wird mir immer in positiver Erinnerung bleiben. Ich wünsche euch alles Gute für die Zukunft in Dresden oder anderswo.

Meinen langjährigen guten Freunden **Damian** und **Rina**, **Costa**, **Chrisaan**, **Dani**, und **Sebastian** danke ich für die Aktivitäten, Reisen, Unterhaltungen und netten Abende, aber ganz besonders dafür, mich in den richtigen Momenten aus meinem Alltag abzuholen. Ihr nehmt mich so wie ich bin, dafür bin ich euch zutiefst dankbar.

Bedanken möchte ich mich auch bei den **Biochemiker/Chemiker Fußballern**, die mir regelmäßig mit sportlicher Betätigung dabei geholfen haben den Kopf frei zu bekommen.

Ohne meine **Familie**, meine **Mutter**, meinen **Vater**, **Carsten**, meine Brüder **Philipp** und **Dennis** und meine **Großeltern** wäre ich nicht hier und mit Sicherheit wäre das Leben weniger erfüllt. Ich danke euch für die bedingungslose Unterstützung in schwierigen Momenten und den Spaß den wir gemeinsam haben. Ihr habt mir

geholfen die intensiven letzten drei Jahre meiner Dissertation durchhalten und genießen zu können.

Ganz zum Schluss möchte ich mich bei **Daniela** und ihrer Familie bedanken.

Daniela, du hast mein Leben in den letzten Jahren bereichert und wir haben zusammen viele schöne und manche schwierige oder anstrengende Situationen erlebt und gemeistert. Deine Geduld, dein Humor, dein Charme, deine große Unterstützung und deine Liebe haben die letzten Jahre besonders gemacht und ohne dich wäre diese Arbeit nicht möglich gewesen. Ich bin unglaublich dankbar, dass du an meiner Seite bist.



(Eidesstattliche) Versicherungen und Erklärungen

(§ 8 Nr. 6 PromO BayNAT)

Hiermit erkläre ich mich einverstanden, dass die elektronische Fassung der Dissertation unter Wahrung meiner Urheberrechte und des Datenschutzes einer gesonderten Überprüfung hinsichtlich der eigenständigen Anfertigung meiner Dissertation unterzogen werden kann.

(§ 8 Nr. 8 PromO BayNAT)

Hiermit erkläre ich an Eides statt, dass ich diese Arbeit selbständig verfasst und keine anderen als die von mir angegebenen Quellen und Hilfsmittel benutzt habe.

(§ 8 Nr. 9 PromO BayNAT)

Hiermit erkläre ich, dass ich nicht bereits anderweitig ohne Erfolg versucht habe, eine Dissertation einzureichen oder mich der Doktorprüfung zu unterziehen.

(§ 8 Nr. 10 PromO BayNAT)

Hiermit erkläre ich, dass ich keine Hilfe von gewerblichen Promotionsberatern bzw. -vermittlern in Anspruch genommen habe und diese auch künftig nicht in Anspruch nehmen werde.

.....

(Ort, Datum, Unterschrift)